

Felix Schwietert

DYNAMICS AND FORCES IN THE MITOTIC SPINDLE

Dynamics and Forces in the Mitotic Spindle

Felix Schwietert

2022

Dissertation
zur Erlangung des Grades eines
Doktors der Naturwissenschaften

vorgelegt an der
Fakultät Physik
Technische Universität Dortmund

Erstgutachter: Prof. Dr. Jan Kierfeld
Zweitgutachter: Prof. Dr. Herre Jelger Risselada

Datum der Verteidigung: 16.09.2022

Abstract

Microtubules are cylindrical cytoskeletal filaments. Their polymerization dynamics is characterized by a dynamic instability between phases of growth and shrinkage. The stochastic switches from shrinkage to growth and vice versa are called rescues and catastrophes, respectively. Experimental observations characterized the latter ones as multistep processes. In the first part of this thesis, we extend the empirical Dogterom–Leibler model of dynamic instability to discuss the effect that a multistep catastrophe mechanism has on the distribution of microtubule lengths in the two regimes of bounded and unbounded growth. We show that, in the former case, the steady state length distribution is non-exponential and has a lighter tail if multiple steps are required to undergo a catastrophe. If rescue events are possible, we detect a maximum in the distribution, i.e., the microtubule has a most probable length greater than zero. In the regime of unbounded growth, the length distribution converges to a Gaussian distribution whose variance decreases with the number of catastrophe steps.

In the mitotic spindle, microtubules attach to chromosomes via kinetochores, and their depolymerization forces give rise to stochastic chromosome oscillations during metaphase. In the second part of this thesis, we investigate the cooperative stochastic microtubule dynamics in spindle models consisting of ensembles of parallel microtubules, which are attached to kinetochores via elastic linkers. We include the dynamic instability of microtubules and forces on microtubules and kinetochores from elastic linkers. A one-sided model with a single kinetochore exposed to an external force is solved analytically employing a mean-field approach based on Fokker–Planck equations. The solution establishes a bistable force–velocity relation of the kinetochore. Coupling the kinetochores of two such bistable systems elastically in the full two-sided model gives rise to oscillations, which can explain stochastic chromosome oscillations in metaphase. We derive constraints on linker stiffness and microtubule number for these oscillations. Including poleward microtubule flux into the model, we can provide an explanation for the experimentally observed suppression of chromosome oscillations in cells with high flux velocities. Chromosome oscillations persist in the presence of polar ejection forces, however, with a reduced amplitude and a phase shift between sister kinetochores. Moreover, polar ejection forces are necessary to align the chromosomes at the spindle equator and stabilize an alternating oscillation pattern of the two kinetochores. Finally, we modify the model such that microtubules can only exert tensile forces on the kinetochore. Then, induced microtubule catastrophes after reaching the kinetochore are necessary to stimulate oscillations. The model parameters can be adapted to reproduce experimental results for kinetochore oscillations in PtK1 cells quantitatively.

The microtubule-binding Ndc80 complex is an integral part of kinetochores and is essential to transmit forces from dynamic microtubule ends to the chromosomes. The Ndc80 complex has a rod-like appearance and its mechanical properties are considered important for the dynamic interaction between kinetochores and microtubules. In the final part of this thesis, we present a novel method that allows us to time-trace the effective stiffness of Ndc80 complexes following shortening microtubule ends against an applied force in optical trap experiments. Applying this method to wild type Ndc80 and three further variants, we reveal that each variant exhibits strain stiffening, i.e., the effective stiffness increases under tension that is built up by a depolymerizing microtubule. The strain stiffening relation is roughly linear and independent of the dynamic state of the microtubule. We introduce an elastic model, which shows that the strain stiffening can be traced back to the specific architecture of the Ndc80 complex and the bending elasticity of flaring protofilaments. The model reproduces the roughly linear strain stiffening behavior if a force-dependent binding affinity is taken into account.

Zusammenfassung

Mikrotubuli sind zylinderförmige Filamente und Teil des Zytoskeletts. Ihre Polymerisationsdynamik zeichnet sich durch eine dynamische Instabilität von Wachstums- und Schrumpfphasen aus. Die zufälligen Wechsel vom schrumpfenden in den wachsenden Zustand und umgekehrt werden als Rettungen bzw. Katastrophen bezeichnet. Letztere können experimentellen Beobachtungen zufolge als Mehrschrittprozesse beschrieben werden. Im ersten Teil dieser Arbeit wird das empirische Dogterom-Leibler-Modell der dynamischen Instabilität erweitert, um auszuarbeiten, welche Auswirkungen eine Mehrschrittkatastrophe auf die Längenverteilung eines Mikrotubulus in den Regimen gebundenen und ungebundenen Wachstums hat. Es zeigt sich, dass die Mikrotubuluslängen im gebundenen Regime nicht mehr exponentiell und weniger endlastig verteilt sind, wenn eine Katastrophe aus mehreren Schritten besteht. Wenn Rettungen möglich sind, hat die Verteilung ein Maximum und der Mikrotubulus somit eine wahrscheinlichste Länge, die größer ist als 0. Im Regime ungebundenen Wachstums nähert sich die Längenverteilung einer Normalverteilung an, die mit steigender Anzahl der Katastrophenschritte schmaler wird.

In der Mitosespindel sind Mikrotubuli durch Kinetochore mit den Chromosomen verbunden und üben so Kräfte aus, die in der Metaphase zu stochastischen Oszillationen der Chromosomen führen. Im zweiten Teil dieser Arbeit untersuchen wir in Modellen der Mitosespindel die kollektive Dynamik von Mikrotubuli, die durch elastische Federn an Kinetochore gebunden sind. Die Modelle beinhalten die dynamische Instabilität der Mikrotubuli und die Kräfte, die durch die elastischen Verbindungen wirken. Für ein einseitiges Modell mit nur einem Kinetochor, das einer externen Kraft ausgesetzt ist, können mithilfe einer Molekularfeldnäherung Fokker-Planck-Gleichungen aufgestellt und gelöst werden. Aus der Lösung folgt eine bistabile Abhängigkeit der Kinetochorgeschwindigkeit von der externen Kraft. Im zweiseitigen Modell mit zwei elastisch gekoppelten Kinetochoren führt die Bistabilität zu Oszillationen, die denen der Chromosomen in der Metaphase gleichen. Das Modell kann erklären, warum in Zellen mit einem schnellen polwärtigen Mikrotubulusfluss keine Oszillationen beobachtet wurden. Polare Auswurfkräfte gewährleisten im Modell eine Anordnung der Kinetochore am Spindeläquator und führen zu geregelteren Oszillationen mit verringerter Amplitude. Wenn das Modell so geändert wird, dass die Mikrotubuli nur Zugkräfte auf das Kinetochor ausüben können, treten Oszillationen nur unter der Voraussetzung auf, dass in der Nähe der Kinetochore Katastrophen induziert werden. Die Modellparameter können so angepasst werden, dass die modellierten Oszillationen auch in quantitativer Hinsicht mit Messungen in PtK1-Zellen übereinstimmen.

Ein wichtiger Bestandteil des Kinetochors sind stäbchenförmige Ndc80-Komplexe, die den Mikrotubulus binden und deren elastischen Eigenschaften als wichtig für die Kraftübertragung vom Mikrotubulus auf das Chromosom erachtet werden. Im letzten Teil dieser Arbeit wird eine Methode präsentiert, die es erlaubt, den zeitlichen Verlauf der effektiven Steifigkeit von Ndc80-Komplexen zu ermitteln, die in einer optischen Falle entgegen einer Kraft dem schrumpfenden Ende eines Mikrotubulus folgen. Die Anwendung der Methode auf mehrere Experimente zeigt, dass sowohl der Wildtyp als auch drei weitere Ndc80-Varianten steifer werden, wenn der schrumpfende Mikrotubulus sie unter Spannung setzt. Die gemessene Steifigkeit hat eine annähernd lineare Abhängigkeit von der angelegten Kraft und ist unabhängig vom dynamischen Zustand des Mikrotubulus. Mithilfe eines elastischen Modells kann die Versteifung auf die spezielle Architektur des Ndc80-Komplexes sowie auf das Biegen gekrümmter Protofilamente zurückgeführt werden. Ein Modell mit einer kraftabhängigen Bindungsaffinität reproduziert die lineare Beziehung zwischen Steifigkeit und Kraft.

Preface

The thesis you are currently holding in your hands or, more likely, seeing on your screen is written by a physicist and can be assigned to the field of theoretical biophysics. The thesis has three main parts, which are presented in Chapters 2 to 4, respectively. Although loosely connected, each of these parts stands on its own and can be read independently. To make my work accessible to other physicists, each of the above chapters is preceded by a brief section that provides the reader with the necessary knowledge of the cell biological processes studied subsequently. As a theoretical physicist, I apologize for any inaccuracies that a reader with a stronger biological and experimental background than mine may find in those sections or anywhere else in this thesis.

Parts of Chapters 2, 3 and 4 have already been published elsewhere, see the list below. Moreover, Chapter 2 builds on a bachelor's thesis that I have co-supervised, and Chapter 3 is based upon my own master's thesis. It is specified at the appropriate places in the main text which results are new and originally obtained as part of my doctoral research.

Felix Schwietert

Publications of the author

Associated with Chapter 2

Felix Schwietert, Lina Heydenreich, and Jan Kierfeld

Dynamics and length distributions of microtubules with a multistep catastrophe mechanism
bioRxiv (2022). DOI: [10.1101/2022.08.19.504495](https://doi.org/10.1101/2022.08.19.504495)

Associated with Chapter 3

F. Schwietert and J. Kierfeld

Bistability and oscillations in cooperative microtubule and kinetochore dynamics in the mitotic spindle
New Journal of Physics 22.5 (2020), 053008. DOI: [10.1088/1367-2630/ab7ede](https://doi.org/10.1088/1367-2630/ab7ede)

F. Schwietert

Mikrotubuli- und Kinetochor-Dynamik in der Mitosespindel
Masterarbeit, TU Dortmund, 2016

Associated with Chapter 4

F. Schwietert, V. A. Volkov, P. J. Huis in 't Veld, M. Dogterom, A. Musacchio, and J. Kierfeld

Strain stiffening of Ndc80 complexes attached to microtubule plus ends
Biophysical Journal (2022), in press. DOI: [10.1016/j.bpj.2022.09.039](https://doi.org/10.1016/j.bpj.2022.09.039)

Contents

Abstract	iii
Zusammenfassung	v
Preface	vii
1 Introduction	1
2 Multistep dynamics of single microtubules	7
2.1 Structure, functions and dynamics of microtubules	8
2.1.1 Structure and functions of microtubules	8
2.1.2 Filament dynamics and dynamic instability	9
2.2 Modeling dynamics of single microtubules	11
2.2.1 Classical four parameter model of dynamic instability	13
2.2.2 Microtubule dynamics with a multistep catastrophe	14
2.2.3 Results for the bounded regime	16
2.2.4 Results for the unbounded regime	20
2.3 Discussion	22
3 Cooperative microtubule and kinetochore dynamics in the mitotic spindle	25
3.1 The cell cycle	27
3.1.1 Mitosis and cytokinesis	28
3.1.2 The kinetochore–microtubule interface	32
3.1.3 Forces in the mitotic spindle	33
3.2 Model of the mitotic spindle	35
3.2.1 Overview of existing spindle models	35
3.2.2 One-dimensional model of the mitotic spindle	40
3.2.3 One-sided spindle model	42
3.2.4 Simulations	43
3.3 Mean-field theory for bistability and chromosome oscillations	44
3.3.1 Mean-field theory for bistability in the one-sided model	44
3.3.2 Bistability gives rise to oscillations in the two-sided model	51
3.3.3 Constraints on linker stiffness and microtubule number for bistability and oscillations	56
3.4 Generalizations of the minimal spindle model	60
3.4.1 Poleward microtubule flux	60
3.4.2 Polar ejection forces	62
3.4.3 Confinement and catastrophe promotion at the kinetochore	66
3.4.4 Reproduction of kinetochore oscillations in PtK1 cells	72
3.5 Discussion	76

4	Strain stiffening of the Ndc80 complex	85
4.1	The Ndc80 complex	86
4.2	Strain stiffening in experiments	88
4.2.1	Optical trap experiments	88
4.2.2	Time-tracing reveals strain stiffening in single experiments	92
4.2.3	Collective analysis of the stiffening behavior	94
4.2.4	Independence from MT state	95
4.3	Strain stiffening explained by Ndc80 and microtubule structure	97
4.3.1	Stiffness of PLL-PEG	99
4.3.2	Stiffness of the Ndc80 complex	100
4.3.3	Microtubule stiffness	103
4.3.4	Effective stiffness of protofilament bending	107
4.3.5	Catch bond behavior can minimize the cooperative stiffness	109
4.4	Discussion	110
5	Summary and outlook	117
 APPENDIX		125
A	Appendix to Chapter 2	127
A.1	Solution for an age-dependent catastrophe rate	127
A.2	Stationary solution for an infinite step catastrophe process	128
B	Appendix to Chapter 3	129
B.1	Behavior of linker length distributions near the boundary linker extensions	129
B.2	Mean-field theory assuming identical linker extensions	130
B.3	Alternative polar ejection force distributions	133
C	Appendix to Chapter 4	135
C.1	Optical traps and stiffness calibration	135
C.2	Further examples of stiffness time-tracing	136
C.3	Robust regression by minimization of the Huber loss	138
C.4	Worm-like chain model of the Ndc80 complex	138
 Bibliography		141
 Notation		159

Since the cell is the fundamental building block of life, its investigation is one of the main branches of biology [1]. While cell biology was and is still dominated by biochemical methods and approaches, the interest in the physical properties of cells, their compartments and intracellular processes has grown steadily since the middle of the 20th century when biochemistry had long become established as an own area of research [2, 3]. As a consequence, physics does not only enrich today's cell biological research methodologically by providing and improving measuring tools but also conceptually by offering additional and often necessary perspectives on cell biological subjects both by experimental and theoretical approaches. Parallel to physics, also mathematics entered the field of biology [4]. Similarly to the fruitful interplay between physics and mathematics in the last four centuries, biology has been pronounced to not only benefit from but also to bring forward mathematics by giving rise to questions that require development of novel mathematics to be answered [5].

The entries of both physics and mathematics into biological research have been facilitated by several developments. One booster was the development of modern and automated experimental methods. An example of such revolutionizing experimental tools are force spectroscopic instruments like the atomic force microscope (AFM) [6] or optical [7] and magnetic tweezers [8], which allow for measuring as well as applying forces on cells or single macromolecules at the piconewton scale [9]. Typical experiments either examine responses to an external force, e.g., stretching of DNA [10–12] or protein unfolding [13–15], or measure distances and forces that are actively generated by cellular components like motor proteins [16–18] or cytoskeletal filaments [19–21]. Thereby, mechanical forces have been revealed to play an essential role for various cellular processes and to provide a third important pathway for the transmission of inter- and intracellular signals besides biochemical and electric signaling [22]. Due to the mechanical character of these forces, their correct description is a deeply physical issue and, therefore, should be carried out on a biophysical rather than a biochemical basis.

A further consequence of the automation in modern experimental techniques is the vastly increased amount of acquired quantitative data. Such quantitative data also needs to be evaluated quantitatively, which often requires sophisticated statistical methods. Moreover, owing to the quantification of biological data, it is common

¹ Similarly, in physics, which is classically divided into experimental and theoretical physics, computational physics emerged as an additional branch that bridges theory and experiment [25].

² As reported by Freeman Dyson [26], Enrico Fermi ascribed this quote to John von Neumann in 1953. Allowing the four or five parameters to be complex, the statement was actually shown to be true [27].

³ “Milk production at a dairy farm was low so the farmer wrote to the local university, asking help from academia. A multidisciplinary team of professors was assembled, headed by a theoretical physicist, and two weeks of intensive on-site investigation took place. The scholars then returned to the university, notebooks crammed with data, where the task of writing the report was left to the team leader. Shortly thereafter the farmer received the write-up, and opened it to read on the first line: ‘Consider a spherical cow...’” [28]

⁴ Expressed in the above metaphors, the models and approaches used in this thesis are closer to the spherical cow than to von Neumann’s elephant.

today to interpret experimental results by means of quantitative models instead of merely deducing qualitative statements [23, 24]. Both data evaluation and modeling have been facilitated by the enormous evolution of computational resources. The widespread use of computer simulations led to the term *in silico* in reference to the “classical” *in vivo* and *in vitro* experiments.¹

A theoretical model of a cell biological system always has to be a simplification due to the sheer complexity of the cell and its constituents. Even if a detailed *ab initio* approach that starts from a molecular basis were realizable given the available computational resources, it would not have to be helpful. A model that perfectly reflects the real system is just as complex and as hard to grasp, and thus, it will possibly produce no new insights that could not be deduced from the real system, too [23, 24]. Moreover, for any further detail that is included in a model, additional assumptions have to be made and additional parameters are required. If these parameters are not experimentally accessible, they can either be guessed a priori and then left unchanged, or they can be fitted a posteriori to make the model reproduce the behavior of the real system. The more parameters are left free in the fitting process, the greater the chance to find a combination providing the sought results, but the smaller the reliability of the found parameters regarding their uniqueness and their accordance with reality. As John von Neumann once said: “With four parameters I can fit an elephant, and with five I can make him wiggle his trunk.”²

Instead of trying to incorporate as many details as possible, a minimal model that is only based on a few simplifying assumptions often is more valuable. If such a model exhibits the same or at least a similar behavior as the real system, it can reveal the decisive mechanisms, and then be extended step by step to approach a more realistic representation. However, as for extremely detailed models, there is also the opposite risk of simplifying a model to such an extent that crucial parts of the real system are omitted. Oversimplified models are humorously referred to as “spherical cows” based a famous joke about theoretical physicists.³ After all, the task of model building is to find an appropriate balance between feasibility and attention to detail. In this thesis, we follow the strategy to keep the models as simple as possible without ignoring the core elements of the real system, and to vary only a few crucial parameters to investigate their influence in a qualitative manner rather than seeking an artificial quantitative agreement by simultaneously adjusting multiple parameters.⁴

Depending on the matter of interest, the degree of simplification can differ between different models of the same object. This is illustrated in Fig. 1.1 on the example of a microtubule (MT), which is present in all models used in this thesis. MTs are dynamic tubular filaments

and part of the cytoskeleton, where they fulfill various functions. For instance, they serve as tracks for intracellular transport, stabilize the cell and certain cellular structures, and build up the mitotic spindle, which drives the chromosome segregation during mitosis. MTs are built up by cylindrically arranged protofilaments, which themselves are chains of tubulin heterodimers.⁵ In the following two chapters, where we are only interested in the length of a MT and its dynamics, we neglect the tubular shape and the microscopic structure, and treat the MT as a straight line that can grow and shrink continuously (Fig. 1.1A) [29–32]. Later, in Chapter 4, where we examine the elastic properties of the bent protofilaments at the MT tip, we use a finer grained model that considers the individual protofilaments as bendable beams (Fig. 1.1B) [33, 34]. If one is interested in the special polymerization dynamics of a MT in consideration of its discreteness, a first approximation could be the model in Fig. 1.1C, where the MT is mapped to a one-dimensional polymer with rings of tubulin dimers as its monomers [35–38]. In order to investigate how the polymerization depends on the interactions between tubulins within the same and within neighboring protofilaments, a model should reflect the complete spatial structure on a microscopic scale with a tubulin (dimer) as the smallest element (Fig. 1.1D) [39–43]. Even such models contain several degrees of coarse-graining as the tubulins are proteins that have a complex structure themselves (Fig. 1.1E) and consist of a chain of hundreds of amino acids at the molecular scale (Fig. 1.1F) [44].

Quantitative models can further be classified by their implementation, which can be mathematical or computational [23, 46]. Computational models can theoretically be arbitrarily complex but are restricted by computational power and time. Results are obtained by running simulations, which can also include stochastic elements (Monte Carlo (MC) simulations). A simulation is suitable to generate a sample path of a stochastic process, e.g., motion of a Brownian particle. To obtain general results, one has to average over many instances of the same stochastic simulation.⁶ Therefore, a systematic analysis of parameter changes can be computationally very costly so that such analyses are often limited to find one combination of parameters via trial and error that reproduces observations made in the real system. However, as mentioned above, finding such a single parameter set is not a proof for an accordance with reality, though it may pretend the opposite. Mathematical models, on the other hand, are based on algebraic or (partial) differential equations, which can be solved numerically or, if possible, analytically. In the case of a stochastic system, the result of a mathematical model may be a mean value or even the whole, maybe time dependent probability distribution instead of a single sample as obtained from a stochastic simulation. In order to

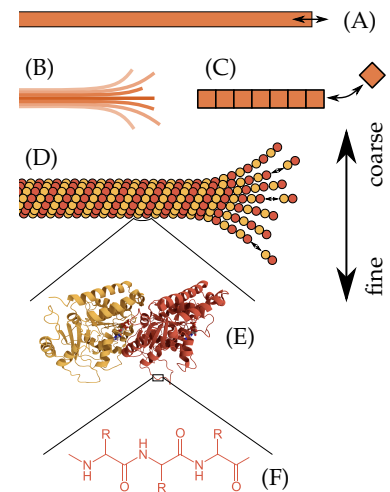


Figure 1.1: Scales of coarse-graining on the example of a microtubule. (A) MT as a continuous 1-dim. object. (B) MT with continuous protofilaments. (C) MT as a discrete 1-dim. polymer. (D) 3-dim. microscopic MT structure as built up by tubulin dimers. (E) Spatial Structure of a tubulin dimer, adapted from [45]. (F) Chemical structure of a generic polypeptide.

⁵ More detailed information about MTs, their structure and their functions is presented in Sec. 2.1.

⁶ This is called *ensemble mean*. In order to describe a system that is in a steady state like the thermodynamic equilibrium, averaging over a long running single simulation is sufficient, since here, the ensemble mean is the same as the time mean according to the ergodic hypothesis.

⁷ and in a sense also because of the stronger simplification since it may make the model comprehensible in the first place.

keep the equations solvable, mathematical models usually require more simplifications and/or a higher degree of coarse-graining than computational models. Despite the stronger simplification,⁷ a mathematical model may provide a greater step towards understanding not only what are the basic mechanisms but also how they work. Once a mathematical model is solved, detection and a systematic analysis of the crucial parameters are possible.

The method of choice should be a combination of both mathematical and computational approaches. In this thesis, the usual approach is to initially develop a model with an appropriate degree of simplification but irrespective of its later implementation. While the initial models can always be implemented in a computational simulation, a mathematical solution, which we want to use for a deeper analysis of the crucial mechanisms, often requires stronger simplifications. However, the mathematical and the computational model are probably identical in a particular limit, which can be, for instance, short or long times or distances, few or many particles, or a steady state of a dynamic system. Therefore, the mathematical results can be used to validate the computational simulations on the one hand, and on the other hand, any conclusion drawn from the mathematical model that lies out of the limits where it is exact can be verified by simulations.

In this thesis, we examine different aspects of MT dynamics and mitosis by means of dynamic and mechanical models. Mitosis is a crucial part of the eukaryotic cell cycle and describes the division of the cell nucleus, which contains the DNA organized in chromosomes. The proper division of the beforehand replicated chromosomes ensures that the two daughter cells that exist after cell division contain the same genetic information. The main results are presented in Chapters 2–4. Though these chapters are loosely connected by their overall topic, they are presented in a widely independent way. Each chapter begins with its own introduction followed by a propaedeutic section about the biological objects and processes that are examined thereafter. Moreover, there are individual discussions at the ends of Chapters 2–4. Only in the summary and outlook in Chapter 5, we review our work from a more global perspective and discuss in some aspects which implications the beforehand independently obtained results have on each other and how they could be linked in future work.

In the following, we give a brief outline of this thesis, referring to the more detailed introductions at the beginning of Chapters 2–4. In Chapter 2, we examine the polymerization dynamics of single MTs using a coarse-grained model as depicted in Fig. 1.1A. MT dynamics is characterized by stochastic switches between phases of constant growth and constant shrinkage, which was first quantified by the empirical Dogterom–Leibler model [29, 30]. While in this

model, the state transitions are assumed to be Poisson processes with constant transition rates, it has later been observed *in vitro* that the transition from growth to shrinkage is better described with an age-dependent transition rate or as a process that requires multiple steps [47–49]. Here, we account for this observation by incorporating such multistep process into the Dogterom–Leibler model. Multistep dynamics results in MT length distributions that are narrower than in the single step model and have a maximum and a lighter tail in the steady state. These dynamic changes may help the MT to adapt for its different functions within the cell.

Chapter 3 is about the cooperative dynamics of MTs and chromosomes during mitosis. Mitosis is driven by the mitotic spindle, in which MTs emerge from two opposite spindle poles. The MTs can bind to kinetochores, two of which are located on opposite sites on each chromosome. When the chromosome is bidirectionally attached, shrinking MTs can pull the two sister chromatids apart and transport them into two daughter nuclei. Before the chromatids are separated, they are aligned in a plate at the spindle equator, where they do not rest but oscillate along the pole to pole axis [50–56]. In order to understand the occurrence of these oscillations, we employ a one-dimensional model of the mitotic spindle that is based on the minimal model of Banigan *et al.* [57]. The model contains a single chromosome represented by two elastically coupled kinetochores, and two opposite ensembles of MTs, which can stochastically bind to the chromosome via simple elastic linkers. Chromosome oscillations can be traced back to a bistable relation between kinetochore velocity and an external force in a one-sided model with only one chromatid and one MT ensemble. A mean-field approach allows us to describe bistability and chromosome oscillations mathematically, and to find lower bounds of the MT–kinetochore linker stiffness for their occurrence. Moreover, the mathematical solution helps us to understand the effects of several additional phenomena like poleward MT flux or polar ejection forces, which we incorporate into the minimal model in the later sections.

MTs are linked to the kinetochore via rod-like Ndc80 complexes. Ndc80 complexes were observed to stiffen under force in recent optical trap experiments [58], which were repeated with three different variants of the Ndc80 complex [59]. In Chapter 4, we first reanalyze these experiments with a novel method that allows us to time-trace the stiffness during MT growth and shrinkage. Later, we develop an elastic model based on the structure of the Ndc80 complex and the elastic properties of the attached MT and its protofilaments. Comparison of the strain stiffening in the experiment and the model suggests that Ndc80–MT binding is enhanced by tension.

Multistep dynamics of single microtubules

2

The *cytoskeleton* is an essential part of a biological cell. It is a filamentous scaffold that—to mention just a few of its functions—provides mechanical stability, defines the cell shape, and is responsible for cell motility as well as intracellular motion and transport processes. Unlike the static human skeleton, the cytoskeleton is a highly dynamic system, whose structures can be assembled and rearranged rapidly, which allows the cell to adapt to altered circumstances.¹

In eukaryotic cells,² the cytoskeleton consists of three types of protein filaments: microtubules, actin filaments, and intermediate filaments, see Fig. 2.1. *Intermediate filaments* do not appear in all eukaryotic cells, but can be found in some metazoans, for instance, in vertebrates. The term intermediate filaments covers a whole family of rope-like protein filaments with a diameter of approximately 10 nm. Due to their ability to withstand tensile forces, their main function is the mechanical stabilization of the cell.

Actin filaments, also called microfilaments, are with a diameter of 8 nm the thinnest of the cytoskeletal filaments. They consist of two F-actin³ strands winded helically around each other as sketched in Fig. 2.2. Each actin subunit has a binding site for adenosine triphosphate (ATP), which tends to be hydrolyzed to adenosine diphosphate (ADP) when it is incorporated into the filament. Since the asymmetrical subunits are aligned with the same orientation within an F-actin strand, i.e., they are assembled head-to-tail, the actin filament itself exhibits a structural polarity: one can differ a slowly polymerizing minus end with an exposed ATP binding site and a fast polymerizing plus end. Together with hydrolysis of the bound ATP, the different reaction kinetics of the two ends result in a polymerizing behavior similar to the one of microtubules, which is described in the following section. With a persistence length of approximately 20 μm [62], actin filaments are comparatively flexible. Within the cell, they are often cross-linked to more rigid networks, for instance, in the actin cortex, which lies beneath the plasma membrane and stabilizes the shape of the cell. A second prominent function of actin filaments is the interplay with myosin motor proteins in muscle cells, which is responsible for muscle contraction.

In this chapter, we focus on the third filament type, the *microtubules* (MTs). After giving a brief overview of the structure and functions of MTs, we discuss their specific polymerization dynamics, which is characterized by stochastic switches between a growing and a

Large parts of this chapter have already been published as a preprint in Ref. [60].

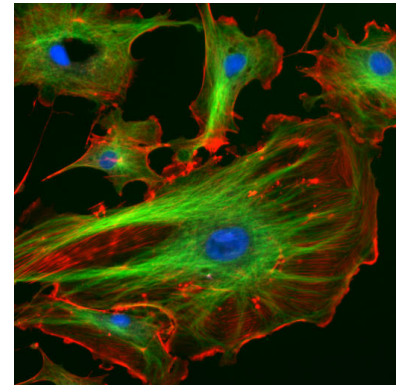


Figure 2.1: Eukaryotic cytoskeleton. The picture shows bovine pulmonary artery endothelial cells. Microtubules are stained green, actin filaments are red, the nucleus blue. [61]

¹ In the short introduction to this chapter as well as the following section 2.1, we generally refer to Alberts *et al.* [1] for any biological information that we present without citing a specific reference.

² The cells of eukaryotes, including animals and plants, are characterized by a cell nucleus containing the chromosomes, see Fig. 2.1.

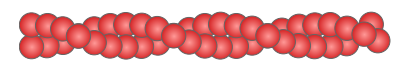


Figure 2.2: Structure of actin filaments.

³ The term F-actin (filamentous) denotes actin proteins that are bound in an actin filament. Free actin monomers are called G-actin (globular).

shrinking state. These dynamics and the consequential length distributions are classically quantified by an empirical four parameter model that describes the state transitions as Poisson processes with constant transition rates [29, 30]. However, *in vitro* measurements that have shown that the growth durations of MTs are not distributed exponentially as one would expect for a constant transition rate led to the conclusion that the catastrophe, which is how the transition from the growth to the shrinking state is called, is rather the result of a series of multiple stochastically occurring steps instead of a single stochastic event [47–49]. In order to account for these observations, we extend the classical four parameter model and examine how the length distributions of MTs are affected by a multistep catastrophe mechanism.

2.1 Structure, functions and dynamics of microtubules

2.1.1 Structure and functions of microtubules

The subunit of a MT is a heterodimer composed of an α -tubulin and a β -tubulin, which are bound non-covalently, see Fig. 2.3A. Both α - and β -tubulin have a binding site for guanosine triphosphate (GTP), however, only the GTP that is bound to the β -tubulin can be hydrolyzed to guanosine diphosphate (GDP) whereas the α -bound GTP is enclosed in the dimer. We will see below that the hydrolysis of tubulin-bound GTP is crucial for the characteristic polymerization dynamics of MTs. A chain of tubulin dimers that are jointed head-to-tail, i.e., α - and β -tubulin appear alternately as shown in Fig. 2.3B, forms a protofilament. Finally, MTs are hollow cylinders consisting of 13 parallel protofilaments⁴ in a slightly helical arrangement. Since within a MT, the subunits form both longitudinal attachments to subunits of the same protofilament as well as lateral attachments to subunits of neighboring protofilaments, the tubulin dimers are tightly bound in the MT lattice and hence can only be added or removed at the ends of the MT. Moreover, due to these multidirectional interactions and the cylindrical structure, MTs are rather stiff filaments with a persistence length in the range of millimeters [62].

⁴ Although MTs with 13 protofilaments are predominant in most species [63, 64], there are several counterexamples. For instance, the nematode *Caenorhabditis elegans* has MTs with 11 and 15 protofilaments [65]. The so-called accessory MTs in axonemes of insect sperm consist of 13–20 protofilaments [66], and even accessory MTs with 40 protofilaments have been observed [67].

As a consequence of the parallel arrangement of protofilaments, the MT inherits their polarity that derives its origin in the head-to-tail alignment of the subunits. Therefore, as with the actin filaments, one can differ a slowly polymerizing minus end, which is the end where the α -tubulins are exposed, and a highly dynamic plus end with β -tubulin. *In vivo*, the minus end is often bound in a *microtubule organizing center* (MTOC) like the centrosome in metazoa while the

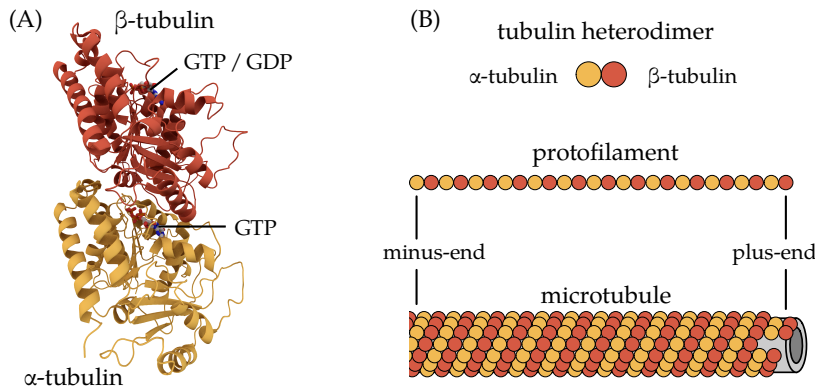


Figure 2.3: Microtubule structure. (A) Structure of the α - β -tubulin heterodimer, adapted from [45]. While the GTP that is bound to the α -tubulin is enclosed in the dimer, the β -bound GTP can be hydrolyzed to GDP. (B) The tubulin heterodimer is the subunit of the MT. A chain of subunits forms a protofilament. Due to the head-to-tail order of the heterodimers, the protofilament is a polar structure with a plus and a minus end. This polarity is inherited by the MT, which is a hollow cylindrical filament composed of 13 slightly helically arranged protofilaments.

free plus end is able to grow and shrink in a stochastic process called *dynamic instability* [68]. Before discussing the details of dynamic instability and its connection to GTP hydrolysis in the following section, we will first give a brief outline of the main functions of MTs inside the cell.

MTs fulfill different functions during the course of a eukaryotic cell cycle. Roughly, one can differ the interphase, in which the cell grows and replicates its organelles, and the M-Phase, which contains the mitosis and the cytokinesis. During interphase, an aster of MTs that emerge from the MTOC spans the cytoplasm.⁵ These MTs stabilize the cell and function as tracks for *motor proteins*, in particular for dyneins and kinesins, which transport various cell organelles from the cell center to the membrane and vice versa. During mitosis, there are two MT asters that form the bipolar mitotic spindle. In the spindle, we can find three types of MTs: while the astral and the interpolar MTs regulate spindle position and length, respectively, the kinetochore MTs search and capture the chromosomes, pull their chromatids apart and thereby ensure the proper separation of the replicated DNA to the two daughter cells. In chapter 3, we take a closer look on the mitotic spindle and the interplay between kinetochore MTs and chromosomes.

Besides these two major functions, MTs play important roles in certain structures of several specialized cells. In neurons, for instance, they are aligned parallelly along the axon where they serve as tracks for transport by motor proteins. Another example are MT bundles that form the core of flagella and cilia, which are hairy appendages that are important for cell motility.

2.1.2 Filament dynamics and dynamic instability

We start this section with a brief, more general overview of polymerization dynamics of filaments. Though, we do this based on the example of MTs, which are the filaments of our interest, we note that the following paragraph applies analogously to actin filaments.⁶

⁵ Such interphase MTs can be seen in Fig. 2.1.

⁶ The subunit of actin filaments is G-actin (instead of tubulin dimers in MTs) and contains ATP that can be hydrolyzed to ADP (instead of GTP and GDP).

⁷ While the mean number of subunits that leave the filament per second is constant, the number of added subunits is proportional to their concentration C in the vicinity of the MT end. At the critical concentration, both rates are the same and the filament has a constant length: $k_{\text{off}} = k_{\text{on}}C_c$.

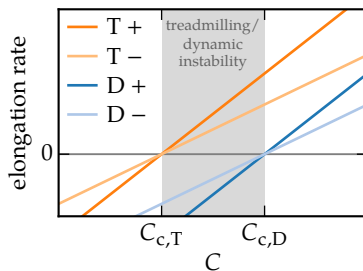


Figure 2.4: Elongation rates of the plus and the minus end in dependence of the subunit concentration C and the form of the exposed subunit (T or D). The elongation rate is defined as $k_{\text{on}}C - k_{\text{off}}$. Its sign determines whether the MT is growing or shrinking. When both ends are of the same type, their critical concentrations are equal ($C_{c,T}$ or $C_{c,D}$). Treadmilling and dynamic instability can occur for concentrations $C_{c,T} < C < C_{c,D}$.

As mentioned before, a MT has a fast polymerizing plus end and a slow minus end. “Fast” and “slow” in this context mean that the minus end has both a smaller polymerization rate k_{on} and a smaller depolymerization rate k_{off} than the plus end. However, the critical concentration⁷ $C_c = k_{\text{off}}/k_{\text{on}}$ of free subunits is the same for the two ends so that both ends either polymerize or depolymerize simultaneously. This situation changes when the GTP hydrolysis is taken into account. Depending on whether the β -tubulin carries a GTP or a GDP molecule, one can differ between a T-form and a D-form of a subunit. While free subunits are mostly found in the T-form, their β -bound GTP tends to be hydrolyzed to GDP after the incorporation into the filament. Thus, the tubulin dimers in the middle of the MT usually carry a GDP molecule. The form of the subunits that are exposed at the end is determined by a race between polymerization and hydrolysis: When new subunits are added before the currently exposed subunits are hydrolyzed, the end is formed by a *GTP cap* consisting of T-subunits, which is the typical situation at the plus end. On the other hand, when the hydrolysis is faster than the addition of new subunits, we find the D-form at the end, which usually applies to the slowly polymerizing minus end. The decisive factor for the polymerization dynamics of filaments is that the critical concentration of an end with T-form subunits is smaller than the critical concentration of a D-end, $C_{c,T} < C_{c,D}$. Hence, at tubulin concentrations between these two critical concentrations, a filament is growing at a T-end and shrinking at a D-end, see Fig. 2.4, which is the basis for the two characteristic mechanisms of filament dynamics: treadmilling [69] and dynamic instability [68]. If both ends are free, it is probable that the minus end consists of D-subunits and depolymerizes while the plus end has a GTP cap and polymerizes so that the filament effectively moves in the direction of the plus end. This effective motion, which is called *treadmilling*, is usually associated with actin filaments, but was also observed for MTs *in vitro* [70] as well as *in vivo* [71].

Dynamic instability occurs when the filament has only one free end as it is usually the case for MTs *in vivo*, whose minus ends are usually bound in a MTOC. Such MTs can only (de)polymerize at their plus ends, which we will also refer to as MT tips in the following. Since the mentioned race between polymerization and hydrolysis is a stochastic process, the form of the subunits at the plus end, and therefore—at appropriate tubulin concentrations—the direction of polymerization is a stochastic property, too. The term “dynamic instability” describes the stochastic switching between periods of growth/polymerization and shrinkage/depolymerization as illustrated in Fig. 2.5. As long as the MT tip is stabilized by a GTP cap, the MT is growing. When the GTP hydrolysis overtakes the addition of new subunits, the GTP cap vanishes and the MT

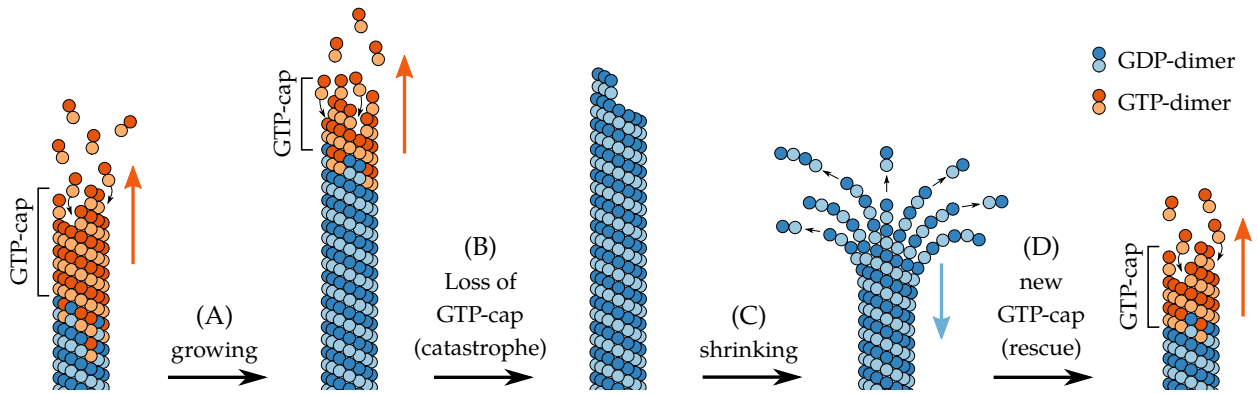


Figure 2.5: Dynamic instability. (A) When the plus end is stabilized by the GTP cap, the MT is growing by incorporating GTP dimers from the solution. Within the MT lattice, the hydrolysis of GTP to GDP is catalyzed. (B) When the hydrolysis is faster than the incorporation of new GTP dimers, the GTP cap vanishes and the MT undergoes a catastrophe. (C) Without the stabilizing GTP cap, the protofilaments curl outwards and depolymerize. (D) The MT is rescued and starts growing again when a new GTP cap emerges.

undergoes a *catastrophe*: without the stabilizing cap, the protofilaments curl outwards⁸ and depolymerize, the MT switches to the shrinking state. A shrinking MT can switch back to the growing state when a new GTP cap is formed at its tip. Such an event is called *rescue*. The stochastic emergence of a new GTP cap is not completely understood. One idea is that not all GTP molecules are hydrolyzed to GDP in the inner MT lattice. Then, the residual T-subunits can build GTP islands, which form a new GTP cap when they are reached by the shrinking MT tip. [73, 74].

In vivo, the polymerization dynamics of MTs does not only depend on the concentration of tubulin dimers but is influenced by a variety of *microtubule associated proteins* (MAPs). MAP is a general term for any protein that binds to a MT, including the aforementioned motor proteins. An example for motor proteins that affect MT dynamics are the members of the kinesin-13 family like MCAK,⁹ which act as catastrophe factors by destabilizing the MT tip. Another important group of MAPs are the *plus end tracking proteins* (+TIPs), which accumulate and stay attached at the plus end of a (de)polymerizing MT. For instance, XMAP215 stabilizes the plus end and increases the polymerization rate. The end-binding protein EB1 recruits other +TIPs and can connect the plus end with different cellular structures, e.g., with the cell cortex. There are also MAPs that are not directly correlated with the polymerization dynamics but mediate other functions by MT binding, such as the MT crosslinker MAP2 or the MT severing protein katanin.

⁸ We note that the widely held notion that the protofilaments of a shrinking MT are curved while being straightened by the stabilizing GTP cap during growth is outdated as it was recently observed that the protofilaments of growing MTs also exhibit a curvature that is similar to the curvature of depolymerizing protofilaments [72]. However, this microscopic detail is not relevant for the coarse-grained model used in the next section.

⁹ mitotic centromere-associated kinesin

2.2 Modeling dynamics of single microtubules

A first mathematical description of dynamic instability was provided by the Dogterom–Leibler model [29, 30], which is an empirical description of the experimental observation that MT length exhibits phases of constant growth and constant shrinkage [75, 76]. The model is based on four constant parameters: a (de)polymerization velocity for the growth and the shrinkage

state, and two transition rates for the occurrence of catastrophes or rescues. Depending on these parameters, the MT can either be in a bounded regime, in which its lengths approach a stationary exponential distribution, or in a regime of unbounded growth.

Later on, Odde *et al.* [47] and, more recently, Stepanova *et al.* [48] and Gardner *et al.* [49] found that the durations of the growth intervals are not distributed exponentially, as one would expect due to a constant catastrophe rate. Instead, the measured distributions could be well described by a multistep process, which means that the MT ages and the catastrophe rate increases during growth. While it was concordantly reported from control groups of *in vitro* experiments that a MT has to pass approximately three steps to undergo a catastrophe [47, 49, 77], it was also shown in the same experiments that the number of steps depends on concentrations of kinesins [49] or MT targeting agents (MTAs)¹⁰ [77].

¹⁰ MTAs are chemical compounds that affect the dynamic properties of MTs. They are used as drugs for cancer treatment as they inhibit the division of cancer cells by destabilizing the MTs in the mitotic spindle. [78]

The underlying mechanism of MT aging is still under debate and several microscopic models have been proposed. For instance, it was suggested that a catastrophe is triggered by a certain number of “sub-catastrophes” of single protofilaments [37]. A mechanochemical approach led to the conclusion that the MT tip becomes more tapered during growth which promotes catastrophe [41]. Another model, which included Brownian dynamics of single tubulin molecules, revealed that MT aging might be a much more complex stochastic process relying on a fluctuating MT tip and an increasing number of curled protofilaments [42].

Here, we do not concentrate on the microscopic details of MT aging but on the consequences a multistep catastrophe mechanism has for the distribution of MT lengths. For that purpose, we extend the empirical Dogterom–Leibler model by subdividing the growing state into a certain number of sub-states a MT has to pass to undergo a catastrophe. In the regime of bounded growth, the stationary form of the resulting master equations has to be solved numerically, except for the case that MTs can not be rescued. However, taking advantage of the results of Jemseena and Gopalakrishnan [32], who set up and analyzed master equations for dynamic instability with an age-dependent catastrophe rate, we are able to compute exact values for the mean MT length and higher momenta and to provide an approximation that comprises the key characteristics of the distribution. While Jemseena and Gopalakrishnan made up heuristic functions to directly fit the age-dependency of catastrophe, our work is based on the model that catastrophe is a multistep process with equal transition rates for each step. Our main results are similar to those obtained by Jemseena and Gopalakrishnan: The duration of MT growth becomes less stochastic if more steps are necessary to undergo a catastrophe, which results in a more narrow length distribution with a lighter tail. In particular, the

distribution has a maximum if rescues are possible, i.e., the MT has a most probable length greater than zero, in contrast to the monotonically decreasing exponential distribution that follows from a single-step catastrophe. To go beyond the work of Ref. [32], we also examine the regime of unbounded growth, where the MT lengths approach a Gaussian distribution like in the case of a single-step catastrophe [29, 30] but with a variance that decreases with the number of steps that are necessary to trigger a catastrophe.

2.2.1 Classical four parameter model of dynamic instability

The Dogterom–Leibler model [29, 30] is an empirical, coarse-grained MT model that neglects the microscopic and spatial structure of the MT and instead approximates the MT as a continuous one-dimensional object. According to the model, the MT is either in a growing (+) or in a shrinking (–) state in which it is polymerizing or depolymerizing, respectively. Neither the stochastic nature nor the discreteness of (de)polymerization is accounted for. Instead, the continuous one-dimensional MT grows or shrinks with a constant velocity v_+ or v_- , as it is sketched in Fig. 2.6 and has been observed similarly in experiments [75, 76]. The velocities are given by $v_{\pm} = k_{\pm} \Delta x$, where Δx is the monomer length¹¹ and k_{\pm} are the effective elongation rates for a MT with (+) and without (–) a GTP cap as they are defined in Fig. 2.4. Thus, the constant velocities are based on the assumption that the concentration of free subunits stays constant despite (de)polymerization, i.e., the MT is located in an infinitely large reservoir of free tubulin dimers.

The MT can switch from the growing to the shrinking state with the catastrophe rate ω_c and vice versa with the rescue rate ω_r as sketched in Fig. 2.7A. Both rescue and catastrophe are modeled as Poisson processes with constant transition rates, i.e., the growth (shrinking) duration is distributed exponentially and its mean is given by $\langle \tau_+ \rangle = \omega_c^{-1}$ ($\langle \tau_- \rangle = \omega_r^{-1}$). Due to the constant growth (shrinking) velocity, also the length gain (loss) during one period of growth (shrinkage) is distributed exponentially with an average of $\langle x_+ \rangle = v_+ \langle \tau_+ \rangle$ ($\langle x_- \rangle = v_- \langle \tau_- \rangle$). Introducing probability densities $p_{\pm}(x, t)$ for the MT length x in the growing and the shrinking states at time t , dynamic instability can be described by a system of two Fokker–Planck equations (FPEs) [30]:

$$\begin{aligned} \partial_t p_+(x, t) &= -\omega_c p_+(x, t) + \omega_r p_-(x, t) - v_+ \partial_x p_+(x, t), \\ \partial_t p_-(x, t) &= \omega_c p_+(x, t) - \omega_r p_-(x, t) + v_- \partial_x p_-(x, t), \end{aligned} \quad (2.1)$$

where the overall probability density $p(x, t) = p_+(x, t) + p_-(x, t)$ has to be normalized at any time. The mean velocity of the MT tip

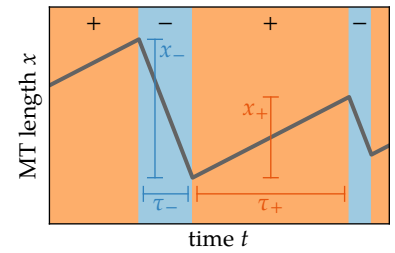
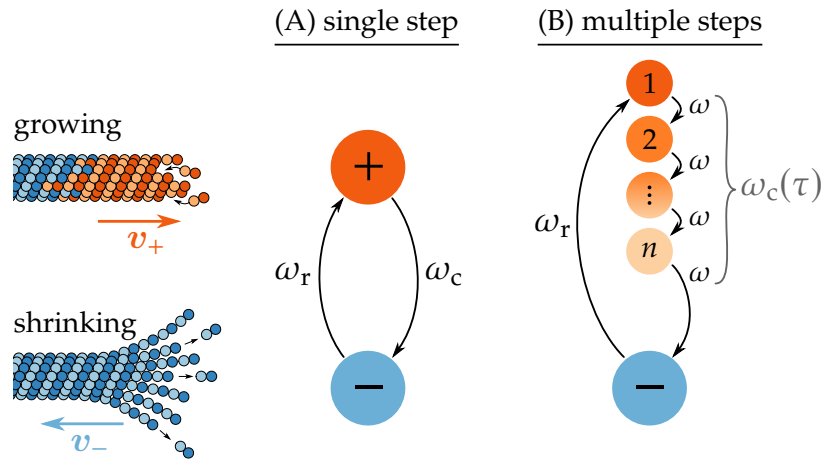


Figure 2.6: MT trajectories. The MT exhibits phases of growth (+) and shrinkage (–) with constant velocities v_{\pm} . The durations τ_{\pm} of these phases as well as the covered distances $x_{\pm} = v_{\pm} \tau_{\pm}$ are distributed exponentially in the Dogterom–Leibler model, which contradicts experimentally observed non-exponential distributions of τ_+ . This contradiction is dealt with in the following section by means of an extended model.

¹¹ Since a MT consists of 13 protofilaments, the effective monomer length is not the size of one tubulin dimer (8 nm) but $8/13$ nm = 0.62 nm.

Figure 2.7: Models of dynamic instability. The MT is either in a growing or in a shrinking state, in which its tip moves with constant velocities v_+ or v_- . (A) In the classical Dogterom–Leibler model, catastrophe is a single step process with a constant rate ω_c . (B) When catastrophe is modeled as a multistep process, the growing state is divided into n sub-states, and a growing MT has to pass n sub-steps, each with rate ω , before it undergoes a catastrophe. This n -step process can be summarized by means of an age-dependent catastrophe rate $\omega_c(\tau)$.



is given by

$$V = \frac{\langle x_+ \rangle - \langle x_- \rangle}{\langle \tau_+ \rangle + \langle \tau_- \rangle} = \frac{\omega_r v_+ - \omega_c v_-}{\omega_r + \omega_c}. \quad (2.2)$$

With a reflecting boundary at $x = 0$, i.e., a MT undergoes a forced rescue as soon as it shrinks back to zero length,¹² a negative V assures that MT growth is bounded. Then, the overall probability density converges to a stationary exponential distribution with the mean length

$$\langle x \rangle = \frac{v_+ v_-}{\omega_c v_- - \omega_r v_+}. \quad (2.3)$$

If $V > 0$, MT growth is unbounded and there is no stationary distribution. The probability density approaches a Gaussian distribution

$$p(x, t) = \frac{1}{\sqrt{4\pi Dt}} \exp\left(-\frac{(x - Vt)^2}{4Dt}\right) \quad (2.4)$$

with the diffusion constant

$$D = \frac{\omega_c \omega_r (v_+ + v_-)^2}{(\omega_c + \omega_r)^3}. \quad (2.5)$$

2.2.2 Microtubule dynamics with a multistep catastrophe

In the following, we extend the Dogterom–Leibler model¹³ in a way that takes account of the experimental observation that MT catastrophe is a multistep process [47–49], see Fig. 2.7B. For this purpose, we introduce the number of steps n a growing MT has to pass to undergo a catastrophe. As long as a MT has not passed all n steps, it continues growing with v_+ . Therefore, the growing state can be divided into n sub-states $i = 1 \dots n$. In the mentioned experiments [47–49], the conclusion that MT catastrophe is a

¹² In other words, a new MT is nucleated in the moment the MT disappears.

¹³ The extension of the Dogterom–Leibler model is the main work of this chapter. As mentioned in the Preface, it builds on the bachelor’s thesis of Lina Heydenreich [79], where the Dogterom–Leibler model was extended for a two-step catastrophe and solved analytically. My work is the generalization for an arbitrary n -step process that is presented in the following sections.

multistep process was derived from characterizing the observed growth durations τ_+ as *gamma distributed*, see Fig. 2.8:

$$p_{\tau_+}(\tau_+) = \frac{\omega (\omega \tau_+)^{n-1}}{\Gamma(n)} e^{-\omega \tau_+}, \quad (2.6)$$

with the gamma function $\Gamma(n) = \int_0^\infty t^{n-1} e^{-t} dt$ [80]. A gamma distribution implies that each catastrophe step occurs with the same rate ω and that backward steps are not allowed, i.e., the states $i = 1 \dots n$ are passed in a prescribed order as sketched in Fig. 2.7B. Since rescue is still described as a single-step process, MT dynamics is now characterized by a set of five parameters n , v_- , v_+ , ω_r and ω . Besides the time τ_+ a MT spends in the growing state, also the length gain $x_+ = v_+ \tau_+$ during one growth interval is gamma distributed, see Fig. 2.8:

$$p_{x_+}(x_+) = \frac{c (c x_+)^{n-1}}{\Gamma(n)} e^{-c x_+}, \quad c \equiv \frac{\omega}{v_+}. \quad (2.7)$$

On average, a MT grows for a duration of $\langle \tau_+ \rangle = n \omega^{-1}$, and its tip covers a distance of $\langle x_+ \rangle = n v_+ \omega^{-1}$ during that interval. Together with the mean shrinking duration ω_r^{-1} and distance $v_- \omega_r^{-1}$, we deduce the mean tip velocity analogously to Eq. (2.2):

$$V_n = \frac{v_+ n \omega^{-1} - v_- \omega_r^{-1}}{n \omega^{-1} + \omega_r^{-1}} = \frac{n \omega_r v_+ - \omega v_-}{n \omega_r + \omega}. \quad (2.8)$$

Again, the sign of V_n determines whether MT growth is bounded and a stationary state exists. We note that MT growth is stabilized and may leave the bounded regime if more steps are required to trigger a catastrophe ($n > \omega v_- / \omega_r v_+$) while the other parameters remain constant, see Fig. 2.9.

For a general mathematical description, we assign a probability density $p_i(x, t)$ to each sub-state $i = 1 \dots n$ of a growing MT. The total growing state density is given by $p_+(x, t) = \sum_i p_i(x, t)$. The stochastic time evolution of the probability densities is described by a system of $n + 1$ FPEs:

$$\begin{aligned} \partial_t p_-(x, t) &= \omega p_n(x, t) - \omega_r p_-(x, t) + v_- \partial_x p_-(x, t) \\ \partial_t p_1(x, t) &= -\omega p_1(x, t) + \omega_r p_-(x, t) - v_+ \partial_x p_1(x, t) \\ \partial_t p_i(x, t) &= \omega p_{i-1}(x, t) - \omega p_i(x, t) - v_+ \partial_x p_i(x, t), \end{aligned} \quad (2.9)$$

for $i = 2 \dots n$.

Due to the reflecting boundary, the probability current density

$$j(x, t) = v_+ p_+(x, t) - v_- p_-(x, t) \quad (2.10)$$

has to vanish at $x = 0$. Furthermore, in any stationary state ($\partial_t p_i(x, t) = 0$), the current density is constant in space, as can be

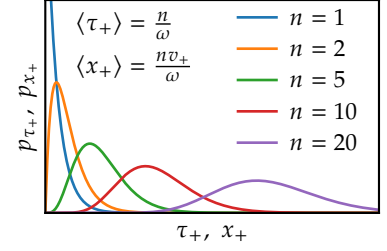


Figure 2.8: Gamma distributions. Both the growth durations τ_+ and the length gains $x_+ = v_+ \tau_+$ are gamma distributed according to Eqs. (2.6) and (2.7) for a n -step catastrophe.

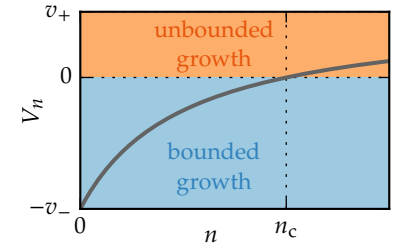


Figure 2.9: The mean velocity V_n increases with n , since the more steps are required for a catastrophe, the longer the MT stays in the growing state. At $n = n_c = \omega v_- / \omega_r v_+$, MT growth switches from the bounded ($V_n < 0$) to the unbounded regime ($V_n > 0$).

seen by summing up Eqs. (2.9):

$$0 = \partial_x \left(-v_+ \sum_{i=1}^n p_i(x) + v_- p_-(x) \right) = -\partial_x j(x). \quad (2.11)$$

Together with $j(x=0) = 0$, this implies that, in a steady state, the probability current density has to vanish everywhere. With the resulting relation

$$p_-(x) = \frac{v_+}{v_-} p_+(x) = \frac{v_+}{v_-} \sum_{i=1}^n p_i(x), \quad (2.12)$$

we can eliminate $p_-(x)$ in the stationary FPEs and achieve:

$$\partial_x \vec{p}_+(x) = M \vec{p}_+(x), \quad (2.13)$$

with $\vec{p}_+(x) = (p_1(x), p_2(x), \dots, p_n(x))^T$,

$$M = \begin{pmatrix} r - c & r & r & r & \cdots & r \\ c & -c & 0 & 0 & \cdots & 0 \\ 0 & c & -c & 0 & \cdots & 0 \\ \vdots & \ddots & \ddots & \ddots & \ddots & \vdots \\ 0 & \cdots & 0 & c & -c & 0 \\ 0 & \cdots & 0 & 0 & c & -c \end{pmatrix}, \quad (2.14)$$

¹⁴ $p_-(x)$ is substituted by Eq. (2.12) in the second step.

¹⁵ With the (numerically determined) eigenvalues λ_j and -vectors \vec{v}_j of the matrix M , the solution of Eq. (2.13) can be written as

$$\vec{p}_+(x) = \sum_{j=1}^n a_j \vec{v}_j e^{\lambda_j x}$$

or $p_i(x) = \sum_{j=1}^n a_j S_{ij} e^{\lambda_j x}$,

with $S = (\vec{v}_1, \dots, \vec{v}_n)$. The coefficients a_j follow from the initial condition (2.15) at $x = 0$:

$$\begin{aligned} \vec{p}_+(x=0) &= S \vec{a} \stackrel{!}{=} \vec{p}_0, \\ \Rightarrow \vec{a} &= S^{-1} \vec{p}_0, \quad a_j = p_0 (S^{-1})_{j1}, \end{aligned}$$

with $\vec{a} = (a_1, \dots, a_n)^T$. Finally, the constant p_0 is determined by the normalization condition:

$$\begin{aligned} 1 &= \int_0^\infty p(x) dx \\ &= p_0 \left(1 + \frac{v_+}{v_-} \right) \\ &\quad \times \sum_{i,j=1}^n (S^{-1})_{j1} S_{ij} \left(-\frac{1}{\lambda_j} \right), \end{aligned}$$

where $\text{Re } \lambda_j < 0$.

and the abbreviations $r = \omega_r/v_-$ and $c = \omega/v_+$. Due to the reflecting boundary condition, a growing MT with length 0 must be in state 1, which provides the initial condition for Eq. (2.13):

$$\vec{p}_+(x=0) = \vec{p}_0 \equiv (p_0, 0, \dots, 0)^T = p_0 \vec{e}_1. \quad (2.15)$$

The parameter p_0 is determined by the normalization condition $\int_0^\infty p(x) dx = 1$, with¹⁴

$$p(x) = p_+(x) + p_-(x) = \left(1 + \frac{v_+}{v_-} \right) \sum_{i=1}^n p_i(x). \quad (2.16)$$

2.2.3 Results for the bounded regime

In general, Eq. (2.13) can only be solved numerically, e.g., by numerical diagonalization of the coefficient matrix M .¹⁵ However, for the experimentally relevant case [49] that a MT can not be rescued ($\omega_r = r = 0$) except for the forced rescue at the boundary

$x = 0$, the solution can be expressed analytically:¹⁶

$$p_i(x) = \frac{c}{n \left(1 + \frac{v_+}{v_-}\right)} \frac{(cx)^{i-1}}{(i-1)!} e^{-cx}, \quad (2.17)$$

$$p(x) = \left(1 + \frac{v_+}{v_-}\right) \sum_{i=1}^n p_i(x) = \frac{c}{n} Q(n, cx), \quad (2.18)$$

where $Q(n, x) = \Gamma(n, x)/\Gamma(n)$ is the regularized form of the upper incomplete gamma function $\Gamma(n, x) = \int_x^\infty t^{n-1} e^{-t} dt$ [80].

In order to approach a solution of the general case ($\omega_r > 0$), we make use of the results of Jemseena and Gopalakrishnan [32], who calculated the Laplace transform

$$\tilde{p}(s) = \int_0^\infty p(x) e^{-sx} dx \quad (2.19)$$

of the steady state length distribution for the case of an arbitrary age-dependent catastrophe rate $\omega_c(\tau)$, where the age τ is the time that has passed since the last rescue event. Given an arbitrary probability density $p_{\tau_+}(\tau_+)$ of growth durations τ_+ , the associated age-dependent catastrophe rate is defined by¹⁷

$$\omega_c(\tau) = \frac{p_{\tau_+}(\tau)}{P_{\tau_+}(\tau)} = -\partial_\tau \ln P_{\tau_+}(\tau), \quad (2.20)$$

where $P_{\tau_+}(\tau) = \int_\tau^\infty p_{\tau_+}(t) dt$ is the survival probability of a growing MT. Combining that with the results of Jemseena and Gopalakrishnan [32], we find¹⁸

$$\tilde{p}(s) = \left(\frac{1}{\langle x_+ \rangle} - r \right) \frac{1 - \tilde{p}_{x_+}(s)}{s - r (1 - \tilde{p}_{x_+}(s))} \quad (2.21)$$

with the Laplace transform $\tilde{p}_{x_+}(s)$ of the probability density of growth distances $p_{x_+}(x)$. To achieve a result for the n -step catastrophe process, we substitute the Laplace transform of $p_{x_+}(x)$ from Eq. (2.7) into Eq. (2.21):¹⁹

$$\tilde{p}(s) = \left(\frac{c}{n} - r \right) \frac{1 - \left(\frac{c}{c+s}\right)^n}{s - r \left(1 - \left(\frac{c}{c+s}\right)^n\right)}. \quad (2.22)$$

If $r = 0$, inverse transformation yields the probability density from Eq. (2.18). For the general case with rescues ($r > 0$), the inverse Laplace transform $\tilde{p}(s) \rightarrow p(x)$ can not be executed analytically. Nonetheless, we are able to compute exact results for the mean MT length $\langle x \rangle$ and the variance $\text{Var}(x) = \langle x^2 \rangle - \langle x \rangle^2$ by interpreting

¹⁶ Since for $r = 0$, the matrix M has only one eigenvalue $\lambda = c$ with geometric multiplicity 1, Eq. (2.13) can not be solved as described above in Sidenote ¹⁵. Writing out the rows of Eq. (2.13) gives the inhomogeneous equations $p'_i(x) = cp_{i-1}(x) - cp_i(x)$ ($i = 2..n$), which are solved by

$$p_i(x) = a_i(x) e^{-cx}, \\ a_i(x) = \int_0^x ca_{i-1}(x') dx'.$$

Starting from the first row of Eq. (2.13), $p'_1(x) = -cp_1(x)$, and the initial condition (2.15), $p_1(0) = p_0$, we find $a_1 = p_0$. The further coefficients $a_i(x)$ can be determined iteratively, which yields

$$a_i(x) = \frac{(cx)^{i-1}}{(i-1)!}.$$

Adjusting p_0 for normalization finally results in the solution as given in Eq. (2.17).

¹⁷ With an age-dependent catastrophe rate $\omega_c(\tau)$, the evolution of the survival probability $P_{\tau_+}(\tau)$, which is the probability that a MT is still growing after a time τ , is given by

$$\dot{P}_{\tau_+}(\tau) = -\omega_c(\tau) P_{\tau_+}(\tau).$$

With $p_{\tau_+}(\tau) = -\dot{P}_{\tau_+}(\tau)$, we find $\omega_c(\tau)$ as defined in Eq. (2.20).

¹⁸ The derivation is presented in Appendix A.1.

¹⁹ The gamma distribution of growth distances (2.7) and its Laplace transform are:

$$p_{x_+}(x) = \frac{c(cx)^{n-1}}{\Gamma(n)} e^{-cx}, \\ \tilde{p}_{x_+}(s) = \left(\frac{c}{c+s}\right)^n \quad [80].$$

the Laplace transform as moment-generating function:

$$\langle x^m \rangle = (-1)^m \frac{\partial^m}{\partial s^m} \tilde{p}(s) \Big|_{s=0}, \quad (2.23)$$

$$\langle x \rangle = \frac{n+1}{2(c-nr)} = \frac{n+1}{2} \frac{v_+v_-}{v_-\omega_c - nv_+\omega_r}, \quad (2.24)$$

$$\text{Var}(x) = \frac{n+1}{12} \frac{2n(n-1)r + (n+5)c}{c(c-nr)^2}. \quad (2.25)$$

Moreover, we can approximate $\tilde{p}(s)$ for large s as

$$\frac{\tilde{p}(s)}{\frac{c}{n} - r} = \frac{(c+s)^n - c^n}{(s-r)(c+s)^n + rc^n} \approx \frac{(c+s)^n - c^n}{(s-r)(c+s)^n}. \quad (2.26)$$

Then, inverse transformation is possible and provides an approximation of $p(x)$ for short MT lengths:²⁰

$$p(x) \approx \left(\frac{c}{n} - r\right) e^{rx} \left(1 - \left(\frac{c}{c+r}\right)^n P(n, (c+r)x)\right), \quad (2.27)$$

where $P(n, x) = 1 - Q(n, x)$ is the regularized lower incomplete gamma function [80].

In the following, we compare the results with stochastic simulations that solve the equation of motion of the MT for fixed time steps Δt . Dynamic instability is included by stochastic switching events.²¹ The time step has to be sufficiently small to ensure $\omega_i \Delta t \ll 1$ for both rescue events and catastrophe steps. For better comparability, we assume that the catastrophe step rate is proportional to n ,

$$\omega = n\omega_0, \quad c = nc_0, \quad c_0 = \frac{\omega_0}{v_+}, \quad (2.28)$$

with a constant ω_0 so that the mean growth time $\langle \tau_+ \rangle = n\omega^{-1} = \omega_0^{-1}$ as well as the mean velocity V_n (2.8) are independent of n , and the MT remains in the bounded regime despite increasing n . We choose the values as listed in Tab. 2.1 to assure that V_n is negative and MT growth is bounded.

Fig. 2.10 shows the results in absence of rescue events ($r = 0$) except for the forced rescues at $x = 0$. The analytical predictions from Eqs. (2.17) and (2.18) perfectly match with the results from the simulations. The overall probability densities are monotonically decreasing functions and converge towards a step function $c_0 \Theta(c_0^{-1} - x)$ for large n . This uniform distribution for an infinite step catastrophe process can be made plausible by considering the growth distances x_+ : Since the standard deviation of the gamma distribution (2.7) is given by $\Delta x_+ = \sqrt{n}c^{-1}$, the relative error of growth distances $\Delta x_+ / \langle x_+ \rangle = 1/\sqrt{n}$ vanishes for large n . Moreover, as we assumed that $c = nc_0$, also the absolute deviation decreases as $1/\sqrt{n}$ whereas the mean growth distance stays constant. Conse-

²⁰ Let $\mathcal{L}[f(x)](s) = \tilde{f}(s)$ denote the Laplace transform as defined in Eq. (2.19). The Laplace transform of a convolution of two functions $f(x)$ and $g(x)$ is given by the product of the individual Laplace transforms [80]:

$$\mathcal{L}\left[\int_0^x f(u)g(x-u)du\right](s) = \tilde{f}(s)\tilde{g}(s).$$

The approximation in Eq. (2.26) can be written as

$$\frac{\tilde{p}(s)}{\frac{c}{n} - r} \approx \frac{1}{s-r} \left(1 - \tilde{p}_{x_+}(s)\right).$$

With $\mathcal{L}[e^{rx}](s) = 1/(s-r)$ and $\mathcal{L}[\delta(x)](s) = 1$, the inverse transform of the approximation is given by

$$\frac{p(x)}{\frac{c}{n} - r} \approx \int_0^x e^{r(x-u)} \left(\delta(u) - p_{x_+}(u)\right) du,$$

which results in Eq. (2.27).

²¹ Starting the simulation with a MT at length $x = 0$ in growing state $i = 1$, these concrete steps are executed in each time step:

1. If the MT is in
 - a) growing state $i < n$, switch to state $i + 1$ with probability $1 - \exp(-\omega\Delta t)$.
 - b) growing state $i = n$, switch to the shrinking state (catastrophe) with probability $1 - \exp(-\omega\Delta t)$.
 - c) shrinking state, switch to growing state 1 (rescue) with probability $1 - \exp(-\omega_r\Delta t)$.
2. Update MT length depending on whether it is in a growing (+) or in the shrinking state (-):

$$x(t + \Delta t) = x(t) \pm v_{\pm}\Delta t.$$
3. If $x < 0$, set $x = 0$ and switch to growing state 1 (forced rescue).

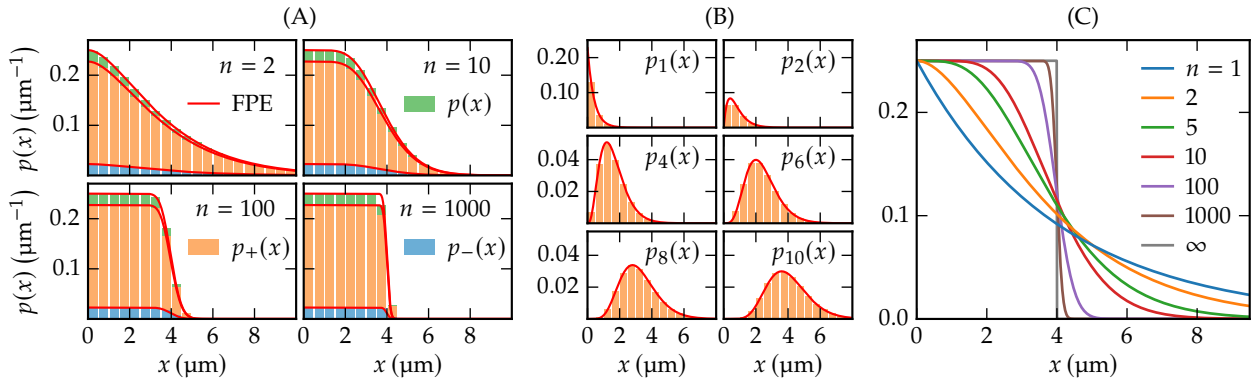


Figure 2.10: Analytical and simulation results in absence of rescue events. (A) Overall probability densities with various n . (B) Single state distributions in a 10-step process. In all cases the analytical FPE solutions following Eqs. (2.17) and (2.18) (red lines) match with the distributions measured in simulations (bars). (C) For an infinite-step process, the overall probability density converges to a step function.

quently, the more steps a MT has to pass to undergo a catastrophe, the more deterministic and predictable the length gain becomes. In the infinite step limit, the MT tip always covers the same distance during one growth interval. Then, in the absence of rescue events, a MT grows from $x = 0$ to $x = c_0^{-1}$ where it undergoes a catastrophe, and shrinks back to zero length where it is rescued again, finally resulting in a uniform distribution of MT lengths.

If rescues are possible ($r > 0$), the probability density functions are not monotonic anymore but increase exponentially for short MT lengths up to a maximum, see Fig. 2.11A. The exponential increase and the maximum are well described by the approximation (2.27). After the maximum, however, the approximation deviates from the real distribution. In that region, the probability densities measured in stochastic simulations are only fitted well by the numerical solution of Eq. (2.13), which is also the case for the single state densities $p_i(x)$ depicted in Fig 2.11B. If the number of steps n increases, the maximum becomes sharper and moves towards longer MT lengths up to $x = c_0^{-1}$. In the infinite step limit, the probability density approaches a piecewise defined function that initially grows exponentially as $(c - r) \exp(rx)$ until it has a step discontinuity at $x = c_0^{-1}$. Moreover, there are non-analyticities of higher order at each multiple of c_0^{-1} .²² Like in the absence of rescues, this behavior can be explained with the determinism of MT growth distances in the infinite step limit: Since the rescue rate is greater than zero, a MT can be rescued before shrinking back to zero length and is able to grow beneath the single growth distance c_0^{-1} . Nevertheless, a MT that grows from zero length after a forced rescue and undergoes a catastrophe at $x = c_0^{-1}$ still shrinks back to zero with the probability $\exp(-r/c) = 82\%$. These 82% alone would result in a step function again, and only in 18% of the growth cycles that start from $x = 0$, the MT reaches lengths $x > c_0^{-1}$, finally leading to the step discontinuity.

Table 2.1: Parameters used in stochastic simulations.

Parameter	Value
Step rate ω_0	0.005 s^{-1}
Rescue rate ω_r	0.01 s^{-1}
Growth vel. v_+	$0.02 \mu\text{m s}^{-1}$
Shrinking vel. v_-	$0.2 \mu\text{m s}^{-1}$

²² The full formula of $p(x)$ for $n \rightarrow \infty$ and its derivation can be found in Appendix A.2.

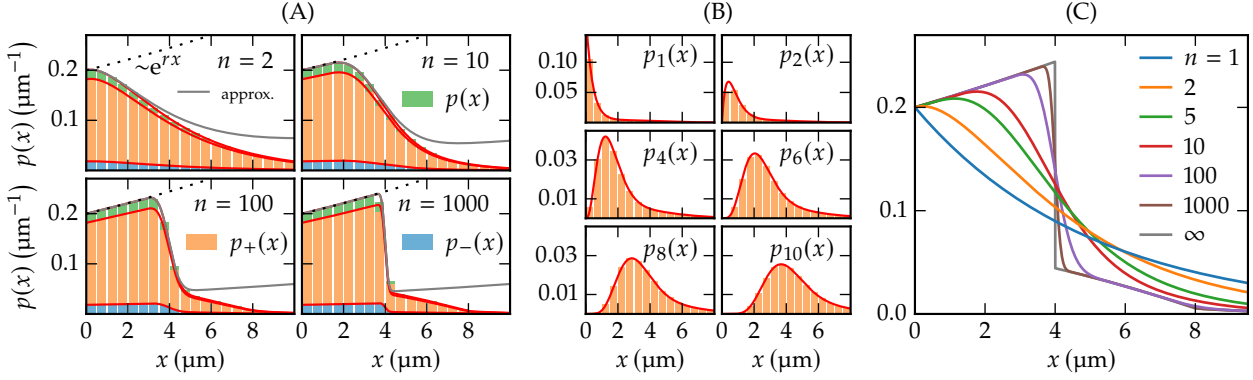


Figure 2.11: Deterministic and simulation results with $r > 0$. The deterministic results (red) are calculated by numerical diagonalization of the matrix M from Eq. (2.14). (A) Overall probability densities with various n . For short MT lengths, they grow exponentially (dashed lines) and can be approximated by Eq. (2.27) (gray lines). (B) Single state distributions in a 10-step process. In all cases the deterministic results (red lines) match with the distributions measured in simulations (bars). (C) For an infinite-step process, the overall probability density converges to a piecewise defined function that grows exponentially as $(c - r) \exp(rx)$ until it has a step discontinuity at $x = c_0^{-1}$.

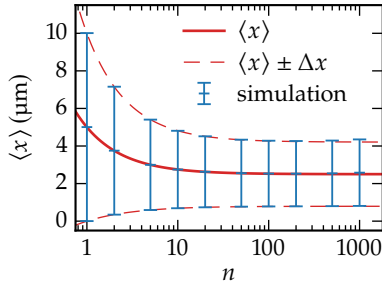


Figure 2.12: Mean length and deviation. The mean MT length $\langle x \rangle$ and its standard deviation $\Delta x = \sqrt{\text{Var}(x)}$ measured in simulations (blue) match with the analytical predictions (red) from Eqs. (2.24) and (2.25).

As it can be seen in Fig. 2.12, Eqs. (2.24) and (2.25) correctly describe the mean length and its variance measured in stochastic simulations. If the number of catastrophe steps and the step rate are increased proportionally, the mean length decreases by up to one half of the single-step value.

2.2.4 Results for the unbounded regime

In the regime of unbounded growth, there is no stationary solution which is why we need to analyze the time dependent FPEs (2.9). Since the full equations can not be solved analytically, we aim to find an approximation that is approached after long times. As $V_n > 0$ in the unbounded regime, this limit is likewise an approximation for long MTs.

We define the Fourier transform as

$$q_i(k, t) = \int_{-\infty}^{\infty} e^{-ikx} p_i(x, t) dx, \quad (2.29)$$

and apply it to the master equation (2.9):

$$\partial_t \vec{q}(k, t) = A(k) \vec{q}(k, t), \quad (2.30)$$

with $\vec{q}(k, t) = (q_1(k, t), \dots, q_n(k, t), q_-(k, t))^T$ and

$$A(k) = \begin{pmatrix} -\omega - iv_+k & 0 & \cdots & 0 & \omega_r \\ \omega & \ddots & \ddots & & 0 \\ 0 & \ddots & \ddots & \ddots & \vdots \\ \vdots & \ddots & \ddots & -\omega - iv_+k & 0 \\ 0 & \cdots & 0 & \omega & -\omega_r + iv_-k \end{pmatrix}. \quad (2.31)$$

The fundamental solutions of Eq. (2.30) are given by

$$\vec{q}_j(k, t) = \vec{v}_j(k) e^{\lambda_j(k)t}, \quad (2.32)$$

where $\lambda_j(k)$ and $\vec{v}_j(k)$ are the eigenvalues and eigenvectors of $A(k)$, respectively. The eigenvalues are defined implicitly by the characteristic polynomial:

$$\begin{aligned} 0 &= f(\lambda(k), k) \equiv \det(A(k) - \lambda(k)I_{n+1}) \\ &= (-1)^n \omega_r \omega^n + (-1)^{n+1} (\omega_r - i v_- k + \lambda(k)) \\ &\quad \times (\omega + i v_+ k + \lambda(k))^n. \end{aligned} \quad (2.33)$$

An approximation for long MTs in real space corresponds to the limit of small k in Fourier space. For $k = 0$, $\lambda_0(k = 0) = 0$ is the only non-negative eigenvalue²³ and therefore provides the only fundamental solution $\vec{q}_j(k, t)$ that does not vanish for $t \rightarrow \infty$. To approximate the dispersion relation $\lambda_0(k)$ for long MTs after long times, we expand it around $k = 0$ by use of the implicit function theorem:

$$\begin{aligned} \lambda'_0(k = 0) &= \left. \frac{\partial \lambda_0(k)}{\partial k} \right|_{k=0} = - \left. \frac{\partial_k f(\lambda_0, k)}{\partial_{\lambda_0} f(\lambda_0, k)} \right|_{k=0} = -i V_n, \quad (2.34) \\ \left. \frac{\partial^2 \lambda_0(k)}{\partial k^2} \right|_{k=0} &= - \left. \frac{\left(\partial_k^2 + 2\lambda'_0 \partial_{\lambda_0} \partial_k + \lambda_0'^2 \partial_{\lambda_0}^2 \right) f(\lambda_0, k)}{\partial_{\lambda_0} f(\lambda_0, k)} \right|_{k=0} \\ &= -n(n+1) \frac{\omega_r \omega (v_+ + v_-)^2}{(n\omega_r + \omega)^3} \equiv -2D_n. \end{aligned} \quad (2.35)$$

This results in the dispersion relation

$$\lambda_0(k) \approx -i V_n k - D_n k^2, \quad (2.36)$$

which corresponds to a diffusion process with diffusion constant D_n and drift V_n , which is the mean velocity as deduced in Eq. (2.8).

Normalization of the overall probability density is translated into Fourier space by the condition²⁴ $q(0, t) = 1$, so that we find $q(k, t) \approx \exp(\lambda_0(k)t)$. Finally, an inverse Fourier transform shows that the overall probability density of MT lengths approaches a Gaussian distribution:

$$p(x, t) \approx \frac{1}{\sqrt{4\pi D_n t}} \exp\left(-\frac{(x - V_n t)^2}{4D_n t}\right). \quad (2.37)$$

One can easily see that D_n , and thus the standard deviation of MT lengths vanish for large n if the other parameters remain constant. Together with Eq. (2.8) this means that an increase of the number of catastrophe steps favors growth over shrinkage and thereby can make the MT leave the bounded regime, where a further increase of n favors growth even more until catastrophes are almost completely suppressed.

²³ After expanding Eq. (2.33) for $k = 0$, we can write it as

$$0 = \sum_{i=1}^n a_i (\lambda(0))^i.$$

Since all coefficients a_i turn out to have the same sign, all further solutions besides $\lambda_0(0) = 0$ must have a negative real part.

²⁴ $q(k, t)$ denotes the Fourier transform of the overall probability density:

$$\begin{aligned} q(k, t) &= \int_{-\infty}^{\infty} e^{-ikx} p(x, t) dx \\ &= \sum_{i=1}^n q_i(k, t). \end{aligned}$$

The normalization condition follows from

$$\begin{aligned} q(0, t) &= \int_{-\infty}^{\infty} e^{-i \cdot 0 \cdot x} p(x, t) dx \\ &= \int_{-\infty}^{\infty} p(x, t) dx \stackrel{!}{=} 1. \end{aligned}$$

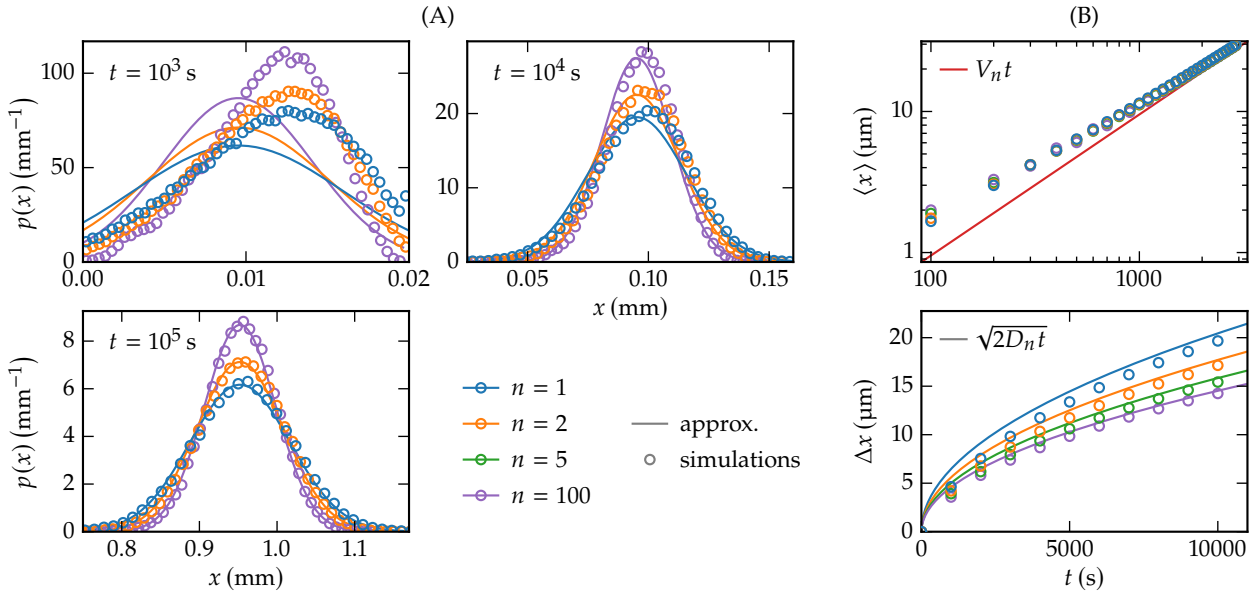


Figure 2.13: Analytical and simulation results in the unbounded regime. (A) Overall probability densities with various n at three different times, and the corresponding Gaussian approximations. As described, the results only match for large times ($t \gtrsim 10\,000$ s), whereas at the beginning (see $t = 1000$ s), the initial and the boundary condition, which are not incorporated in the approximation, still have a significant influence on the simulation results. For $n = 1$ there is even a considerable amount of MTs ($\exp(-\omega_0 t) = 0.67\%$) with length $v_+ t = 0.02$ mm that have not undergone a catastrophe yet. (B) Time evolution of the mean MT length $\langle x \rangle$ and its standard deviation Δx for various n . The simulations converge to the values of the Gaussian distribution.

In Fig. 2.13, the results are compared to stochastic simulations. Here again, we assume that the catastrophe step rate is proportional to n so that the mean growth duration and the mean velocity are constant. Then, the diffusion constant D_n does not vanish for large n but still decreases by up to one half of the single-step value. We use the same parameters as in Tab. 2.1 but with a ten times higher rescue rate ($\omega_r = 0.1 \text{ s}^{-1}$) in order to induce an unbounded state with $V_n > 0$. At the beginning of the simulations both the initial and, since the MTs are still short, the boundary condition cause the length distribution to significantly deviate from the Gaussian approximation. After long times, however, the MTs gained so much length that the probability of reaching the boundary is negligible. Then, the approximation provides an accurate description of the simulation results.

2.3 Discussion

Based on experimental results that characterize MT growth periods as gamma distributed and conclude that catastrophe is a multistep process [47, 49], we extended the empirical Dogterom–Leibler model [29, 30] in order to analyze the consequences a multistep catastrophe mechanism has for the distribution of MT lengths. The multistep process has two main effects on the growth durations of a MT, which also underlie the consequential changes in the length distributions: Firstly, if the number of catastrophe steps is increased while keeping the rate of a single step constant, the growth durations become longer and the MT may leave the bounded regime. Secondly, the growth periods and hence the length gain during

one growth interval are less stochastic if more steps are necessary to trigger a catastrophe.

In the case of bounded growth, the stationary length distribution has a steep descent in the vicinity of the mean growth distance n/c . In absence of rescues, the steep descent follows an area where the probability density is only slowly decreasing and becomes nearly constant for large n . If rescues are allowed, the distribution is exponentially increasing and has a maximum before it decreases sharply. In both cases, the length distributions are lighter tailed than the exponential distribution resulting from a single-step catastrophe, i.e., a multistep catastrophe reduces the number of MTs that are longer than the mean growth length. As a consequence, the mean MT length decreases by up to one half the single-step value if the number of catastrophe steps and the step rate are increased proportionally.²⁵

²⁵ See Fig 2.12.

Taking into consideration that there are MT regulators that do not only affect the velocities or the transition rates but also the number of catastrophe sub-steps [49], we conclude that by such a regulation, a MT has more potent ways to adapt to special situations inside the cell: while altering the classical four parameters only adjusts the range of MT lengths, which stay exponentially distributed in the single-step case,²⁶ variation of the additional parameter n changes the shape of the length distribution. As similarly discussed by Gardner *et al.* [49], this could be beneficial during mitosis. For instance, during prometaphase, the steep descent in the length distribution can appropriately limit the area that is explored by MTs in order to fasten search-and-capture [81] of chromosomes. In metaphase, accumulation of MT lengths around the maximum of the distribution may support the precise positioning of chromosomes in the metaphase plate and the maintenance of spindle length.²⁷

²⁶ provided that they do not leave the bounded regime

Stationary length distributions that have a maximum for short MT lengths before they apparently decrease exponentially and are similar to the ones in Fig. 2.11 have been measured in several experimental studies [82–87]. Though some of these studies have already been cited as evidence for a multistep catastrophe mechanism [49, 88], there are different reasons why this interpretation is dubious: In contrast to our model with a fixed minus and a dynamic plus end, the *in vitro* studies in Refs. [82, 86] examined free MTs that could polymerize simultaneously at both ends. Therefore, the shape of the length distribution can be rationalized by a convolution of the respective exponential distributions at the plus and the minus end, which are both obeying single-step dynamics [86]. In Ref. [83], the deviation from an exponential distribution for short MT lengths is attributed to the image resolution being too low to detect very short MTs. The results in Refs. [84, 85, 87] seem to be

²⁷ Any new terms used in this paragraph (prometaphase, search-and-capture etc.) are explained in the detailed description of mitosis in Sec. 3.1.1.

more in line with our model, yet these publications do not provide a quantitative evaluation of the measured length distributions, which makes a valid conclusion difficult. Besides, Refs. [84, 85] are *in vivo* experiments so that additional effects due to MAPs or spatial restrictions are likely.

In the regime of unbounded growth, the MT lengths approach a Gaussian distribution as in the single-step case but with a reduced variance. *In vivo*, the stabilization of MT growth due to an increase of the number of catastrophe steps might help interphase MTs, which have been shown to be in the unbounded regime [29, 89], to reach the cell boundary. On the other hand, at the transition from interphase to mitosis, MT lengths are significantly reduced in order to prepare the mitotic spindle assembly [85, 90]. The restructuring of the MT array may be supported by a reduction of the number of catastrophe steps, which destabilizes the MTs and shifts them to the bounded regime. This hypothesis is supported by the observation of Gardner *et al.* [49] that MCAK, which plays a key role for the control of MT dynamics during mitosis [91, 92], promotes catastrophes by reducing the required steps from $n = 3$ to $n = 1$ and simultaneously keeping the step rate ω constant.

Cooperative microtubule and kinetochore dynamics in the mitotic spindle

3

While we examined the polymerization dynamics of individual MTs in the last chapter, the subject of this chapter is an extensive analysis of the coupled dynamics of MT ensembles and chromosomes during cell division. The biological cell is the fundamental building block of all life, may it be unicellular organisms, like bacteria or yeasts, or multicellular life forms as plants or animals including humans.¹ All cells consist of a cytoplasm that is surrounded by the plasma membrane. The cytoplasm contains various organelles that fulfill different tasks. Examples are the ribosomes that enable protein biosynthesis, centrosomes serving as a MTOC, mitochondria, which are well known as “powerhouse of the cell” [96], or chloroplasts, which are responsible for photosynthesis.² Each cell of an organism contains its full genetic information in form of DNA (deoxyribonucleic acid). Depending on whether the DNA is distributed freely in the cytoplasm or whether it is organized in chromosomes and stored in a cell nucleus, cells can be classified as prokaryotes or eukaryotes, respectively. While prokaryotes comprise the unicellular domains of bacteria and archaea, eukaryotes form a third domain including the kingdoms of plants, fungi and animals [97].

Every cell existing in today’s world has its origin in the division of another, pre-existing cell. This principle of cell theory has already been stated in 1858 by Rudolph Virchow [98] with his famous words “Omnis cellula e cellula”.³ A very important task during cell division is the maintenance of the genetic information, i.e., the previously replicated DNA has to be distributed equally to the two daughter cells. Eukaryotic cells repeatedly pass through the cell cycle, during which the cell organelles are duplicated first and later divided into two identical daughter cells. The essential task of proper division of the DNA occurs during *mitosis*, which is part of a cell cycle. Mitosis describes the division of the cell nucleus and the proper distribution of the previously duplicated chromosomes. It is driven by the *mitotic spindle*, a molecular machine that consists of two opposite MT asters organized in two MTOCs, which build the two spindle poles. The MTs can bind to the sister chromatids from opposite sides via kinetochores, protein structures that are located at the centromere, and pull them apart in order to move them into the two daughter nuclei. During metaphase, i.e., in the moment before the sister chromatids are separated, the chromosomes are aligned in a plate at the spindle equator. It has been observed in several vertebrate cells that chromosomes do not rest in this

Large parts of this chapter have already been published in Ref. [93], which is licensed under CC BY 4.0 [94]. Moreover, some parts have already been part of my master’s thesis [95]. This includes the mitotic spindle model (Secs. 3.2.2–3.2.4), the mean-field theory for the one-sided model (parts of Sec. 3.3.1), and the derivation of the bistable regime in the c – M parameter plane (Fig. 3.16), which was the final result of my master’s thesis. New results, originally obtained as part my doctoral research, are the application of the mean-field theory to the two-sided model (Secs. 3.3.2 and 3.3.3), the generalizations in Sec. 3.4 and the extensive discussion in Sec. 3.5.

¹ The short introduction into cell biology and cell division in the following two paragraphs is based on the book of Alberts *et al.* [1].

² These examples are not present in all species; e.g., prokaryotes do not contain centrosomes or mitochondria, and chloroplasts can only be found in plant cells.

³ Latin for “every cell (arises) from another cell”.

metaphase plate but exhibit oscillations along the pole to pole axis known as *directional instability* [50–56], whereas in *Drosophila* embryos and *Xenopus* eggs a directional instability does not occur [99, 100].

Although several theoretical models that reproduce chromosome oscillations have been proposed in the past [57, 101–106],⁴ a quantitative understanding of the underlying mechanics of the MT–kinetochore–chromosome system is still lacking. The objective of this chapter is to gain new insights into the mechanisms of directional instability and to quantify conditions on several parameters for its occurrence. For that purpose, we start from the minimal model of Banigan *et al.* [57], which contains a single chromosome whose motion is solely driven by the force dependent dynamic instability of the MTs that are attached to the kinetochores via elastic linkers. Banigan *et al.* could trace back the chromosome oscillations to a bistable relation between the kinetochore velocity and an external force, which they observed in stochastic simulations of a model with only one spindle pole and one kinetochore. Here, we increase the understanding and the applicability of this minimal model dramatically by employing a novel mean-field approach based on Fokker–Planck equations (FPEs) that allows us to derive the bistable force–velocity relation mathematically and to quantify the parameter range for a bistability in the parameter plane of MT–kinetochore linker stiffness and the number of attached MTs.

By interpreting the force–velocity relation as phase space diagram for the full model with two spindle poles and two connected kinetochores as in Ref. [57], we show that bistability in the monopolar model is a necessary condition for kinetochore oscillations in the bipolar model. Beyond that, we are able

1. to quantify an oscillatory regime, in which kinetochores exhibit directional instability, in the parameter plane of linker stiffness and MT numbers predicting that linkers have to be sufficiently stiff;
2. to describe kinetochore motion in this oscillatory regime, calculate frequencies which agree with *in vivo* measurements [55] and to explain frequency doubling of breathing⁵ compared to single kinetochore oscillations;
3. to describe kinetochore motion in the non-oscillatory regime as fluctuations around a fixed point.

Later, in Sec. 3.4, we generalize the minimal model in several aspects, which allows us

⁴These models are reviewed in Sec. 3.2.1.

⁵As explained below, the term *breathing oscillations* describes the oscillations of the inter-kinetochore distance.

4. to show that high poleward flux velocities move the system out of the oscillatory regime and thereby explain why directional instability has been observed in mitotic vertebrate cells but not in *Drosophila* embryos and *Xenopus* eggs (Sec. 3.4.1);
5. to show that polar ejection forces reduce the amplitude of oscillations, induce a phase shift between sister kinetochores and are necessary to align the chromosome at the spindle equator (Sec. 3.4.2);
6. to derive as necessary condition for oscillations that either MTs must be able to apply pushing forces on the kinetochore or a catastrophe has to be induced with an increased catastrophe rate when a MT reaches the kinetochore (Sec. 3.4.3);
7. to provide a set of model parameters that reproduce experimental results for kinetochore oscillations in PtK1 cells quantitatively (Sec. 3.4.4).

All these results are validated by stochastic simulations in order to justify the assumptions that underlie our mathematical predictions.

In particular, we quantify lower bounds for linker stiffnesses that allow for oscillations and whose values depend on the behavior of MTs growing against the kinetochore. If kinetochore MTs can exert pushing forces, we find oscillations for linker stiffnesses $c > 16 \text{ pN } \mu\text{m}^{-1}$; also if MT catastrophes are induced upon reaching the kinetochore, we find oscillations in a similar range of linker stiffnesses. These constraints provide useful additional information on MT–kinetochore linkers, whose molecular nature is not completely unraveled up to now.

Before introducing the one-dimensional spindle model and presenting and discussing our results in Secs. 3.2.2 to 3.5, we start with a short summary of the relevant biological facts about the eukaryotic cell cycle and mitosis, followed by a brief overview of existing spindle models and their key differences.

3.1 The cell cycle

The cell cycle⁶ of eukaryotic cells can be divided into the *interphase* and the *M phase* (**m**itosis) as sketched in Fig. 3.1. Roughly speaking, the cell grows and replicates its components during interphase, and is divided in M phase. The cell cycle of a human somatic cell lasts approximately 20 hours from which the M phase takes only 1 h.⁷ Since it is crucial for the maintenance of life that the two daughter cells contain exactly the same genetic information, the proper replication and segregation of the chromosomes, which

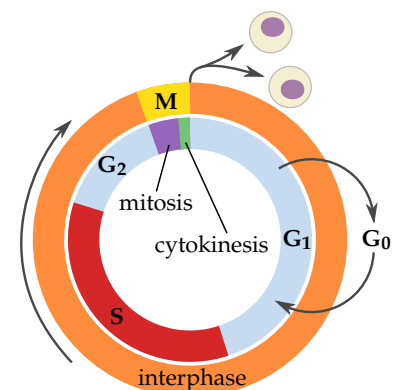


Figure 3.1: Phases of the cell cycle. Adapted from [107]. The chromosomes are replicated in S phase and the cell is divided in M phase. M and S phase are separated by two gap phases G₁ and G₂. A cell may rest in the non-dividing G₀ phase.

⁶ The following description of the cell cycle as well as the sections about mitosis (3.1.1) and the forces acting in the mitotic spindle (3.1.3) are based on the book of David O. Morgan [92].

⁷ The cell cycle can be much faster in other cells, e.g., 90 min in budding yeast or only 30 min and less in some metazoan embryos.

⁸ The centrosome is the major MTOC in animal cells, and—as we will see below—the two copies organize the mitotic spindle, which drives the chromosome segregation.

⁹ Mitosis and cytokinesis are explained in more detail below.

¹⁰ This is the case for most cells in the human body. E.g., most neurons and skeletal muscle cells are terminally differentiated and stay in G_0 until they or the whole organism dies, and liver cells rest in G_0 but can restart division when the liver is damaged [1].

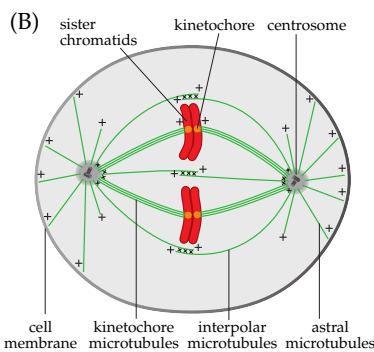
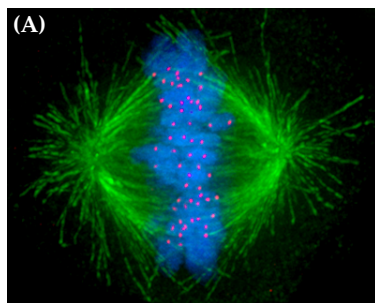


Figure 3.2: Mitotic spindle. (A) Microscopic image of a human mitotic spindle [108]. MTs are shown in green, Chromosomes in blue and kinetochores in red. (B) Sketch of the mitotic spindle. MTs are bound to the centrosomes with their minus ends while their plus ends are radiating outwards. Astral MTs interact with the cell boundary, interpolar MTs are cross-linked to opposite interpolar MTs via motor proteins, kinetochore MTs are attached to the chromatids via kinetochores.

Fig. (B) is adapted with permission from Ref. [92]; copyright (2007) by Oxford University Press.

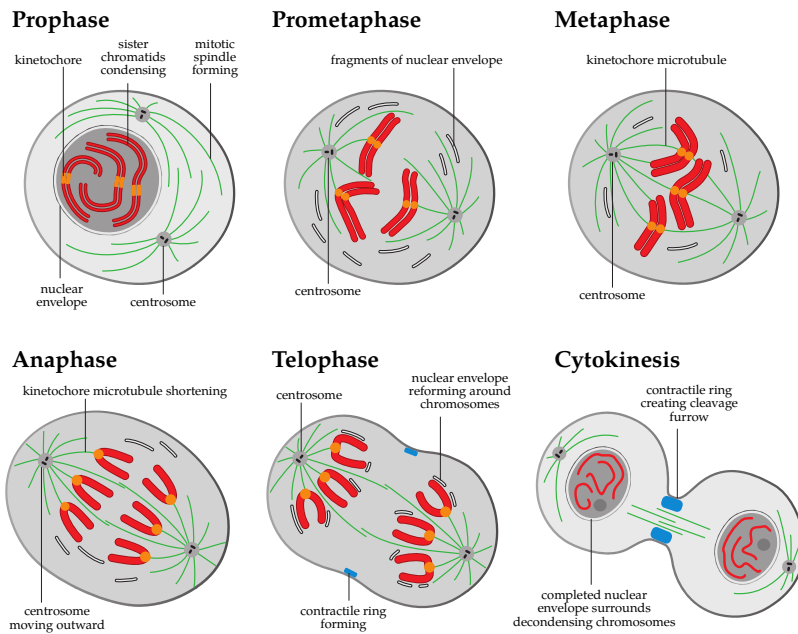
carry the genetic information in form of DNA and are located in the cell nucleus in eukaryotic cells, are of particular importance. The chromosomes are replicated each to two identical sister chromatids during *S phase* (synthesis), which is part of the interphase. It is ensured that each chromosome is duplicated only once. In animal cells, also the centrosome⁸ is duplicated during *S phase*. Other cell components, e.g., membranes or cell organelles, are reproduced throughout the whole cell cycle. The sister chromatids are segregated during *mitosis*, which is the first part of *M phase*. Mitosis is organized by the *mitotic spindle*, which consists of a large number of MTs pulling the sister chromatids apart. After mitosis, the cell contains two nuclei with the same set of chromosomes and is finally divided in a process called *cytokinesis*.⁹

Between *M* and *S phase*, there are two *gap phases* G_1 and G_2 , see Fig. 3.1. During these gap phases, the cell has additional time to grow and can monitor whether the environmental conditions are favorable for the entry into the following phase. Only if certain checkpoints are fulfilled, the cell switches from G_1 to *S phase* or from G_2 to *M phase*. Especially G_1 phase can last very long and the cell can even switch to a non-dividing rest phase called G_0 .¹⁰

Since the subject of this chapter is the dynamics of chromosomes during mitosis, we next explain the *M phase* in more detail. The following is a short description of a protein structure called *kinetochore*, which connects the chromatids with MTs. In preparation for the development of a mechanical model for chromosome dynamics, we close this section by discussing the relevant forces that act on the chromatids in the mitotic spindle.

3.1.1 Mitosis and cytokinesis

The mitosis is the division of the cell nucleus, which contains the replicated chromosomes after interphase. It is driven by the *mitotic spindle*, a complex molecular machine with a bipolar structure built by two opposite MT asters, which are located at the two spindle poles. The MTs within these asters can be characterized by the three different tasks they fulfill, see Fig. 3.2: *astral MTs* radiate outwards the spindle, and their plus ends interact with the cell cortex thereby controlling the position of the mitotic spindle within the cytoplasm; *interpolar MTs* build the scaffold of the spindle by interacting with interpolar MTs emerging from the opposite pole; finally, *kinetochore MTs* link directly to the chromosomes in the centromere region via protein complexes called *kinetochores*, and via these links, they can apply tensile forces, which are responsible for the segregation of the sister chromatids. In vertebrate cells, 10 to 40 MTs can be attached to the same kinetochore [109, 110] building a *kinetochore fiber* (k-fiber).



Mitosis consists of five phases—prophase, prometaphase, metaphase, anaphase and telophase—which we explain in the following and which are sketched and summarized in Fig. 3.3. Our explanation concentrates on the mitosis in vertebrate cells, however, we add comments on the differences to other species where it is appropriate.

Prophase

During prophase, two major processes are executed, chromosome condensation and initiation of spindle assembly by centrosome separation. At the end of interphase, the duplicated chromosomes in the nuclear envelope have the form of long, tangled chromatin strands. During prophase, the chromosomes condense, which means that each chromatid is densely packed and is linked by a cohesin bond with its sister chromatid that contains the same genetic information.¹¹ Outside the nucleus, the two copies of the centrosome move apart along the nuclear envelope to build the two spindle poles. This motion is mainly driven by two motor proteins: minus end directed dynein connects the plus ends of astral MTs with the cell cortex and pulls the centrosomes apart; kinesin-14 cross-links two antiparallel interpolar MTs, one with its head and the other with its motor domain. Since kinesin-14 are minus end directed motors, they pull the two centrosomes together and thereby balance the effect of the dynein motors at the cell cortex.

Figure 3.3: Phases of mitosis and cytokinesis.

Prophase: The chromosomes condense and the mitotic spindle starts forming.

Prometaphase: After nuclear envelope breakdown, the MTs search and capture the chromosomes.

Metaphase: The chromosomes are aligned in the metaphase plate at the spindle equator.

Anaphase: The chromosomes are segregated by shortening kinetochore MTs, and the spindle elongates.

Telophase: The spindle is disassembled and new nuclear envelopes form around the segregated chromosome sets.

Cytokinesis: The cell is divided by a contractile ring.

This figure is adapted with permission from Ref. [92]; copyright (2007) by Oxford University Press.

¹¹ The condensed, X-shaped chromosomes are well-known from karyograms and can only be observed during mitosis.

¹² This is not the case in yeast cells where mitosis takes place inside the nucleus. Moreover, instead of centrosomes, the MTs are organized by spindle pole bodies that are embedded in the nuclear envelope.

¹³ In cells without centrosomes, e.g., higher plant cells, chromosome attachment and even the whole spindle assembly itself is a self-organized process. In plant cells, the minus ends are organized by means of MAPs in two spindle poles.

¹⁴ There are three kinds of erroneous attachments: in a *syntelic* attachment, both sister kinetochores are attached to the same pole; in a *merotelic* attachment, one kinetochore is attached to both poles; in a *monotelic* attachment, one kinetochore is attached to one pole while its sister is unattached. A proper bipolar attachment is called *amphitelic*.

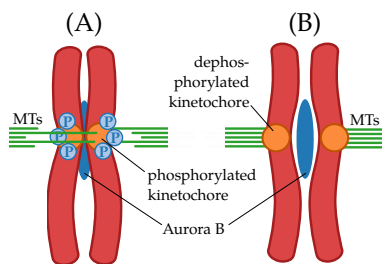


Figure 3.4: Error correction by Aurora B kinase. (A) In case of an erroneous attachment (here merotelic), the inter-kinetochore tension is low and the kinetochores are phosphorylated by Aurora B, which is located at the centromere. Phosphorylation decreases the MT binding affinity so that the erroneous attachments are deleted. (B) In case of an amphitelic attachment, the opposite MT ensembles pull the attached kinetochores apart towards low Aurora B concentrations. The resulting dephosphorylation of the kinetochores stabilizes the correct MT attachments.

Prometaphase

Prometaphase starts with the breakdown of the nuclear envelope.¹² This does not only release the condensed chromosomes into the cytoplasm but also a variety of motor and other proteins that regulate MT dynamics and support spindle assembly. As a consequence, there are more but shorter MTs than during interphase, which switch their polymerization states more rapidly. Proteins increasing the catastrophe rate, such as MCAK, which is part of the kinesin-13 family, play a major role for this conversion. Two further classes of motor proteins are released with nuclear envelope breakdown: kinesin-5 and the chromokinesins kinesin-4 and -10. While the latter ones mediate the polar ejection forces, which are explained below, kinesin-5 has two plus end directed motor domains that push antiparallel interpolar MTs apart, and regulates spindle length and position in interplay with the aforementioned dynein and kinesin-14 motors.

It is essential for mitosis that the chromosomes are attached properly to the two opposite poles via their kinetochores. This is achieved by two processes: centrosome mediated *search-and-capture* [81] and self-organization of MTs around the chromosomes.¹³ In the former process, the dense arrays of MTs that emerge from the centrosomes and rapidly grow and shrink *search* the space for chromosomes. During the search, a kinetochore might be attached laterally to a MT, which can be converted by different motor proteins to a proper end-on attachment of the kinetochore to the plus end so that the chromosome is *captured*. In the self-organized process, MTs nucleate around the chromosomes, may attach to a kinetochore, and are organized into an antiparallel array by the mentioned motor proteins. The spindle poles are established later by motors and MAPs that organize the minus ends.

Although the back-to-back arrangement of sister kinetochore pairs promotes the proper bipolar attachment of a chromosome to the two opposite spindle poles, there may still be erroneous attachments.¹⁴ An indicator for a correct attachment is the inter-kinetochore tension: when kinetochore MTs pull from both sides, the tension is high, otherwise it is low. Depending on the tension, the kinase Aurora B, which is located at the centromere between the two kinetochores, phosphorylates parts of the kinetochores and thereby influences the binding affinity and the dynamic parameters of the attached MTs in a way that favors a bipolar arrangement with high tension, see Fig. 3.4 [91, 111, 112].

Metaphase

After the completion of spindle assembly, the chromosomes are aligned in a plane at the spindle equator, the *metaphase plate*. It has been observed in somatic cells of several vertebrates¹⁵ that the chromosomes do not rest in this position but exhibit *directional instability* [50], which means that they regularly switch between moving *polewards* (P) and moving *away from the pole* (AP) resulting in an oscillation along the pole-to-pole axis. If present, these oscillations are stochastic and on the time scale of minutes, i.e., on a much larger time scale than the dynamic instability of single MTs. Both single kinetochores and the inter-kinetochore distance oscillate, but inter-kinetochore or *breathing oscillations* occur with twice the frequency of single kinetochore oscillations [55]. It is the major objective of this chapter to identify the origin of directional instability and the conditions that are necessary for its occurrence.

¹⁵ Examples are porcine LLC-PK1 cells [52], Newt lung cells [50, 51], human U2OS, HeLa and RPE1 cells [53, 54, 113], or PtK1 and PtK2 cells of a rat-kangaroo [55, 56].

Anaphase

When all chromosomes are correctly attached to the two opposite spindle poles, the sister chromatids are separated by loss of the cohesin bonds. This event marks the metaphase-to-anaphase transition. Without the cohesin bonds, the chromatids can be segregated, which is achieved by two processes. In anaphase A, the chromatids are pulled towards the spindle poles by shrinking kinetochore MTs. In anaphase B, the centrosomes, which are surrounded by the segregated chromatids after anaphase A, move away from each other, which is mainly driven by kinesin-5 motors that push overlapping antiparallel interpolar MTs apart.

Telophase

Mitosis is accomplished in telophase, which is mainly characterized by the disassembly of the mitotic spindle. During that process, the MTs detach from the kinetochores and assume the polymerization dynamics from interphase with few but long MTs, i.e., the changes from prometaphase are revised. Moreover, two nuclear envelopes form around the segregated chromosome sets,¹⁶ which decondense and assume the tangled form they have during interphase. At the end of telophase, the cell contains two spatially separated nuclei each comprising an identical and complete set of chromosomes.

¹⁶ In budding yeast, where mitosis takes place inside the nucleus, the nucleus is elongated during anaphase and divided during cytokinesis.

Cytokinesis

After mitosis, the cell itself is divided by cytokinesis. Cytokinesis is driven by a contractile ring,¹⁷ which is composed of actin filaments

¹⁷ Higher plant cells are not divided by a contractile ring. Instead, a new cell wall is formed between the two nuclei and divides the cytoplasm.

and myosin motors and already starts forming during telophase. The contractile ring encircles the cell membrane between the two daughter nuclei and centrosomes, and divides the cytoplasm by contracting and thereby constricting the cell. With the completion of cytokinesis, the M phase is finished and the cell has been divided into two daughter cells that enter the G₁ phase of another cell cycle.

3.1.2 The kinetochore–microtubule interface

The kinetochores, two of which are located at the centromere of each condensed chromosome, play a crucial role for mitosis as they transmit the forces from depolymerizing MTs that pull the sister chromatids apart.¹⁸ Within the MT lattice, mechanical energy is stored originating from the GTP hydrolysis. When the GTP cap is lost and the MT starts to shrink with its protofilaments curling outwards,¹⁹ this energy is released and a single protofilament can generate power strokes of up to 5 pN [21]. Though the more than 100 protein species composing the kinetochore have been identified in the past, it is still not completely understood how these proteins are arranged to facilitate force coupling to the MTs.

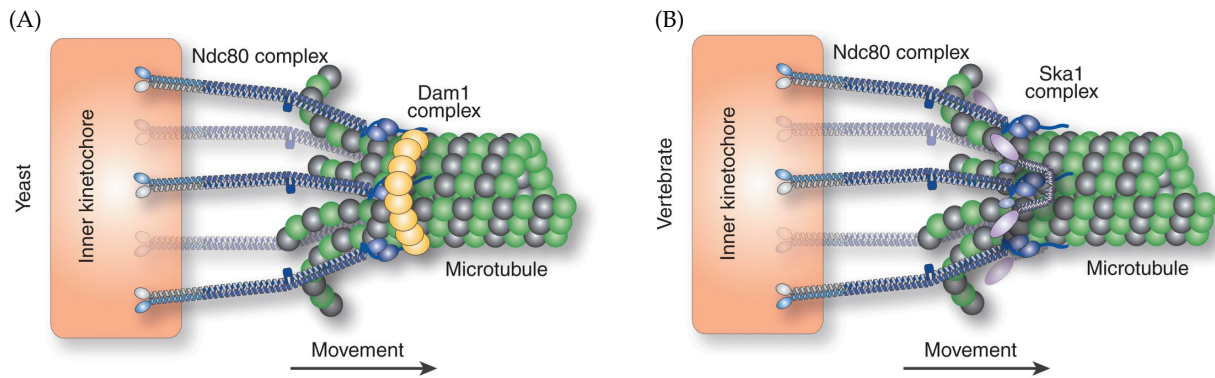
A kinetochore consists of an inner kinetochore that is connected to the chromatid and an outer kinetochore attached to the MTs, see Fig. 3.5. While some of the proteins that build up the inner kinetochore are bound to centromeric DNA throughout the whole cell cycle [116], the outer kinetochore is only assembled during mitosis [117]. Investigating the question how the outer kinetochore binds the MTs, during the last two decades, rod-like *Ndc80* complexes crystallized as the major component of force transmission [118–120]. One end of an *Ndc80* complex can bind directly to the MT lattice via a globular CH domain and an unstructured tail [121]. Human kinetochores contain about 250 *Ndc80* complexes [122], from which approximately 30% are engaged in MT binding [123]. *In vitro* experiments have shown that *Ndc80* complexes can only trace depolymerizing MTs and withstand tensile forces if they are oligomerized [58, 120].

In budding yeast, MT tracing is accomplished by ring-like *Dam1* complexes that surround the MTs, are linked by *Ndc80* complexes and can be moved by depolymerizing curled protofilaments as sketched in Fig. 3.5A [124–128]. While *Dam1* can only be found in yeast cells, *Ska1* complexes may have a similar function in metazoan and plant cells [129–132], see Fig. 3.5B, which is emphasized by *in vitro* experiments showing that *Ska1* increases the MT binding affinity of *Ndc80* and the ability of this bond to withstand large forces [59].²⁰

¹⁸ This section is based on the reviews of Cheeseman [114] and Long *et al.* [115].

¹⁹ See Sec. 2.1.2 and Fig. 2.5.

²⁰ The experiments in Refs. [58, 59] are the subject of Chapter 4, where we furthermore discuss possible binding mechanisms between *Ndc80* complexes and a MT more thoroughly.



Besides the proteins involved in MT binding, the kinetochore also contains regulatory proteins that control MT dynamics, e.g., proteins of the kinesin-13 family that promote catastrophes [133].²¹ Moreover, in experiments with reconstituted yeast kinetochores, the attached MTs exhibited force dependent dynamic instability, e.g., tension enhanced rescues and growth but suppressed catastrophes [134]. Also the binding affinity turned out to depend on force, and in particular, detachment of depolymerizing MTs was suppressed if tension was high, which means that kinetochores provide *catch bonds* that tighten under tension. Since, as written above, high tension is a marker for a correct bipolar attachment, this catch bond behavior supports avoidance and correction of erroneous attachments during prometaphase.

3.1.3 Forces in the mitotic spindle

Before introducing a mechanical model of the mitotic spindle, we need to know the relevant forces that are acting during mitosis. Above, we already described the effects of dynein, kinesin-5 and kinesin-14, which apply forces on the spindle poles via astral or interpolar MTs and thereby determine the length and the position of the mitotic spindle. Since we aim to examine the dynamics of chromosomes and for that purpose use a model assuming fixed spindle pole positions, these forces are not of interest in the following.

The three major forces that act on a chromosome are sketched in Fig. 3.6. The first to mention is the poleward force that is exerted by depolymerizing kinetochore MTs²² in a mechanism as discussed in Fig. 3.5. Since two chromatids are linked by the cohesin bond, a depolymerizing kinetochore MT that pulls a chromatid polewards simultaneously exerts an AP-directed force on the sister chromatid. With a bipolar attached chromosome, this results in a tug-of-war of the opposite k-fibers. Later, when the cohesin bond is lost in anaphase, the depolymerizing kinetochore MTs are the main driver of chromatid segregation.

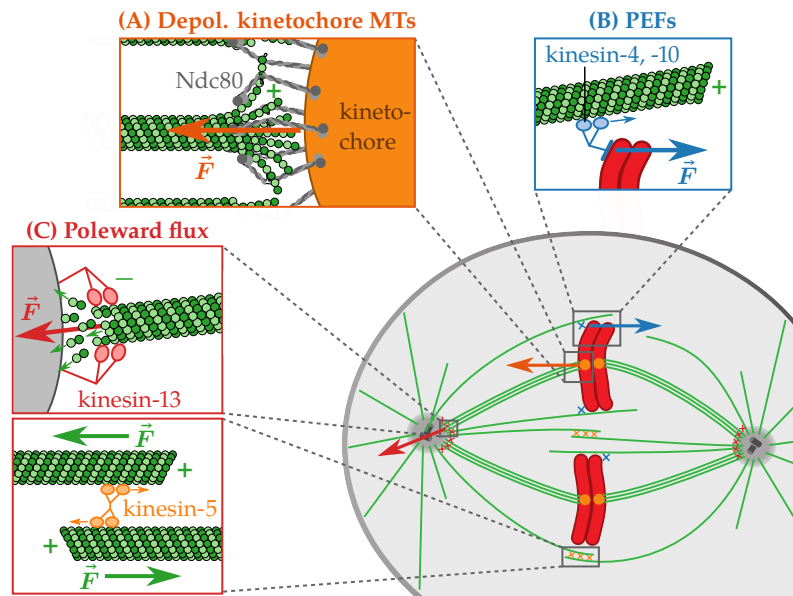
Figure 3.5: Kinetochores-MT interface. MTs are connected to the inner kinetochore via rod-like Ndc80 complexes. (A) In yeast cells, the Ndc80 complexes are attached to a Dam1 ring that surrounds the MT and can trace the depolymerizing plus end. (B) Vertebrate cells do not contain Dam1 rings, but the the Ndc80-MT binding is supported by Ska1 complexes. This figure is reproduced with permission from Ref. [114]; copyright (2014) by Cold Spring Harbor Laboratory Press.

²¹ MCAK, a catastrophe promoter present in vertebrate cells, is included in our model in Sec. 3.4.3.

²² Although polymerizing MTs may also be able to generate *compressive* forces in other situations [135–138], there is evidence that kinetochore MTs lack this ability [51, 139].

Figure 3.6: Forces acting on the chromosomes. (A) Depolymerizing MTs that are connected to the kinetochore via Ndc80 fibrils pull the chromatid polewards. (B) Polar ejection forces (PEFs). Plus end directed chromokinesins push the chromatid arms away from the pole. (C) Poleward microtubule flux. Kinesin-13 depolymerizes the minus ends at the centrosome, resulting in a tubulin flux from the plus to the minus end. For interpolar MTs, poleward flux is supported by kinesin-5 with two plus end directed motor domains.

The cartoon of the spindle is adapted from Ref. [92]; copyright (2007) Oxford University Press; see Fig. 3.2B.



Another poleward acting force results from the *poleward microtubule flux* which describes the kinesin-13 driven depolymerization of MTs at their minus ends near the centrosome. During metaphase, on the one hand, the depolymerization of kinetochore MTs is balanced by their polymerizing plus ends so that the MT length stays constant and there is a continuous flux of tubulin from the plus to the minus end.²³ For interpolar MTs, this balance is supported by kinesin-5 pushing antiparallel MTs apart. On the other hand, during anaphase, poleward flux accelerates the segregation of sister chromatids as the kinetochore MTs are depolymerized at both ends simultaneously.

Finally, *polar ejection forces* (PEFs) are the only AP-directed forces.²⁴ They are exerted by plus end directed chromokinesins of the kinesin-4 and kinesin-10 families, whose motor domains move along non-kinetochore MTs while their head domains are attached to the chromosome arms. In the vicinity of the spindle pole, PEFs may also be a consequence of the dense array of growing MTs pushing the chromosome arms directly without assistance of chromokinesins. During prometa- and metaphase, the PEFs push the chromosomes towards the spindle equator and ensure their positioning in the metaphase plate [140]. Since PEFs would impede the chromatid segregation, they are eliminated by destruction of the chromokinesins in anaphase.

Beside the three mentioned active forces—depolymerizing kinetochore MTs, poleward flux and PEFs—which act on the two sister chromatids from opposite poles, a moving chromatid is always exposed to *viscous drag* which results from the high viscosity of the cytoplasm. During Metaphase, all forces are balanced in a way that the chromosomes are arranged in the metaphase plate and may exhibit directional instability. We examine this force balance

²³ This behavior can be compared to treadmilling of free MTs, see Sec. 2.1.2. The difference is that treadmilling MTs move in plus end direction while the spindle MTs undergoing poleward flux are held at a constant position by the involved motor proteins.

²⁴ with the exception of indirect forces transmitted from the sister chromatid via the cohesin bond

in the following sections by means of a mechanical model, and show how and under which conditions the interplay of these three major forces induces directional instability of chromosomes.

3.2 Model of the mitotic spindle

In this section, we introduce the one-dimensional spindle model that should respect the considerations about the acting forces made in the previous section and is examined throughout this chapter by means of both stochastic simulations and a novel deterministic mean-field approach. Beforehand, we review some similar, formerly developed models to point out the benefits of our work and in particular of our mean-field approach.

3.2.1 Overview of existing spindle models

There is a huge variety of mitotic spindle models focusing on different aspects and phases of mitosis as reviewed in Refs. [46, 141–144]. Examples for such aspects are the assembly of the mitotic spindle [145–148], control of spindle position [149–153] and spindle length [141, 154, 155], or the search-and-capture of chromosomes during prometaphase [81, 156–160].

Our model focuses on the chromosome dynamics during metaphase and can be associated with a set of several theoretical models that have been proposed over the last 20 years and reproduce chromosome oscillations [57, 101–106], see Tab. 3.1.²⁵ These models have in common that they simplify the mitotic spindle to a quasi-one-dimensional geometry, neglect explicit spindle pole dynamics, and contain two ensembles of MTs growing from the two spindle poles. The MTs link the two opposite poles to a single chromosome, which is represented by two kinetochores that are connected by a spring (the cohesin bond).²⁶ Kinetochores dynamics are defined by a balance of the several forces that act on the chromatids. These forces may include viscous drag and the kinetochores follow overdamped motion [57, 102–105], or they are assumed to reach force balance instantaneously under the influence of MT depolymerization and polymerization forces because the friction force is small [101, 106]. Fig. 3.7 depicts the generic composition of such one-dimensional force balance models.

Several MT depolymerization and polymerization forces are included in the models. Possibly, poleward MT flux is included [57, 102], which describes a constant flux of tubulin from the plus ends towards the spindle pole and is probably driven by plus end

²⁵ More models are reviewed, e.g., in Refs. [142, 161].

²⁶ There are other one-dimensional models that also address chromosome dynamics but differ in one of these points from the mentioned references. Spindle pole dynamics can be examined by including interpolar [162] or astral MTs [163], thereby also considering control of spindle length and/or position. Models for budding yeast spindles with only one MT per kinetochore (instead of a MT ensemble) are proposed in Refs. [164–166]. Furthermore, models with a single spindle pole [167, 168] deal with oscillations in monooriented chromosomes which have been observed during prometaphase [50, 169] or after severing the cohesin bond [170]. Such a monopolar model is the starting point of our mean-field approach.

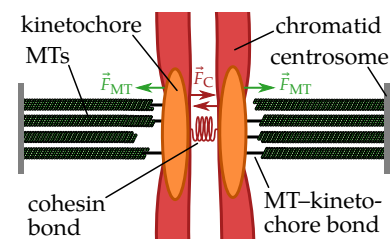


Figure 3.7: One-dimensional force balance models. The single chromosome is modeled as a pair of sister kinetochores connected via a (visco-) elastic spring that represents the cohesin bond. From each of the two fixed centrosomes, an ensemble of MTs emerges, which may be attached to the associated kinetochore. The nature of the MT-kinetochore bond varies from model to model, see Tab. 3.1. Kinetochore dynamics are determined by a force balance. The main forces include depolymerizing MTs pulling the kinetochores apart (\vec{F}_{MT} , green), the elastic force of the cohesin bond (\vec{F}_C , red) and maybe viscous drag.

Ref. (year)	Linker model	Catch bonds	Equal force sharing	Force-dep. rescue/catastr.	Poleward MT flux	PEFs	MT pushing forces
Joglekar [101] (2002)	Hill sleeve		No	No	No	Yes	No
Civelekoglu [102] (2006)	Motor	No	No	Yes	Yes	Yes	Yes
Civelekoglu [105] (2013)	Viscoelastic	Yes	No	Yes	No	Yes	No
Shtylla [103, 104] (2010)	Hill sleeve		Yes	No	No	Yes	Yes
Banigan [57] (2015)	Elastic	Yes	No	Yes	Yes	No	Yes
Klemm [106] (2018)	Permanent		Yes	Yes	No	No	Yes
This work	Elastic	Yes	No	Yes	Sec. 3.4.1	Sec. 3.4.2	Sec. 3.4.3

Table 3.1: Overview of assumptions of models exhibiting stochastic chromosome oscillations. In the referred sections we discuss how poleward flux, PEFs and the absence of pushing forces affect kinetochore dynamics in the model used for this work.

directed kinesin-5 motors pushing overlapping antiparallel interpolar MTs apart and kinesin-13 proteins that depolymerize MTs at the centrosome [171]. The main poleward forces on kinetochores are generated by depolymerization of MTs, which builds up and transmits a poleward force via the MT-kinetochore link. Only in the model of Civelekoglu-Scholey *et al.* [102], the main poleward force is generated by MT depolymerization motors at the spindle poles. In order to be able to exert poleward pulling forces, the MT-kinetochore bond needs to remain intact during depolymerization and “slide” with the depolymerizing MT plus end. The force that can be exerted depends on the nature of this bond and is high if it is a catch bond that tightens under tension [134]. All models include switching between polymerizing and depolymerizing MT states. In most models, this switching is caused by stochastic catastrophe and rescue events.²⁷ Only Shtylla and Keener [103, 104] do not introduce explicit MT catastrophes, but catastrophe-like events are triggered by a chemical feedback loop if MTs approach the kinetochore.

²⁷ The stochastic switching between polymerizing and depolymerizing states is known as “dynamic instability” [68], see Sec. 2.1.2.

The two ensembles of MTs are engaged in a kind of tug-of-war and exert antagonistic forces via the spring connecting the kinetochores: poleward (P) depolymerization forces of one ensemble generate an antipoleward (AP) force on the other kinetochore. Experiments suggest that kinetochore MTs can only exert P-directed pulling forces by depolymerization but are not able to directly exert AP-directed pushing forces on the kinetochore during polymerization [51, 139]. During directional instability, the spindle switches between the left and the right ensemble pulling actively in P-direction by depolymerization while the respective other ensemble is passively following in AP-direction by polymerization without actively pushing. Nevertheless, some models have included AP-directed MT pushing forces [57, 102–104, 106]. Antagonistic AP-directed forces on the kinetochores can also be generated by polar ejection forces (PEFs). They originate from non-kinetochore MTs interacting with the chromosome arms via collisions or chromokinesins belonging to the kinesin-4 and kinesin-10 families [172] and pushing them thereby towards the spindle equator. The action of different P- and

AP-directed forces can move kinetochores back and forth and also tense and relax the inter-kinetochore cohesin bond.

The models differ in their assumptions about the MT–kinetochore link and the mechanism how MT dynamics is directed by mechanical forces to give rise to kinetochore and inter-kinetochore distance oscillations. The model by Joglekar and Hunt [101] uses the thermodynamic Hill sleeve model [156] for the MT–kinetochore connection, which assumes equally spaced rigid linkers that diffuse on the discrete MT lattice. Shtylla and Keener [103, 104] combine a continuous version of the Hill sleeve model with a negative chemical feedback between the force at the MT–kinetochore interface and the depolymerization rate. In Hill sleeve models, there is no effect of MT insertion and, thus, force onto the MT dynamic instability, i.e., on catastrophe and rescue rates. The Hill sleeve can transmit pulling forces onto the kinetochore up to a critical force above which MTs pull out of the sleeve [101], and there is evidence that the Hill sleeve exhibits catch-bond-like behavior [173]. However, more recent studies show that the kinetochore is not rigid, as supposed in the Hill sleeve model, but should be viewed as a flexible framework [174]. Moreover, Ndc80 fibrils have been suggested as main force transmitter [118–120], which motivated Keener and Shtylla to modify their Hill sleeve model by replacing the rigid attachment sites with elastic linkers and allowing for a force feedback onto MT depolymerization [34]. Nonetheless, sleeve models remain speculative as electron microscopy has not yet revealed appropriate structures [175, 176]. Civelekoglu-Scholey *et al.* [102] proposed a model in which MTs and kinetochores are linked by motor proteins (dyneins) walking towards the MT minus end. These links have no catch bond like behavior, but are assumed to be able to transmit tension onto MTs, which promotes MT rescue. In Ref. [106], no explicit linkers are introduced but permanent MT–kinetochore links are assumed that can transmit both pulling and pushing forces onto MTs. Since the exact nature of MT–kinetochore linking structures is not known, a model of the MT–kinetochore link as a generic elastic structure seems reasonable, which is based only on the available solid information about the kinetochore–MT interface with as little further speculation as possible.²⁸ Such an approach can be found in recent models where the MTs are linked to the kinetochore via (visco-)elastic springs [57, 105].²⁹ The MT–kinetochore bond can be modeled as a catch bond, and the elastic linkers also transmit forces back onto the MT allowing for a force feedback onto MT dynamics as it has been measured in Ref. [134].

In the model of Shtylla and Keener [103], MTs that are attached to the same kinetochore share the force from the cohesin bond equally and exhibit synchronous dynamics. The last assumption is contradictory to the experimental observation that one kinetochore

²⁸ A generic elastic linker is probably the most simple and least speculative way to model the kinetochore structure depicted in Fig. 3.5 with rod-like Ndc80 complexes as main force transmitters.

²⁹ While Civelekoglu *et al.* [105] model single Ndc80 complexes as viscoelastic springs attaching to and detaching from a MT individually, Banigan *et al.* [57] summarize the proteins engaged in a MT–kinetochore bond to a simple elastic spring with a constant stiffness.

MT ensemble does not coherently (de)polymerize but always consists of a mixture of both states [177, 178]. Klemm *et al.* [106] take into account this observation by dividing each MT ensemble into a growing and a shrinking sub-ensemble, but also make the strong assumption of equal force sharing between the MTs within each sub-ensemble. All other models allow for individual MT dynamics and for different forces between MTs depending on the distances of MTs to the kinetochore.

The main mechanism for oscillations differs between the models depending on the main antagonistic AP-directed force that switches a depolymerizing P-directed ensemble back into AP-directed polymerization. Switching can be triggered by the AP-directed force that the other ensemble can exert via the cohesin spring during depolymerization and by AP-directed PEFs if MT catastrophes are suppressed or rescues are promoted under tension. In the model by Joglekar and Hunt [101], AP-directed PEFs are essential for switching. Civelekoglu-Scholey *et al.* [102] proposed a model in which force is transmitted by motor proteins. By variation of the model parameters, they were able to reproduce a wide range of chromosome behavior observed in different cell types. In this model, a depolymerizing P-directed ensemble switches because tension in the cohesin spring and PEFs promote rescue events. A modified model [105] uses viscoelastic catch bonds and accounts for the observation that in PtK1 cells only chromosomes in the center of the metaphase plate exhibit directional instability [55]. This dichotomy is explained with different distributions of PEFs at the center and the periphery of the metaphase plate.³⁰ In the model by Shtylla and Keener [103, 104], MT catastrophe-like events are only triggered by a chemical feedback so that kinetochore oscillations become coupled to oscillations of the chemical negative feedback system: AP-directed MT polymerization exerts pushing forces onto the kinetochore but triggers switching into a depolymerizing state, and MT depolymerization exerts P-directed pulling forces and triggers switching back into a polymerizing state.

Whereas in Refs. [101, 102, 105] AP-directed PEFs are present and in the model by Joglekar and Hunt [101] also essential for realistic kinetochore oscillations, Banigan *et al.* [57] presented a minimal model with simple elastic linkers and neglecting PEFs. They were able to trace chromosome oscillations back to a bistable force-velocity relation of a kinetochore in their monopolar or one-sided minimal spindle model, where a single kinetochore under force is connected to one or several MTs. Referring to experiments with budding yeast kinetochores [134], they modeled MT dynamics with force-dependent velocities, catastrophe and rescue rates. In this model, kinetochore oscillations arise solely from the collective behavior of attached MTs under force and the resulting interplay

³⁰ This explanation turns out to probably be wrong as we discuss at the end of Sec. 3.5.

between P-directed depolymerization forces and AP-directed polymerization forces of the opposing MT ensembles. Force-dependent velocities, catastrophe and rescue rates are essential to trigger switching of kinetochore motion and oscillations in this model. However, MTs can exert pushing forces so that it is unclear to what extent the oscillation mechanism remains functional if pushing forces are absent as suggested experimentally.³¹ Also the recent model by Klemm *et al.* [106], which aims to describe kinetochore dynamics in fission yeast, does not rely on PEFs. It uses a permanent MT–kinetochore bond and oscillations result from the interplay between MT depolymerization and polymerization forces via force-dependent MT dynamics; also in this model MTs can exert pushing forces. Moreover, the model includes kinesin-8 motors that enhance the catastrophe rate and have a centering effect on the chromosome positions.

Finally, the models can be classified into purely computational work based on stochastic simulations [57, 101, 102, 105] and mathematical models solving deterministic differential equations [103, 104, 106]. While on the one hand such mathematical approaches often facilitate a deeper insight into the underlying mechanisms of the modeled system, on the other hand they usually require stronger simplifications in order to keep the equations at least numerically solvable and are therefore even more artificial than computational models. The simplification made in the mathematical models of Shtylla *et al.* [103, 104] and Klemm *et al.* [106] is the aforementioned equal force sharing among the kinetochore MTs, which is not necessary in the computational models, where an ensemble of individual MTs can be simulated quite easily. However, while the assumption of equal force sharing is exact for systems with a single MT and might still be a reasonable approximation when only a few MTs are linked to the kinetochore,³² it is likely to fail for larger MT ensembles. In this chapter, we close this gap by introducing a novel mathematical approach containing *non-uniform* MT distributions that correctly describes systems with a large number of MTs. An essential part in our quantitative analysis is a mean-field solution of the one-sided model of Banigan *et al.* [57], starting from FPEs for the length distribution of the MT–kinetochore linkers. The only mean-field approximation is to neglect stochastic velocity fluctuations of the attached kinetochore.³³

In all Refs. [57, 101–106], a sufficient set of ingredients is given for the respective model to exhibit oscillations including a specific choice of parameter values. It is a much harder task to give necessary conditions and parameter ranges for oscillations, which means to obtain quantitative bounds on model parameters, than to give a sufficient set of conditions. This is the aim of the present chapter within a model that starts from the minimal model by Banigan

³¹ We answer this question in Sec. 3.4.3.

³² Klemm *et al.* [106] model fission yeast with four MTs per kinetochore. Since they divide each foursome of MTs into a growing and a shrinking sub-ensemble, i.e., four ensembles to describe eight MTs, assuming an equally shared force for MTs within the same sub-ensemble does not seem to be an over-simplification.

³³ This is the necessary simplification to keep our mathematical model solvable, comparable to the strong assumption of equal force sharing in Refs. [103, 104, 106]. In Appendix B.2, we present an (less successful) approach assuming equal force sharing but in exchange allowing for velocity fluctuations.

et al. [57] and generalizes this model in several respects in later sections, see Tab. 3.1. In this way we discuss the complete inventory of possible forces acting on the kinetochore and their influence on oscillations.

3.2.2 One-dimensional model of the mitotic spindle

We use a one-dimensional model of the mitotic spindle as depicted in Fig. 3.8, which is based on the generic model in Fig. 3.7 and similar to the model from Ref. [57]. The x -coordinate specifies positions along the one-dimensional model, and we choose $x = 0$ to be the spindle equator. The spindle model contains a single chromosome represented by two kinetochores, which are linked by a spring with stiffness c_k and rest length d_0 . Two centrosomes margin the spindle at fixed positions $\pm x_c$, i.e., the dynamics of the centrosomes are neglected.³⁴ From each centrosome, a constant number of M MTs emerges with their plus ends directed towards the spindle equator. Each MT exhibits dynamic instability [68] and attaches to and detaches from the corresponding kinetochore stochastically. The MTs are confined by the centrosomes. It is reasonable to assume that they undergo a forced rescue and detach from the kinetochore if they shrink to zero length. Attached MTs are connected to the kinetochore by a linker, which we model as a Hookean polymeric spring with stiffness c and zero rest length. This spring exerts a force $F_{mk} = -c(x_m - X_k)$ on each MT, and each MT exerts a counter force $-F_{mk}$ on the kinetochore, where X_k and x_m are the positions of the kinetochore and the MT tip.

In the following, we define all MT parameters for MTs in the left half of the spindle model; for MTs in the right half, velocities v and forces F have opposite signs.³⁵ In the left half, tensile forces on the MT–kinetochore link arise for $X_k > x_m$ and pull the MT in the positive x -direction, $F_{mk} > 0$. In Ref. [134], the velocities of MT growth v_{m+} and shrinkage v_{m-} as well as the rates of catastrophe ω_c , rescue ω_r and detachment³⁶ $\omega_{d\pm}$ have been measured while MTs were attached to reconstituted yeast kinetochores. They can all be described by an exponential dependence on the force F_{mk} that acts on the MT plus end:

$$v_{m\pm} = v_{\pm}^0 \exp\left(\frac{F_{mk}}{F_{\pm}}\right), \quad \omega_i = \omega_i^0 \exp\left(\frac{F_{mk}}{F_i}\right), \quad (3.1)$$

(for $i = r, c, d+, d-$) with $F_+, F_r, F_{d+} > 0$ and $F_-, F_c, F_{d-} < 0$ for the characteristic forces, because tension ($F_{mk} > 0$) enhances growth velocity, rescue and detachment of a growing MT, while it suppresses shrinking velocity, catastrophe and detachment of a shrinking MT. We note that we use signed velocities throughout this chapter, i.e., $v_{m-} < 0$ and $v_{m+} > 0$. Suppression of detachment

³⁴For a one-dimensional spindle model including centrosome dynamics and astral MTs, see for instance Ref. [163].

³⁵E.g., when a MT in the right half is growing with the (positive) velocity v_{m+} , its tip moves in the negative x -direction: $\dot{x}_m = -v_{m+}$.

³⁶There are different detachment rates $\omega_{d\pm}$ for growing (+) and shrinking (−) MTs.

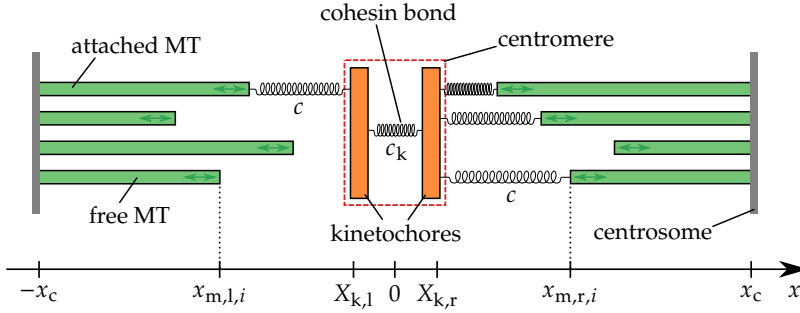


Figure 3.8: One-dimensional model of the mitotic spindle. M MTs arise from each centrosome, which margin the spindle. Each MT undergoes dynamic instability and can attach to / detach from the corresponding kinetochore. The MT–kinetochore linkers are modeled as elastic springs with stiffness c . The kinetochores are connected via a spring with stiffness c_k representing the cohesin bond.

of shrinking MTs is the catch bond property of the MT–kinetochore link. The attachment rate is assumed to follow a Boltzmann distribution,

$$\omega_a = \omega_a^0 \exp\left(\frac{c(X_k - x_m)^2}{2k_B T}\right), \quad (3.2)$$

according to the elastic energy of the MT–kinetochore linker.

The kinetochore motion is described by an overdamped dynamics,

$$v_k \equiv \dot{X}_k = \frac{1}{\gamma}(F_{kk} + F_{km}), \quad (3.3)$$

with the friction coefficient γ , and the forces

$$F_{kk} = c_k(X_{k,r} - X_{k,l} - d_0), \quad (3.4)$$

$$F_{km} = - \sum_{\text{att. MTs}} F_{mk}, \quad (3.5)$$

originating from the cohesin bond between the kinetochores and the MT–kinetochore linkers of all attached MTs, respectively.

We use parameter values as listed in Tab. 3.2. Most of them are obtained from experiments, in particular those of the load dependent MT dynamics. The parameters from Tab. 3.2 are kept constant until Sec. 3.4.4, where we fit the model as a proof of concept to experimental data of chromosome oscillations in PtK1 cells. Before, we follow our actual aim, which is to achieve a deeper understanding of the mechanisms that underlie directional instability by studying the influence of only a few crucial parameters.

For that purpose, we start with the investigation of the minimal model in which we detect the MT number M and especially the stiffness c of the MT–kinetochore linker as crucial parameters. In the minimal or basic model, we neglect poleward flux and PEFs and use the same simple spring model for the MT–kinetochore linker as Banigan *et al.* [57] where the MT plus ends are able to “overtake” the kinetochore³⁷ and thereby exert pushing forces $F_{km} > 0$ on the kinetochore, which could be interpreted as a compression of the

³⁷ $x_m > X_k$, again for MTs in the left half of the spindle

Table 3.2: Model parameters. The parameters listed here are kept constant except for Sec. 3.4.4.

Transition parameters	ω_i	ω_i^0 (s ⁻¹)	F_i (pN)	
Catastrophe	ω_c	0.0019	-2.3	[134]
Rescue	ω_r	0.024	6.4	[134]
Detachment of growing MT	ω_{d+}	0.000 11	3.8	[134]
Detachment of shrinking MT	ω_{d-}	0.035	-4.0	[134]
Attachment rate	ω_a	1.0		estimated
Velocity parameters	$v_{m\pm}$	v_{\pm}^0 (nms ⁻¹)	F_{\pm} (pN)	
Growth	v_{m+}	5.2	8.7	[134]
Shrinkage	v_{m-}	-210.0	-3.2	[134]
Other parameters	Symbol	Value		
Cohesin bond stiffness	c_k	20 pN μm^{-1}		estimated
Cohesin bond rest length	d_0	1 μm		[51]
Centrosome position	x_c	6.8 μm		[54]
Friction coefficient	γ	1 pN s μm^{-1}		estimated
Thermal energy	$k_B T$	4 pN nm		estimated

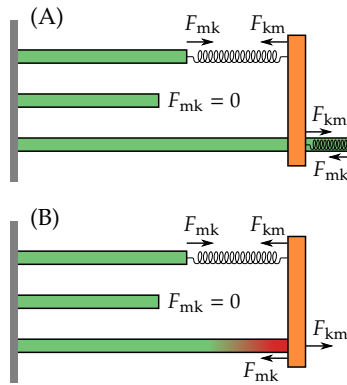


Figure 3.9: Boundary condition at the kinetochore. (A) In the minimal model, the MTs are not confined by the kinetochore but can grow across it and pull it thereby away from the pole. (B) This can be interpreted as compression of a MT that grows against and pushes the kinetochore. In Sec. 3.4.3, we lift the assumption of pushing MTs.

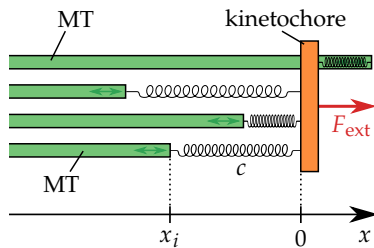


Figure 3.10: One-sided model of the mitotic spindle. The cohesin bond is replaced by the external force F_{ext} . MTs are not confined by a centrosome and permanently attached to the single kinetochore so that the MT–kinetochore distances $x_i = x_{m,i} - X_k$ are the only relevant coordinates.

MT–kinetochore linker, see Fig. 3.9. Later, we generalize the minimal model as described in Tab. 3.1. Each of the model extensions involves one additional parameter, and in a first approach, we add each extension separately in order to analyze its specific influences on kinetochore dynamics. In a first step, we add poleward MT flux, which describes a constant flux of tubulin from the plus ends towards the spindle pole [171], by shifting the MT velocities $v_{m\pm}$ by a constant flux velocity v_f . PEFs, which push the kinetochore away from the pole [172], are included in a second step as external forces that depend on the absolute positions of the kinetochores and a force constant k . Finally, we take account of the hypothesis that MTs are not able to apply pushing forces on the kinetochore [51, 139] by modifying the model such that the growth of a MT is stalled when it reaches the kinetochore and a stalled MT might have an increased catastrophe rate $\omega_c^{\text{kin}} > \omega_c^0$.

3.2.3 One-sided spindle model

Following the approach of Banigan *et al.* [57], we introduce a one-sided model that contains only the left half of the two-sided basic model from Fig. 3.8 with a single kinetochore and a single MT ensemble as depicted in Fig. 3.10. In the one-sided model, the cohesin bond is replaced by a constant external force F_{ext} so that Eq. (3.3) simplifies to

$$v_k = \frac{1}{\gamma}(F_{ext} + F_{km}). \quad (3.6)$$

Banigan *et al.* worked out that the kinetochore may move in P- or AP-direction with a velocity that depends on the external force, and moreover can exhibit a hysteresis that is the basis of chromosome

oscillations in the two-sided model. To be able to trace kinetochore motion in simulations for a sufficiently long time even if its velocity is negative, we neglect the centrosome in our one-sided model so that the kinetochore and the MTs can move unrestrictedly in any direction.³⁸ We can also consider the MTs as unconfined in the two-sided model with centrosomes, as long as the mean distance of MTs from the spindle equator is sufficiently small, $|\langle x_m \rangle| \ll |x_c|$. In the one-sided model, we moreover assume that the MTs are permanently attached to the kinetochore ($\omega_{\text{det}} = 0$) because otherwise all MTs may be detached at the same time, and the kinetochore and the MT tips may drift apart without reattachment.³⁹ As a consequence of these two assumptions, both MT and kinetochore dynamics solely depend on their relative distances x_i and not on absolute positions, which simplifies the analysis. This is what allows for the mean-field approach presented below in the first place.

3.2.4 Simulations

We perform simulations of both the one- and the two-sided model by integrating the deterministic equations of motion for MTs and kinetochores,⁴⁰ and include stochastic switching events between growth and shrinking as well as for attachment to and detachment from the kinetochore for each MT. For the integration, we employ an Euler algorithm with a fixed time step $\Delta t \leq 1 \times 10^{-3}$ s, which is small enough to ensure $\omega_i \Delta t \ll 1$ for all stochastic switching events (see Tab. 3.2).

Concretely, in each time step the following steps are executed:

1. The forces F_{mk} , F_{km} , F_{kk} and F_{PEF} that are exerted by the MT–kinetochore linkers, the cohesin bond and the PEFs are calculated from the positions of the kinetochores and the MT positions. In the one-sided model, F_{kk} is replaced by the external Force F_{ext} .
2. Following Eqs. (3.1) and (3.2), the rates for a rescue or a catastrophe (ω_r , ω_c) and, if enabled, for attachment/detachment (ω_a , $\omega_{\text{d}\pm}$) are computed for each MT in dependence of the force F_{mk} that is applied on its tip. Transitions are executed stochastically with the according probability $p_i = 1 - \exp(-\omega_i(F_{\text{mk}})\Delta t)$.
3. The velocities of the MTs $v_{m,i}$ and the kinetochores v_k are determined with Eqs (3.1) and (3.3).

³⁸ In terms of the model parameters, this assumption can be expressed as $x_c = \infty$, i.e., the one-sided model contains infinitely long MTs.

³⁹ This behavior is very probable for large external forces: When the kinetochore is pulled strongly, also the tension F_{mk} in the MT–kinetochore linkers is high, which increases the rescue rate and the detachment rate of growing MTs according to Eq. (3.1). If no MT is attached, the kinetochore velocity is given by $v_k = F_{\text{ext}}/\gamma$ and exceeds the unloaded MT growth velocity v_+^0 for large forces so that the MTs have no chance to catch up with and to be reattached to the kinetochore.

⁴⁰ The equation of motion of the kinetochores is given by Eqs. (3.3) and (3.6) in the two- and the one-sided model, respectively. Motion of the MT tips is defined by $\dot{x}_{m,i} = v_{m\pm,i}$ for $i = 1, \dots, M$ with $v_{m\pm,i}$ from Eq. (3.1).

4. The new positions of the kinetochores X_k and the MT tips $x_{m,i}$ are calculated with an Euler step:

$$X_k(t + \Delta t) = X_k(t) + v_k \Delta t, \quad (3.7)$$

$$x_{m,i}(t + \Delta t) = x_{m,i}(t) + v_{m,i} \Delta t. \quad (3.8)$$

5. The kinetochore and MT positions are revised if they violate any of the enabled boundary conditions (confinement at the centrosome and/or the kinetochore, forced rescue at the centrosome).

3.3 Mean-field theory for bistability and chromosome oscillations

In simulations of the one-sided spindle model, kinetochore movement exhibits bistable behavior as a function of the applied force [57], i.e., within a certain force range there are two metastable states for the same external force: in one state, the MTs predominantly grow and the kinetochore velocity is positive while in the other state, the kinetochore has a negative velocity as a consequence of mainly shrinking MTs. It depends on the history which of these two states is assumed: when the system enters the bistable area in consequence of a force change, the kinetochore velocity will maintain its direction (following its current metastable branch) until the force is sufficiently large that the system leaves the bistable area again (the current metastable branch becomes unstable). We first present a mean-field approach that allows us to reproduce the hysteresis by means of deterministic FPEs. By this approach, we can easily obtain constraints on the linker stiffness c and MT number M for the occurrence of bistability, which is hardly feasible from stochastic simulations. Furthermore, we show that the hysteresis of the one-sided model can explain stochastic chromosome oscillations in metaphase if two one-sided models are coupled in the full two-sided model. As for the bistability in the one-sided model, we again determine a regime of chromosome oscillations in the c - M parameter plane.

3.3.1 Mean-field theory for bistability in the one-sided model

As for the simulations of the one-sided model, we make two assumptions for our Fokker–Planck mean-field approach. First, we assume that all M MTs are always attached to the kinetochore. Because the MT–kinetochore links are catch bonds, this assumption is equivalent to assuming that these links are predominantly

under tension. We will check below by comparison with numerical simulations to what extent this assumption can be justified. Secondly, we neglect that MTs are confined by a centrosome so that, as mentioned above, the only relevant coordinates are the relative MT–kinetochore distances x_i , which measure the extension of the i -th linker.

We obtain a system of FPEs for the M MT–kinetochore distances x_i ($i = 1, \dots, M$) and decouple the MT dynamics in a mean-field approximation that neglects kinetochore velocity fluctuations. The MTs are coupled because they are attached to the same kinetochore: each MT experiences a force $F_{\text{mk},i} = -cx_i$ from the elastic linker to the kinetochore, which is under tension (compression) for $x_i < 0$ ($x_i > 0$); the kinetochore is subject to the total counter force $F_{\text{km}} = c \sum_i x_i$. Therefore, the kinetochore velocity v_k is a stochastic variable depending on *all* distances x_i , on the one hand, but determines the velocities $\dot{x}_i = v_{\text{m}\pm}(x_i) - v_k$ of MTs relative to the kinetochores, on the other hand. The equations can be decoupled to a good approximation because the one-sided system assumes a steady state with an approximately stationary kinetochore velocity v_k after a short time.⁴¹ In our mean-field approximation, we then assume a constant kinetochore velocity $v_k \equiv \langle v_k \rangle$ and neglect all stochastic fluctuations around this mean. Unlike stochastic simulations, in which a prescribed force F_{ext} acts on the kinetochore, the mean-field approach starts from a prescribed kinetochore velocity and obtains as a result the external force that is necessary to move the kinetochore with the given velocity. The mean kinetochore velocity is determined by the mean linker extension $\langle x \rangle$ via

$$v_k = \frac{1}{\gamma'}(F_{\text{ext}} + cM\langle x \rangle). \quad (3.9)$$

Fluctuations around the mean value are caused by fluctuations of the force $F_{\text{km}} = c \sum_i x_i$ around its mean $\langle F_{\text{km}} \rangle = Mc\langle x \rangle$, which become small for large M according to the central limit theorem. Therefore, the mean-field approach applies to cells in which many MTs are attached to a single kinetochore, as it is the case in mammalian cells with 20–25 MTs per kinetochore [109].

If v_k is no longer a stochastic variable, the dynamics of the MT–kinetochore extensions x_i decouple. Then, the probability distribution for the M extensions x_i factorizes into M identical factors $p(x_i, t) = p_+(x_i, t) + p_-(x_i, t)$, where $p_{\pm}(x, t) dx$ are the probabilities to find one particular MT in the growing (+) or shrinking (–) state with a MT–kinetochore linker extension x at time t . We can

⁴¹ rather than, for example, a cooperative oscillation as for a MT ensemble pushing against an elastic barrier [179]

derive two FPEs for the dynamic evolution of $p_{\pm}(x, t)$,

$$\partial_t p_+(x, t) = -\omega_c(x) p_+(x, t) + \omega_r(x) p_-(x, t) - \partial_x (v_+(x) p_+(x, t)), \quad (3.10)$$

$$\partial_t p_-(x, t) = \omega_c(x) p_+(x, t) - \omega_r(x) p_-(x, t) - \partial_x (v_-(x) p_-(x, t)), \quad (3.11)$$

where $v_{\pm}(x)$ denotes the relative velocity of MT and kinetochore,

$$v_{\pm}(x) \equiv v_{m\pm}(x) - v_k = v_{\pm}^0 \exp\left(-\frac{cx}{F_{\pm}}\right) - v_k, \quad (3.12)$$

and $\omega_{c,r}(x) = \omega_{c,r}^0 \exp(-cx/F_{c,r})$. The velocity v_k is no longer stochastic but self-consistently determined by (3.9). We note that these FPEs are equivalent to single MT FPEs with position-dependent velocities, catastrophe and rescue rates [29, 30, 180, 181].⁴²

We now obtain the force-velocity relation of the whole MT ensemble by first solving the FPEs (3.10) and (3.11) in the stationary state $\partial_t p_{\pm}(x, t) = 0$ and then calculating the mean linker extension $\langle x \rangle$ for a given kinetochore velocity v_k using the stationary distribution $p_{\pm}(x)$. The external force that is necessary to move the kinetochore with velocity v_k then follows from Eq. (3.9),

$$F_{\text{ext}} = \gamma v_k - cM\langle x \rangle(v_k). \quad (3.13)$$

The MT–kinetochore distance x is limited to a maximum or a minimum value x_{max} or x_{min} for a given kinetochore velocity $v_k > 0$ or $v_k < 0$, respectively, see Tab. 3.3. These limiting values are reached if the relative MT–kinetochore velocities vanish after the linker extension x has adjusted. First we consider $v_k < 0$ and a shrinking MT. If we start with a compressed linker ($x > 0$), the MT starts to shrink fast, the compression is reduced and the linker may get under tension ($x < 0$) because the relative velocity is negative, $\dot{x} = v_-(x) < 0$. The MT–kinetochore distance x continues to decrease until $\dot{x} = v_-(x_{\text{min}}) = 0$ in Eq. (3.12), where the shrinking velocity of the MTs is the same as the prescribed kinetochore velocity ($v_{m-} = v_k$). Further shrinking to $x < x_{\text{min}}$ is not possible but distances $x > x_{\text{min}}$ can be reached if MTs are rescued. If $v_k < 0$ and the MT grows, on the other hand, there is no upper bound on x as the relative velocity $\dot{x} = v_+(x)$ is always positive; x starts to grow into the compressive regime $x > 0$ and continues to grow without upper bound.⁴³ Analogously, if $v_k > 0$ and MTs grow, x grows until $\dot{x} = v_+(x_{\text{max}}) = 0$, and smaller distances can be reached by catastrophe but there is no lower bound on x for shrinking MTs.

Linker extensions x_{max} (x_{min}) are reached as stationary states if catastrophes (rescues) are suppressed, for instance because of

⁴² The FPEs of a single MT with constant rates and velocities are discussed in Sec. 2.2.1, see Eq. (2.1).

⁴³ For very large compressive linker extensions, MT growth is suppressed, but the kinetochore still moves such that $v_+(x) \approx -v_k > 0$.

	MT shrinks	MT grows
$v_k > 0$	$v_-(x) < -v_k$ always $x_{\min} = -\infty$	$v_+(x) > 0$ for $x < x_{\max}$ $x_{\max} = (F_+/c) \ln(v_+^0/v_k)$
$v_k < 0$	$v_-(x) < 0$ for $x > x_{\min}$ $x_{\min} = (F_-/c) \ln(v_-^0/v_k)$	$v_+(x) > v_k$ always $x_{\max} = \infty$
$v_k = 0$	$v_-(x) < 0$ always $x_{\min} = -\infty$	$v_+(x) > 0$ always $x_{\max} = \infty$

large forces, such that MTs can grow (shrink) for sufficiently long times. If catastrophes or rescues are suppressed and the external force F_{ext} is prescribed rather than a kinetochore velocity, all MTs and the kinetochore reach a stationary state in which they move with the same velocity $v_{m,i} = v_k = \tilde{v}_{\pm}$, which is implicitly given by Eq. (3.13):⁴⁴

$$F_{\text{ext}} = \gamma \tilde{v}_{\pm} - cMx_{\text{max,min}}. \quad (3.14)$$

Solving for \tilde{v}_{\pm} , we find

$$\tilde{v}_{\pm} \equiv \frac{MF_{\pm}}{\gamma} W\left(\frac{\gamma v_{\pm}^0}{MF_{\pm}} \exp\left(\frac{F_{\text{ext}}}{MF_{\pm}}\right)\right), \quad (3.15)$$

where $W()$ denotes the Lambert W function.⁴⁵

In the complete absence of stochastic switching between growth and shrinking by catastrophes and rescues, the MT ensemble reaches stationary states with peaked distributions $p_+(x) \propto \delta(x_{\max} - x)$ and $p_-(x) \propto \delta(x - x_{\min})$. Stochastic switching shifts and broadens these peaks, and the FPEs (3.10) and (3.11) lead to a distribution $p_{\pm}(x, t)$ of linker extensions x in the growing and shrinking states with statistical weight $p_{\pm}(x, t) > 0$ in the whole interval $x_{\min} \leq x \leq x_{\max}$. At the boundaries x_{\min} and x_{\max} of this interval, the probability current density

$$j(x, t) \equiv v_+(x, t)p_+(x, t) + v_-(x, t)p_-(x, t) \quad (3.16)$$

has to vanish. Furthermore, in any stationary state ($\partial_t p_{\pm}(x, t) = 0$) the current density is homogeneous, as can be seen by summing up the FPEs (3.10) and (3.11):

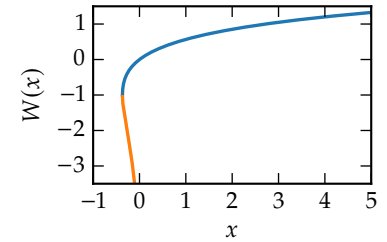
$$0 = \partial_x(v_+(x)p_+(x) + v_-(x)p_-(x)) = \partial_x j(x). \quad (3.17)$$

Since $j = 0$ at the boundaries, this implies that $j = 0$ everywhere in a steady state. The resulting relation $v_+(x)p_+(x) = -v_-(x)p_-(x)$ can be used to reduce the stationary FPEs to a single ordinary

Table 3.3: Boundary conditions of the mean-field approach. The maximum and the minimum value x_{\max} or x_{\min} of the stationary linker extension distribution $p(x)$ follow from conditions $v_-(x_{\min}) = 0$ and $v_+(x_{\max}) = 0$. The distance x_{\min} (x_{\max}) is a function of the prescribed kinetochore velocity v_k and has to be specified separately depending on the direction of v_k . The distance x_{\min} (x_{\max}) is approached if the MTs shrink (grow) for a sufficiently long time.

⁴⁴ Note that $x_{\text{max,min}}$ is a function of the kinetochore velocity $v_k = \tilde{v}_{\pm}$, see Tab. 3.3.

⁴⁵ The Lambert W function is defined by $x = W(x)e^{W(x)}$ and consists of two branches [80] (see figure below), from which only the upper branch (blue) is relevant in Eq. (3.15), where the argument of $W()$ is always positive.



differential equation with the solution [180]

$$p_{\pm}(x) = \frac{\pm \mathcal{N}}{v_{\pm}(x)} \exp\left(-\int \left(\frac{\omega_c(x)}{v_+(x)} + \frac{\omega_r(x)}{v_-(x)}\right) dx\right) \quad (3.18)$$

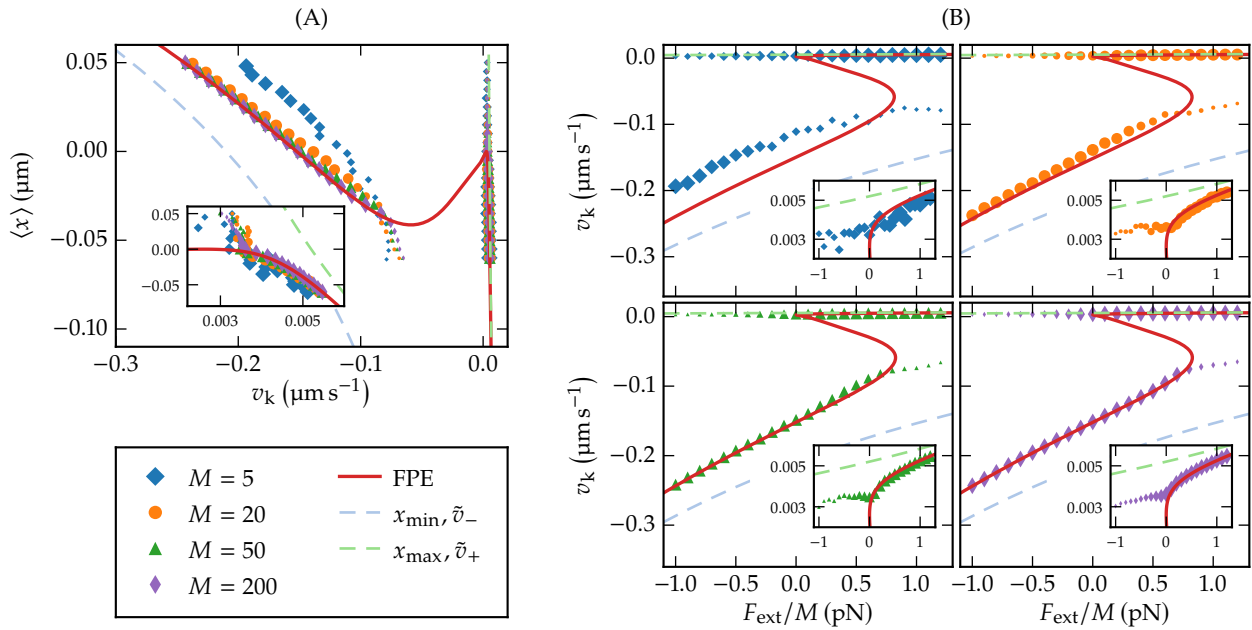
for the stationary distribution of linker extensions x in the growing and shrinking states. The normalization constant \mathcal{N} must be chosen so that the overall probability density $p(x) \equiv p_+(x) + p_-(x)$ satisfies

$$\int_{x_{\min}}^{x_{\max}} p(x) dx = 1. \quad (3.19)$$

Obviously, $p_{\pm}(x) = 0$ for $x > x_{\max}$ and $x < x_{\min}$. The stationary probability densities $p_{\pm}(x)$ from Eq. (3.18) can then be used to calculate the mean distance $\langle x \rangle$ as a function of the kinetochore velocity v_k , which enters through Eq. (3.12) for $v_{\pm}(x)$. The integral in the exponent in Eq. (3.18) as well as the normalization can be evaluated numerically to obtain an explicit $\langle x \rangle(v_k)$ -relation, which is shown in Fig. 3.11A.

At this point it should be noted that in the mean-field theory, the $\langle x \rangle(v_k)$ -relation is *independent* of the MT number M . Therefore, we call it *master curve* henceforth. In Fig. 3.11A, we compare the mean-field theory result with stochastic simulations and find that the mean-field approach becomes exact in the limit of large M , where fluctuations in the kinetochore velocity around its mean in Eq. (3.9) can be neglected.

The master curve is a central result and the basis for all further discussion. Together with the force balance (3.13) on the kinetochore, the master curve gives the force-velocity relation for the MT-kinetochore system. A positive slope of the master curve, as it can occur for small $v_k \approx 0$ (see Fig. 3.11A), gives rise to an instability of the MT-kinetochore system: where the slope is positive, a positive kinetochore velocity fluctuation $\delta v_k > 0$ leads to a MT-kinetochore linker compression $\delta \langle x \rangle > 0$. According to the force balance (3.13), a compression $\delta \langle x \rangle > 0$ puts additional forward-force on the kinetochore leading to a positive feedback and further increase $\delta v_k > 0$ of the kinetochore velocity. This results in an instability, which prevents the system to assume mean linker extensions $\langle x \rangle$ in this unstable regime. This is confirmed by stochastic simulation results in Fig 3.11A, which show that the unstable states are only assumed transiently for very short times. Therefore, occurrence of a positive slope in the master curve in Fig. 3.11A is the essential feature that gives rise to bistability in the one-sided model and, finally, to oscillations in the full two-sided model.



Now we want to trace the origin of this instability for small $v_k \approx 0$. If the MTs are growing (shrinking) for a long time, all linker extensions assume the stationary values $x \approx x_{\max}(v_k)$ ($x \approx x_{\min}(v_k)$) from Tab. 3.3, where the MT velocity adjusts to the kinetochores velocity, $v_k \approx v_{m\pm}(x)$. If the kinetochores velocity increases in these states by a fluctuation (i.e., $\delta v_k > 0$), the MT-kinetochores linkers are stretched (i.e., $\delta x < 0$), which slows down the kinetochores again, resulting in a stable response. This is reflected in the negative slopes of both $x_{\max}(v_k)$ (for $v_k > 0$) and $x_{\min}(v_k)$ (for $v_k < 0$). Because of constant stochastic switching between catastrophes and rescues, the mean linker extension exhibits fluctuations around x_{\max} and x_{\min} , but we expect also the master curve $\langle x \rangle(v_k)$ to have a negative slope for a wide range of velocities v_k . Fig. 3.11A shows that this is actually the case for kinetochores velocities v_k around the force-free growth or shrinking velocities v_{\pm}^0 of the MTs, i.e., if the imposed kinetochores velocity v_k roughly “matches” the force-free growing or shrinking MT velocity. Then a small mismatch can be accommodated by small linker extensions x , which do not dramatically increase fluctuations by triggering catastrophe or rescue events.

The situation changes for small negative or small positive values of the kinetochores velocity around $v_k \approx 0$. For $v_k \lesssim 0$, MT-kinetochores linkers develop logarithmically growing large negative extensions x_{\min} (see Tab. 3.3) corresponding to a slow kinetochores trailing fast shrinking MTs that strongly stretch the linker. Likewise, for $v_k \gtrsim 0$, MT-kinetochores linkers develop logarithmically growing large positive extensions x_{\max} corresponding to a slow kinetochores trailing fast growing MTs that strongly compress the linker. Around $v_k \approx 0$, the system has to switch from large

Figure 3.11: Mean-field results compared to stochastic simulations of the one-sided model. (A) The master curve $\langle x \rangle(v_k)$ from the mean-field approach (red line) agrees with simulation results for different MT-numbers $M = 5, 20, 50, 200$. The dashed lines mark $x_{\min, \max}(v_k)$ from Tab. 3.3. We run simulations with constant external forces and average over 80 simulations for each force. Initially, the MT-kinetochores distance is either x_{\min} or x_{\max} while all MTs grow or shrink with velocity \tilde{v}_{\pm} , respectively. The system then enters a (meta-)stable state, in which we measure the mean kinetochores velocity and MT-kinetochores distances. The marker size depicts the time the system rests in this state on average, which is a measure for its stability (maximum marker size corresponds to $t_{\text{rest}} \geq 1000$ s). As predicted, the mean-field approach turns out to be correct in the limit of many MTs, and in this limit the $\langle x \rangle(v_k)$ -relation is independent of the MT-number M . (B) Resulting force-velocity relations for different MT-numbers $M = 5, 20, 50, 200$. The dashed lines show the large velocity limit $v_k \approx \tilde{v}_{\pm}$ given by Eq. (3.15). We used a linker stiffness of $c = 20 \text{ pN } \mu\text{m}^{-1}$ both in (A) and (B).

negative x to large positive x because the resulting tensile force $F_{\text{mk}} = -cx$ on the shrinking MT destabilizes the shrinking state and gives rise to MT rescue at least for $x < -F_r/c$.

Therefore, also the mean value $\langle x \rangle$ switches from negative to positive values resulting in a positive slope of the master curve if the stationary distributions $p_-(x)$ and $p_+(x)$ remain sufficiently peaked around the linker extensions x_{min} and x_{max} , also in the presence of fluctuations by catastrophes and rescues. We find by an expansion to the leading order that the stationary distribution assumes a power law behavior around x_{max} or x_{min} ,⁴⁶

$$p(x) \propto p_+(x) \propto (x_{\text{max}} - x)^{\alpha_+} \quad \text{for } v_k > 0, \quad (3.20)$$

$$p(x) \propto p_-(x) \propto (x - x_{\text{min}})^{\alpha_-} \quad \text{for } v_k < 0, \quad (3.21)$$

which is illustrated by the exemplary overall probability densities $p(x)$ plotted in Fig. 3.12. Since the exponents α_{\pm} depend on the MT–kinetochore stiffness c as $\alpha_{\pm} + 1 \propto 1/c$ in the presence of fluctuations, distributions are peaked (i.e., have a large kurtosis) and bistability emerges if the MT–kinetochore linker stiffness c is sufficiently large such that deviations of the MT velocity from the kinetochore velocity become suppressed by strong spring forces. This is one of our main results and is quantified in Sec. 3.3.3. We also find that $\alpha_{\pm} + 1 \propto (|v_k/v_{\pm}^0|)^{-1-|F_{\pm}/F_c|}$ such that the distributions become also peaked around $x_{\text{min,max}}$ in the limit of large kinetochore velocities $|v_k|$. Then, the velocity approaches $v_k \approx \tilde{v}_{\pm}(F_{\text{ext}})$ for a prescribed external force such that \tilde{v}_{\pm} from Eq. (3.15) represents the large velocity and large force limit of the force–velocity relation of the kinetochore, see Fig. 3.11B. The influence of c and v_k can also be seen in Fig. 3.12, where the distributions are unpeaked in a wider range of kinetochore velocities for $c = 7 \text{ pN nm}^{-1}$ than for $c = 20 \text{ pN nm}^{-1}$.

In the unstable regime around $v_k \approx 0$, the linker length distribution $p(x)$ is typically broad without pronounced peaks and has a minimal kurtosis (as a function of v_k) in the presence of catastrophe and rescue fluctuations. In this regime, the system assumes a state with a heterogeneous stationary distribution of growing and shrinking MTs, i.e., the total probabilities to grow or shrink become comparable, $\int p_+(x) dx \sim \int p_-(x) dx$. If the kinetochore velocity is increased, $\delta v_k > 0$, the system does not react by $\delta x < 0$, i.e., by increasing the average tension in the linkers in order to pull MTs forward, but by *switching* MTs from the shrinking to the growing state (on average), which then even allows to relax the average linker tension.

Using the force balance (3.13) on the kinetochore, the master curve is converted to a force–velocity relation for the MT–kinetochore system; the results are shown in Fig. 3.11B. The bistability in the

⁴⁶ The derivation is presented in Appendix B.1. The entire exponents are:

$$\alpha_+ = -1 + \frac{\omega_c^0 F_+}{c v_+^0} \left(\frac{v_k}{v_+^0} \right)^{-1+F_+/F_c},$$

$$\alpha_- = -1 + \frac{\omega_r^0 F_-}{c v_-^0} \left(\frac{v_k}{v_-^0} \right)^{-1+F_-/F_r}.$$

Since $\alpha_{\pm} > -1$, the distribution is always normalizable, even though it diverges at x_{max} or x_{min} for $\alpha_{\pm} < 0$. However, if the peaks are sharp ($\alpha_{\pm} \gtrsim -1$), their numerical integration in order to calculate the normalization constant \mathcal{N} is not readily feasible. Instead, we need to integrate over intervals $[x_{\text{min}} + \Delta x, x_{\text{max}}]$ or $[x_{\text{min}}, x_{\text{max}} - \Delta x]$ with Δx 's as small as possible and then extrapolate to $\Delta x = 0$ based on the knowledge of the exponents α_{\pm} . This procedure is described in more detail in my master thesis [95].

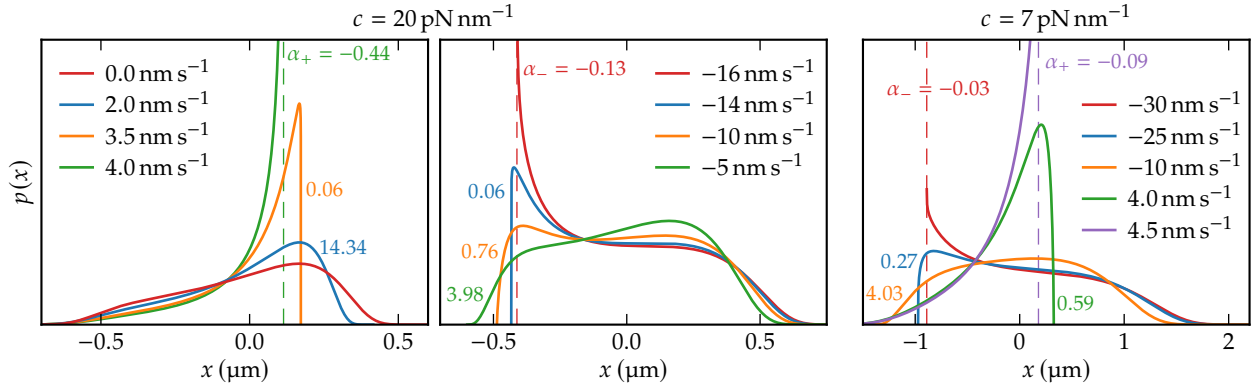


Figure 3.12: Power law behavior in the probability densities of linker extensions. The overall densities $p(x) = p_+(x) + p_-(x)$ following from Eq. (3.18) are shown for various combinations of linker stiffnesses c and kinetochore velocities v_k . For $v_k > 0$ ($v_k < 0$), they show the predicted power law behavior at x_{\max} (x_{\min}) that is determined by α_+ (α_-). For $c = 20 \text{ pN nm}^{-1}$, the distributions are peaked ($\alpha_{\pm} < 0$) if $v_k > 3.54 \text{ nm s}^{-1}$ ($v_k < -14.6 \text{ nm s}^{-1}$). Thus, the mean linker extension stays near x_{\max} (x_{\min}) also in the vicinity of $v_k = 0$ so that it has to have a positive slope to get from x_{\min} to x_{\max} during the evolution from negative to positive velocities, resulting in a bistability. For $c = 7 \text{ pN nm}^{-1}$, which we show in Sec. 3.3.3 to lie below the lower bound for bistability, the distributions themselves as well as the unpeaked region ($\alpha_{\pm} > 0$, $-29.3 \text{ nm s}^{-1} < v_k < 4.41 \text{ nm s}^{-1}$) are broader so that the mean linker extension evolves monotonically from x_{\min} to x_{\max} when v_k is increased and crosses $v_k = 0$.

⁴⁷ See Appendix B.2.

master curve directly translates to a bistability in the force–velocity relation of the MT ensemble, and we obtain a regime with three branches of possible velocities for the same external force. The upper and the lower branches agree with our simulation results as well as previous simulation results in Ref. [57], and our mean-field results become exact in the limit of large M . These branches correspond to the two stable parts of the master curve with negative slope that are found for kinetochore velocities v_k roughly matching the force-free growth or shrinking velocities v_{\pm}^0 of the MTs. The mid branch corresponds to the part of the master curve with positive slope where the system is unstable. Fig. 3.11B demonstrates that this instability is confirmed by stochastic simulation results.

Finally, we note that a simpler theoretical approach, where it is assumed that all linkers assume *identical* extensions $x_i \approx x$ and all attached MTs are in the same state (growing or shrinking), is exact for a single MT ($M = 1$) by definition but not sufficient to obtain a bistable force–velocity relation for MT ensembles ($M > 1$).⁴⁷ The same assumption of identical MT positions has already been used to study an ensemble of MTs that are connected to the same kinetochore via Hill sleeve like linkers [103, 173]. The model of Klemm *et al.* [106] divides each MT ensemble into a growing and a shrinking sub-ensemble, and assumes equal load sharing only between MTs within each sub-ensemble. Together with a force-sensitive rescue force, this is sufficient to obtain a bistable force–velocity relation in a corresponding one-sided model.

3.3.2 Bistability gives rise to oscillations in the two-sided model

As already worked out by Banigan *et al.* [57], the bistability in the force–velocity relation of the one-sided MT ensemble can be considered to be the cause for stochastic oscillations in the two-sided model. Each ensemble can be either on the lower branch of the force–velocity relation, where it mainly depolymerizes and

exerts a P-directed pulling force ($v_k < 0$), or on the upper branch, where it mainly polymerizes and exerts an AP-directed pushing force ($v_k > 0$). The external force in the one-sided model is a substitute for the spring force $F_{kk} = c_k (X_{k,r} - X_{k,l} - d_0)$ of the cohesin bond in the full model with a stiffness c_k and rest length d_0 . Since the cohesin force is a linear function of the inter-kinetochore distance, the force–velocity relation can be treated as distance–velocity or phase space diagram where both kinetochores move as points along the force–velocity relation, see Fig. 3.13A. The cohesin bond always affects the two kinetochores in the same way because action equals reaction: if the cohesin spring is stretched, both kinetochores are pulled away from their pole (AP); if it is compressed, both kinetochores are pushed polewards (P). Thus, the kinetochores always have the same position on the F_{kk} -axis in the F_{kk} – v_k diagram in Fig. 3.13A if F_{kk} on the horizontal axis is defined as the force on the kinetochore in AP-direction. Likewise, we define v_k on the vertical axis as the velocity in AP-direction.⁴⁸ The upper/lower stable branch of the force–velocity relation is denoted by $v_k^\pm(F_{kk})$. Typically, a kinetochore on the upper (lower) branch has $v_k^+ > 0$ ($v_k^- < 0$) and, thus, moves in AP-(P-)direction. Using $F_{kk} = c_k (X_{k,r} - X_{k,l} - d_0)$ for the spring force, we find

$$\dot{F}_{kk} = -c_k (v_{k,r} + v_{k,l}), \quad (3.22)$$

i.e., kinetochores move with the sum of their AP-velocities along the force–velocity curve in the F_{kk} – v_k diagram.

Oscillations arise from the two kinetochores moving through the hysteresis loop of the bistable force–velocity relation as described Fig. 3.13A. Three states are possible, see Fig. 3.13B. In state 0, both kinetochores move in AP-direction ($v_k = v_k^+$), i.e., in opposite directions towards each other, relaxing the F_{kk} -force from the cohesin bond. In terms of the v_k – F_{kk} diagram, both kinetochores are on the upper branch and move to the left with the velocity $\dot{F}_{kk} = -2c_k v_k^+ < 0$ according to Eq. (3.22). After reaching the lower critical force F_{\min} of the hysteresis loop, one of the two kinetochores reverses its direction and switches to the lower branch resulting into states 2 or 2', where one kinetochore continues its motion in AP-direction with $v_k^+ > 0$ trailing the other (leading) kinetochore, which now moves in P-direction with $v_k^- < 0$, i.e., both kinetochores move in the same direction. In the v_k – F_{kk} diagram, this results in a motion to the right with velocity $\dot{F}_{kk} = c_k (-v_k^- - v_k^+) > 0$ because MTs typically shrink much faster than they grow.⁴⁹ For the same reason, moving on opposite P- and AP-branches increases the kinetochore distance and builds up F_{kk} -force in the cohesin bond. After reaching the upper critical force F_{\max} of the hysteresis loop, it is always the kinetochore on the lower branch moving in P-direction that switches back⁵⁰ and state 0 is reached again. This behavior is

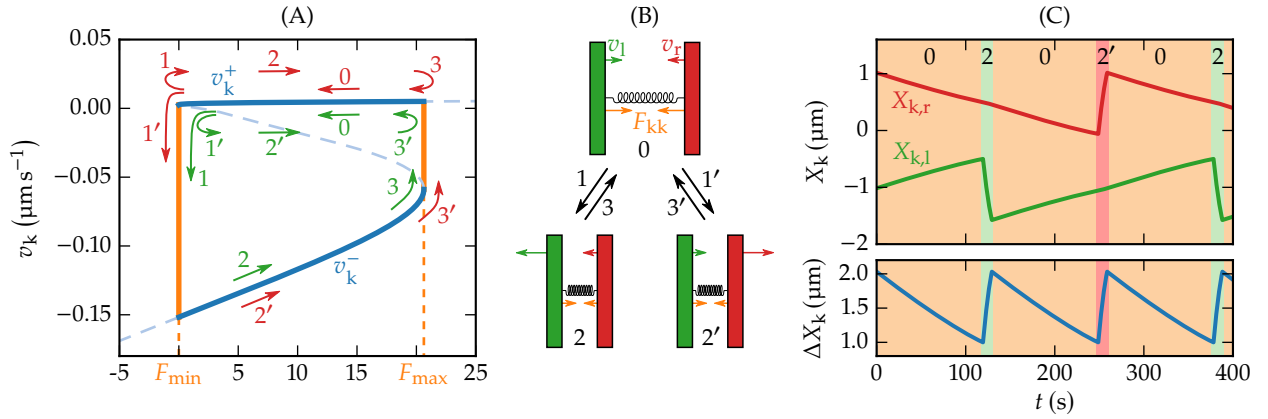
⁴⁸ By these definitions, it follows that

$$\begin{aligned} F_{kk,l} &\equiv F_{kk}, & F_{kk,r} &\equiv -F_{kk}, \\ v_{k,l} &\equiv \dot{X}_{k,l}, & v_{k,r} &\equiv -\dot{X}_{k,r} \end{aligned}$$

for the left and the right kinetochore.

⁴⁹ $-v_-^0 \gg v_+^0$, see Tab. 3.2

⁵⁰ If it were the trailing kinetochore that switches from the upper to the lower branch, both kinetochores would move in P-direction, away from each other, which would increase the cohesin tension beyond $F_{kk} > F_{\max}$ where only the upper branch is stable.



in agreement with experimental results [55]. The system oscillates by alternating between state 0 and one of the states 2 or 2', which is selected randomly with equal probability.

For each of the states 0, 2 and 2' depicted in Fig. 3.13AB, the two branches $v_k^\pm = v_k^\pm[F_{kk}]$ provide deterministic equations of motion for the kinetochore positions. Inserting $F_{kk} = c_k (X_{k,r} - X_{k,l} - d_0)$, we obtain both kinetochore velocities as functions of the kinetochore positions and find

$$\begin{aligned}
 \text{state 0: } \dot{X}_{k,l} &= v_k^+ [c_k (X_{k,r} - X_{k,l} - d_0)] > 0, \\
 \dot{X}_{k,r} &= -v_k^+ [c_k (X_{k,r} - X_{k,l} - d_0)] < 0, \\
 \text{state 2: } \dot{X}_{k,l} &= v_k^- [c_k (X_{k,r} - X_{k,l} - d_0)] < 0, \\
 \dot{X}_{k,r} &= -v_k^+ [c_k (X_{k,r} - X_{k,l} - d_0)] < 0, \\
 \text{state 2': } \dot{X}_{k,l} &= v_k^+ [c_k (X_{k,r} - X_{k,l} - d_0)] > 0, \\
 \dot{X}_{k,r} &= -v_k^- [c_k (X_{k,r} - X_{k,l} - d_0)] > 0.
 \end{aligned} \tag{3.23}$$

Solving these equations gives idealized deterministic trajectories of the sister kinetochores when we also assume that the left and the right kinetochore pass the lower branch alternately such that the order of states is a periodic sequence $0 - 2 - 0 - 2' - 0 - \dots$ as shown in the example in Fig. 3.13C. Then, single kinetochores oscillate with half the frequency of inter-kinetochore (breathing) oscillations, just as observed in PtK1 cells [55]. Moreover, we can obtain numerical values of the frequencies directly from the trajectories. For a MT-kinetochore linker stiffness $c = 20 \text{ pN } \mu\text{m}^{-1}$ and 20 to 25 MTs per kinetochore, which is a realistic number for mammalian cells [109], we get periods of 206 s to 258 s and 103 s to 129 s for kinetochore and breathing oscillations, respectively. These values coincide with experimental results of 239 s and 121 s measured in PtK1 cells [55].

The calculated trajectories are idealized since they neglect stochastic fluctuations that occur in simulations of the two-sided model and have two main effects on the kinetochore dynamics, which already

Figure 3.13: Bistability gives rise to oscillations in the two-sided model. (A,B) Different states of sister kinetochore motion can be deduced from the bistability of the force-velocity relation: either both kinetochores are in the upper branch (0) or one is in the upper and the other one in the lower branch (2, 2'). In the first case, both kinetochores move away from their pole (AP) towards each other. Thus, the spring force F_{kk} decreases until it reaches F_{\min} . Since the upper branch is not stable anymore below F_{\min} , either the left (1) or the right (1') kinetochore switches to the lower branch and changes direction to poleward motion (P). The system is then in state 2 or 2', where both kinetochores move into the same direction: the leading kinetochore P, the trailing kinetochore AP. As P- is much faster than AP-movement (MT shrinkage is much faster than growth), the inter-kinetochore distance and the spring force are increasing. Above F_{\max} only AP-movement is stable which is why the leading kinetochore changes direction (3, 3') and the system switches to state 0 again. (C) Solution of the equations of motion (3.23) for $c = 20 \text{ pN } \mu\text{m}^{-1}$ and $M = 25$ with an imposed periodic order of states (0 - 2 - 0 - 2' - 0 - ...). The initial condition is $F_{kk} = F_{\max}$ (both kinetochores at the right end of the upper branch).

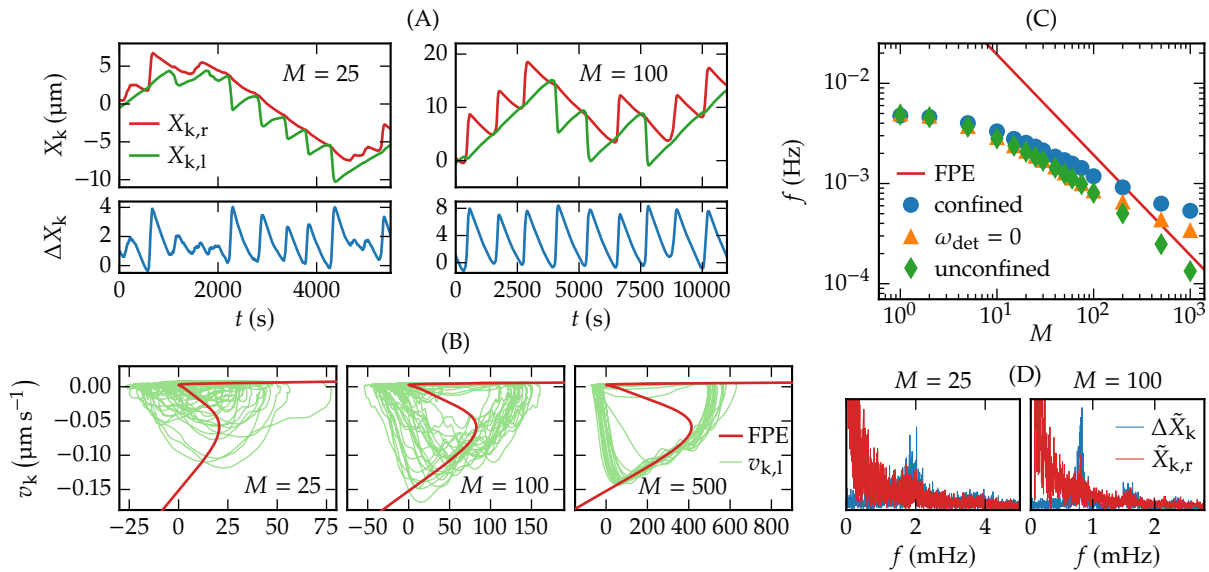


Figure 3.14: Oscillations in stochastic simulations of the unconfined model compared to mean-field results. (A) Kinetochore trajectories and breathing oscillations in the two-sided model without confinement ($x_c \rightarrow \infty$) and detachment ($\omega_d = 0$). The kinetochores behave as described in Fig. 3.13 with a random order of states $2/2'$. The breathing oscillations are regular enough to assign a frequency by Fourier analysis, see (D). With less MTs, oscillations are more fluctuative. (B) Kinetochore velocity against cohesin force in simulations of the unconfined two-sided model without detachment (green). For many MTs, the velocity follows very precisely the predicted hysteresis from the mean-field approach (red). (C) Double-logarithmic plot of frequencies of breathing oscillations as a function of MT number M : calculated from the mean-field approach according to Fig. 3.13 (red) and measured in simulations of the unconfined (green diamonds) as well as the confined model with detachable catch bonds (blue circles) and with permanent attachment (orange triangles). Confinement becomes relevant for large MT numbers. In the presence of detachable catch bonds only 75% of the MTs are attached on average, which corresponds to a simple shift of the curve to lower MT numbers. (D) Trajectories from (A) in Fourier space. While $\tilde{X}_{k,r}$ has its maximum at $f = 0$ due to the random order of states in Fig. 3.13, $\Delta \tilde{X}_k$ has a distinct peak that becomes sharper for large M indicating regular breathing oscillations. For all simulations, the MT-kinetochore linker stiffness was $c = 20 \text{ pN } \mu\text{m}^{-1}$.

arise in simulations that comply with the assumptions behind the mean-field theory:⁵¹ Firstly, the sister kinetochores do not pass the lower branch alternately but in random order. Therefore, in stochastic simulations, we observe phases where one kinetochore moves in AP-direction for several periods while the other one changes its direction periodically but moves polewards on average, see Fig. 3.14A. Since this does not affect the trajectory of the inter-kinetochore distance, breathing oscillations still occur in a more or less regular manner, which allows us to measure their frequencies by Fourier analysis. We show below that additional PEFs suppress this random behavior and force the kinetochores to pass the lower branch alternately. As a second effect of the stochastic character of the simulation, kinetochores do not change the branch instantaneously after crossing the critical forces F_{max} or F_{min} . Instead, they tend to maintain their primary state for a while (Fig. 3.14B) and follow the metastable states that we also observe in simulations of the one-sided model (Fig. 3.11B). Hence, the frequencies we measure in the simulations are smaller than those calculated from the Fokker-Planck mean-field approach (Fig. 3.14C). The latter effect vanishes in the limit of many MTs (large M): the switching points approach the theoretical values F_{max} and F_{min} , and the simulated breathing frequencies converge to our mean-field predictions.

So far, we have demonstrated that the mean-field theory correctly describes kinetochore dynamics in simulations of the unconfined model where we suppress detachment in order to prevent unattached MTs from shrinking towards infinity. As shown in Fig. 3.15A, kinetochore oscillations also survive in simulations of the confined model independently of whether the MTs are able to detach from the kinetochore, i.e., to rupture the catch bond.

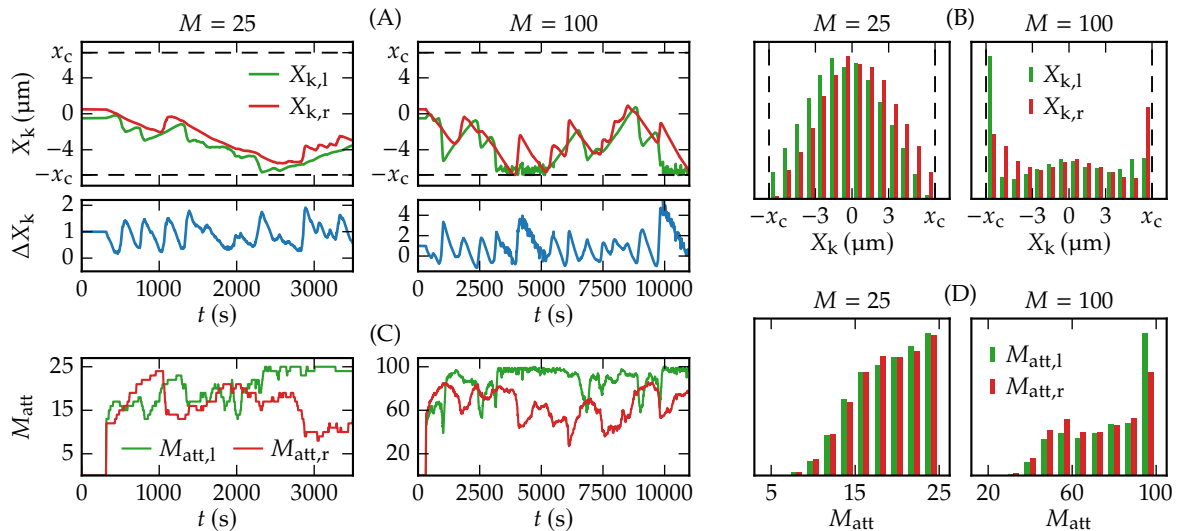


Figure 3.15: Dynamics in the confined model with detachable MTs.

(A) Kinetochore positions X_k and inter-kinetochore distance ΔX_k over time in simulations with a total number of $M = 25$ and $M = 100$ MTs per spindle pole. Oscillations as described in Fig. 3.13 are recognizable. With 100 MTs one kinetochore can get stuck to the centrosome for a while. (B) Distribution of kinetochore positions. The kinetochores are not aligned to the spindle equator and for $M = 100$ they are most likely to be found near the centrosomes. (C) Number of attached MTs M_{att} over time. MTs are more likely to be attached when the correspondent kinetochore is near the centrosome since the free MTs can be reattached to the kinetochore faster in that case. (D) Distribution of M_{att} . On average 75 % of the MTs are attached independently of the total MT number M .

However, confinement by the centrosome influences the kinetochore dynamics in the limit of large M : since more MTs exert a higher force on the kinetochore, it is possible that one of the two sisters gets stuck at the centrosome for a while, see Fig. 3.15AB. Hence, the frequencies measured in the confined two-sided model deviate from the frequencies in the unconfined case above $M \approx 200$ (Fig. 3.14C).

If we enable detachment in our simulations, we find that the number of attached MTs correlates with the kinetochore position (see Fig. 3.15C) since due to the exponential distribution of free MTs and the distance dependent attachment rate (3.2), detached MTs are more likely to be reattached to the kinetochore the closer it is to the centrosome. Moreover, on average, about 75 % of the MTs are attached independently of the total MT number (Fig. 3.15CD). Therefore, the catch bond nature of the link leads to an effective behavior similar to a system without detachment but with less MTs, which explains the difference in frequencies between the confined models with and without detachment in Fig. 3.14C. We conclude that detachment does not play a major role for the occurrence of kinetochore oscillations in cells with many MTs as despite detachment there are always enough MTs attached to justify our mean-field approximation. Hence, (periodic) changes in the number of attached MTs as they can be seen in Fig. 3.15C are rather a passive consequence than an active source of kinetochore oscillations. This argumentation may not be tenable, if just a few MTs are attached to a kinetochore, so that even detachment of a single MT affects the total force acting on the kinetochore significantly. Then, detachment can be the primary cause of directional instability as worked out by Gay *et al.* [162], who modeled the mitotic spindle of fission yeast.

⁵¹ As a reminder: We assumed permanent MT-kinetochore bonds ($\omega_d = 0$) and ignored the confinement at the centrosome ($x_c \rightarrow \infty$).

Taking into account the results of the last paragraph, we mainly investigate the unconfined model with permanently attached MTs in the following sections. This procedure is reasonable as we do not lose any qualitative key features of kinetochore dynamics on the one hand, and, on the other hand, gain a much better comparability of our mean-field theory with the appropriate stochastic simulations.

⁵² This includes confined/unconfined systems and permanent/detachable bonds.

We finally note that in all cases we examined,⁵² the kinetochore oscillations become more fluctuative if less MTs are attached. This leads to the conclusion that kinetochore oscillations are a result of the collective dynamics of an ensemble of MTs that exhibit a force-dependent dynamic instability individually. Such a behavior can not be described correctly based on the simple assumption that all linkers have the same extension, i.e., that MTs share the load equally and all attached MTs are in the same state (growing or shrinking).⁵³ Therefore, the model of Shtylla and Keener [103], which does assume equal load sharing and synchronous MT dynamics, requires a chemical feedback as an additional mechanism in order to obtain kinetochore oscillations. The model of Klemm *et al.* [106] divides each MT ensemble into a growing and a shrinking sub-ensemble, and assumes equal load sharing only between MTs within each sub-ensemble. Together with a force-sensitive rescue force, this is sufficient to obtain oscillations.

⁵³ See Appendix B.2.

3.3.3 Constraints on linker stiffness and microtubule number for bistability and oscillations

We already argued above in Sec. 3.3.1 that bistability (and thus oscillations) can only emerge if the MT–kinetochore linker is sufficiently stiff. To analyze the influence of the linker stiffness c and the MT number M on bistability quantitatively, the transformation from the master curve to the force–velocity relation is visualized in Fig. 3.16A as search for the intersections of the master curve with linear functions

$$\langle x \rangle = \frac{1}{cM}(\gamma v_k - F_{\text{ext}}). \quad (3.24)$$

In the limit of large M , these linear functions have zero slope. Bistable force–velocity relations with three intersection points are only possible if the master curve has positive slope for intermediate v_k resulting in a maximum and a minimum. The extrema of the master curve vanish, however, in a saddle-node bifurcation if the linker stiffness drops below $c_{\text{bist}} = 7.737 \text{ pN } \mu\text{m}^{-1}$, which is, therefore, a lower bound for the occurrence of bistability. In the case of finite MT numbers M , bistable force–velocity relations can

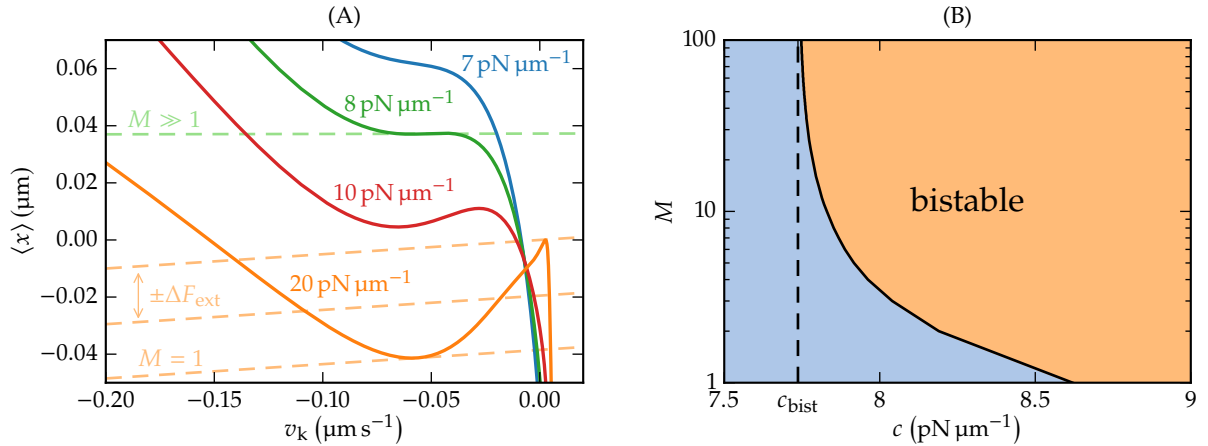


Figure 3.16: Constraints for bistability in the one-sided model. (A) Master curves for different linker stiffnesses c and linear functions according to Eq. (3.24). In the limit of large M , the linear functions have zero slope and bistability occurs if the master curve has two extrema, which is the case for $c > c_{\text{bist}}$. For finite M , bistable solutions are possible if the linear functions have a smaller slope than the inflection point of the master curve. (B) Resulting bistable regime in the parameter plane of linker stiffness c and MT number M .

only be found if the slope in the inflection point of the master curve exceeds γ/cM , which is the slope of the linear function (3.24). This allows us to quantify a bistable regime in the parameter plane of linker stiffness c and MT number M as shown in Fig 3.16B.

We showed in Sec. 3.3.2 that bistability of the one-sided model is a necessary condition for oscillations in the two-sided model. However, as we show now, bistability in the one-sided model is *not sufficient* for oscillations in the full model. If the force–velocity relation is interpreted as phase space diagram for the two kinetochores, kinetochores only switch branches in the v_k – F_{kk} diagram if their velocity changes its sign at the turning points F_{min} and F_{max} . If this is not the case since one of the two branches crosses $v_k = 0$ like, for example, the right branch for $c = 10 \text{ pN } \mu\text{m}^{-1}$ in Fig. 3.16A, which transforms to the upper branch of the force–velocity relation, the intersection point is a stable fixed point in the phase space diagram as sketched in Fig. 3.17A. At this fixed point, kinetochore motion relaxes to zero velocity and just exhibits fluctuations around an equilibrium distance instead of oscillations.

As a sufficient condition for oscillations, we have to require—besides bistability—a strictly positive velocity in the upper and a strictly negative velocity in the lower branch in the v_k – F_{kk} diagram. Based on this condition, we quantify an oscillatory regime in the parameter plane of linker stiffness c and MT number M in Fig. 3.18A. In the limit of many MTs, the sufficient condition for oscillations can be formulated in terms of the master curve: the maximum of the master curve has to be located at a positive and the minimum at a negative velocity. This is the case for $c > c_{\text{osc}} = 15.91 \text{ pN } \mu\text{m}^{-1}$, which is, therefore, a lower bound for the occurrence of oscillations. This constraint on the linker stiffness for metaphase chromosome oscillations provides additional information on MT–kinetochore linkers, whose molecular nature is not known up to now.

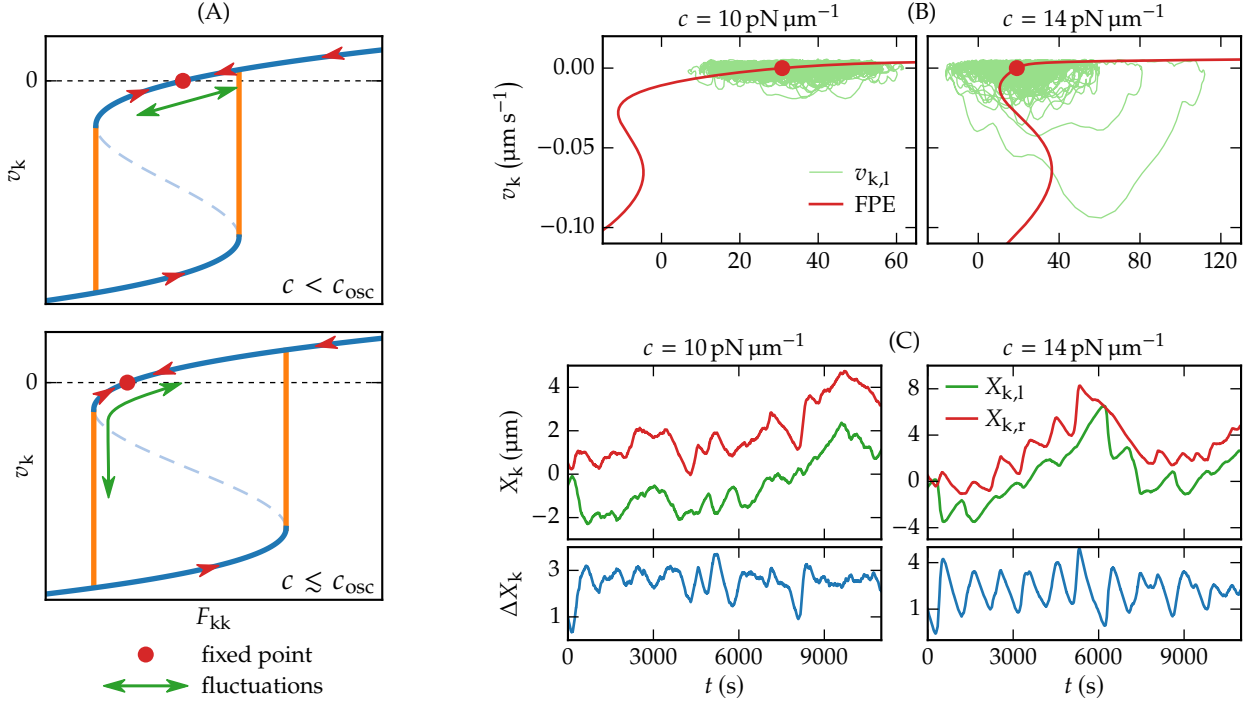


Figure 3.17: Kinetochore dynamics in the non-oscillatory regime.

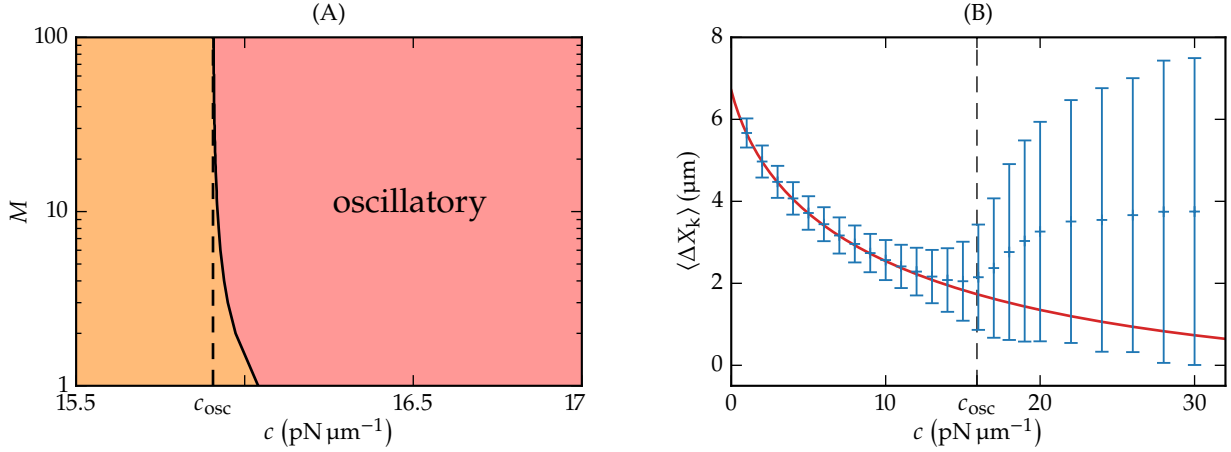
(A) Schematic explanation of kinetochore motion in the non-oscillatory regime based on the force–velocity relation. Where the upper branch crosses zero velocity, the inter-kinetochore distance has a fixed point, around which it fluctuates. With higher linker stiffnesses c , the fixed point comes closer to the left turning point F_{min} . If c is just slightly smaller than c_{osc} , fluctuations can be large enough for the kinetochore distance to leave the upper stable branch. Then, one of the two sister kinetochores passes once through the lower branch. (B,C) This behavior can be observed in simulations. While at $c = 10 \text{ pN } \mu\text{m}^{-1}$, kinetochores just fluctuate around the fixed point, at $c = 14 \text{ pN } \mu\text{m}^{-1}$, the kinetochores occasionally pass through the hysteresis loop. Simulations were performed with an unconfined system and 100 MTs on each side.

Because of stochastic fluctuations, the transition between the oscillatory and the non-oscillatory regime is not sharp in our simulations. In the non-oscillatory regime, kinetochores fluctuate around a fixed point of inter-kinetochore distance, where the upper branch crosses $v_k = 0$. However, these fluctuations can be large enough for the inter-kinetochore distance to shrink and leave the upper branch on the left side, especially for stiffnesses c slightly below c_{osc} . If that happens, one kinetochore passes once through the lower branch of the force–velocity relation just as in an oscillation. The difference to genuine oscillations is that these are randomly occurring single events (resulting in a Poisson process). Randomly occurring oscillations are visualized in Fig. 3.17 for $c < c_{\text{osc}}$ and $c \gtrsim c_{\text{osc}}$. Moreover, the force–velocity relations as well as the kinetochore trajectories measured in corresponding simulations are shown.

In the non-oscillatory regime, the fixed point should determine the mean inter-kinetochore distance $\langle \Delta X_k \rangle = \langle X_{k,r} - X_{k,l} \rangle$. Solving the stationary FPEs for $v_k = 0$, we compute the (external) force F_0 that has to be applied to one kinetochore to stall its motion:

$$F_0 = \gamma v_k - cM\langle x \rangle = -cM\langle x \rangle(v_k = 0). \quad (3.25)$$

In the two-sided model, this force is applied to the kinetochores by the cohesin bond at the fixed point. With $F_{kk} = c_k(\Delta X_k - d_0)$, we



compute the corresponding mean inter-kinetochore distance:

$$\langle \Delta X_k \rangle = \frac{F_0}{c_k} + d_0 = -\frac{cM}{c_k} \langle x \rangle (v_k = 0) + d_0. \quad (3.26)$$

Fig. 3.18B shows that simulations agree with this result in the non-oscillatory regime. At c_{osc} the transition to the oscillatory regime can be recognized where the mean inter-kinetochore distance deviates from the fixed point (3.26). Moreover, the variance of ΔX_k increases significantly at c_{osc} due to the transition to the oscillatory regime.

In order to provide an overview and to make orientation easier for the reader, we summarize in Fig. 3.19 where the stochastic simulations from the last three sections and the master curves in Fig. 3.16A are located in the parameter plane of linker stiffness c and MT number M , and which regime they are part of.

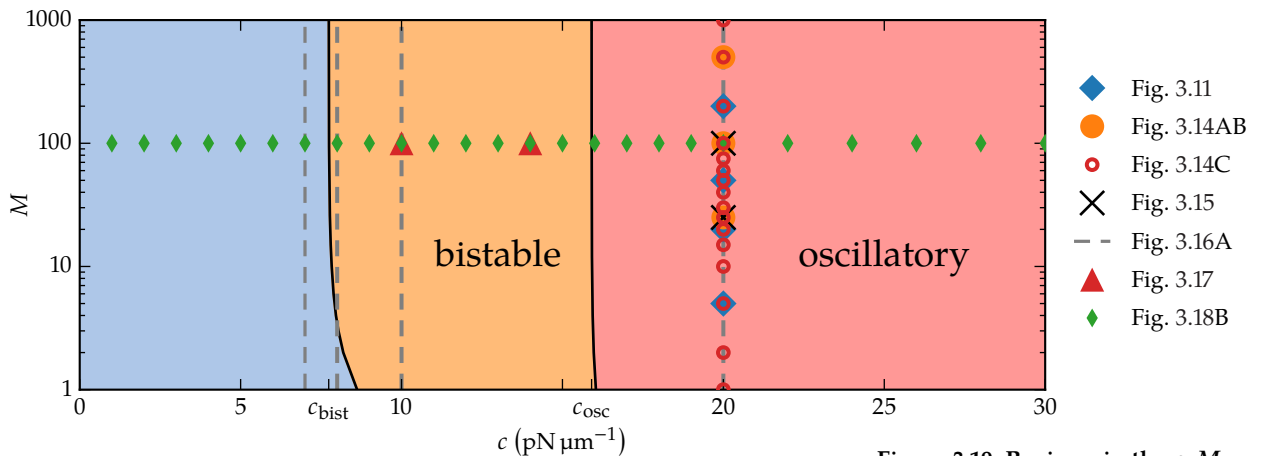


Figure 3.18: Constraints for oscillations in the two-sided model. (A) Oscillatory regime in the parameter plane of linker stiffness c and MT number M . $c_{\text{osc}} = 15.91 \text{ pN } \mu\text{m}^{-1}$ is a lower bound for the occurrence of oscillations. (B) Mean inter-kinetochore distance according to Eq. (3.26) (red) and measured in simulations of the unconfined system with $M = 100$ (blue). Below $c_{\text{osc}} = 15.91 \text{ pN } \mu\text{m}^{-1}$ (dashed line), both results match whereas in the oscillatory regime the mean inter-kinetochore distance diverges from the fixed point, and its standard deviation increases notably due to the oscillations.

Figure 3.19: Regimes in the c - M parameter plane with locations of the master curves from Fig. 3.16A and the simulations from Figs. 3.11, 3.14, 3.15, 3.17 and 3.18

3.4 Generalizations of the minimal spindle model

In the previous section, we presented a mean-field solution for the minimal model that let us reproduce the bistability of kinetochore velocity already found by Banigan *et al.* [57] in stochastic simulations and grasp the occurrence of directional instability by interpreting the (bistable) force–velocity relation as a phase space diagram for the two-sided model with possibly emerging fixed points. Beyond that, we were able to quantify boundaries in the c – M parameter plane for both bistability and chromosome oscillations, which was a first demonstration of the advantages that our mean-field approach has over sole stochastic simulations. Those advantages become even more manifest in the following three sections, in each of which we add an extension to the minimal model and analyze its effects on kinetochore dynamics by means of our theoretical mean-field framework. We start with the inclusion of poleward flux, which results in a shift of the force–velocity relation that may generate a fixed point thereby suppressing chromosome oscillations. Later, we include PEFs as global forces that depend on the absolute kinetochore positions. They turn out to provide an alternating oscillation pattern⁵⁴ and chromosome alignment at the spindle equator. As a last extension, we take into account that MTs are probably not able to apply compressive forces on the kinetochore [51, 139] by assuming MT growth to be confined at the kinetochore instead of applying the boundary condition from Fig. 3.9. Then, catastrophe promotion at the kinetochore is a necessary condition for the occurrence of directional instability. As for the minimal model, we verify all results by means of stochastic simulations. In a final section, we combine all extensions with the aim of fitting stochastic simulations of our model to resemble certain characteristics of kinetochore trajectories observed in PtK1 cells. During that process, our theoretical understanding obtained from the mean-field approach proves beneficial in identifying the parameter changes that have the desired effects.

⁵⁴ in contrast to the random choice of states 2 and 2' in the oscillation mechanism of the minimal model as depicted in Fig. 3.13

3.4.1 Poleward microtubule flux

The first additional effect that we include is poleward MT flux, which was observed in several metazoan cells (Tab. 3.4). It describes the constant flux of tubulin from the plus ends towards the spindle pole and is probably driven by plus end directed kinesin-5 motors pushing overlapping antiparallel MTs apart as well as kinesin-13 proteins that are located at the centrosome and depolymerize the MTs at their minus ends [171]. During metaphase, spindle and MT length can be maintained by simultaneous polymerization at the

Cell type	v_f (nm s ⁻¹)	Directional instability
LLC-PK1 (porcine)	8.3 [52]	Yes [52]
PtK1 (rat-kangaroo)	7.7 [183]	Yes [55]
PtK2 (rat-kangaroo)	10 [52]	Yes [56]
Newt lung	9.0 [184]	Yes [50]
U2OS (human)	8.8 [53]	Yes [53]
<i>Drosophila</i> embryo	32 [185]	No [99]
<i>Xenopus</i> egg	37 [186]	No [100]

plus ends [182], which results in a behavior similar to treadmilling⁵⁵ of free MTs [70].

Poleward flux can be easily included in our model by subtracting a constant flux velocity v_f from the MT velocity. Then, the relative MT–kinetochore velocities (3.12) become

$$v_{\pm}(x) = v_{\pm}^0 \exp\left(-\frac{cx}{F_{\pm}}\right) - v_f - v_k. \quad (3.27)$$

Hence, the flux velocity can be treated as an offset to the constant kinetochore velocity in the solution of the stationary FPEs. The final effect is a shift of both the master curves and the force–velocity relations by v_f towards smaller kinetochore velocities v_k as shown in Fig. 3.20A. If the shift is so large that the left turning point F_{\min} of the force–velocity hysteresis is located at a negative velocity, poleward flux suppresses directional instability because a fixed point emerges, and we expect similar behavior as for intermediate linker stiffnesses in the previous section (Fig. 3.17). In the limit of many MTs, the maximum flux velocity that still allows directional instability is given by the velocity in the maximum of the master curve, which provides the boundary of the oscillatory regime in the parameter plane of linker stiffness c and poleward flux velocity v_f that is depicted in Fig. 3.20B. Phase space diagrams (Fig. 3.20C) and kinetochore trajectories (Fig. 3.20D) from simulations with appropriate flux velocities confirm our arguments exhibiting similar behavior as for intermediate linker stiffnesses in Fig. 3.17. For small flux velocities, the boundary of the oscillatory regime in Fig. 3.20B approaches our above result $c_{\text{osc}} = 15.91 \text{ pN } \mu\text{m}^{-1}$. For increasing flux velocities, the oscillatory regime shrinks, and its boundary has a maximum at $c \approx 50 \text{ pN } \mu\text{m}^{-1}$ with $v_f \approx 3.11 \text{ nm s}^{-1}$. We conclude that kinetochore oscillations can be suppressed by moderate flux velocities independently of the linker stiffness.

Our theory also agrees with simulation results of Banigan *et al.* [57], who observed in their model that large flux velocities suppress kinetochore oscillations while bistability is maintained. However, they were not able to coherently explain this behavior⁵⁶ whereas

Table 3.4: Metaphase poleward flux velocities v_f and occurrence of directional instability. Chromosome oscillations have only been observed in cells with moderate flux velocities ($v_f \lesssim 10 \text{ nm s}^{-1}$) whereas they are suppressed by large v_f . For a more detailed review of poleward flux measurements, see Ref. [182].

⁵⁵ Treadmilling MTs polymerize at their plus end and simultaneously depolymerize at their minus end resulting in an effective motion in the plus end direction, see Sec. 2.1.2.

⁵⁶ Banigan *et al.* attributed the suppression of oscillations to the shift of the force–velocity relation towards higher forces, and did not recognize the emergence of a fixed point due to the shift along the v_k -axis.

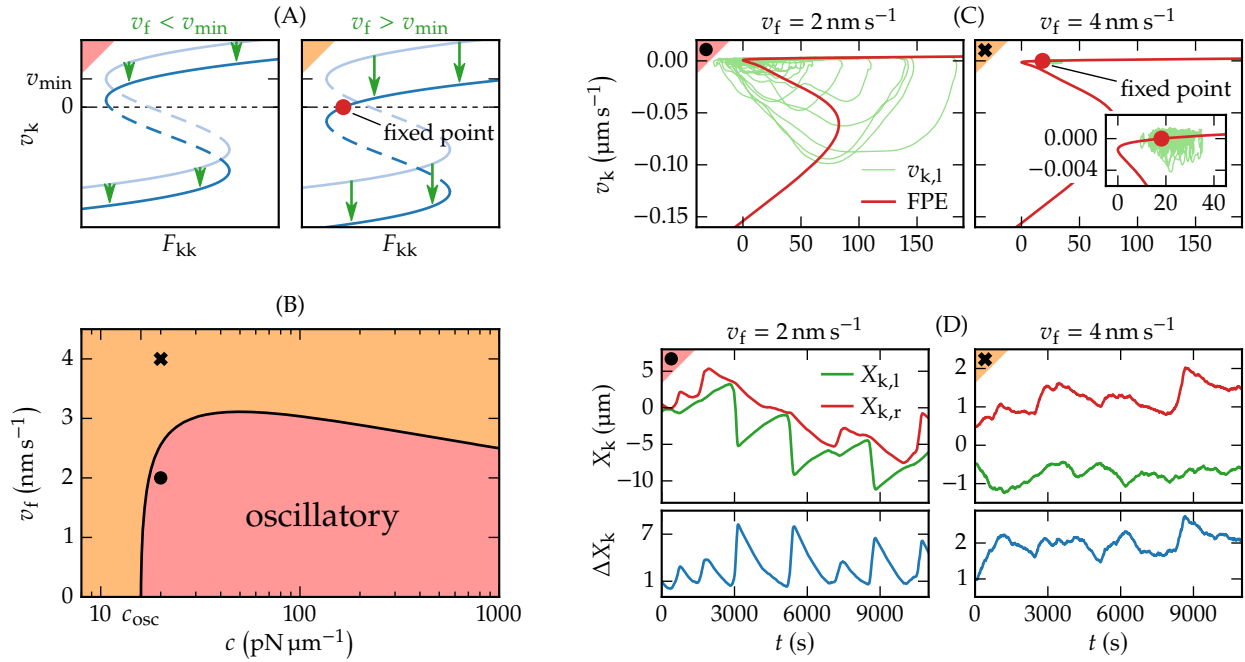


Figure 3.20: Poleward flux suppresses oscillations. (A) Due to Eq. (3.27), the force–velocity relation is shifted by the amount of the flux velocity v_f towards smaller kinetochore velocities. If the flux is slower than the kinetochore velocity v_{\min} in the left turning point F_{\min} , the kinetochores still oscillate. For larger flux velocities, a fixed point arises on the upper branch and the kinetochores behave as described in Fig. 3.17. (B) Oscillatory regime in the parameter plane of c and v_f in the limit of many MTs. Fast poleward flux suppresses kinetochore oscillations for arbitrary linker stiffnesses c . (C,D) Phase space diagrams and MT trajectories from simulations of the unconfined two-sided model with $c = 20$ pN μm⁻¹ and $M = 100$. While at $v_f = 2$ nm s⁻¹ the system is still in the oscillatory regime, where hysteresis is recognizable in phase space, at $v_f = 4$ nm s⁻¹, kinetochores exhibit fluctuative motion as described in Fig. 3.17.

our mean-field approach provides such an explanation quite easily by the emergence of a fixed point. Moreover, our results explain the experimentally observed correlation between flux velocity and directional instability. Kinetochore oscillations have been observed in the mitotic vertebrate cells listed in Tab. 3.4 (LLC-PK1, PtK1/2, newt lung, U2OS), which have poleward flux velocities not exceeding 10 nm s⁻¹, whereas in the mitosis of a *Drosophila* embryo as well as in meiosis of a *Xenopus* egg, where flux velocities are three to four times higher, chromosomes do not exhibit directional instability.

3.4.2 Polar ejection forces

As a next extension of the basic model, we now include polar ejection forces (PEFs). They originate from non-kinetochore MTs interacting with the chromosome arms and pushing them thereby towards the spindle equator, either through collisions with the chromosome arms or via chromokinesins [172], and provide additional pushing forces on kinetochores. Therefore, they can be included into the model by adding forces $F_{\text{PEF},r}(X_{k,r})$ and $F_{\text{PEF},l}(X_{k,l})$ acting on kinetochores, which depend on the *absolute* position of the kinetochores [105]. Due to the exponential length distribution of free MTs as well as the spherical geometry of the MT asters, the density of non-kinetochore MTs decreases monotonically with the distance from the spindle pole. Therefore, we assume that PEFs reach their maximum at the centrosome and vanish at the spindle equator ($X_k = 0$), where opposite PEFs compensate each other. This assumption is supported by the monotonic PEF distribution

that has been measured *in vivo* by Ke *et al.* [187]. Here, we will only discuss linearized PEFs⁵⁷

$$F_{\text{PEF},l}(X_{k,l}) = -kX_{k,l}, \quad F_{\text{PEF},r}(X_{k,r}) = kX_{k,r}, \quad (3.28)$$

where the spring constant k defines the strength of the forces, and the signs are chosen so that a positive force acts in AP-direction.

To determine kinetochore trajectories of the two-sided model in the presence of PEFs, we can start from the same force–velocity relations as for the basic model. In the presence of PEFs, the total forces $F_{k,l}$ and $F_{k,r}$ that act on the left and the right kinetochore in AP-direction depend on the absolute kinetochore positions $X_{k,l}$ and $X_{k,r}$:

$$F_{k,l} = F_{\text{kk}}(\Delta X_k) + F_{\text{PEF},l}(X_{k,l}), \quad (3.29)$$

$$F_{k,r} = F_{\text{kk}}(\Delta X_k) + F_{\text{PEF},r}(X_{k,r}). \quad (3.30)$$

We can investigate the motion of kinetochores in the full two-sided model again by using a phase space diagram. In the presence of PEFs, we use a v_k – F_k diagram with the total force F_k in AP-direction on the horizontal axis and the velocity v_k in AP-direction on the vertical axis. Because the total forces contain the external PEFs, they are no longer related by action and reaction and, thus, the two kinetochores no longer have the same position on the F_k -axis, but they still remain close to each other on the F_k -axis as long as the cohesin bond is strong enough.

A kinetochore on the upper/lower branch moves in AP-/P-direction with $v_k^\pm(F_k)$ if $v_k^+ > 0$ ($v_k^- < 0$). A kinetochore on the upper AP-directed branch will relax its AP-directed PEFs while a kinetochore on the lower P-directed branch will build up AP-directed PEFs. After a time of equilibration, the kinetochores behave as described in Fig. 3.21. When one kinetochore changes its direction from P to AP (switches to the upper branch), the sister kinetochore, which was on the upper branch before, becomes the leading⁵⁸ kinetochore. Therefore, the kinetochores do not reach the left turning point F_{min} at the same time so that it is always the leading kinetochore that switches to the lower branch. Since, in general, the absolute P-velocity is much larger than the AP-velocity⁵⁹ and the kinetochores move along the F_k -axis with

$$\dot{F}_{k,l} = -c_k(v_{k,r} + v_{k,l}) - kv_{k,l}, \quad (3.31)$$

$$\dot{F}_{k,r} = -c_k(v_{k,r} + v_{k,l}) - kv_{k,r}, \quad (3.32)$$

the AP-directed PEF contribution to the total force increases faster on the lower branch than on the upper one. As a result, the P-moving kinetochore overtakes its sister on the F_k -axis before switching back to the upper branch such that the leading kineto-

⁵⁷ We show in Appendix B.3 that other force distributions do not differ qualitatively in their influence on the kinetochore dynamics.

⁵⁸ Here, “leading” refers to the position in the force velocity phase space.

⁵⁹ $-v_k^-$ for the lower branch is much larger than $+v_k^+$ for the upper branch

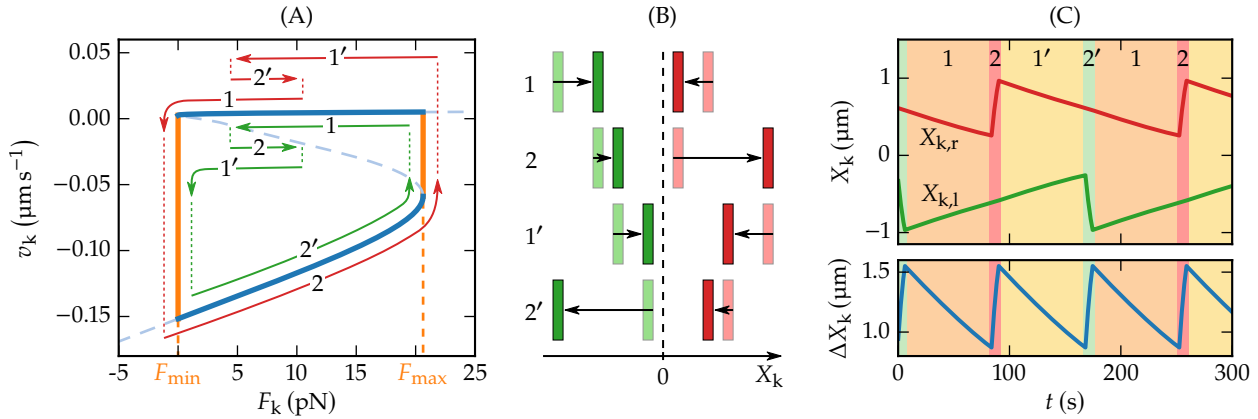


Figure 3.21: Kinetochore dynamics in the presence of PEFs. (A,B) After a certain time of equilibration, the system periodically passes through the states 1–2–1′–2′.

At the beginning of state 1, the left kinetochore (green) has just switched from P- to AP-movement so that both kinetochores are on the upper branch. Both kinetochores move in AP-direction, which means that both the cohesin force and the PEFs decrease and both kinetochores move left in the force–velocity diagram. Due to different PEFs, the right kinetochore (red) reaches the left turning point F_{\min} first and switches to the lower branch, which marks the start of state 2. This state is dominated by the fast P-movement of the right kinetochore, which causes a steep increase of both F_{kk} and $F_{PEF,r}$. Therefore, the right kinetochore moves to the right in the force–velocity diagram. Meanwhile, the left sister still moves in AP-direction, and $F_{k,l}$ increases slightly as the increase of F_{kk} is larger than the decrease of $F_{PEF,l}$. Since $\dot{F}_{k,r} > \dot{F}_{k,l}$, the right kinetochore overtakes its sister on the F_k -axis before it reaches the right turning point and switches to the upper branch. The then following states 1′ and 2′ are the exact opposite to 1 and 2 with swapped kinetochores, which ensures an alternating oscillation pattern. (C) Solution of the corresponding equations of motion for $c = 20 \text{ pN } \mu\text{m}^{-1}$, $k = 10 \text{ pN } \mu\text{m}^{-1}$ and $M = 25$.

⁶⁰ again, “leading” and “trailing” in terms of phase space positions

chore automatically becomes the trailing kinetochore in the next oscillation period.⁶⁰ This periodic change of kinetochore positions in the force–velocity diagram leads to both regular breathing and regular single kinetochore oscillations as the kinetochores alternately pass the lower branch. Solving appropriate equations of motions similar to Eq. (3.23) for each of the states depicted in Fig. 3.21AB,⁶¹ we determine the deterministic trajectories in Fig. 3.21C confirming this regular alternating oscillation pattern.

The alternating oscillation pattern robustly survives in stochastic simulations in the presence of moderate PEFs ($k \sim 10 \text{ pN } \mu\text{m}^{-1}$) as we demonstrate in Fig. 3.22A by means of the kinetochore trajectories in real space. In Fig. 3.22B, emergence of regular oscillations is illustrated in Fourier space: whereas for rather small values of k , single kinetochore oscillations are still irregular resulting in a nearly monotonic decreasing Fourier transform, for $k = 10 \text{ pN } \mu\text{m}^{-1}$, single kinetochore motion has a distinct peak in the Fourier space indicating a regular shape of oscillations in real space. Moreover, frequency doubling of breathing compared to single kinetochore oscillations can directly be recognized by comparing the corresponding Fourier transforms. As a consequence of regular oscillations, the kinetochores stay near the spindle equator and can not get stuck to one of the centrosomes as in the basic model, see histograms of kinetochore positions in Fig. 3.22C. We conclude that PEFs are necessary to assure proper chromosome alignment in the metaphase plate at the spindle equator. This is consistent with an experiment by Levesque and Compton [140], who observed mitosis of vertebrate cells after suppressing the activity of chromokinesins and thus PEFs. This resulted in 17.5% of the cells in at least one chromosome being not aligned at the equator but located near a spindle pole.

Moreover, PEFs reduce the amplitude and increase the frequency of oscillations. The amplitude decreases for increasing PEF strength k as the kinetochores have to cover a smaller distance between the turning points at F_{\min} and F_{\max} . The increase of the frequency is

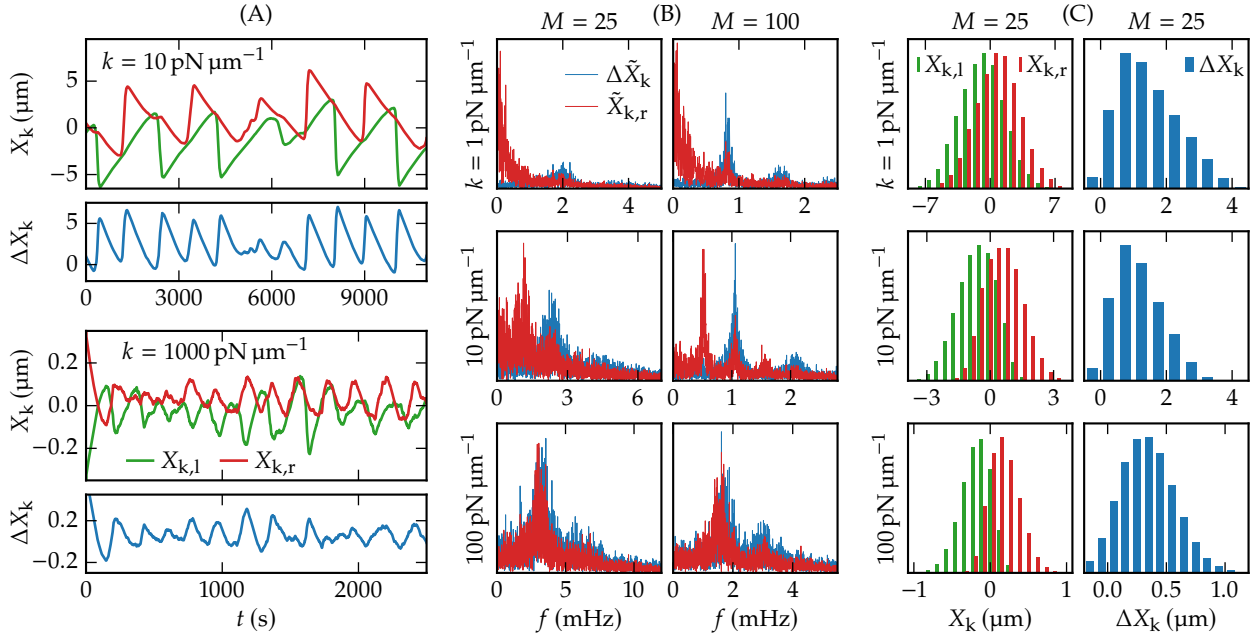


Figure 3.22: Kinetochores motion in simulations with PEFs. (A) Kinetochore trajectories with different PEF constants k from simulations with $M = 100$, $c = 20 \text{ pN } \mu\text{m}^{-1}$ and without confinement at the spindle poles. The PEFs force the kinetochores to oscillate regularly and to stay near the spindle equator. For $k = 10 \text{ pN } \mu\text{m}^{-1}$, kinetochores oscillate as described in Fig. 3.21. Since with strong PEFs, kinetochores tend to switch to the lower branch simultaneously when reaching F_{\min} in the phase space at the same time, for $k = 1000 \text{ pN } \mu\text{m}^{-1}$, oscillations are in antiphase due to symmetric initial conditions before the system equilibrates at $t \approx 1500 \text{ s}$. After equilibration, periods of antiphase oscillations reappear over and over again due to fluctuations. Stronger PEFs cause a more fluctuative kinetochore motion. Especially for moderate MT numbers, this can lead to suppression of kinetochore oscillations. (B) Single (right) kinetochore and breathing oscillations in Fourier space. For weak PEFs ($k = 1 \text{ pN } \mu\text{m}^{-1}$), single kinetochore oscillations are still irregular and $\tilde{X}_{k,r}$ has its maximum at $f = 0$. If $k = 10 \text{ pN } \mu\text{m}^{-1}$, $\tilde{X}_{k,r}$ has a distinct peak at half the breathing frequency, indicating regular oscillations as described in Fig. 3.21 and frequency doubling of breathing compared to single kinetochore oscillations. With sufficiently strong PEFs ($k \gtrsim 100 \text{ pN } \mu\text{m}^{-1}$), frequency doubling is lost as a consequence of antiphase oscillations and the peaks of $\tilde{X}_{k,r}$ and $\Delta\tilde{X}_k$ coincide with each other. (C) Histograms of kinetochore positions and inter-kinetochore distances for the realistic case of $M = 25$. Chromosomes are aligned at the spindle equator despite missing confinement at the centrosome. The range of kinetochore positions is narrower and the distances smaller if PEFs are stronger.

linear in k , which can be deduced from the linear increase of the absolute phase space velocity $|\dot{F}_k|$, see Eqs. (3.31) and (3.32).

Since PEFs do not have any influence on the underlying master curves and force–velocity relations, they do not affect the kinetochore velocities v_k and never completely suppress kinetochore oscillations in the deterministic Fokker–Planck model but only reduce their amplitude and increase their frequency. For strong PEFs, however, this gives rise to kinetochore motion with a fluctuative character, see Fig. 3.22. The same observation was made in the model of Civelekoglu–Scholey *et al.* [105]. Additionally, we detect sister kinetochore oscillations being in antiphase if PEFs are strong enough ($k \gtrsim 100 \text{ pN } \mu\text{m}^{-1}$), see Fig. 3.22A. This follows from the phase space velocities \dot{F}_k being dominated by the strong PEFs compared to inter-kinetochore tension: Imagine, both kinetochores are in the upper branch of the phase space and reach the turning point F_{\min} at nearly the same time. When now one of the two

⁶¹ Compared to Eq. (3.23), we need to replace the cohesin force F_{kk} in the argument of $v_k^\pm[\cdot]$ with the total forces $F_{k,l}$ and $F_{k,r}$ from Eqs. (3.29) and (3.30):

$$\begin{aligned}\dot{X}_{k,l} &= v_k^\pm[F_{k,l}(X_{k,l}, X_{k,r})], \\ \dot{X}_{k,r} &= -v_k^\pm[F_{k,r}(X_{k,l}, X_{k,r})],\end{aligned}$$

where the branch the kinetochore is located on in the current state determines the choice of $v_k^+[\cdot]$ or $v_k^-[\cdot]$.

kinetochores switches to the lower branch and starts moving polewards, its sister does not change its direction in phase space as in state 2/2' in Fig. 3.21A but continues moving left since the decrease of PEFs due to its poleward motion can not be compensated by the increasing AP-directed cohesin tension if $k \gg c_k$:

$$|\dot{F}_{\text{PEF}}| = k |v_k^+| > |\dot{F}_{\text{kk}}| = c_k |v_k^+ + v_k^-|. \quad (3.33)$$

As a consequence, the kinetochore will switch to the lower branch just after its sister, and both kinetochores pass the lower branch simultaneously, i.e., move apart from each other, finally resulting in antiphase oscillations. While the antiphase behavior vanishes after a certain time of equilibration in the deterministic model, in stochastic simulations, periods of antiphase oscillations can be observed over and over again regardless of whether the system has been equilibrated before. A characteristic of antiphase oscillations is the loss of frequency doubling, which also appears in the Fourier space, where the peaks of single kinetochore and breathing motion coincide with each other if PEFs are strong, see Fig. 3.22B. Since antiphase kinetochore oscillations have not been observed experimentally, we conclude that *in vivo*, PEFs are weak compared to the inter-kinetochore tension but strong enough to assure chromosome alignment at the spindle equator. Compared to experimental results [50, 51, 54–56, 105], $k = 10 \text{ pN } \mu\text{m}^{-1}$ seems a reasonable choice in our model as it assures regular oscillations with frequency doubling, keeps the inter-kinetochore distance within a suitable range of $(1.2 \pm 0.7) \mu\text{m}$, and aligns kinetochores in a realistic maximum distance of $3 \mu\text{m}$ from the spindle equator with a standard deviation of $0.88 \mu\text{m}$ in the lifelike case of $M = 25$.

3.4.3 Confinement and catastrophe promotion at the kinetochore

So far, we assumed that kinetochore MTs are also able to exert pushing forces, which arise in the basic model from the absence of boundary conditions at the kinetochore as described in Fig. 3.9. During oscillations, we find on average slightly less (48%) MT-kinetochore links under tension, while a substantial part of linkers also exerts pushing forces. Two experimental results suggest, however, that MTs can not exert pushing forces if they are attached to the kinetochore:⁶² in Ref. [51], it was shown that the link between chromosomes is always under tension; the experiments in Ref. [139] demonstrated that, after removal of the cohesin bond, AP-moving kinetochores immediately stop indicating that kinetochore MTs can not exert pushing forces, while P-moving kinetochores continue moving due to MT pulling forces.

⁶² Of course, this is not equivalent to a total absence of any AP-directed forces, as there may still be PEFs mediated by interpolar MTs and chromokinesins.

In view of these experimental results and in order to answer the question whether MT pushing forces are essential for bistability and oscillations, we analyze variants of our basic model, where MT growth is confined at the kinetochore, i.e., where the relative coordinate $x = x_m - X_k$ is limited to $x \leq 0$ such that MTs can only exert tensile forces on the kinetochore. This implies that the MT undergoes a catastrophe if it reaches the kinetochore, i.e., if the relative coordinate reaches $x = 0$ from below in the one-sided model. Different choices for the corresponding catastrophe rate ω_c^{kin} at $x = 0$ are possible:

- (i) A reflecting boundary, i.e., $\omega_c^{\text{kin}} = \infty$, where a catastrophe is immediately triggered if the MT plus end reaches the kinetochore.
- (ii) A “waiting” boundary condition, where the *relative* velocity $v_+ = v_{m+} - v_k = 0$ stalls if the MT reaches $x = 0$.⁶³ In contrast to the reflecting boundary condition, the catastrophe rate ω_c^{kin} at the kinetochore is finite so that the MT waits at the kinetochore until it undergoes a catastrophe for a mean waiting time $1/\omega_c^{\text{kin}}$, as similarly observed in metaphase of PtK1 cells [177]. Because $x = 0$ also results in $F_{mk} = 0$, the force-free catastrophe rate seems a natural choice, $\omega_c^{\text{kin}} = \omega_c^0$, see Eq. (3.1), which should be realized in the absence of any additional catastrophe regulating proteins at the centromere.
- (iii) If catastrophes are promoted by regulating proteins, but not immediately as for (i), we obtain intermediate cases of waiting boundary conditions with $\omega_c^0 < \omega_c^{\text{kin}} < \infty$. In mammalian cells, such regulating mechanisms could be provided by the kinesin MCAK, which is localized at the centromere during metaphase [188] and has been reported to increase the catastrophe rate of MTs roughly 7-fold [189]. Therefore, waiting boundary conditions with an increased catastrophe rate appear to be the most realistic scenario.

We introduce a numerical catastrophe enhancement factor $n \geq 1$ characterizing the increased catastrophe rate, $\omega_c^{\text{kin}} = n\omega_c^0$. Within this general scenario, reflecting boundary conditions (i) are recovered for $n = \infty$ and waiting boundary conditions (ii) with the zero force catastrophe rate for $n = 1$. We discuss the general case (iii) in the following.

In our basic model, where MTs can exert pushing forces on kinetochores, the pushing phases where $x > 0$ can also be interpreted as an effective waiting phase at the kinetochore with a catastrophe rate that is effectively increased by the pushing forces. Therefore, the behavior of our basic model resembles a model with waiting boundary conditions with an increased catastrophe rate $n > 1$ at

⁶³ In the simulation, we set the MT velocity to $v_{m+} = v_k$.

⁶⁴ According to Tab. 3.3,

$$x_{\max} = \frac{F_+}{c} \ln\left(\frac{v_+^0}{v_k}\right) \text{ for } v_k > 0,$$

we find that

$$\begin{aligned} x_{\max} &> 0 \text{ if } v_k < v_+^0, \\ x_{\max} &< 0 \text{ if } v_k > v_+^0. \end{aligned}$$

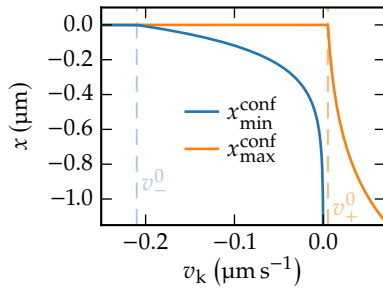


Figure 3.23: Minimum and maximum linker extension with confinement at the kinetochore. The confinement allows only for tensile linker extensions ($x < 0$), see Eq. (3.34).

the kinetochore. MT pushing forces are not essential for bistability and oscillations and have a similar effect as an increased catastrophe rate at the kinetochore as our detailed analysis will show.

In the Fokker–Planck solution for the one-sided model, all confining boundary conditions limit the maximum MT–kinetochore distance x_{\max} to zero where it is positive in the basic model.⁶⁴ When x_{\max} is negative in the basic model, confining boundary conditions do not modify the results, since the MTs are not able to reach the fast kinetochore. For fast negative kinetochore velocities $v_k < v_-^0$, the minimum distance x_{\min} becomes positive while x_{\max} is zero. Then, all confining boundary conditions fix the MT tips to the kinetochore position as they do not shrink fast enough to move away from the poleward-moving kinetochore after a catastrophe resulting in $\langle x \rangle = 0$ and $F_{\text{ext}} = \gamma v_k$. All in all, confinement leads to the following maximal and minimal values for the MT–kinetochore distance x modifying Tab. 3.3 as depicted in Fig. 3.23:

$$x_{\max}^{\text{conf}} = \begin{cases} 0, & v_k < v_+^0 \\ x_{\max}, & v_k \geq v_+^0 \end{cases}, \quad x_{\min}^{\text{conf}} = \begin{cases} 0, & v_k < v_-^0 \\ x_{\min}, & v_k \geq v_-^0 \end{cases}. \quad (3.34)$$

We calculate the master curves $\langle x \rangle(v_k)$ for all three types of confining boundary conditions, see Fig. 3.24A. Because $x_{\max}^{\text{conf}} \leq 0$ for any confining boundary condition, also $\langle x \rangle \leq 0$, i.e., the complete master curves lie in the regime of tensile MT–kinetochore linker forces reflecting the fact that pushing forces are strictly suppressed. Therefore, the MT–kinetochore catch bond is on average under tension establishing a more firm MT–kinetochore connection during the stochastic chromosome oscillations in metaphase. Oscillations then become a tug-of-war, in which both sets of MTs only exert pulling forces onto each other.

With a waiting boundary condition at the kinetochore, the probability densities $p_{\pm}(x, t)$ have to be supplemented with the probability $Q(t)$ to find a MT at the kinetochore ($x = 0$). Besides the FPEs (3.10) and (3.11) for the probability densities, we also have to solve the equation for the time evolution of $Q(t)$:

$$\partial_t Q(t) = v_+(0) p_+(0, t) - \omega_c^{\text{kin}} Q(t). \quad (3.35)$$

The analogous model for a free MT that grows against a rigid wall has already been solved in Refs. [180, 190]. In the stationary state, Eq. (3.35) leads to

$$Q = \frac{p_+(0) v_+(0)}{\omega_c^{\text{kin}}}. \quad (3.36)$$

⁶⁵ Since $Q \propto p_+(0) \propto \mathcal{N}$, the overall density $p(x)$ is proportional to the normalization constant \mathcal{N} as well, and normalization can be achieved as in the basic model by simply adjusting \mathcal{N} .

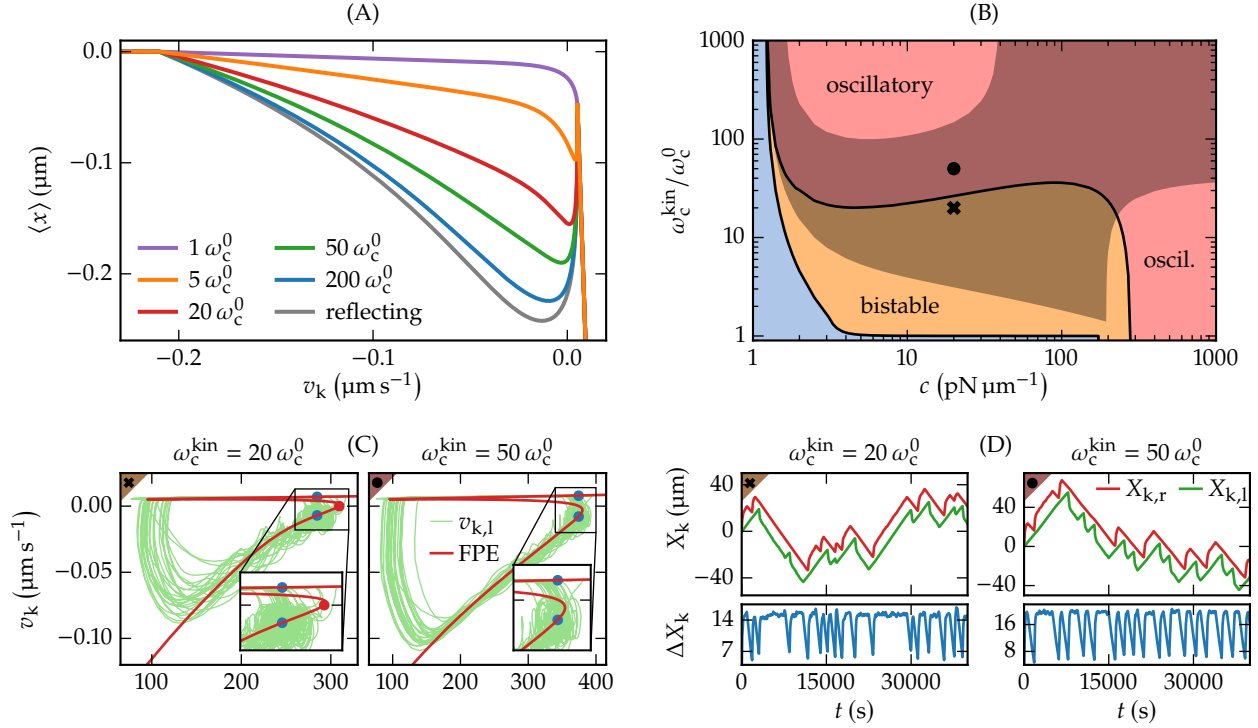


Figure 3.24: Microtubule confinement at the kinetochore. (A) Master curves of a system with a waiting boundary condition for various $\omega_c^{\text{kin}} = n \omega_c^0$ and $c = 20 \text{ pN } \mu\text{m}^{-1}$. (B) Regimes in the parameter plane of c and ω_c^{kin} in the limit of many MTs. Outside the blue region, the master curve is bistable. In the orange region, the left branch of the master curve and, therefore, the lower branch of the v_k - F_{kk} diagram cross $v_k = 0$, which leads to a fixed point suppressing oscillations, whereas in the red region oscillations are possible. In stochastic simulations, kinetochores already oscillate at much smaller ω_c^{kin} than predicted by the master curves. Additionally, a new kind of fixed point, which is depicted in (C), emerges in the shaded region. (C,D) Phase space diagrams and kinetochore trajectories from simulations of the unconfined two-sided model with $c = 20 \text{ pN } \mu\text{m}^{-1}$ and $M = 100$. The blue dots mark the new kind of fixed point, where the leading kinetochore in the lower branch moves with the same velocity as the trailing kinetochore in the upper branch. Then, the inter-kinetochore distance remains constant, while the center of mass moves with a constant velocity as in (D) for $\omega_c^{\text{kin}} = 20 \omega_c^0$ at $t \approx 25000$ s. In the presence of PEFs, these fixed points are absent and the shaded region in (B) does not apply.

For the probability densities $p_{\pm}(x)$, we get the same solution as for the basic model without confinement, see Eq. (3.18), except for the normalization constant. The overall probability density can then be written as

$$p(x) = p_+(x) + p_-(x) + Q\delta(x) \quad (3.37)$$

and has to satisfy the normalization condition⁶⁵

$$\int_{x_{\text{min}}^{\text{conf}}}^{x_{\text{max}}^{\text{conf}}} p(x) dx = \int_{x_{\text{min}}^{\text{conf}}}^{x_{\text{max}}^{\text{conf}}} (p_+(x) + p_-(x)) dx + Q = 1. \quad (3.38)$$

From the overall probability density $p(x)$, we obtain the master curves, which are shown in Fig. 3.24A for $n = 1, 5, 20, 50, 200, \infty$ and a linker stiffness of $c = 20 \text{ pN } \mu\text{m}^{-1}$. Again, we can analyze the master curves for extrema in order to obtain constraints on the linker stiffness c and the catastrophe enhancement factor $n = \omega_c^{\text{kin}} / \omega_c^0$ for the occurrence of bistability and oscillations. The results of this analysis are depicted in Fig. 3.24B as colored regions. It turns out that extrema in the master curve and, thus, bistability occur if the linker stiffness is sufficiently high, $c > c_{\text{bist}}$. For the zero force catastrophe rate ($n = 1$), we find a high threshold value $c_{\text{bist}} = 178 \text{ pN } \mu\text{m}^{-1}$, whereas in the limit of a reflecting boundary ($n = \infty$) the threshold is very low at $c_{\text{bist}} = 1.218 \text{ pN } \mu\text{m}^{-1}$.

We remind that a sufficient condition for oscillations is the absence of a stable fixed point, where one of the two branches in the v_k -

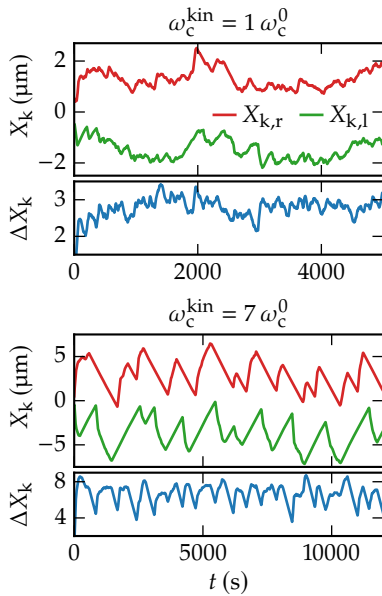


Figure 3.25: Stochastic simulations with confinement at the kinetochore and PEFs. The simulations were performed with $c = 20 \text{ pN nm}^{-1}$, $M = 100$ and $k = 10 \text{ pN nm}^{-1}$. While the kinetochores exhibit a fluctuative motion without catastrophe promotion (top), oscillations are recognizable for $n = 7$ (bottom) although it lies outside the oscillatory regime in Fig. 3.24B. The new type of fixed point is unstable due to the presence of PEFs.

F_{kk} diagram crosses $v_k = 0$. In contrast to the basic model, the maxima of the master curve are now located at a positive velocity for $n > 1$. Therefore, oscillations are suppressed by a fixed point $v_k^- = 0$ on the lower branch in the v_k - F_{kk} diagram, which occurs if the velocity is positive in the minimum of the master curve. In general, oscillations occur if the linker stiffness is sufficiently high, $c > c_{\text{osc}}$. Again, we find a high threshold value $c_{\text{osc}} = 280 \text{ pN } \mu\text{m}^{-1}$ for $n = 1$ and a low threshold $c_{\text{osc}} = 1.237 \text{ pN } \mu\text{m}^{-1}$ for a reflecting boundary condition ($n = \infty$).

For $n < 10$, the threshold values remain high. Moreover, at such high linker stiffnesses and for small n , the simulations of the two-sided model do not show the expected behavior: for $n = 1$ and high linker stiffnesses in the oscillatory regime, the kinetochore trajectories do not exhibit regular oscillations. Naively, one could argue that kinetochore oscillations are suppressed due to the lack of a pushing force and can be restored by additional PEFs. However this is not the case, since, as stated above, PEFs do not affect the master curve, which determines the regime of kinetochore motion. One reason for the absence of oscillations is that for the zero force catastrophe rate ($n = 1$), the waiting time $1/\omega_c^{\text{kin}} = 1/\omega_c^0 \sim 500 \text{ s}$ at the kinetochore is large compared to the typical oscillation periods, which are in the range of 100 s to 200 s.

Fig. 3.24B also shows that oscillations require increased catastrophe rates with $n \gtrsim 20$ over a wide range of linker stiffnesses from $c = 10 \text{ pN } \mu\text{m}^{-1}$ to $c = 200 \text{ pN } \mu\text{m}^{-1}$. For $n > 1$, at the boundary between the bistable and the oscillatory regime in Fig. 3.24B, a fixed point $v_k^- = 0$ appears on the lower branch of the v_k - F_{kk} phase space diagrams, which can suppress oscillations. This fixed point is, however, less relevant because the kinetochores only occasionally pass the lower branch simultaneously, which is necessary to reach this fixed point. Furthermore, this fixed point is located near the right turning point F_{max} so that the kinetochores can easily leave the fixed point by a stochastic fluctuation as in Fig. 3.17. For these two reasons, in stochastic simulations, oscillations already occur for $n \gtrsim 5$, which is at a much lower n than the deterministically predicted $n \gtrsim 20$, but not for $n = 1$, i.e., in the absence of a catastrophe promoting mechanism, see Fig. 3.25.

The fixed point analysis of the v_k - F_{kk} phase space diagrams reveals that also a new type of fixed point corresponding to a non-oscillatory motion emerges for $n \lesssim 100$ in the shaded regions in Fig. 3.24B. In this new type of fixed point, which is marked by blue dots in Fig. 3.24C, the leading P-moving kinetochore in the lower branch of the master curve has the same velocity as the trailing AP-moving kinetochore in the upper branch so that $\dot{F}_{kk} = -c_k(v_{k,r} + v_{k,l}) = 0$, and the inter-kinetochore distance remains constant while the center of mass moves with a constant

velocity, as it can be seen in Fig. 3.24D. In the presence of PEFs, however, this new type of fixed point does not survive, see Fig. 3.25, because for the P-moving kinetochore, the AP-directed PEFs increase whereas they decrease for an AP-moving kinetochore. Then, the upper blue dot in Fig. 3.24C moves to the left while the lower blue dot moves to the right such that this new type of fixed point is unstable in the presence of PEFs. Therefore, PEFs are essential in the entire shaded region in Fig. 3.24B to re-establish oscillations.

We conclude that both the linker stiffness $c > 10 \text{ pN } \mu\text{m}^{-1}$ and the catastrophe rate ω_c^{kin} at the kinetochore⁶⁶ have to be sufficiently large to obtain bistability and oscillations. Because additional catastrophe promoting proteins are necessary to increase the catastrophe rate at the kinetochore, the lowest values of n , which still enable oscillations, might be advantageous in the cellular system. We note that poleward flux can influence existence and positions of fixed points: an intermediate flux velocity can eliminate a fixed point on the lower branch by moving it into the unstable area of the phase space diagram; if flux is sufficiently large, it can establish additional fixed points on the upper branch of the phase space diagrams, which suppress oscillations as in the basic model.

Moreover, the linker stiffness has to be sufficiently high to give linker extensions compatible with experimental results. An important part of the MT–kinetochore link is the Ndc80 complex,⁶⁷ which is a rod-like fibril of total length around 60 nm [191, 192] consisting of two coiled-coil regions with a flexible hinge that can adopt bending angles up to 120° with a broad distribution [192]. This bending corresponds to linker length changes of $|x| \sim 50 \text{ nm}$. Moreover, fluorescent labeling showed total intra-kinetochore stretches around 100 nm [193] or 50 nm [56]. Therefore, we regard linker extensions $x \lesssim 100 \text{ nm}$ as realistic values. For large $n \gg 20$, only a small linker stiffness is necessary to enable oscillations. At the small threshold stiffness, the average linker length $|\langle x \rangle|$ is typically $1 \mu\text{m}$ in this regime. Increasing the linker stiffness leads to a decreasing linker length $|\langle x \rangle|$. We conclude that for $n \gg 20$, experimental observations of linker extensions $|x| \lesssim 100 \text{ nm}$ put a stronger constraint on linker stiffness than the experimental observations of oscillations. Linker stiffnesses significantly above $5 \text{ pN } \mu\text{m}^{-1}$ and, thus, far above c_{osc} are necessary to obtain a realistic linker length.

For n in the range of 10 to 20, which is compatible with the experimental result $n \sim 7$ for the catastrophe promoter MCAK [189], and a linker stiffness $c = 20 \text{ pN } \mu\text{m}^{-1}$, the increased catastrophe rate at the kinetochore leads to a realistic behavior with linker extensions $x \sim 100 \text{ nm}$, see Fig. 3.24A, which are also compatible with the experimental results [56, 191–193]. This parameter regime is within the shaded regions in Fig. 3.24B and PEFs are necessary to establish oscillations. The linker extension is independent of

⁶⁶ $n \gtrsim 20$ or $n \gtrsim 5$ in the presence of stochastic fluctuations

⁶⁷ Ndc80 complexes and their mechanical properties are the subject of Chapter 4.

PEFs as they do not affect the master curves. The reason why in such a parameter range of n and c , the more realistic model with waiting boundary conditions at the kinetochore exhibits a similar behavior as the basic model is that the pushing phases ($x > 0$) in the basic model have a similar duration as the waiting times at the kinetochore in the more realistic model.

3.4.4 Reproduction of kinetochore oscillations in PtK1 cells

In the previous three sections, we examined the effects of three different extensions by adding them separately to the basic model. Each of these extensions is quantified by one additional parameter: the velocity v_f of poleward flux, the force constant k of PEFs, and the increased catastrophe rate ω_c^{kin} for MTs that are stalled at the kinetochore. During the analysis of the influence that a variation of these three parameters as well as a variation of c and M has on the kinetochore dynamics and the occurrence of oscillations, the deterministic mean-field approach—in particular the interpretation of the force–velocity relation as phase space diagram with potentially emerging fixed points—turned out to be a powerful tool that let us accomplish this task with lower effort and, moreover, provided a deeper insight than the sole use of stochastic simulations.

We now use our gained knowledge for demonstrating that the parameters of our model can be adjusted to reproduce certain characteristics of chromosome dynamics in PtK1 cells,⁶⁸ which are well quantified in the literature [55, 105]. In doing so, we only concentrate on the oscillating chromosomes in the center of the PtK1 spindle, but do not address the chromosomes in the periphery that do not exhibit directional instability [55, 105, 196, 197].⁶⁹ For the purpose of reproduction, we do not only include all extensions simultaneously, but also adjust the experimental parameters from Tab. 3.2, which we took for granted so far. This adjustment is reasonable in that the parameters for MT dynamics stem from experiments with budding yeast kinetochores [134], which can only bind one MT [198], whereas the mean-field theory is only correct if the kinetochores are attached to multiple MTs as in metazoan cells like PtK1. Moreover, in budding yeast, the Ndc80 fibrils are connected to MTs via ring-like Dam1 complexes [124, 125, 127, 128], which do not appear in metazoan cells [114]. For the sake of realism, we also allow the MTs to detach from the kinetochore. Though the mean-field theory relies on permanent bonds, it still helps to systematically identify the parameter changes that implicate the purposed effects.

⁶⁸ The PtK1 cell line is derived from kidney cells of female long-nosed potoroo (*Potorous tridactylus*), which are marsupials from the rat-kangaroo family [194, 195].

⁶⁹ We discuss this dichotomy later by attributing the motion of the peripheral chromosomes to fluctuations around a fixed point in the non-oscillatory regime.

Before going over the fitting procedure, we note that in this section, we discard the principle of keeping the model simple, which we followed so far by adding one generalization at a time and analyzing the influences of just a few parameters. It is obviously not surprising to find a solution that resembles the experimental data by fitting the model with a large number of free parameters, and there are probably other combinations of parameters than the one obtained below that resemble the experiments in a similar or even better manner. Therefore, this section does not claim to provide a final parameter set predicting real values, but should rather be seen as a proof of concept.⁷⁰

Our model exhibits a large difference of P versus AP-velocity (~ 100 vs. ~ 4 nm s⁻¹, see Fig. 3.18), which is the origin of frequency doubling and also appears in PtK1 cells but not in this extent (~ 19 vs. ~ 16 nm s⁻¹) [55]. As a consequence, in our model, both kinetochores move towards each other in AP-direction (state 0 in Fig. 3.13) most of the time, whereas in the experiment, mostly one kinetochore moves in P- while the trailing sister is moving in AP-direction (state 2/2' in Fig. 3.13). In a first step we respect this discrepancy by adjusting the master curve (or force-velocity relation) in a way that the two stable branches fit the experimentally measured velocities. This objective is achieved by modifying the force-free MT velocities v_{\pm}^0 , which shifts the upper/lower branch up- or downwards, and the corresponding characteristic forces F_{\pm} , which alters the slope of the upper/lower branch as visualized in Fig. 3.26. Moreover, as a last parameter of MT dynamics, we change the rescue rate ω_r^0 in order to adjust the MT-kinetochore distance to a realistic value. In a second step, we fit the measured frequencies and amplitudes by varying the parameters that do not affect the master curves (c_k, k).

Using the model with confinement at the kinetochore, we assume a ten times increased catastrophe rate $\omega_c^{\text{kin}} = 10 \omega_c^0$ according to experimental results [189]. We set the linker stiffness to $c = 20$ pN μm^{-1} and keep it unchanged henceforth since this value results in strongly bistable master curves and the manifold consequences that a further modification of c has on kinetochore dynamics are hard to handle. The flux velocity is $v_f = 8$ nm s⁻¹, see Tab. 3.4. The force-free MT growth velocity v_+^0 has to be greater than v_f for two reasons: Firstly, detached MTs would not have a chance to reach the kinetochore again, otherwise. Secondly, this choice prevents a fixed point at the upper branch, as the left turning point in phase space, which is the maximum of the master curve, is located at $v_k = v_+^0 - v_f$ when the MTs are confined at the kinetochore. We increase the force-free growth velocity roughly four-fold to $v_+^0 = 20$ nm s⁻¹ so that the minimum AP-velocity $v_+^0 - v_f = 12$ nm s⁻¹ in the left turning point F_{min} lies

⁷⁰ To put it in John von Neumann's words: we fit the elephant in this section.

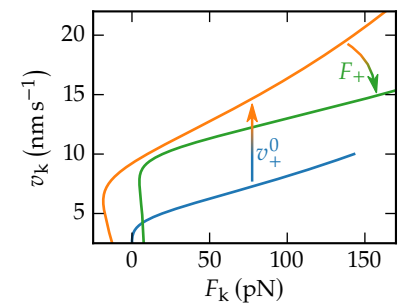


Figure 3.26: Effects of varying the MT velocity parameters. While an increase of the zero force velocity v_+^0 predominantly shifts up the upper branch of the force-velocity relation (blue to orange, $v_+^0 \rightarrow 2v_+^0$), the main effect of increasing the characteristic force F_+ is a decrease of the slope (orange to green, $F_+ \rightarrow 2F_+$). Modifications of the shrinking parameters v_-^0 and F_- have analogous effects on the lower branch.

below the observed mean velocity of $\sim 16 \text{ nm s}^{-1}$. In order to adjust the maximum AP-velocity, we reduce the characteristic force of MT growth to $F_+ = 5 \text{ pN}$, which leads to a steeper upper branch in the phase space diagram. The force-free shrinking velocity v_-^0 should be smaller than the observed P-velocity since the lower, P-directed branch always lies above it. Analogously to the upper branch and F_+ , also the slope of the lower branch can be adjusted by varying the characteristic force F_- : an increase of F_- , i.e., a decrease of its absolute value, steepens the lower branch and thereby slows down the poleward motion. It turns out that it is a good choice to keep the values for v_-^0 and F_- from Tab. 3.2 unchanged. Finally, we reduce the rescue rate ω_r^0 , which lets MTs shrink to smaller lengths x_m , shifts the minimum of the master curve downwards and increases the MT-kinetochore distance $|x| = |X_k - x_m|$ to a realistic value.

Since we enable detachment in this section, we set $M = 35$ as it results in a mean number of ~ 20 attached MTs. Finally, we adjust the strength of PEFs k and the cohesin bond stiffness c_k to the following conditions: Firstly, the PEFs have to be strong enough to assure proper chromosome alignment at the equator as well as a regular oscillation pattern, but should not dominate compared to the inter-kinetochore tension in order to prevent antiphase oscillations. Secondly, k and c_k affect the amplitude and the frequency of kinetochore oscillations, which should resemble experimental results, in the same manner: an increase of both k and c_k decreases the amplitude and increases the frequency. We find that $k = 20 \text{ pN } \mu\text{m}^{-1}$ and $c_k = 20 \text{ pN } \mu\text{m}^{-1}$ fulfill both conditions. In Tab. 3.5, we list all parameters that have been changed compared to Tab. 3.2.

The resulting kinetochore dynamics is shown in Fig. 3.27. The simulated kinetochore trajectories in Fig. 3.27A are very similar to the experimental results in Refs. [55, 105] as they exhibit frequency doubling of breathing compared to single kinetochore oscillations and move predominantly in phase, i.e., there is a leading P- and a trailing AP-kinetochore as in state 2/2' in Fig. 3.13. The motion of

Table 3.5: Parameters to reproduce kinetochore oscillations in PtK1 cells. Parameters not listed here have been unchanged compared to Tab. 3.2.

Description	Symbol	Value
Zero force rescue rate	ω_r^0	0.012 s^{-1}
Zero force MT growth velocity	v_+^0	20 nm s^{-1}
Characteristic force of MT growth	F_+	5 pN
Catastrophe rate at the kinetochore	ω_c^{kin}	0.019 s^{-1}
MT flux velocity	v_f	8 nm s^{-1}
PEF strength	k	$20 \text{ pN } \mu\text{m}^{-1}$
Cohesin bond stiffness	c_k	$20 \text{ pN } \mu\text{m}^{-1}$
MT-kinetochore linker stiffness	c	$20 \text{ pN } \mu\text{m}^{-1}$
Number of MTs	M	35

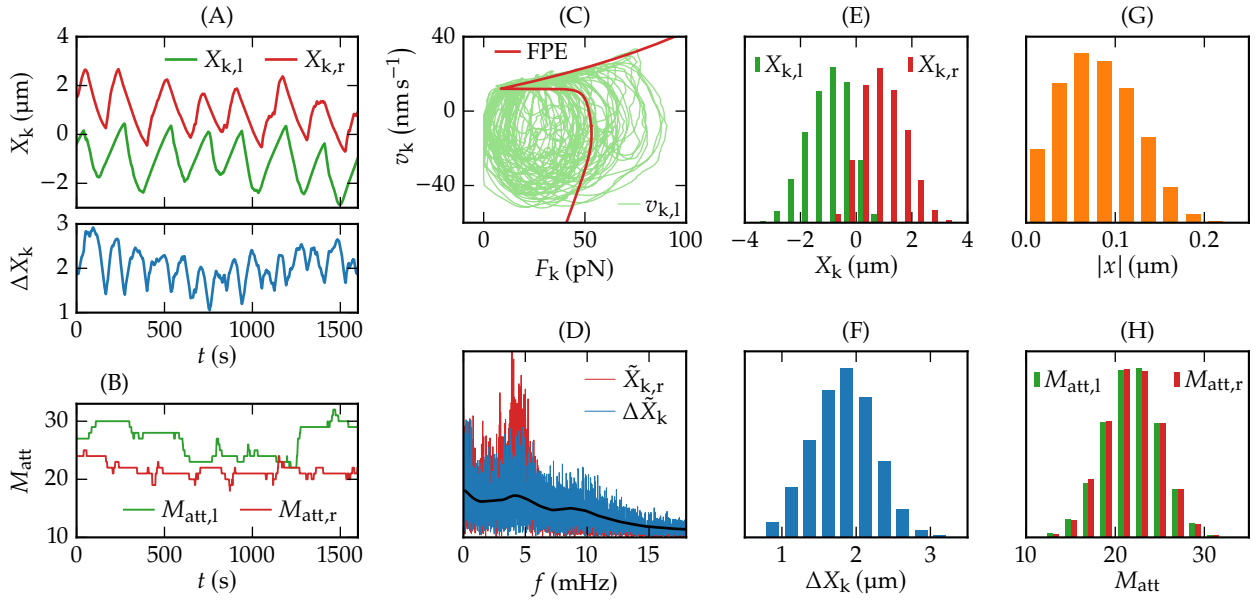


Figure 3.27: Reproduction of kinetochore oscillations in PtK1 cells. (A) Kinetochore positions and inter-kinetochore distance over time. Although the breathing oscillations are rather fluctuative, frequency doubling is recognizable. (B) Number of attached MTs over time. (C) Kinetochore motion in phase space (green) compared to the mean-field force–velocity relation (red, calculated with the mean number of attached MTs). (D) Position of the right kinetochore and inter-kinetochore distance in Fourier space. Fluctuative breathing oscillations lead to a Fourier transform with broad maxima, which are almost only recognizable in the smoothed curve (black). (E–H) Distributions of kinetochore positions X_k , inter-kinetochore distance ΔX_k , MT-kinetochore distance $|x|$, and the number of attached MTs M_{att} .

the inter-kinetochore distance is rather fluctuative, resulting in a broad Fourier transform, in which the maximum at the breathing frequency is hardly recognizable, see Fig. 3.27D. This is the only significant difference to the real kinetochore motion. The distributions of kinetochore positions as well as inter-kinetochore and MT-kinetochore distances (Fig. 3.27E–G) are in good agreement with experimental results [105].

In Tab. 3.6, we list several characteristic quantities of kinetochore oscillations that have also been determined experimentally for PtK1 cells. Comparison with our model results shows quantitative agreement. In particular, the large discrepancy in the P- and AP-velocities is eliminated.

Table 3.6: Characteristic quantities of model kinetochore oscillations from Fig. 3.27 compared to experimental results in PtK1 cells.

Description	Model	Experiment
Mean P velocity	21.5 nm s^{-1}	19.0 nm s^{-1} [55]
Mean AP velocity	15.7 nm s^{-1}	15.7 nm s^{-1} [55]
Single kinetochore frequency	4.27 mHz	4.14–4.23 mHz [55]
Breathing frequency	$\sim 8.6 \text{ mHz}$	8.25 mHz [55]
Mean inter-kinetochore distance	$(1.83 \pm 0.42) \mu\text{m}$	$(1.90 \pm 0.44) \mu\text{m}$ [105]
Mean MT-kinetochore distance	$(0.081 \pm 0.042) \mu\text{m}$	$(0.11 \pm 0.04) \mu\text{m}$ [105]
Standard deviation of kinetochore position	$0.76 \mu\text{m}$	$0.5\text{--}1.1 \mu\text{m}$ [105]
Mean number of attached MTs	21.4	20–25 [109]

3.5 Discussion

We provided an analytical mean-field solution of the one-sided spindle model introduced by Banigan *et al.* [57], which becomes exact in the limit of large MT numbers. The mean-field solution is based on the calculation of the mean linker extension $\langle x \rangle$ as a function of a constant kinetochore velocity v_k (the master curve). Together with the equation of motion of the kinetochore, we obtained the force–velocity relation of the one-sided model from the master curve. Our solution clearly shows that the force feedback of linkers onto the MT depolymerization dynamics is essential for a bistable force–velocity relation within the minimal model. The shape of the distribution $p_{\pm}(x)$ of linker lengths in Eq. (3.18) is governed by this force feedback, and we traced the bistability back to the peakedness (kurtosis) of this distribution.

Applying the mean-field solution of the one-sided to the two-sided model, we were able to deepen and to expand the understanding of the mechanisms that drive kinetochore dynamics in the mitotic spindle, including the occurrence of oscillations in the minimal model as well as the effects of several model extensions. In the following, we discuss these results and their applicability to experimental observations.

Directional instability is an emergent phenomenon of collective MT dynamics

Interpreting the bistable force–velocity relation as phase space diagram for kinetochore dynamics in the two-sided model, we mathematically characterized regular kinetochore oscillations as an emergent result of collective dynamics of coupled MTs that exhibit dynamic instability individually. Our theory becomes exact in the limit of large MT numbers M . This interpretation of oscillations is underpinned by the experimental observations that kinetochore oscillations in budding yeast [164, 199, 200], where each kinetochore is attached to one MT [198], as well as in fission yeast [106, 201], where two to four MTs interact with the same kinetochore [202], have a considerably more fluctuative character than the regular oscillations in vertebrate cells [50–56] with ~ 20 MTs per kinetochore [109, 110].

We were able to deduce idealized kinetochore oscillations, whose periods conform with experimental results [55]. For a MT–kinetochore linker stiffness $c = 20 \text{ pN } \mu\text{m}^{-1}$ and 20–25 MTs per kinetochore, we got periods of 206 s to 258 s and 103 s to 129 s for kinetochore and breathing oscillations, respectively. Our approach

reproduced the frequency doubling of breathing compared to single kinetochore oscillations observed in the experiment [55]. Both in the model and in the experiment, this doubling originates from the different velocities of AP- and P-moving kinetochores, which ensure that an AP-to-P switch (1/1' in Fig. 3.13) is always followed by a P-to-AP switch of the same kinetochore (3/3' in Fig. 3.13).⁷¹ In the minimal model, the velocity difference is, however, much larger than it has been observed *in vivo*. As a consequence, in the basic model with 20–25 MTs, an AP-to-P switch follows 96 s to 119 s after a P-to-AP switch of the sister kinetochore,⁷² which is 93% of a breathing period, whereas in PtK2 cells a mean interval of merely 6 s has been measured [56]. In other words, in the basic model, most of the time both kinetochores move towards each other in AP-direction (state 0 in Fig. 3.13), whereas in the experiment, mostly one kinetochore moves in P- while the trailing sister is moving in AP-direction (state 2/2' in Fig. 3.13). In our model, different AP- and P-velocities are based on the fact that the MT shrinkage is much faster than growth. The model parameters for MT dynamics were taken from experimental measurements with yeast kinetochores [134], which, however, are distinct from kinetochores in the metazoan spindles our model is intended to represent. Therefore, we demonstrated in Sec. 3.4.4 that the described discrepancy can be eliminated by adjusting some MT parameters, and, moreover, the model can reproduce kinetochore oscillations in PtK1 cells quantitatively.

Stiffness of the MT–kinetochore linker

Our analytical approach also allowed us to go beyond the results of Banigan *et al.* [57] and quantify constraints on the linker stiffness c and the MT number M for the occurrence of bistability in the one-sided model and for the occurrence of oscillations in the full model. We found that bistability requires linker stiffnesses above $c_{\text{bist}} \approx 8 \text{ pN } \mu\text{m}^{-1}$. Bistability is, however, not sufficient for oscillations. Our phase space interpretation showed that bistability only leads to directional instability if the two branches of the force–velocity relation are also separated by the zero velocity line. This condition quantifies the oscillatory regime in the parameter plane of c and M . We predicted that oscillations should only be observable if the MT–kinetochore linker stiffness is above $c_{\text{osc}} \approx 16 \text{ pN } \mu\text{m}^{-1}$. Our model can thus provide additional information on the MT–kinetochore linkers whose molecular nature is unknown up to now. Several Ndc80 fibrils, which cooperatively bind to the MT, are an important part of the MT–kinetochore link, and the stiffness of this Ndc80 link has been determined recently using optical trap measurements [58]. These experiments found stiffnesses above $\sim 20 \text{ pN } \mu\text{m}^{-1}$, which are compatible with our bounds. Moreover,

⁷¹ As a reminder: When both kinetochores are in the slow upper branch (AP) in Fig. 3.13 and reach the left turning point F_{min} , one kinetochore switches to the fast lower branch (AP to P) and switches back the upper one (P to AP) soon after, while its sister stays in the AP branch and does not change its direction of motion.

⁷² assuming a forced periodic order of states 2 and 2', i.e., the two kinetochores pass the lower branch alternately as in Fig. 3.13C

⁷³ We examine the strain stiffening of Ndc80 complexes in Chapter 4 by re-evaluating the experimental data of Volkov, Huis in 't Veld *et al.* [58, 59] and attributing the stiffening to the specific structure of an Ndc80 complex.

they found a stiffening of the link under force,⁷³ which could be included in our model in future work.

Fixed points explain observation of “paused” kinetochores

The derivation of the lower bound for the stiffness for the occurrence of oscillations is based on the occurrence of a new zero AP-velocity fixed point in the force–velocity diagram of the kinetochores, which suppresses oscillations upon decreasing the stiffness. Analogously to resting in the fixed point in our model, it has been observed in newt lung cells that oscillations are occasionally (11 % of time) interrupted by phases in which the kinetochores pause their motion [50]. This indicates that the spindle of newt lung cells operates near the boundary between the oscillatory and the non-oscillatory regime resulting in a kinetochore motion as described in Fig. 3.17 with a fixed point very close to the left turning point F_{\min} .

Poleward flux suppresses kinetochore oscillations

Also the influence of poleward flux to the system could be examined by a fixed point analysis of the force–velocity diagram. Since poleward MT flux shifts the force–velocity relation towards smaller AP-velocities of the kinetochore, the upper branch may cross zero velocity establishing again a fixed point suppressing oscillations. This explains why high flux velocities suppress directional instability and rationalizes the correlation between kinetochore oscillations and poleward flux observed in several cells (Tab. 3.4).

Polar ejection forces provide an alternating oscillation pattern and chromosome alignment at the spindle equator

Furthermore, we added linearly distributed PEFs, which depend on the absolute kinetochore positions. Their main effect is a phase shift between the sister kinetochores in their phase space trajectories, which leads to regularly alternating kinetochore oscillations and, finally, forces the kinetochores to stay near the spindle equator. Consistently, experimental results showed that a proper formation of the metaphase plate is not assured if PEFs are suppressed [140]. Moreover, budding yeast cells, which lack the necessary number of interpolar MTs to build up PEFs, enter anaphase without aligning the chromosomes in a metaphase plate beforehand [199]. Since the PEFs do not affect the master curves and phase space diagrams deterministically, they never completely suppress oscillations but only reduce their amplitude and increase their frequency, while

the kinetochore velocities v_k are unchanged. This is consistent with experiments of Ke *et al.* [187], who observed an increase in amplitude but no influence on the occurrence of oscillations and the velocity of chromosomes after severing the chromosome arms and thereby weakening the PEFs. In stochastic simulations, the kinetochore oscillations are more fluctuative in the presence of PEFs, see Fig. 3.22. A similar observation was made in the model of Civelekoglu-Scholey *et al.* [105]. Moreover, in stochastic simulations, sister kinetochores tend to oscillate in antiphase and frequency doubling of breathing compared to single kinetochore oscillations is lost if PEFs are strong compared to the inter-kinetochore tension ($k \gg c_k$). Since to our knowledge such antiphase oscillations have not been observed *in vivo*, we conclude that the inter-kinetochore tension is the dominating force for directional instability.⁷⁴

Consistently with experimental observations in both fission yeast [203, 204] and human cells [205], kinesin-8 motors investigated in the model of Klemm *et al.* [106] have a similar centering effect as the PEFs in our model. Since fission yeast does not contain chromokinesins [206], the Klemm model does not include PEFs whereas our model does not include kinesin-8. It remains an open question whether and how the similar effects of PEFs and kinesin-8 cooperate if both are present. As kinesin-8 depolymerizes MTs in a length-dependent manner [207, 208], it could be included in our model by a catastrophe rate ω_c that depends on the MT length x_m . While such MT length-dependent catastrophe rates can easily be implemented in the stochastic simulations, they are difficult to include into our mean-field theory, which is based on solving the FPEs (3.10) and (3.11) in relative coordinates rather than absolute MT lengths.

Catastrophe promotion at the kinetochore

Finally, we lifted the assumption that MTs are able to apply pushing forces on the kinetochores because experiments suggest that MTs only exert tensile forces [51, 139]. For that purpose, we confined MT growth at the kinetochore by catastrophe-triggering boundary conditions. The catastrophe rate for a MT at the kinetochore ω_c^{kin} can, in principle, range from the force-free MT catastrophe rate ω_c^0 , which is realistic in the absence of any catastrophe promoting proteins, up to infinity if a catastrophe is immediately triggered. In the presence of the centromere-associated regulating protein MCAK, increased catastrophe rates $\omega_c^{\text{kin}} = 7\omega_c^0$ are expected [189]. We found that *both* the linker stiffness c *and* the catastrophe rate ω_c^{kin} at the kinetochore have to be sufficiently large to obtain bistability and oscillations. We found, in particular, that the force-free MT catastrophe rate is not sufficient to lead to oscillations, which

⁷⁴The occurrence of antiphase oscillations might be tested experimentally if it is possible to artificially promote the PEFs, for instance, by increasing the concentration of chromokinesins.

shows that catastrophe-promoting proteins are essential to induce oscillations. In the presence of PEFs, oscillations can be recovered even for relatively small catastrophe rates: for $\omega_c^{\text{kin}}/\omega_c^0 \sim 5$, we found no oscillations in the absence of PEFs; for $\omega_c^{\text{kin}}/\omega_c^0 < 2$, we found no oscillations at all. Moreover, the linker stiffness has to be sufficiently high to give linker extensions below 100 nm compatible with experimental results [56, 191–193]. For $\omega_c^{\text{kin}}/\omega_c^0 = 20$, and a linker stiffness of $c = 20 \text{ pN } \mu\text{m}^{-1}$, we found realistic behavior. Our results can explain experimental observations in Ref. [133], where PtK2-cells were observed under depletion of centromeric MCAK, which decreases ω_c^{kin} . Then, in accordance to our results in Fig. 3.24CD, where the right turning point F_{max} of the hysteresis is shifted to the left by reducing ω_c^{kin} , the oscillation frequency increased and the mean centromere stretch decreased, while the “motility rates”, i.e., the velocities did not change.

Force-free one-sided model reflects Anaphase A

Though we concentrated on chromosome dynamics during metaphase throughout the entire chapter, our model can also be used to discuss anaphase A. By the loss of the cohesin bonds at the anaphase onset, the formerly bipolar spindle is transformed to two monopolar spindles,⁷⁵ each of which can be described by our one-sided model. Since there are no PEFs during anaphase, no force is applied on the two separated chromatids besides the pulling force of the kinetochore MTs.⁷⁶ For most of the various force–velocity relations that we have calculated, the left turning point F_{min} is either far above or very close to $F = 0$ so that at zero force the lower branch is the only stable one or should at least be preferred to the upper branch.⁷⁷ As a consequence, the kinetochore velocity in the one-sided model is negative on average when no force is applied, which correctly reflects the poleward motion of the chromatids during anaphase.

Influence of the cohesin bond

In the following final paragraphs, we substantiate the applicability of our model by discussing that the mean-field approach and the force–velocity diagram of kinetochore motion are suitable to rationalize various further experimental results and to formulate well-founded hypotheses. To this end, we start with the experiments of Jaqaman *et al.* [113] who observed an increase of oscillation amplitudes and periods when they weakened the cohesin bonds in HeLa cells. In our model, a smaller cohesin stiffness c_k has the same two effects because the inter-kinetochore distance has to be larger to reach the turning points F_{min} and F_{max} of the hysteresis loop,

⁷⁵ neglecting the interpolar MTs that still connect the two centrosomes and push them apart in anaphase B

⁷⁶ i.e., $F_{\text{ext}} = 0$ in terms of our model

⁷⁷ In the basic model with $c = 20 \text{ pN nm}^{-1}$, we find $F_{\text{min}} \approx 0$, see for instance Figs. 3.11B and 3.14B. For smaller c , F_{min} may also lie above or below 0 as in Fig. 3.17. In the latter case however, the system is outside the oscillatory regime and the upper branch has a negative velocity at $F = 0$ resulting in a poleward motion again. When the MTs are confined at the kinetochore, the upper branch lies at large positive forces, which is plausible since there is no force left to drive an AP motion when the MTs can not push the kinetochore.

and the phase space velocity $\dot{F}_{kk} = c_k(v_{k,r} + v_{k,l})$ and, therefore, the frequencies are proportional to c_k .

Effects of Hec1 phosphorylation

Next, our theoretical approach can be applied to the observations in Refs. [111, 209–211] on the effects of phosphorylation of Hec1, which is part of the mammalian Ndc80 complex, onto kinetochore dynamics. Dephosphorylation leads to hyper-stable MT–kinetochore attachments, increases the inter-kinetochore distance, damps or completely suppresses oscillations, and lets the kinetochores more often be found in a “paused state”. The increase of the inter-kinetochore distance can be explained with the hyper-stable MT–kinetochore attachments: in the oscillatory regime, the bistable area of the force–velocity relation increases if more MTs are attached to the kinetochore, see Fig. 3.11B; in the non-oscillatory regime, the mean distance $\langle \Delta X_k \rangle$ is a linear function of M , see Eq. (3.26). However, the suppression of oscillations and the frequent appearance of paused states, which are both effects of leaving the oscillatory regime in our model, can not be explained with an increasing number of attached MTs. Instead, we suggest three additional effects of Hec1 phosphorylation: Firstly, it is imaginable that Hec1 is a catastrophe factor that is activated by phosphorylation, i.e., if phosphorylation is suppressed, the catastrophe rate at the kinetochore ω_c^{kin} decreases. Secondly, phosphorylation of Hec1 could stiffen the Ndc80 complex so that dephosphorylation suppresses oscillations by decreasing the linker stiffness c . However, the stiffness measurements presented in the following chapter make this explanation unlikely.⁷⁸ The third possible explanation is based on the observation of Umbreit *et al.* [212] that phosphorylation of Hec1 suppresses rescues. Following the argumentation in Sec. 3.3.1, we conclude that a decreased rescue rate has a similar effect as an increase of the linker stiffness: since the exponent α_- that defines the leading order of $p(x)$ near x_{\min} is a linear function of ω_r^0 ,⁷⁹ the probability density $p(x)$ becomes sharper for negative kinetochore velocities if rescues are suppressed, finally leading to a bistable master curve that allows for oscillations.

In Ref. [210], besides suppression, Hec1 phosphorylation was also enforced on up to four sites. As a result, the number of attached MTs and the periods of kinetochore oscillations decreased, which is consistent with our model, see Fig. 3.14C. Moreover, kinetochore oscillations were supported but became more erratic just like in our model, where kinetochore motion is more fluctuative if less MTs are attached, see Fig. 3.14. This experimental result reinforces our interpretation of regular kinetochore oscillations as an emergent

⁷⁸ In Chapter 4, we determine stiffnesses of Ndc80 complexes tracing a depolymerizing MT tip in optical trap experiments. The results for phosphorylated Ndc80 complexes do not significantly differ from those of wild type Ndc80, see Fig. 4.15.

⁷⁹ $p_-(x) \propto (x - x_{\min})^{\alpha_-}$,

$$\alpha_- = -1 + \frac{\omega_r^0 F_-}{c v_-^0} \left(\frac{v_k}{v_-^0} \right)^{-1 + F_- / F_r},$$

see Appendix B.1.

phenomenon that results from the collective behavior of stochastic MT dynamics.

Dichotomy of central and peripheral kinetochores in PtK1 cells

We finally discuss the aforementioned dichotomy in the mitotic spindle of PtK1 cells, where, on the one hand, the kinetochores in the center of the metaphase plate do exhibit regular oscillations as we have reproduced them in Sec. 3.4.4, while the trajectories of the peripheral kinetochores, on the other hand, are very fluctuative, hardly show any periodicity, and strongly resemble the fluctuative motion around a fixed point in the non-oscillatory regime of our model [55, 105, 196, 197]. Civelekoglu-Scholey *et al.* [105] explained this dichotomy with different distributions of PEFs in the center and the periphery of the metaphase plate. However, the model kinetochore trajectories in the presence of strong PEFs, which they declare to be representative for the motion of peripheral kinetochores,⁸⁰ still have a regular oscillating shape with only a reduced amplitude and an increased frequency, in agreement with the results of our model in Fig. 3.22, and therefore do not satisfactorily resemble the fluctuative experimental trajectories for peripheral kinetochores from Refs. [55, 105]. For a clear characterization of the experimentally measured motion of peripheral kinetochores as either stochastic fluctuations or regular oscillations, its representation in Fourier space would be helpful as already provided for the central kinetochores by Wan *et al.* [55] and as provided in Fig. 3.22 for our model. If the Fourier transforms do not have any distinct peaks, differences in PEFs are ruled out as a possible explanation for the dichotomy in PtK1 cells according to both our model and the one of Civelekoglu-Scholey *et al.*

⁸⁰ See Fig. 6C in Ref. [105].

Instead of different PEFs, our results suggest differences in linker stiffness or catastrophe promotion as reasons for the dichotomy. For instance, less Ndc80 complexes could participate in the peripheral MT–kinetochore links resulting in a reduced linker stiffness and non-oscillatory behavior. Also a non-uniform MCAK distribution that decreases radially towards the periphery of the metaphase plate could reduce ω_c^{kin} and suppress oscillations of peripheral kinetochores. Differences in poleward flux might be another possible explanation for the dichotomy according to our results. However, Cameron *et al.* [197] observed that the flux velocities in PtK1 cells are the same for all kinetochore MTs.

Parameter	Symbol	Occurrence	Frequency	Amplitude	Additional effects
Linker stiffness	c	Stimulation	Decrease	Increase	Decrease of inter-kinetochore distance in non-oscillatory regime
Poleward flux	v_f	Suppression	Decrease	None	
Polar ejection forces	k	None	Increase	Decrease	PEFs force kinetochores to oscillate alternately and to stay near the spindle equator
Catastrophe rate of stalled MTs	ω_c^{kin}	Stimulation	Decrease	Increase	
Cohesin bond stiffness	c_k	None	Increase	Decrease	
MT number	M	(Stimulation)	Decrease	Increase	

Conclusion

In conclusion, the minimal model with its generalizations can rationalize a number of experimental observations. The predicted responses to the most relevant parameter changes are summarized in Tab. 3.7 and suggest further systematic perturbation experiments. Particularly interesting are the constraints on the MT-kinetochore linker stiffness obtained from our mean-field approach, which provide new insight into the mechanical properties of the kinetochore and are compatible with recent optical trap measurements [58] of the stiffnesses of Ndc80 complexes. These measurements are the subject of the following chapter.

Table 3.7: Summary. The table lists the effects that an increase of the parameter in the first column has on the occurrence, the frequency, and the amplitude of kinetochore oscillations.

Strain stiffening of the Ndc80 complex

4

As we have learned in Sec. 3.1.2, chromatids and their inner kinetochores are bound to MTs during mitosis via attachments created by rod-like Ndc80 complexes. The Ndc80 mediated attachments remain intact while dynamic MTs alternate between growth and shrinkage and transmit depolymerization forces to the kinetochore during the segregation of chromosomes. The exact mechanisms underlying binding and force transmission are not completely understood but are expected to reflect the molecular structure and resulting elastic properties of the Ndc80 complex.

For the mitotic spindle model from the previous chapter, we chose to treat the MT–kinetochore linkers as generic springs. This simple model was motivated by the aim to account for the rod-like structure of the Ndc80 complex with as little complicating assumptions as possible. Similar approaches can be found in several related force balance models of the mitotic spindle [34, 57, 105, 162].¹ By a mathematical analysis of our one-sided model, we revealed that the stiffness of the generic harmonic linker is a critical parameter for the cooperative dynamics of kinetochore MTs and chromatids in the mitotic spindle and for the occurrence of directional instability in particular. This critical role raises interest in the elastic properties of the kinetochore and the stiffness of the linking Ndc80 complexes, which had to be estimated so far in the aforementioned models.

In a recent work by Volkov, Huis in 't Veld *et al.* [58], a first experimental approach to measure the stiffness of Ndc80 complexes was provided by employing optical trapping techniques. Contrary to the assumption of a constant linker stiffness used in the mitotic spindle models, they found the stiffness of Ndc80 complexes to increase under tension. The subject of this chapter is a reanalysis of the above experiments with a focus on the found strain stiffening, followed by an attempt to trace the experimental findings back to the known structural features of the Ndc80 complex, the MT and the curved protofilaments (PFs).

Whereas in the original study, the stiffness was only determined while the Ndc80 complexes were attached to a stalled MT [58], in Sec. 4.2, we re-evaluate the same data with a novel method that allows us to time-trace the stiffness, i.e., to determine the stiffness of Ndc80 complexes tracking a polymerizing or depolymerizing MT against the opposing load from the optical trap. By splitting the force traces into fixed time intervals and analyzing stiffness

Large parts of this chapter have already been published in Ref. [213], which is licensed under CC BY 4.0 [94].

¹These models are reviewed in Sec. 3.2.1.

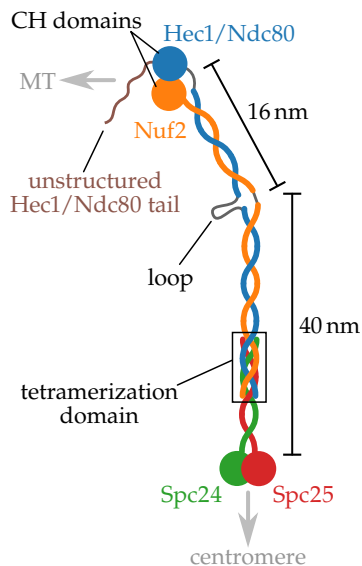


Figure 4.1: Structure of the Ndc80 complex. The Ndc80 complex consists of two coiled coils which are connected in the tetramerization domain. While the Spc24:Spc25 coiled coil is anchored to the centromere, the Ndc80:Nuf2 coiled coil can bind to the MT lattice via the CH domains and the unstructured tail. At a distance of 16 nm from the MT binding domain, the Ndc80 complex has a flexible kink where the coiled coil structure is interrupted by a loop.

² While Ndc80 is present in yeast, it is replaced by the homolog Hec1 in human cells [214]. We use “Ndc80” in the following as a general term for both the Ndc80 and the Hec1 protein.

at each of them, we achieve several advantages: (1) we generate more data over a wider force range; (2) we demonstrate stiffening during force production and not only compare stalled MTs to free ones; (3) we alleviate the concern that different levels of strain stiffening result from differences in MT ends or beads. Moreover, time-tracing allows us to establish that strain stiffening does not depend on the state of the MT end: we observe positive correlation of stiffness with force when the MT stalls, grows, or shrinks. In addition to wild type Ndc80, we also analyze data from MT end tracking experiments with three different variants of the Ndc80 complex, which are partly presented in Ref. [59] but have not been analyzed with regards to the stiffness so far. We observe strain stiffening for each examined Ndc80 variant.

In order to rationalize the experimental findings on strain stiffening of the Ndc80 links, we introduce an elastic model in Sec. 4.3. The model contains serial arrangements of Ndc80 complexes, the PFs and the MT, to each of which we ascribe a stiffness based on their structural features. Describing the Ndc80 complex as an ideal chain with two bonds of different lengths, we show that the strain stiffening is a direct consequence of the characteristic Ndc80 structure with a flexible kink at approximately on third of its length. To better match the measured stiffnesses, it is necessary to include the contributions from MT fluctuations and from PF bending to the total effective stiffness. Finally, to explain the shape of the experimental stiffness–force relations, we also introduce a positive correlation of the number of MT end-attached Ndc80 complexes with MT-generated force.

As a preparation for the analyses described above, we continue with a short section on the structure of the Ndc80 complex and currently discussed models for the Ndc80–MT bond. These binding models are discussed at the end of this chapter in consideration of the meanwhile obtained results.

4.1 The Ndc80 complex

The Ndc80 complex is a rod-like tetramer of 56 nm length consisting of the four proteins Ndc80/Hec1,² Nuf2, Spc24, Spc25 [191, 192], see Fig. 4.1. The four proteins form two α -helical coiled coils, Ndc80:Nuf2 and Spc24:Spc25. While the N-terminal ends³ of Spc24:Spc25 build globular domains that anchor the Ndc80 complex to the inner kinetochore, their C-termini are bound to the N-terminal ends of Ndc80 and Nuf2 in a tetramerization domain [191, 216]. The Ndc80:Nuf2 coiled coil is interrupted by a loop of 40 amino acids [217] resulting in a flexible joint comparable to

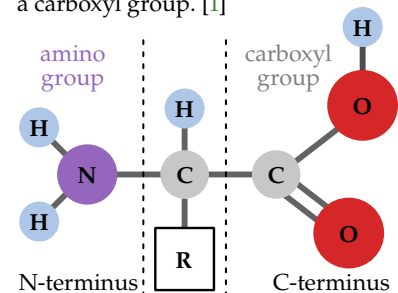
an elbow, which divides the Ndc80 complex into two stiff arms of 40 nm and 16 nm length [192].

The N-terminal ends of both Ndc80 and Nuf2 fold into CH domains⁴ that can directly bind to the MT resembling the plus end tracking protein EB1 [220, 221]. Since the two CH domains are positively charged, it was proposed that they bind directly to the two acidic C-terminal tails of a tubulin dimer, whose distance of 32 Å is moreover similar to the distance of the CH domains (30 Å) [221]. Later, Alushin *et al.* [222] detected that a small region on the Ndc80 CH domain, which they called the “toe”, is responsible for MT binding by recognizing a “toe print” between an α - and a β -tubulin in the MT lattice. The location of the toe print between two tubulin monomers can be the reason why Ndc80 complexes preferentially bind to straight protofilaments [131, 222].

At its very N-terminal end, the Ndc80 protein has an unstructured tail, which has a length of 80 amino acids in human cells [223] and is called *Ndc80 tail* or *N-terminal tail* in the following. The tail is highly positively charged and can be phosphorylated by Aurora kinases on several sites. Phosphorylation of the tail or introduction of negative charges reduces the binding affinity of the Ndc80 complex to a MT [111, 209–212] and the ability of this link to withstand high forces [59]. During prometaphase, the Ndc80 tails are phosphorylated by Aurora B at low inter-kinetochore tensions providing a mechanism to prevent erroneous attachments as described in Fig. 3.4. Moreover, modified binding affinities can explain the several effects discussed in Sec. 3.5 that the enforcement or the prevention of tail phosphorylation have on the dynamics of MTs and chromosomes and on the number of attached MTs per kinetochore during mitosis [111, 209–211].

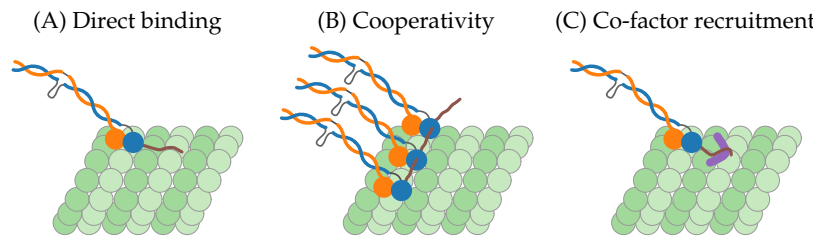
Since besides phosphorylation, also the total deletion of the Ndc80 tail reduces the binding affinity [212, 220], the tail obviously has a significant contribution to MT binding. However, the exact mechanism of this contribution is still unclear, and there are mainly three models [221, 223], which are sketched in Fig. 4.2. A first model proposes that the positively charged tails interact directly with the acidic tubulin tails or other negatively charged sites on the MT [221] based on the observation that even isolated Ndc80 tails are able to bind to a MT [224]. In a second approach, it was suggested that the Ndc80 tail generates cooperativity and clustering by interacting with adjacent Ndc80 complexes, i.e., the contribution of the tail is to increase the number of parallelly attached Ndc80 complexes [222, 225]. Finally, in a third model, the Ndc80 tail recruits co-factors that enhance Ndc80 binding, such as the Ska1 complex in Fig. 3.5 [132]. We note that the models are not exclusive but might coexist side by side to some extent. In all three models, phosphorylation reduces the binding affinity

³ Proteins are chains of amino acids. As sketched below (figure adapted from [215]), an amino acid contains an amino group at one end, a carboxyl group at the other end, and a side chain R. Within a protein, neighboring amino acids are connected by a peptide bond linking the amino and the carboxyl group. As a consequence, the polarity of a single amino acid is inherited by the protein, which therefore has a *N-terminal* end with an amino group and a *C-terminal* end exposing a carboxyl group. [1]



⁴ Calponin homology domains are part of several actin and MT binding proteins [218, 219].

Figure 4.2: Possible roles of the Ndc80 tail in MT binding. (A) The tail binds directly to the MT lattice. (B) The tail generates cooperativity by interacting with neighboring Ndc80 complexes. (C) The tail recruits co-factors.



by decreasing the positive charge of the Ndc80 tail and thereby weakening the electrostatic interaction to the tubulin, the adjacent Ndc80 complex or the co-factor [223]. Moreover, without positive charges, the tail might be able to prevent the CH domains from MT binding by blocking their positive binding sites [212, 221].

Besides the wild type Ndc80 complex ($Ndc80^{wt}$), three further variants, which are sketched in Fig. 4.3, were examined in the experiments that we reanalyze and model in the following two sections. In each of the variants, the MT binding N-terminal end of the Ndc80 subunit was modified in a different way: $Ndc80^{\Delta 80}$ is an Ndc80 complex, whose N-terminal tail is truncated; the mutated CH domain of $Ndc80^{CHmut}$ has a greatly reduced MT binding affinity; and the N-terminal tail of $Ndc80^P$ is phosphorylated.

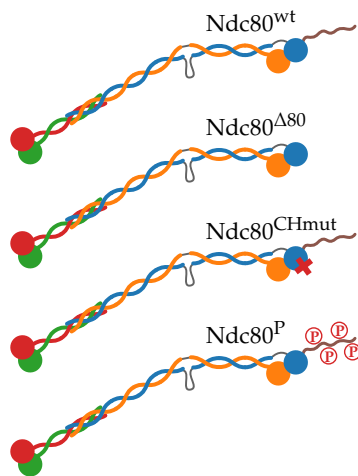


Figure 4.3: Ndc80 variants. In comparison to the wild type Ndc80 complex, $Ndc80^{\Delta 80}$ lacks the N-terminal tail, $Ndc80^{CHmut}$ has a blocked CH domain, and $Ndc80^P$ has a phosphorylated tail.

4.2 Strain stiffening in experiments

Since the essential task of the kinetochore and of the Ndc80 complexes in particular is to track the tip of a depolymerizing MT and to transmit forces to the connected chromatid, the tip-tracking abilities of bare Ndc80 complexes as well as more complex structures, both force-free and under an opposing force, have been subject of several *in vitro* studies [58, 59, 120, 128, 131, 134]. In one of these studies, Volkov, Huis in 't Veld *et al.* have found a first evidence for strain stiffening of the Ndc80 complexes, which emerged as a secondary result of their experiments [58]. In this section, we reanalyze these experiments with a stronger focus on the strain stiffening by means of a novel time-tracing analysis. We also include the data of a subsequent study with mutated Ndc80 complexes [59], which have not been evaluated with regard to the elastic properties so far. Before, we summarize the experiments and the original results as published in Refs. [58, 59] to illustrate the problems that require a novel approach to overcome.

4.2.1 Optical trap experiments

In a previous study, Powers *et al.* [120] examined the tip-tracking abilities of glass beads coated with Ndc80 complexes. They found a lower bound of Ndc80 density for a proper connection between

bead and MT, concluding that the attachment of multiple Ndc80 complexes is necessary to achieve tip-tracking. Concordantly, Schmidt *et al.* [131] reported that single Ndc80 complexes lack tip-tracking activity. To address these observations more systematically, Volkov, Huis in 't Veld *et al.* [58] constructed oligomerized Ndc80 complexes based on tetrameric scaffolds of traptavidin (T) and streptavidin (S).⁵ Since each S within such a scaffold is covalently bound to the Spc24 and Spc25 end domains of an Ndc80 complex, the constructed TS–Ndc80 modules allow for a controlled stoichiometry of Ndc80 complexes varying from $T_3S_1[Ndc80]_1$ to $T_0S_4[Ndc80]_4$, see Fig. 4.4.

Volkov, Huis in 't Veld *et al.* investigated the tip-tracking capabilities of Ndc80 oligomers in three steps. By tracing the interaction of bare TS–Ndc80 modules with depolymerizing MTs, they only observed tip-tracking activity for di-, tri- and tetramerized, but not for individual Ndc80 complexes. Moreover, tip-tracking of TS–Ndc80 assemblies became more robust with each additional Ndc80 complex.

The second step was to examine the ability of the Ndc80 oligomers to transport cargo during tip-tracking. To this end, small glass beads ($d = 1 \mu\text{m}$) were coated with the TS–Ndc80 modules via PLL–PEG. PLL–PEG consists of a poly-L-lysine (PLL) backbone and polyethylene glycol (PEG) side chains, see Fig. 4.5A. The PLL–PEG molecules used in the experiments contained PEG-2000,⁶ which consists of 45 C–C–O segments according to the manufacturer [226]. While the PLL backbone, which carries positive charges, is adsorbed on the negatively charged surface of the glass bead, the ends of the flexible PEG chains can bind the traptavidin of the TS scaffolds as sketched in Fig 4.5B. When the bead was densely coated, it was able to track the MT tip for any TS valency—including monomeric Ndc80—at least in a few cases. When the coating was so sparse, however, that there was only one TS–Ndc80 assembly in the proximity of the MT to connect it with the bead, tip-tracking could only be observed with trimeric Ndc80. These results reinforce the conclusion of Powers *et al.* [120] that multiple Ndc80 attachments are necessary for tip-tracking and, what is more, specify a lower bound of three Ndc80 complexes that should be able to interact with the MT.

Finally, Volkov, Huis in 't Veld *et al.* investigated to what extend the Ndc80–MT link can withstand opposing forces in an experimental setup as sketched in Fig. 4.6. The force was provided by an *optical trap*, in which the Ndc80-coated beads were captured during tip-tracking. When the bead is displaced from the rest position in the trap center ($x = 0$) by the depolymerizing MT, the trap exerts a restoring force F , which can be approximated by Hooke's law, $F = -c_{\text{trap}}x$, and thereby determined via the displacement x

⁵ The experiments and results presented in this section were performed and obtained by Vladimir Volkov, Pim Huis in 't Veld *et al.* [58, 59]. My contribution begins with the reanalysis of the original data in Secs. 4.2.2 ff.

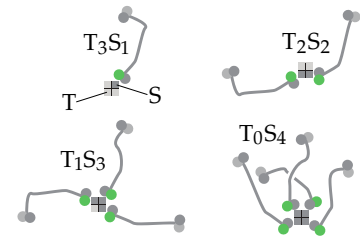


Figure 4.4: Ndc80 oligomers. Ndc80 complexes are oligomerized to n -mers on $T_{4-n}S_n$ scaffolds. Adapted from Volkov *et al.* [58], used under CC BY 4.0 license [94].

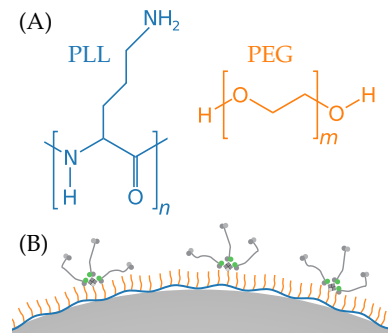


Figure 4.5: Bead preparation with PLL–PEG. (A) Structural formulas of PLL and PEG. (B) PLL is adsorbed on the glass bead and the PEG side chains can bind TS–Ndc80 modules.

⁶ PEG-2000 has a molecular mass of 2000 Da.

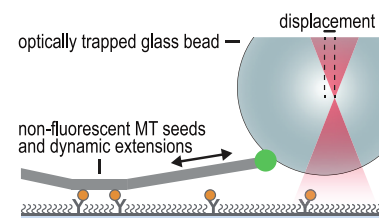
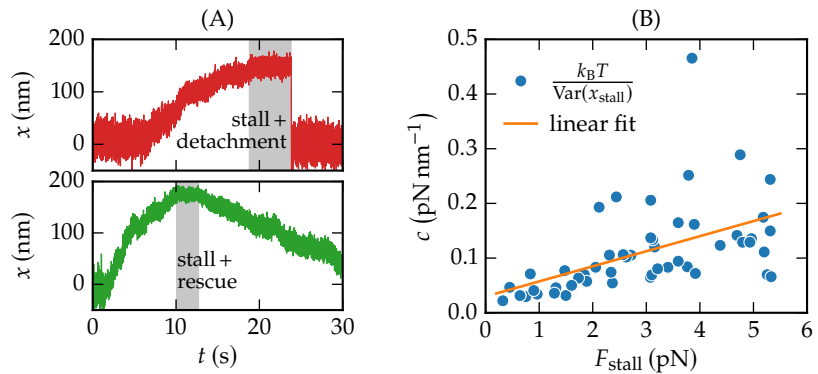


Figure 4.6: Setup of optical trap experiments. When the glass bead is displaced from the trap center by a depolymerizing MT whose seed is affixed to the coverslip, the trap exerts a force that opposes the displacement. Reproduced from Volkov *et al.* [58], used under CC BY 4.0 license [94].

Figure 4.7: Stiffnesses during MT stalls. (A) Bead displacements over time. When a bead is displaced from the trap center ($x = 0$) due to tip-tracking, the depolymerization can be stalled by the opposing force (gray). Stalls can be terminated either by detachment of the bead (top) or by a MT rescue (bottom). (B) Stiffness over stall force. During a stall, the stiffness can be determined by Eq. (4.1). The positive slope of the linear fit indicates strain stiffening.



if the *trap stiffness* c_{trap} is known [227]. The trap stiffness can be obtained from a sample path of a trapped bead that is not displaced by an external force and exhibits a Brownian motion around its equilibrium position in the trap center due to thermal fluctuations. A quite simple way is to apply the *equipartition theorem*, which predicts from the harmonic potential of the trap that, at temperature T ,⁷

$$c_{\text{trap}} = \frac{k_B T}{\text{Var}(x)}. \quad (4.1)$$

However, since the variance is sensitive to drift or any additional, for instance, electronic noise, the trap stiffness tends to be underestimated by the equipartition method [228–230]. In a more accurate and well-established method, which was also used by Volkov, Huis in 't Veld *et al.*, the trap stiffness is obtained from a Lorentzian fit to the *power spectral density* (PSD) of the sampled bead displacements [231–233]. The analysis of the whole spectral information makes the PSD method superior to the equipartition method.⁸

Fig. 4.7A shows two characteristic instances of trajectories of trapped beads tracking a depolymerizing MT. The displacement⁹ increases until the depolymerization force of the MT is counterbalanced by the restoring force of the trap so that the MT is *stalled*. The stall force correlated with the Ndc80 density on the bead for densities below 1000 trivalent TS–Ndc80 modules per bead, but stagnated for larger densities. Coating with monovalent Ndc80 complexes resulted in significantly lower stall forces. There are two ways a stall can end in, both of which were observed by Volkov, Huis in 't Veld *et al.*, see Fig. 4.7A: the bead either detached from the stalled MT and immediately snapped back to the rest position in the trap center, or, if the bead stayed attached for a sufficiently long time, the MT could be rescued, and the bead displacement relaxed gradually by tracing the now growing MT.

Since the mean displacement is constant during a stall, one can easily assign a stiffness to the system of MT, Ndc80 complexes

⁷ The experiments were performed at $k_B T = 4.1 \text{ pN nm} \sim 23.8 \text{ }^\circ\text{C}$.

⁸ See Appendix C.1 for more information about optical traps and stiffness calibration.

⁹ As sketched in Fig. 4.6, the bead displacement x was always measured as the horizontal (parallel to the coverslip) displacement in direction of MT depolymerization. Vertical displacements were not accounted for. Analogously, the force F denotes the horizontal force in direction of the displacement.

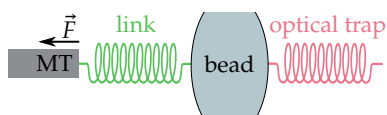


Figure 4.8: Elastic representation of the optical trap experiments. The corresponding setup is sketched in Fig. 4.6. Stiffness measurements always include the stiffnesses of the trap and the MT–bead link. A detailed model of the link is developed and discussed in Sec. 4.3, see Fig. 4.17.

and displaced bead by application of the equipartition method analogously to Eq. (4.1) with a variance that is determined over the duration of the stall. The results of this process, which are depicted in Fig. 4.7B as obtained by Volkov, Huis in 't Veld *et al.* [58], exhibit stiffnesses that increase with the applied stall force, giving a first evidence for strain stiffening. Since the bead is trapped throughout an experiment, the measurements do not solely represent the elasticity of the MT and the link between the bead and the MT, which is depicted as a green dot in Fig. 4.6, but also include the trap stiffness as illustrated in Fig. 4.8. However, the trap stiffness is constant in the examined force range in good approximation, and hence, the observed strain stiffening can be attributed to the MT and the MT-bead link. Within the link, there are several potentially elastic elements, whose contribution to the strain stiffening is discussed in Sec. 4.3 by means of an elastic model.¹⁰ In the current section 4.2, we concentrate on the stiffness measurements themselves.

The stiffness determination from the stalls as done by Volkov, Huis in 't Veld *et al.* has two shortcomings. The first one is that, as mentioned above, the stiffness tends to be underestimated by Eq. (4.1). In contrast to the calibration of the trap stiffness, this problem can not simply be eliminated by use of the more accurate PSD method, which relies on the assumption of a harmonic potential and, thus, can not be applied to a bead that is displaced by anharmonic MT depolymerization forces—in contrast to the equipartition method, which is valid for arbitrary potentials.¹¹ Therefore, a higher uncertainty is the cost we have to pay for the generality of the equipartition method, which allows us to determine anharmonic stiffnesses in the first place. The second shortcoming that should be addressed is the correlation of the stall force with the Ndc80 density on the bead, which does not let us determine whether the stiffening is an intrinsic property of the Ndc80 complex and/or the PF, or whether it arises from a higher number of parallelly attached Ndc80 complexes. We settle this issue in the following section by time-tracing the stiffness and uncovering strain stiffening throughout *single* experiments, i.e., while the Ndc80 density on the bead is constant.

The results of Volkov, Huis in 't Veld *et al.* presented so far were all obtained with wild type Ndc80 complexes [58]. In a subsequent study of the same authors [59], the experiments were repeated with the (trimerized) variants Ndc80^P and Ndc80^{Δ80}, which are sketched in Fig. 4.3. While the phosphorylation of the tail only reduced the duration of the stalls and the fraction of rescues but did not impede the tip-tracking per se, the tailless Ndc80^{Δ80} complexes were hardly able to trace a depolymerizing MT even without an opposing force. An evaluation regarding the stiffness is missing in the subsequent paper. We catch up on this by including the mutants

¹⁰ The elastic model is depicted in Fig. 4.17. The parts of the MT-bead link that are examined in Sec. 4.3 regarding their elastic properties are the Ndc80 complexes, the PLL-PEG and the curved PFs at the MT end. It turns out that Ndc80 complexes exhibit strain stiffening as a consequence of their structure and that the PFs are only relevant if their curved part is sufficiently long while a contribution of PLL-PEG can be omitted.

¹¹ The theoretical framework of the PSD method, which is presented in Appendix C.1, starts from the Langevin equation of a Brownian particle in a harmonic potential. The generality of the equipartition method can be shown by considering an object that is deflected by an external force F in an arbitrary potential $U(x)$. At temperature T , the canonical partition function reads as ($\beta = 1/k_B T$):

$$Z \sim \int dx e^{-\beta(U(x)-Fx)}.$$

The moments of the extension x can be deduced from Z by

$$\langle x^n \rangle = \frac{1}{\beta^n} \frac{\partial_F^n Z}{Z}.$$

Hence, the mean extension and the variance are

$$\begin{aligned} \langle x \rangle &= \frac{1}{\beta} \frac{\partial_F Z}{Z} = \frac{1}{\beta} \partial_F \log Z, \\ \text{Var}(x) &= \langle x^2 \rangle - \langle x \rangle^2 = \frac{1}{\beta} \partial_F \langle x \rangle. \end{aligned}$$

Defining the stiffness as $c = \partial F / \partial \langle x \rangle$, the last equation is equivalent to the equipartition method as given in Eq. (4.1). We note that this is a *thermodynamic* stiffness, which also contains entropic contributions and therefore differs from the purely *mechanical* stiffness given by $\partial_x^2 U(x)$ if the potential is anharmonic.

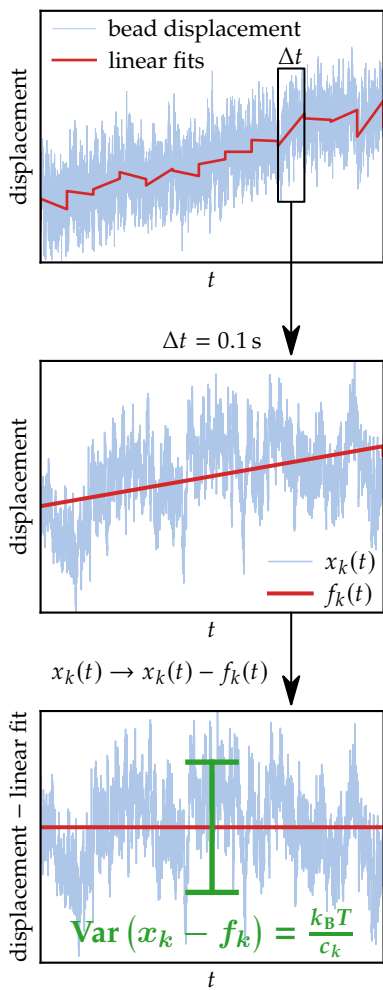


Figure 4.9: Stiffness time-tracing. The signal is divided into intervals of $\Delta t = 0.1$ s, which gives 1000 data points per interval at a sampling rate of 10 kHz. For each interval k , we estimate the evolution of the equilibrium bead position with a linear fit $f_k(t)$. The stiffness of an interval is then given by Eq. (4.2), where the variance equals the mean squared distance of the bead position $x_k(t)$ from the estimated equilibrium $f_k(t)$.

¹² Twelve additional examples are shown in Appendix C.2.

into our reanalysis in the following sections. Moreover, besides Ndc80^{wt} , Ndc80^{P} and $\text{Ndc80}^{\Delta 80}$, we evaluate new experimental data of another mutant, $\text{Ndc80}^{\text{CHmut}}$, which were also recorded by Volkov, Huis in 't Veld *et al.* but have not yet been published elsewhere.

4.2.2 Time-tracing reveals strain stiffening in single experiments

As long as the mean bead position is stationary, e.g., during MT stall, the effective stiffness can be easily calculated from the variance of the bead position x by $k_{\text{B}}T/\text{Var}(x)$. We now present a method that enables us to monitor the stiffness over time, i.e., also during polymerization and depolymerization of the MT, and to observe strain stiffening of the Ndc80 complex in the course of a single experiment. We divide the signal into several intervals k of a certain length Δt for each of which we determine a stiffness as sketched in Fig. 4.9. For that purpose, we do not use the variance over that interval but the mean squared distance from a quasi-equilibrium bead position, which may slowly vary over time. We estimate the drift of the quasi-equilibrium bead position with a linear fit $f_k(t)$ to the entire time-trace $x_k(t)$ in an interval k . Then, the effective stiffness during the interval k is given by the inverse of the mean-square distance:

$$c_k = \frac{k_{\text{B}}T}{\langle (x_k(t) - f_k(t))^2 \rangle}. \quad (4.2)$$

Finally, we can assign a force F_k on the Ndc80 link to each interval, which can be calculated from the trap stiffness and the mean bead position during that interval, $F_k = c_{\text{trap}} \langle x_k \rangle$.

The time interval Δt should be sufficiently small to really describe a local stiffness, but at the same time should cover enough independent displacement measurements for a trustful variance determination. Typical autocorrelation times are $\gamma/c \sim 0.1\text{--}1$ ms, where γ is the friction coefficient and c the stiffness. For our experiments, $\Delta t = 0.1$ s has proven to be a good choice, which results in 100–1000 independent values within each interval.

The results of the time-tracing analysis are shown in Fig. 4.10 for four representative examples for the four Ndc80 variants Ndc80^{wt} , Ndc80^{P} , $\text{Ndc80}^{\Delta 80}$ and $\text{Ndc80}^{\text{CHmut}}$.¹² For each of the Ndc80 variants, there are experiments in which we detect a smooth stiffening behavior when the tension increases, but there are also experiments that do not exhibit any stiffening at all as in Fig. 4.10D. Based on previously observed absence of stiffening during lateral bead–MT attachment [58], we interpret experiments without stiffening as

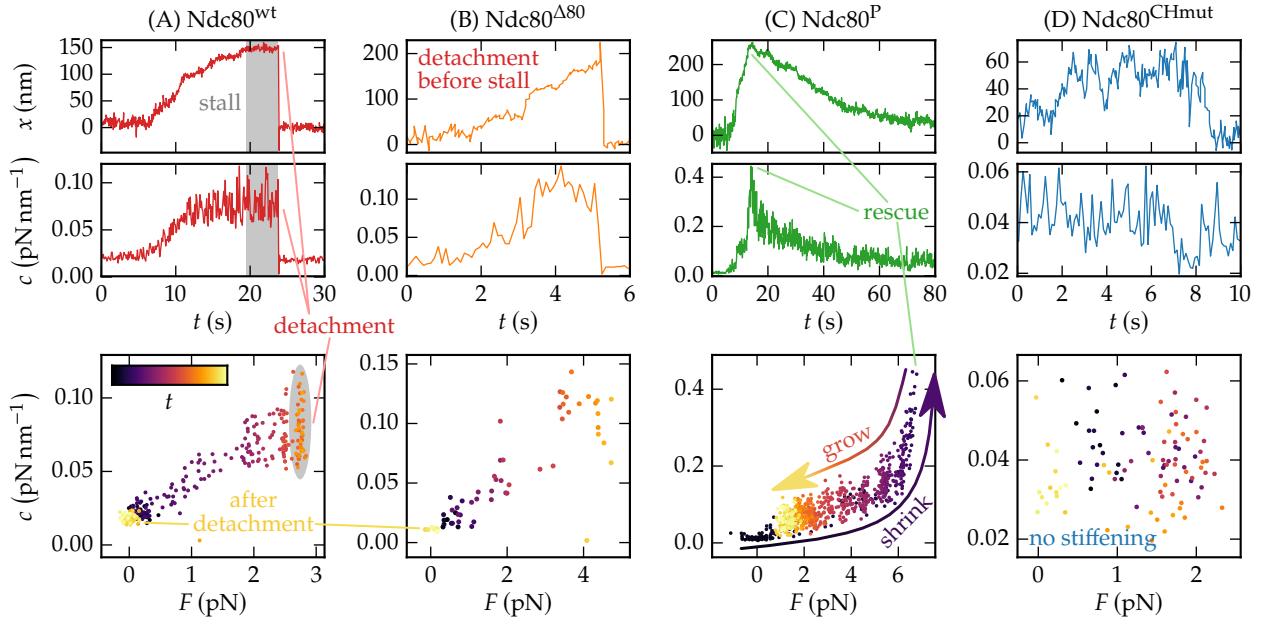


Figure 4.10: Strain stiffening in single experiments. Four representatives of typical experiments are shown. More examples can be found in Appendix C.2. For each experiment, the upper two plots show the piecewise linearized bead position and the stiffness over time while the stiffness–force relation is depicted in the bottom plot, where time is represented by the color gradient. When the force is increased due to the shrinking MT, we observe stiffening in most experiments (A–C). Shrinking usually is followed by a stall phase with constant force and constant stiffness (gray), except for experiments with $\text{Ndc80}^{\Delta 80}$ and $\text{Ndc80}^{\text{CHmut}}$, where the bead often detaches before reaching the stall force (B). The stall is terminated either by detachment (A) or by MT rescue (C). After detachment, the bead snaps back to the trap center ($x = 0$), and we measure the trap stiffness c_{trap} . In case of a rescue, the bead stays attached to the polymerizing MT and the tension decreases until the MT undergoes a catastrophe and starts depolymerizing again.

laterally attached and exclude them from the following analyses. We note that our main results and conclusions that we derive in the following remain unchanged if the experiments without stiffening are not excluded as these experiments exhibited comparably short durations of bead–MT attachment. Experiments with observed stiffening are interpreted as resulting from an end-on attachment¹³ and analyzed further. Stiffening was observed in 32 of 48 experiments with Ndc80^{wt} , 8/24 with $\text{Ndc80}^{\Delta 80}$, 12/32 with $\text{Ndc80}^{\text{CHmut}}$, and 14/29 with Ndc80^{P} .

In the experiments that exhibited stiffening, the MT depolymerization typically stalled at some force for Ndc80^{wt} and Ndc80^{P} , but not for $\text{Ndc80}^{\Delta 80}$ and $\text{Ndc80}^{\text{CHmut}}$, where the bead often detached before it could stall the MT, see Fig. 4.10B, and the stalls that occurred were shorter [59]. This indicates that the detachment force for $\text{Ndc80}^{\Delta 80}$ and $\text{Ndc80}^{\text{CHmut}}$ is usually below the MT stall force under the experimental conditions applied. Therefore, a systematic analysis of these mutants is only enabled by time-tracing of the stiffness prior to detachment as measurements in a stalled state are rarely possible. The decrease in detachment force also confirms that the combination of the tail and the CH domain is essential for force-resisting attachment [59].

A stall can be interrupted in two possible ways: either the bead detaches from the MT (Fig. 4.10A), or MT growth is rescued (Fig. 4.10C). In the first case, the bead snaps back immediately to the equilibrium position of the optical trap, and the measured stiffness is the trap stiffness c_{trap} . In case of a rescue, the bead stays attached to the polymerizing MT and the tension decreases until the MT undergoes a catastrophe and starts depolymerizing again.

¹³ Such an end-on attachment is sketched in Fig. 3.5 and below in Fig. 4.17A

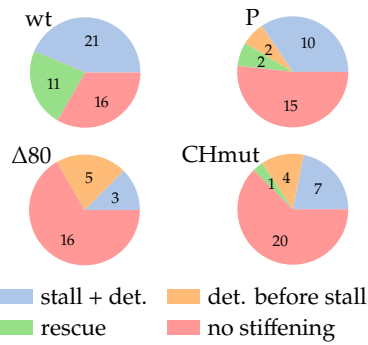


Figure 4.11: Prevalences of the typical events. The pie charts show how frequently the typical events described in Fig. 4.10 occurred for each Ndc80 variant.

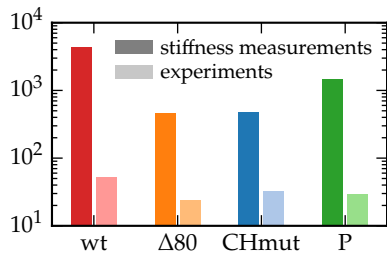


Figure 4.12: Amount of stiffness data. While only one stiffness per experiment can be obtained by the sole use of the stalls (right bars), time-tracing increases the amount of data by 1 to 2 orders of magnitude (left bars).

¹⁴ Bead displacement was determined via a linear conversion from the quadrant photo-detector (QPD) voltage [58]. However, the relation between QPD voltage and bead displacement was only linear within 200 nm from the trap center. Outside this range, the bead displacement and thus the force are underestimated by the linear conversion. This explains the steep ascent in the stiffness–force relation that can be observed in some experiments for large forces, for instance, in Fig. 4.10C for $F > 6$ pN.

¹⁵ While a least squares fit, which minimizes the sum of the squared residuals ϵ_i , is sensitive to outliers, the robust regression method that we use reduces this sensitivity by minimizing the sum of the Huber loss functions

$$\rho(\epsilon_i) = \begin{cases} \frac{1}{2}\epsilon_i^2, & |\epsilon_i| < k \\ k|\epsilon_i| - \frac{1}{2}k^2, & |\epsilon_i| \geq k \end{cases}$$

See Appendix C.3 for more information.

This allows us to investigate stiffening of the Ndc80 complexes in dependence of the dynamic state of the MT in Sec. 4.2.4. Almost all of the typical behaviors that are described above and in Fig. 4.10 can be observed for each in Ndc80 variant but with different frequencies as summarized in Fig. 4.11.

4.2.3 Collective analysis of the stiffening behavior

Another advantage of our time-tracing method is that we generate many more data points from the same number of experiments. While, for example, 53 stiffnesses of Ndc80^{wt} were determined in Ref. [58] from stalling MTs, time-tracing generates 4403 stiffnesses from the same experiments. Also for Ndc80^P, Ndc80^{Δ80} and Ndc80^{CHmut}, we increase the amount of data by 1 to 2 orders of magnitude as compared with just determining a single stiffness for each stall, see Fig. 4.12.

In the following, we utilize the newly generated data to analyze the individual experiments of each Ndc80 variant *collectively*. In doing so, we exclude the stiffness values that correspond to bead positions larger than 200 nm since, here, the determination of bead displacement becomes inaccurate.¹⁴ Fig. 4.13 shows the stiffnesses that were determined from time-tracing the individual experiments in a single plot for each Ndc80 variant. As compared to the sole use of the stalls in the case of Ndc80^{wt}, the new results reveal the strain stiffening more clearly and allow for a more thorough analysis and interpretation.

In order to further characterize the strain stiffening, we fit power law functions $c(F) = AF^m + c_0$ to the cumulated time-traced data in Fig. 4.13 by use of a robust regression minimizing the Huber loss¹⁵ [234, 235]. The exponent m characterizes the observed strain stiffening behavior. We account for the trap stiffness by the offset c_0 for which the fits yield results that, indeed, lie in a range from 0.01 pN nm⁻¹ to 0.025 pN nm⁻¹, see Tab. 4.1, which is in accordance with the trap stiffnesses determined during calibration. While the stiffnesses exhibit a linear dependence on force with exponents m around unity for Ndc80^{wt} and Ndc80^P, the stiffness–force relations of Ndc80^{Δ80} and Ndc80^{CHmut} have a roughly parabolic shape ($m \approx 2$). We note that for Ndc80^{Δ80} and Ndc80^{CHmut}, there are few data for high forces, making the stiffening exponents less reliable.

The stiffening exponents determined in Fig. 4.13 are the result of a fit to the combined data from several experiments, and may be biased by the correlation between the stall force and the Ndc80 densities on the bead. Our new time-tracing analysis, however, dampens this bias compared to the sole analysis of the stalls as stiffnesses

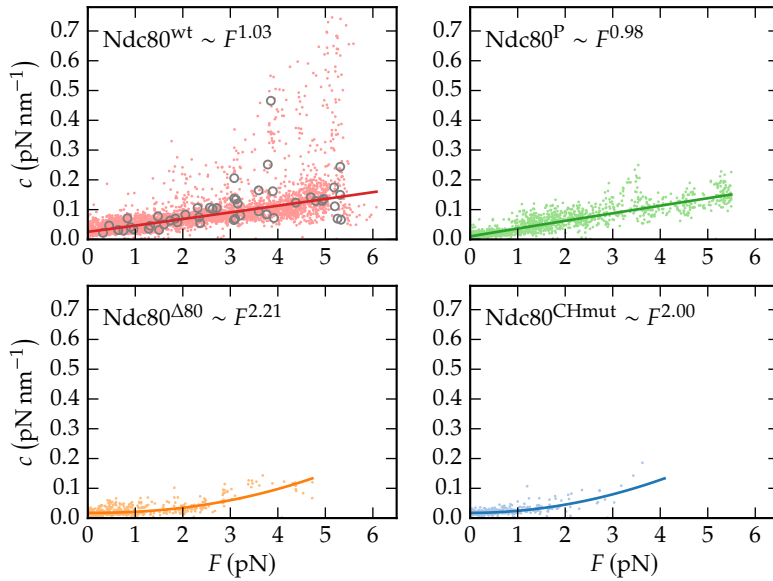


Figure 4.13: Collective analysis via robust power fits. The combined stiffness data from all experiments is cumulated in one plot (dots) for each Ndc80 variant. For Ndc80^{wt}, it can be compared with the stiffnesses as determined by Volkov *et al.* [58] from the MT stalls (gray circles). The lines show robust power fits $c(F) = AF^m + c_0$ to the combined data, where the offset c_0 should respect the trap stiffness. The corresponding fit parameters are listed in Tab. 4.1.

are determined for small forces but at high Ndc80 densities during MT depolymerization in the respective experiments. We also apply the power law regressions to the stiffness–force relations of single experiments. Then, we find most stiffening exponents in a range between 0.5 and 2, but also detect outliers below this range and close to 4, see Fig. 4.14.

For a better visibility and comparability of the strain stiffening of the different Ndc80 variants, we summarize the stiffness measurements in Fig. 4.15A by binning the time-traced stiffnesses of all experiments in bins of 1 pN width and averaging force and stiffness in each of these bins. We find that all variant Ndc80 complexes exhibit similar strain stiffening. The direct comparison in Fig. 4.15B shows that both truncating the tail or modifying the CH domain slightly decrease the stiffness compared to the wild type, especially for small forces, which is where the Ndc80^{Δ80} and Ndc80^{CHmut} data is most reliable according to the number of accumulated stiffness values. This indicates that in all four Ndc80 variants, the remaining intact common parts play a central role in strain stiffening. Differences between variants are due to changes in the Ndc80–MT bond and are addressed in the discussion in Sec. 4.4.

4.2.4 Independence from MT state

When a MT is rescued after the stall, as in the experiment depicted in Fig. 4.10C, the time-traced stiffness follows the same stiffness–force relation in the shrinking and growing states before and after rescue, respectively. The same observation can be made in experiments with several consecutive rescues and catastrophes. This indicates that the stiffness is independent of the MT state,

Table 4.1: Fit parameters of the robust power fits $c(F) = AF^m + c_0$ depicted in Fig. 4.13. The offset c_0 is given in units of pN nm^{-1} , the coefficient A in units of $\text{pN}^{1-m} \text{nm}^{-1}$.

	A	m	c_0
wt	0.022	1.03	0.025
P	0.027	0.98	0.010
Δ80	0.0038	2.21	0.017
CHmut	0.0069	2.00	0.017

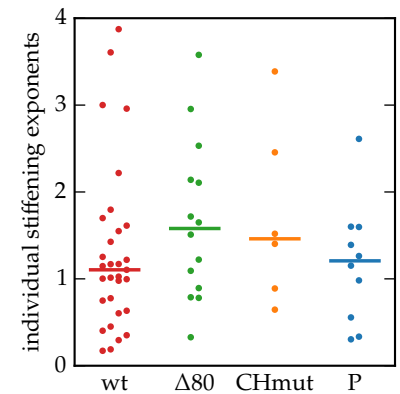


Figure 4.14: Stiffening exponents in individual experiments. The depicted stiffening exponents m result from applying robust power fits to those individual experiments where a proper stiffening is recognizable and the bead was attached to the MT for at least 1 s so that there are ≥ 10 data points to fit to. The horizontal bars mark the medians.

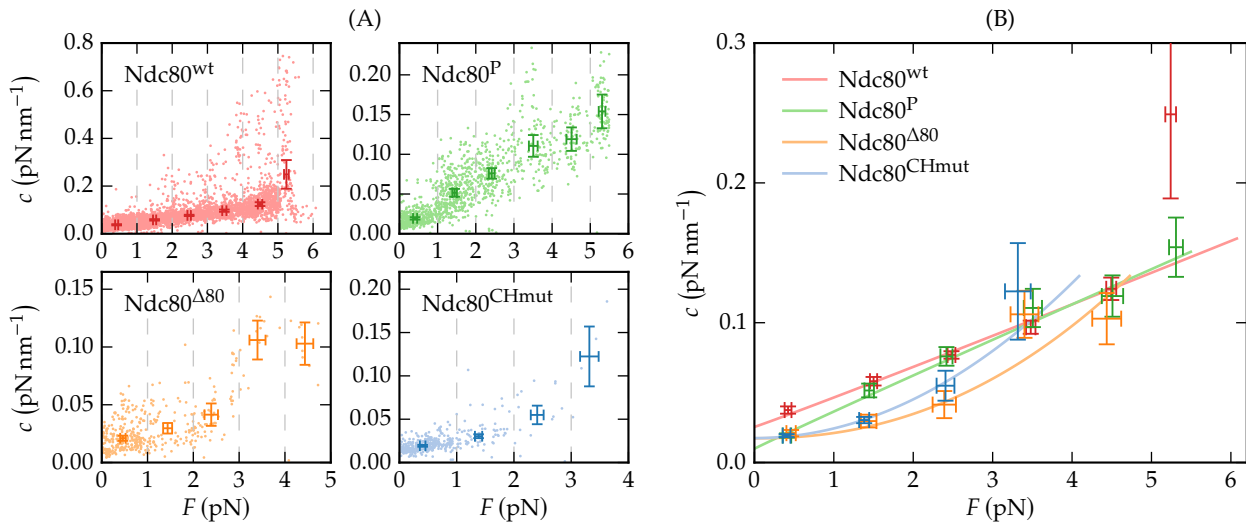
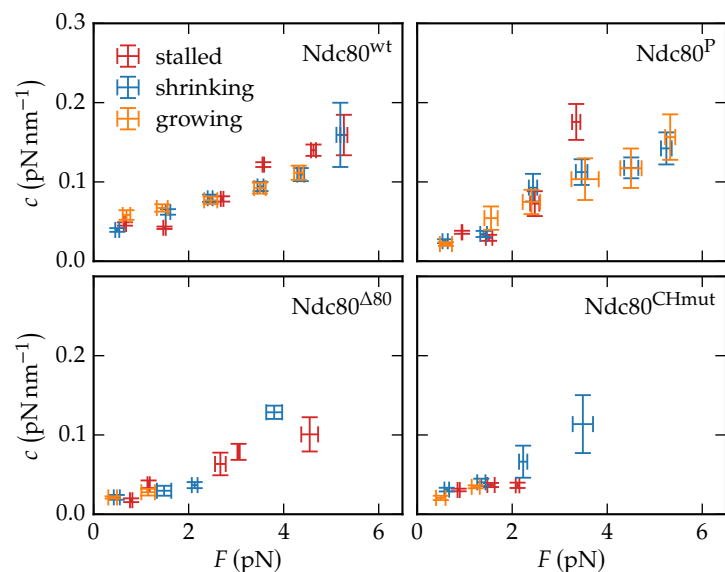


Figure 4.15: Summarized stiffness-force relations. (A) The force axis is divided into bins of 1 pN width, and the cumulated stiffnesses and the forces within each bin are averaged. The error bars represent the standard deviation of the mean in F and in c of the points within each bin, where each experiment is considered as an independent event. (B) Direct comparison of $Ndc80^{wt}$, $Ndc80^P$, $Ndc80^{\Delta 80}$ and $Ndc80^{CHmut}$. The lines show the power fits from Fig. 4.13.

i.e., on whether the Ndc80 complexes are attached to a shrinking, stalled or growing MT. To address this question systematically, we identify the phases of shrinking, stalled and growing MTs in the individual experiments and bin the stiffnesses analogously to Fig. 4.15A but separately for each of the three MT states. The results in Fig. 4.16 do not show a significant dependence on the MT state for any of the four Ndc80 variants. From the elements in the experiment that can be thought to exhibit an effective elasticity, the curved ends of the PFs are the ones that are directly correlated with the MT state. Therefore, we draw two possible conclusions from the observed independence from MT state: either the PFs do not contribute to the total stiffness, or, if they do contribute, their mechanical properties do not depend on whether the MT is growing or shrinking. The contribution of the PFs is one of the questions that we try to answer with a theoretical model in the following section.

Figure 4.16: Independence from MT state. The stiffnesses are evaluated separately for stalled, shrinking and growing MTs, and then summarized bin-wise as described in Fig. 4.15A.



4.3 Strain stiffening explained by Ndc80 and microtubule structure

While the time-tracing analysis presented in the previous section revealed strain stiffening in single experiments, accumulated extensive stiffness data, and allowed for a deeper analysis, the new results raised further questions, which we try to answer in the following by means of an elastic model. The model is based on the structure of the involved components that can be found between the coverslip and the glass bead. In particular, our aims are to reproduce the strain stiffening at least in a qualitative manner, i.e., in terms of the stiffening exponent m ; to clarify the contribution of the PF to the measured stiffness; and to provide an explanation for the observation that the stiffness of Ndc80^{wt} exceeds those of Ndc80^{Δ80} and Ndc80^{CHmut}.

Before modeling the results of the stiffness measurements, we have to identify the elastic elements that contribute to the total stiffness as sketched in Fig. 4.17. The stiffness of the optical trap is always present in the measurements. Its value was determined during the calibration of the optical trap after the bead detached from the MT. Further potentially elastic elements are located between the bead and the MT seed that is fixed on the coverslip. This is on the one hand the MT, which can be thought of to exhibit both a mechanical (due to stretching or bending) and an entropic stiffness (due to thermal fluctuations). On the other hand, the link between the MT and the bead probably has elastic properties. We attribute the elasticity of the link to its four constituents: first, the Ndc80 complex can act as an entropic spring with stiffness c_{Ndc} due to its flexible kink; secondly, stretching the flaring ends of the PFs at the MT tip out of their preferred curvature may produce an effective stiffness c_{PF} for pulling in the axial direction of the MT; thirdly, also the bond between the Ndc80 trimer and the MT may exhibit some effective elasticity c_{bond} , e.g., as a consequence of unbinding and rebinding of individual Ndc80 units; and finally, the PLL-PEG that connects the Ndc80 complexes with the bead should be taken into account as another elastic element between the bead and the MT, generating a fourth stiffness c_{PEG} .

Each of these four stiffnesses may depend on the applied force and exhibit strain stiffening itself. Since the four elements are aligned in series, their inverse stiffnesses sum up to the inverse linker stiffness \tilde{c}^{-1} :

$$\tilde{c}(F) = \left(\frac{1}{c_{\text{PEG}}(F)} + \frac{1}{c_{\text{Ndc}}(F)} + \frac{1}{c_{\text{bond}}(F)} + \frac{1}{c_{\text{PF}}(F)} \right)^{-1}. \quad (4.3)$$

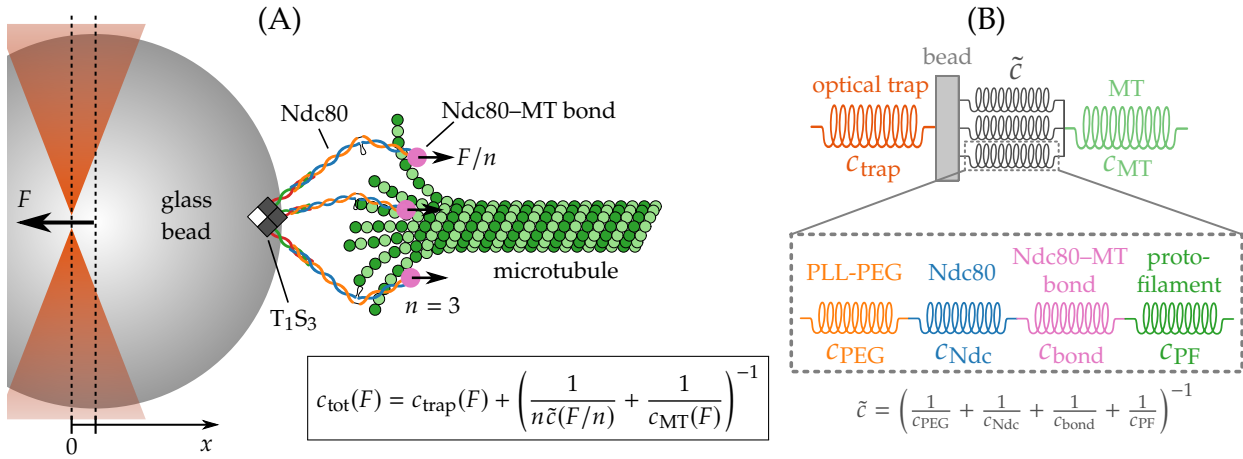


Figure 4.17: Elastic model of the optical trap experiments. (A) Sketch of the experiment (not true to scale) with $n = 3$ attached Ndc80 complexes. We assume that each Ndc80 complex is exposed to the same force F/n . (B) Spring model. Between the bead and the MT, there are four potentially elastic objects, which are aligned in series: the PLL-PEG, the Ndc80 complex, the Ndc80-MT bond and the curved PF. When n Ndc80 complexes are attached to the MT, n of those serial combinations act as parallel springs.

It is important to note that this reduces the total stiffness and that the softest elastic element dominates the total stiffness.

It is possible that multiple Ndc80 complexes are attached parallelly to the MT. For the sake of simplicity, we always assume that each PF can only attach one Ndc80 complex and that the parallel PFs and Ndc80 complexes have the same elongation, respectively. Then, the force F is shared equally between the parallel Ndc80-PF units with stiffness $\tilde{c}(F)$ so that the total linker stiffness that results from n parallelly attached Ndc80 complexes can be written as

$$\tilde{c}_n(F) = n \tilde{c}\left(\frac{F}{n}\right). \quad (4.4)$$

Although parallel stiffnesses add up, the shared force can give rise to an overall reduction $\tilde{c}_n(F) < \tilde{c}(F)$ of the cooperative stiffness if the individual stiffness exhibits strain stiffening $c(F) \propto F^m$ with an exponent $m > 1$.¹⁶ We find below that such strain stiffening behavior is realized both for the Ndc80 and the PF stiffness.

The n parallel linkers \tilde{c} are in series with a single MT with stiffness c_{MT} while the optical trap, whose force is applied on the bead from the opposite side, acts as a parallel spring, see Fig. 4.17. This results in a total stiffness

$$c_{\text{tot}}(F) = c_{\text{trap}}(F) + \left(\frac{1}{n\tilde{c}(F/n)} + \frac{1}{c_{\text{MT}}(F)} \right)^{-1}. \quad (4.5)$$

We note that the force dependence of the trap stiffness is negligible in the examined force ranges so that we can assume $c_{\text{trap}}(F) = \text{const}$ in the following.

The bond between individual Ndc80 complexes and the MT is established by the globular regions at the N-terminal of the complex [191, 220, 221] via calponin homology (CH) domains [222]. Also the N-terminal tail of the Ndc80 subunit is probably involved in

¹⁶ Mathematically, the cooperative stiffness is decreased by adding parallel elements if the derivative of \tilde{c}_n with respect to n is negative:

$$\frac{\partial \tilde{c}_n(F)}{\partial n} = \tilde{c}\left(\frac{F}{n}\right) - \frac{F}{n} \tilde{c}'\left(\frac{F}{n}\right) < 0.$$

The relation $f(x) < x f'(x)$ requires the function f to be convex if $f(x) > 0$, i.e., the strain stiffening of the individual stiffness $c(F)$ has to be superlinear.

MT binding [236, 237]. The effective stiffness of the Ndc80–MT bond is hard to model because the exact binding mechanism to the MT is still elusive. Since the Ndc80 CH domain and the N-terminal tail are relevant for binding to the MT, investigation of the stiffness changes for mutants Ndc80^{Δ80} and Ndc80^{CHmut} as compared to the wild type Ndc80^{w^t} allows us to address this issue in the discussion in Sec. 4.4. Regarding the linker stiffness \tilde{c} , we concentrate on the contributions of the Ndc80 complex itself, the PF and the PLL-PEG in the following.

4.3.1 Stiffness of PLL-PEG

We start our analysis with the PLL-PEG linkage to the bead, whose contribution to the measured stiffnesses should be clarified in addition to those from the Ndc80 complex or the PF. As written above and sketched in Fig. 4.5, PLL-PEG consists of a PLL backbone, which is adsorbed on the glass bead, and flexible PEG side chains, which can bind the Ndc80 oligomers.

Pasche *et al.* [238] examined the elastic properties of PLL with an atomic force microscope (AFM). The PLL was adsorbed on a flat Nb₂O₅ surface in these experiments, i.e., in a similar arrangement as the PLL on the glass bead during the optical trap experiments. From the slope of the force–extension curves that Pasche *et al.* have measured, the stiffness of PLL can be estimated as ~ 100 pN nm⁻¹, which is three orders of magnitude above the stiffnesses that we determined in the previous section. Therefore, a significant contribution of the PLL can be neglected.

The stiffness of the PEG side chains can be estimated on the basis of the extended freely jointed chain (FJC)¹⁷ model by which Oesterhelt *et al.* [239] successfully reproduced the extension–force relations measured in single molecule AFM experiments with PEG. Since the C–C–O segments of PEG that is dissolved in water undergo a conformational transition from a helical to a planar structure when tension is applied, the model includes two distinct segment lengths, one for each of the conformations. Assuming a Boltzmann distributed ratio of helical and planar segments, the authors obtained a contour length $L_C(F)$ that depends on the applied force.¹⁸ We derive the PEG stiffness c_{PEG} from the extension–force relation $L(F)$ that is given in Ref. [239]:¹⁹

$$L(F) = L_C(F) \left(\coth(\beta FL_K) - \frac{1}{\beta FL_K} \right) + N_S \frac{F}{K_S}, \quad (4.6)$$

$$c_{\text{PEG}}(F) = \left(\frac{dL(F)}{dF} \right)^{-1}. \quad (4.7)$$

¹⁷ The FJC, also known as ideal chain, is a polymer model consisting of a chain of stiff bonds with totally flexible hinges, thereby modeling the polymer as a random walk.

¹⁸ From the N_S C–C–O segments, let N_{hel} be in the helical conformation with length L_{hel} , and N_{pl} segments in the planar conformation with length L_{pl} . Assuming a Boltzmann distribution,

$$\frac{N_{\text{hel}}}{N_{\text{pl}}} = e^{\beta \Delta G(F)},$$

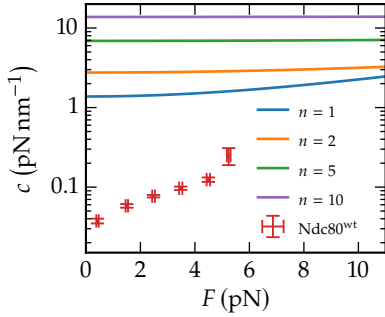
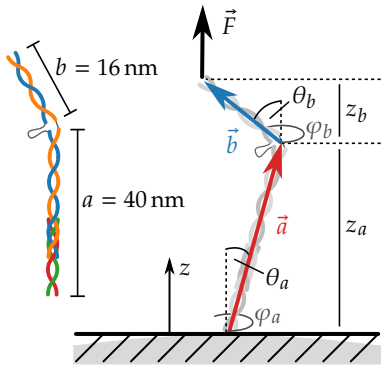
where $\Delta G(F) = \Delta G_0 - F(L_{\text{pl}} - L_{\text{hel}})$ is the free energy difference, the force dependent contour length is given by

$$\begin{aligned} L_C(F) &= N_{\text{pl}} L_{\text{pl}} + N_{\text{hel}} L_{\text{hel}} \\ &= N_S \left(\frac{L_{\text{pl}}}{e^{\beta \Delta G(F)} + 1} + \frac{L_{\text{hel}}}{e^{-\beta \Delta G(F)} + 1} \right). \end{aligned}$$

¹⁹ L denotes the extension in force direction. At low forces, the PEG molecule exhibits an entropic elasticity as described by the first term in Eq. (4.6), which is (except for the force dependence of L_C) the well-known result for a FJC with contour length L_C and Kuhn length L_K that is stretched by a force F [240]. At high forces, on the other hand, the segments themselves are stretched, and the behavior is dominated by the segment elasticity K_S .

Table 4.2: Parameters of the extended FJC model for the PEG stiffness [239].

Description	Symbol	Value
Number of segments	N_S	45
Segment length of the planar conformation	L_{pl}	0.358 nm
Segment length of the helical conformation	L_{hel}	0.28 nm
Kuhn length	L_K	0.7 nm
Zero force free energy difference ($G_{pl} - G_{hel}$)	ΔG_0	$3 k_B T$
Segment elasticity	K_S	150 N m^{-1}
Thermal energy ($\beta = 1/k_B T$)	$k_B T$	4.1 pN nm

**Figure 4.18: PEG stiffness.** The stiffness of n parallel PEG molecules ($nc_{PEG}(F/n)$, colored lines) is more than a factor 10 larger than the measured stiffness of Ndc80^{wt}.**Figure 4.19: Ndc80 complex as entropic spring.** We model the Ndc80 complex as a freely jointed chain with two bonds \vec{a} and \vec{b} , which have the different lengths a and b . The long arm \vec{a} is bound to the glass bead, the short arm \vec{b} to the MT, which applies a force $\vec{F} = F\vec{e}_z$. The glass bead is approximated as a plane surface.

²⁰ Here, the z -coordinate corresponds to the x -direction in Fig. 4.17. This conversion simplifies the following calculations using common spherical coordinates.

Using the parameters from Tab. 4.2, which are taken from Ref. [239] except for the number of segments N_S , which is adapted to the PEG-2000 used in the experiments, we obtain a force-free stiffness of 1.38 pN nm^{-1} , which increases very slowly under tension, see Fig. 4.18. This exceeds the typical MT-Ndc80 stiffnesses determined in the experiments by a factor above 10, and, according to Eq. (4.4), this factor even increases in the examined force range when multiple PEG molecules are arranged in parallel.

We conclude that both the PLL backbone and the PEG chains are too stiff to make a significant contribution to the measured stiffness since $c_{PEG}(F) \gg \check{c}(F)$ in Eq. (4.3). Moreover, the slope of c_{PEG} is too small to be compatible with the experimentally observed strain stiffening so that, after all, the PLL-PEG can be omitted in the following analysis and the experimental results indeed are suitable to obtain information about the elasticity of the Ndc80-MT link.

4.3.2 Stiffness of the Ndc80 complex

After excluding a significant influence of the PLL-PEG, we next include the remaining elements (Ndc80 complex, MT, PF) step by step to discuss their relevance for the observed strain stiffening. We start our analysis with the Ndc80 complex, which is, due to its flexible structure and its force transmitting role in the mitotic spindle, the most promising and probably most interesting candidate.

In order to model the stiffness of the Ndc80 complex under force, we use a simple polymer model that is based on the known structure depicted in Fig. 4.1 with two stiff arms of lengths $a = 40 \text{ nm}$ and $b = 16 \text{ nm}$ that are flexibly connected [191, 192]. In the cell, the long arm is bound to the kinetochore, in the experiment it is bound to the glass bead while the short arm can be attached to a MT. We describe the conformation of the two arms by two vectors \vec{a} and \vec{b} in spherical coordinates as shown in Fig. 4.19:²⁰

$$\vec{a} = a \begin{pmatrix} \sin \theta_a \cos \varphi_a \\ \sin \theta_a \sin \varphi_a \\ \cos \theta_a \end{pmatrix}, \quad \vec{b} = b \begin{pmatrix} \sin \theta_b \cos \varphi_b \\ \sin \theta_b \sin \varphi_b \\ \cos \theta_b \end{pmatrix}. \quad (4.8)$$

The impenetrable glass bead restricts these two vectors in the experiment. Since the diameter of the glass bead (1 μm) is much larger than the Ndc80 complex, we approximate the bead as a plane surface that confines the Ndc80 complex to the upper half space so that $z_a > 0$ and $z = z_a + z_b > 0$, see Fig. 4.19. Experiments have shown that the two arms are connected flexibly within an angular range between 0° and 120° [192].²¹ Since we want to model the Ndc80 complex while it is confined by the glass bead and under the influence of an external stretching force that is applied in z -direction and favors small angles, we can neglect the constraint to angles below 120° . This allows us to perform an explicit analytical calculation as we reduce the Ndc80 complex to a purely entropic FJC with two bonds of different lengths. The only energy is the stretching energy from a constant external force $\vec{F} = F \vec{e}_z$ in positive z -direction,

$$\begin{aligned} E_{\text{FJC}} &= -\vec{F} \cdot (\vec{a} + \vec{b}) = -F(z_a + z_b) \\ &= -F(a \cos \theta_a + b \cos \theta_b). \end{aligned} \quad (4.9)$$

Respecting the confinement to the upper half-space, we obtain the canonical partition function:²²

$$\begin{aligned} Z(F) &= \iint_{z_a, z_b > 0} d\theta_a \sin \theta_a d\theta_b \sin \theta_b e^{-\beta E_{\text{FJC}}} \\ &= \int_0^a \frac{dz_a}{a} e^{\beta F z_a} \int_{-\min(z_a, b)}^b \frac{dz_b}{b} e^{\beta F z_b} \\ &= \frac{2e^{\beta F a} \sinh \beta F b - e^{\beta F b} - \beta F b + 1}{(\beta F)^2 a b}. \end{aligned} \quad (4.10)$$

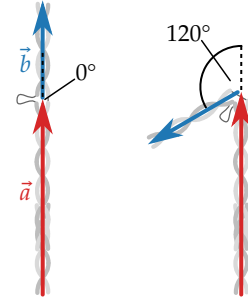
Both the extension–force relation $z(F)$ and the stiffness–force relation $c_{\text{Ndc}}(F)$ in the presence of thermal fluctuations can be obtained from derivatives of the partition function with respect to the force:

$$z(F) = \langle z \rangle = \frac{1}{\beta} \partial_F \ln Z, \quad c_{\text{Ndc}}(F) = \left(\frac{\partial z(F)}{\partial F} \right)^{-1}. \quad (4.11)$$

The explicit results for the extension and the stiffness of the Ndc80 complex are

$$\begin{aligned} z(F) &= -\frac{2}{\beta F} \\ &+ \frac{2e^{\beta F a} (a \sinh \beta F b + b \cosh \beta F b) - be^{\beta F b} - b}{2e^{\beta F a} \sinh \beta F b - e^{\beta F b} - \beta F b + 1}, \end{aligned} \quad (4.12)$$

²¹ At an angle of 0° , the elements \vec{a} and \vec{b} are in line while they are maximally kinked at 120° :



²² In the second step, we substitute $z_a = a \cos \theta_a$ and $z_b = b \cos \theta_b$. The lower bound of the integral over z_b follows from the condition $z = z_a + z_b > 0$, which gives $z_b > -z_a$. However, if $z_a > b$, this condition is fulfilled for any $z_b \in [-b, b]$ so that a distinction of the cases $z_a \leq b$ and $z_a > b$ is necessary.

$$c_{\text{Ndc}}(F) = \left[\frac{2}{\beta F^2} + \beta \frac{2e^{\beta F a} ((a^2 + b^2) \sinh \beta F b + 2ab \cosh \beta F b) - b^2 e^{\beta F b}}{2e^{\beta F a} \sinh \beta F b - e^{\beta F b} - \beta F b + 1} - \beta \left(\frac{2e^{\beta F a} (a \sinh \beta F b + b \cosh \beta F b) - b e^{\beta F b} - b}{2e^{\beta F a} \sinh \beta F b - e^{\beta F b} - \beta F b + 1} \right)^2 \right]^{-1}. \quad (4.13)$$

In the limit of strong forces ($F \gg 1/\beta b = 0.256$ pN), this simplifies to

$$z(F) \approx a + b - \frac{2}{\beta F}, \quad c_{\text{Ndc}}(F) \approx \frac{\beta F^2}{2}, \quad (4.14)$$

²³ The extension of a general FJC with N bonds of length b , i.e., with total contour length $L_C = Nb$, under a force F behaves as [240, 241]

$$Nb \left(\coth \beta F b - \frac{1}{\beta F b} \right) \rightarrow L_C - \frac{N}{\beta F}.$$

The approximation for strong forces is also valid for bonds with different lengths as it is the case in our Ndc80 model with $L_C = a + b$ and $N = 2$.

²⁴ See the paragraph below Eq. (4.4) and Sidenote ¹⁶. A necessary condition is a superlinear strain stiffening of the individual stiffness, which is fulfilled by $c_{\text{Ndc}}(F)$.

which is the same result as for a free FJC²³ since the restriction by the glass bead becomes irrelevant when the Ndc80 complex is stretched by a large force.

Fig. 4.20 shows that the cooperative stiffnesses of n parallel Ndc80 complexes according to Eqs. (4.13) and (4.4) exhibit an apparent strain stiffening in the examined force range. Moreover, as already mentioned above, the cooperative stiffness may be reduced by adding further Ndc80 complexes in parallel.²⁴ As a result, the cooperative stiffness is minimized by the linear envelope in Fig. 4.20 when the number of attached Ndc80 complexes increases with the force. While the recognizable parabolic shape of $c_{\text{Ndc}}(F)$, which has already been derived in Eq. (4.14), contradicts the roughly linear strain stiffening observed in Fig. 4.13, the envelope provides a better agreement in the stiffening exponents. We discuss below that this might indicate a catch bond mechanism.

However, as shown in Fig. 4.20 by the example of Ndc80^{wt}, the Ndc80 model generates stiffnesses that exceed the experimental values by a factor of at least 2-4 even for the minimizing envelope. Taking into consideration that the experimental values depicted in Fig. 4.20 still contain the trap stiffness, which is not included in the theoretical curves, the discrepancy is even slightly larger than it appears in Fig. 4.20. We refrained from correcting the experimental measures by the trap stiffness as the trap stiffness and the time-traced stiffnesses were determined by different methods and are therefore difficult to compare: while the time-traced data was obtained from the equipartition theorem as described in Sec. 4.2.2, the trap stiffness, which was also used for force determination, was calibrated from the PSD [231–233]. In conclusion, one should keep in mind that the experimental values depicted in Fig. 4.20²⁵ probably need to be shifted downwards by an amount of approximately 0.02 pN nm⁻¹.

²⁵ as well as in Figs. 4.22 and 4.24 below

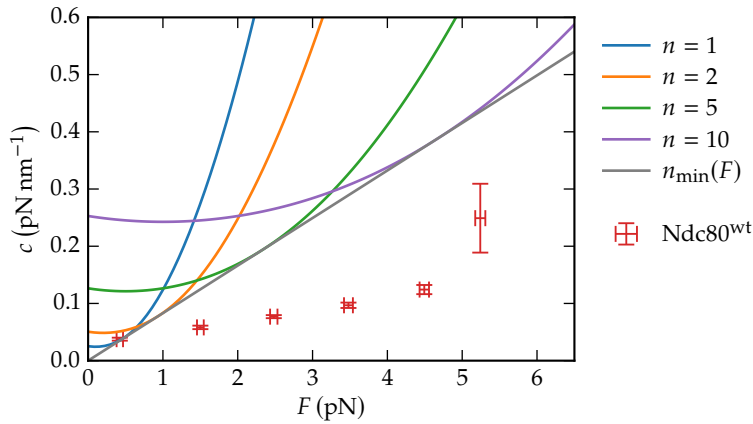


Figure 4.20: Ndc80 stiffness. The stiffness of n parallel Ndc80 complexes $n c_{\text{Ndc}}(F/n)$ according to Eq. (4.13) (colored lines) is by a factor of 2-4 larger than the measurements with wild type Ndc80. The theoretical stiffness is minimized when the number of attached Ndc80 complexes increases linearly with the force ($n_{\text{min}}(F)$, gray line).

We conclude that the stiffness of the Ndc80 complex alone can explain strain stiffening but is not sufficient to explain the measured stiffnesses quantitatively. The fact that the Ndc80 model gives larger stiffnesses than measured motivates the consideration of the additional elastic elements from the MT, the Ndc80–MT bond and the PFs in the total stiffness in Eq. (4.5). These elements are in series to the Ndc80 complex and potentially reduce the total stiffness of the entire Ndc80–MT link. We argued above that the stiffness of the Ndc80–MT bond is hard to quantify, and, therefore, we continue our analysis by investigating the effects of the MT stiffness c_{MT} and the PF stiffness c_{PF} .

4.3.3 Microtubule stiffness

Next, we consider the elasticity of the MT, whose tip can be attached to several Ndc80 complexes. The part of the MT that may contribute to the stiffness measurements is its free end between its fixed seed and its tip with the flaring PFs, whose flexibility is examined separately in the following section. In the experiments, typical lengths L of the free MT end lay between 3 and 10 μm . The MT can be thought of to exhibit two kinds of elasticity: a purely mechanical one due to stretching or bending, or an entropic stiffness that follows from thermodynamic fluctuations as for the Ndc80 complex. We start with the investigation of the mechanical properties.

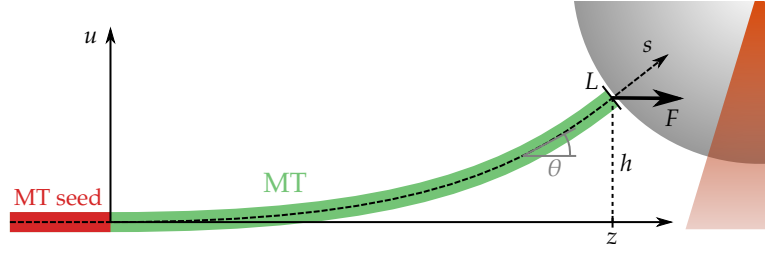
Mechanical stiffness

Given the values of 0.1 to 2 GPa that can be found for the Young's modulus Y of a MT [242], the stiffness of longitudinal MT stretching can be estimated to²⁶ 5 to 330 pN nm^{-1} , which is stiff enough to be ignored in the following.

Since the MT tip is lifted from the coverslip and therefore slightly bent when it is bound to the bead, a horizontal force might not

²⁶ The longitudinal stiffness is given by YA/L , where A is the cross-sectional area of the MT.

Figure 4.21: Model for mechanical MT stiffness. Since the MT tip is lifted by the bead, it may be unbent by a horizontal force, which is associated with an effective stiffness.



only stretch but also unbend the MT as sketched in Fig. 4.21. In the following, we deduce the effective stiffness that is associated with the unbending by modeling the MT as a beam with persistence length L_p whose seed is fixed to the coverslip ($z = u = 0$) and whose tip is forced to a height h by the bead.²⁷ We describe the MT conformation by the local bending angle $\theta(s)$ at the position s along the MT. The curvature is obtained by the derivative $\dot{\theta}(s) = d\theta/ds$. With a force F applied in z -direction, the total energy of the MT is given by the sum of bending and stretching energies:²⁸

$$E_{\text{MT}} = \int_0^L \left(\frac{\alpha}{2} (\dot{\theta}(s))^2 - F \cos \theta(s) \right) ds, \quad (4.15)$$

where $\alpha = k_B T L_p$ denotes the bending stiffness. Since the MT tip is lifted to a height h when it is attached to the bead, the total energy E_{MT} has to be minimized under the constraint

$$h = \int_0^L \sin \theta(s) ds. \quad (4.16)$$

This results in the Euler–Lagrange equation

$$\ddot{\theta} = \frac{F}{\alpha} \sin \theta - \frac{F_h}{\alpha} \cos \theta \stackrel{\theta \ll 1}{\approx} \frac{F}{\alpha} \theta - \frac{F_h}{\alpha}, \quad (4.17)$$

with a Lagrange-multiplier F_h , which corresponds to the force in u -direction that is necessary to hold the MT tip at height h . Due to the fixed MT seed and the unconstrained curvature at the MT tip, the MT conformation has to satisfy the boundary conditions $\theta(0) = 0$ and $\dot{\theta}(L) = 0$, respectively. Altogether, the approximated form of Eq. (4.17) is solved by

$$\theta(s) = \frac{F_h}{F} (1 - \cosh(\lambda s) + \tanh(\lambda L) \sinh(\lambda s)), \quad (4.18)$$

$$F_h = \frac{Fh/L}{1 - \frac{1}{\lambda L} \tanh(\lambda L)}, \quad \lambda \equiv \sqrt{\frac{F}{\alpha}}, \quad (4.19)$$

²⁷ As in the Ndc80 model, the deflection in force direction is denoted by z and corresponds to the direction of bead displacement x in Fig. 4.17.

²⁸ The second term describes the stretching energy $-Fz$ with

$$z = \int_0^L \cos \theta(s) ds.$$

The effective deflection in z -direction and the corresponding stiffness c_{mech} follow from

$$z = \int_0^L \cos \theta(s) ds \approx \int_0^L \left(1 - \frac{\theta^2(s)}{2}\right) ds, \quad (4.20)$$

$$c_{\text{mech}} = \left(\frac{\partial z}{\partial F}\right)^{-1}. \quad (4.21)$$

The explicit result can be written as

$$c_{\text{mech}} = \frac{8\sqrt{F\alpha}}{h^2} \times \frac{(1 - f(\lambda L))^3}{f'(\lambda L) \left((3 + 2\lambda^2 L^2) f(\lambda L) - 3 \right) + 2\lambda L f^2(\lambda L) (1 - f(\lambda L))}, \quad (4.22)$$

with $f(x) \equiv \tanh(x)/x$. For strong forces ($F \gg \alpha/L^2 \sim 0.05$ pN), this can be simplified to

$$c_{\text{mech}} \approx \frac{8L^2}{h^2\sqrt{\alpha}} F^{\frac{3}{2}}. \quad (4.23)$$

Since the persistence length depends on the total length of the MT,

$$L_p = \frac{L_p^\infty}{1 + \frac{L_0^2}{L^2}}, \quad (4.24)$$

with $L_p^\infty = 6.3$ mm and $L_0 = 21$ μm [243], the only required parameters besides temperature are the MT length L and the height h . Given the bead diameter of 1 μm and the distance between the surfaces of the coverslip and the bead (~ 100 nm), we estimate that the height does not exceed $h = 500$ nm.

Fig. 4.22A shows the stiffness of a MT with typical length $L = 5$ μm and $h = 500$ nm in series with several parallel Ndc80 complexes. Though the choice of h provides a lower estimate for $c_{\text{mech}} \propto h^{-2}$, the purely mechanical MT stiffness only slightly reduces the total stiffness as compared to the Ndc80 complexes alone, which it exceeds by a factor greater than 5 in most of the examined force range. We conclude that a mechanical contribution of the MT can be neglected and continue with estimating its entropic stiffness.

Entropic stiffness

We consider the entropic stiffness by describing the MT as a generic semiflexible polymer with persistence length L_p . Then, for sufficiently large forces ($F \gg k_B T/L_p \sim 10^{-6}$ pN), the relation between the applied force F and the mean extension z in force

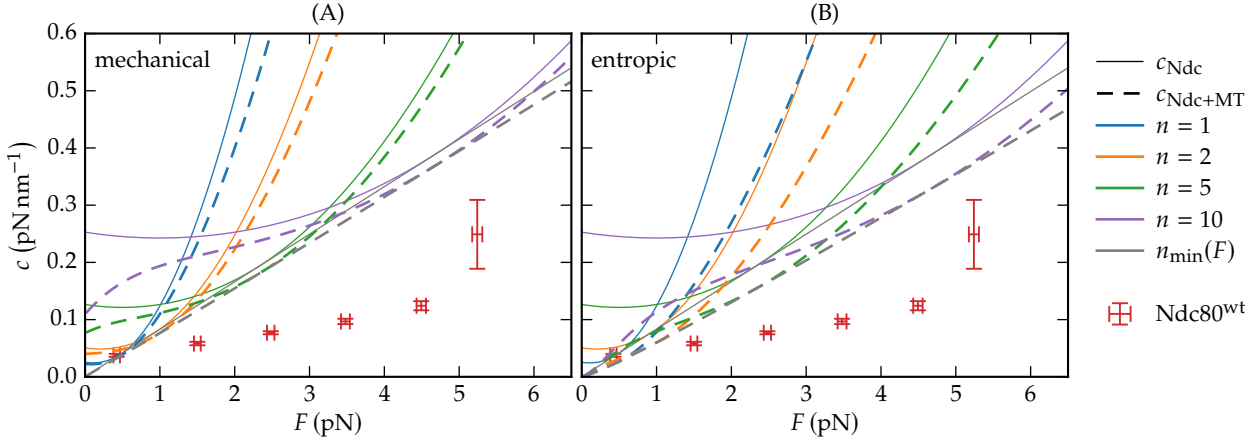


Figure 4.22: Microtubule stiffness. Mechanical and entropic stiffness of a MT in series with n parallel Ndc80 complexes (dashed lines) compared to the sole Ndc80 stiffness (Eq. (4.11), bold lines). (A) With the mechanical MT stiffness according to Eq. (4.23), the total stiffness is only slightly different from the bare Ndc80 stiffness. (B) The contribution of the entropic MT stiffness according to Eq. (4.23) can not be neglected as it significantly reduces the stiffness when it is arranged in series with the Ndc80 complexes.

direction is given by [244]

$$\frac{z}{L} = 1 - \left(\frac{k_B T}{4FL_p} \right)^{\frac{1}{2}}, \quad (4.25)$$

The entropic MT stiffness c_{MT} can again be deduced from the derivative of z with respect to the force:

$$c_{MT}(F) = \left(\frac{\partial z}{\partial F} \right)^{-1} = \frac{4}{L} \left(\frac{L_p}{k_B T} \right)^{\frac{1}{2}} F^{\frac{3}{2}} = \frac{4}{\sqrt{k_B T}} \left(\frac{L_p^\infty}{L^2 + L_0^2} \right)^{\frac{1}{2}} F^{\frac{3}{2}}, \quad (4.26)$$

where the length dependence of the persistence length according to Eq. (4.24) was inserted in the last step. The only necessary parameter besides temperature is the length of the free part of the MT. Due to the length dependent persistence length, the resulting MT stiffness in Eq. (4.26) converges for small MT lengths $L \ll L_0 = 21 \mu\text{m}$. Therefore, the MT stiffness can be assumed to be the same in all experiments, where typical lengths lay between 3 and $10 \mu\text{m}$, and we use $L = 10 \mu\text{m}$ in the following as a general representative.

The entropic stiffness of the MT is of the same order of magnitude as the Ndc80 stiffness, which is a surprising result itself for a MT that is by a factor 100 shorter than its persistence length. Consequently, the sole stiffness of n parallel Ndc80 complexes is significantly reduced when the MT stiffness is added in series, see Fig. 4.22B. Interestingly, the combination of a single MT with stiffening exponent $3/2$ and several ($n \gtrsim 5$) Ndc80 complexes stiffening with F^2 results in a roughly linear behavior in the examined force range, which might explain the measured stiffening exponents in Fig. 4.13. Despite the overall stiffness reduction, our model predictions are still too large as compared to the measurements when only the MT and the Ndc80 complexes are considered. Therefore, we speculate in the next step that the Ndc80 complexes bind to the curved parts of the PFs resulting in an effective stiffness from straightening the PFs.

4.3.4 Effective stiffness of protofilament bending

The Ndc80 complexes apply a force into the axial MT direction²⁹ on the free ends of the PFs, see Fig. 4.23. Since, thereby, the PFs are bent out of their preferred curvature, a restoring force on the Ndc80 complexes builds up, governed by an effective stiffness c_{PF} for strains in the axial direction. In the following, we quantify this stiffness by modeling the PF as a beam with a preferred curvature ϕ and persistence length L_p . The approach is very similar to the mechanical MT model above with the only difference that the PF is intrinsically curved in absence of an external force while the MT curvature is a consequence of the vertical force applied by the optical trap.

As described in Fig. 4.23, the PF is straight and bound by lateral interactions with neighboring PFs for $z < 0$. For $z > 0$, we assume that there are no interactions to neighboring PFs so that the PF can bend freely. The PF conformation is described by the local bending angle $\theta(s)$ at the position s along the PF. The PF curvature is obtained by the derivative $\dot{\theta}(s) = d\theta/ds$. In the absence of an external force, the PF has a preferred (or spontaneous) constant curvature ϕ . Let the Ndc80 complex attach at the position $s = s_0$ and apply a force F in z -direction. Then, the total energy is the sum of bending and stretching energies,

$$E_{\text{PF}} = \int_0^L \frac{\alpha}{2} (\dot{\theta}(s) - \phi)^2 ds - Fz(s_0), \quad (4.27)$$

with the bending stiffness $\alpha = k_B T L_p$ and the total length L of the free PF. The second term describes the stretching in z -direction where the effective deflection is given by the position of the point of force application on the z -axis:

$$z_0 \equiv z(s_0) = \int_0^{s_0} \cos \theta(s) ds. \quad (4.28)$$

The PF is dominated by the interplay of bending and stretching energy such that we can neglect thermal fluctuations and obtain the PF stiffness from the configuration minimizing the total energy E_{PF} . Since the force F only affects the shape of the PF for $s < s_0$ while the curvature at $s > s_0$ stays ϕ , we have to minimize the PF energy with boundary conditions $\theta(0) = 0$ and $\dot{\theta}(s_0) = \phi$. Moreover, since the bending energy vanishes for $s > s_0$, we can summarize Eqs. (4.27) and (4.28) by changing the upper limit of integration in the bending energy from L to s_0 :

$$E_{\text{PF}} = \int_0^{s_0} \left(\frac{\alpha}{2} (\dot{\theta}(s) - \phi)^2 - F \cos \theta(s) \right) ds. \quad (4.29)$$

²⁹ As in the Ndc80 model above, this direction is denoted by the z -axis in the following and corresponds to the x -direction in Fig. 4.17.

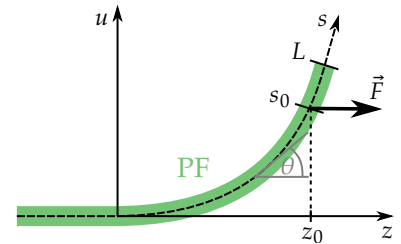


Figure 4.23: Model for protofilament bending. The z -axis marks the direction along the MT, and the u -axis the radial distance from the straight PF, i.e., from the surface of the MT. The PF is described by the local bending angle $\theta(s)$, where s is the position along the curved PF. The Ndc80 complex is attached at $s = s_0$ and applies the force F in z -direction.

The energy minimizing PF configuration satisfies the Euler–Lagrange equation

$$\ddot{\theta}(s) = \frac{F}{\alpha} \sin \theta(s), \quad (4.30)$$

which we solve numerically with a shooting method in order to fulfill the boundary conditions. Finally, the effective stretching stiffness of the PF can be determined from the derivative of the effective deflection $z_0(F)$:

$$c_{\text{PF}} = \left(\frac{dz_0}{dF} \right)^{-1}. \quad (4.31)$$

In the limit of strong forces ($F \gg \alpha/s_0^2 \sim 0.3\text{--}2\text{ pN}$), the PF is stretched, i.e., $\theta(s) \ll 1$, and we can approximate Eq. (4.30) by $\ddot{\theta} = (F/\alpha) \theta$, which can be solved analytically.³⁰

³⁰The differential equation $\ddot{\theta} = (F/\alpha) \theta$ is generally solved by

$$\theta(s) = A \sinh \lambda s + B \cosh \lambda s,$$

with $\lambda = \sqrt{F/\alpha}$. The first boundary condition ($\theta(0) = 0$) yields $B = 0$, the second condition ($\dot{\theta}(s_0) = \phi$) is fulfilled with $A = \phi/\lambda \cosh \lambda s_0$ so that we find

$$\theta(s) = \frac{\phi}{\lambda} \frac{\sinh \lambda s}{\cosh \lambda s_0} \approx \frac{\phi}{\lambda} e^{\lambda(s-s_0)}.$$

Using the approximated form, which is valid for large forces, and expanding $\cos \theta$ in Eq. (4.28) for small θ so that

$$z_0 \approx \int_0^{s_0} \left(1 - \frac{\theta^2}{2} \right) ds,$$

we finally achieve the result in Eq. (4.32).

$$z_0(F) \approx s_0 \left(1 - \frac{\phi^2}{4s_0} \left(\frac{\alpha}{F} \right)^{3/2} \right) \quad (4.32)$$

$$c_{\text{PF}}(F) \approx \frac{8F^{5/2}}{3\phi^2\alpha^{3/2}} \propto F^{5/2}. \quad (4.33)$$

We note the pronounced strain stiffening with $c_{\text{PF}}(F) \propto F^{5/2}$, which is a consequence of bending rigidity together with spontaneous curvature.

The model depends on three parameters: the persistence length L_p , the preferred curvature ϕ , and the point of force application s_0 . Following the results of *in vitro* experiments [72], we use $L_p = 200\text{ nm}$ and $\phi = 20^\circ$ per tubulin dimer throughout this chapter. We have to guess where the Ndc80 complex attaches to the PF. Since the attachment point has to be somewhere on the PF, s_0 has to be smaller than L , which is the length of the curved part of the PF. McIntosh *et al.* [72] measured values in the range of 10 to 80 nm for depolymerizing MTs *in vitro*, with a mean of $(36 \pm 15)\text{ nm}$. In this chapter, we use estimates $s_0 = 20\text{ nm}$ and $s_0 = 50\text{ nm}$.

Fig. 4.24 shows how the stiffness of a MT with c_{MT} in series with n Ndc80 complexes with c_{Ndc} is reduced when a PF with c_{PF} is added in series to each Ndc80 complex.³¹ We see that the influence of PF bending is negligible for $s_0 = 20\text{ nm}$ whereas for $s_0 = 50\text{ nm}$, the PF significantly reduces the total stiffness close to the wild type measures. We conclude that the PF stiffness is only relevant if the Ndc80 complex is attached near the end of a sufficiently long PF. An upper bound for s_0 is given by the total length of the curved part of the PF, for which values of $L = 10\text{--}80\text{ nm}$ have been measured *in vitro* [72]. We note that it is questionable whether such distant attachment points $s_0 > 20\text{ nm}$ are realizable as there is experimental evidence that single Ndc80 complexes are only

³¹Expressed in formulas, the following two stiffnesses are depicted in Fig. 4.24:

$$\left(\frac{1}{c_{\text{MT}}(F)} + \frac{1}{nc_{\text{Ndc}}(F/n)} \right)^{-1},$$

$$\left(\frac{1}{c_{\text{MT}}(F)} + \frac{1}{nc_{\text{Ndc}}(F/n)} + \frac{1}{nc_{\text{PF}}(F/n)} \right)^{-1}$$

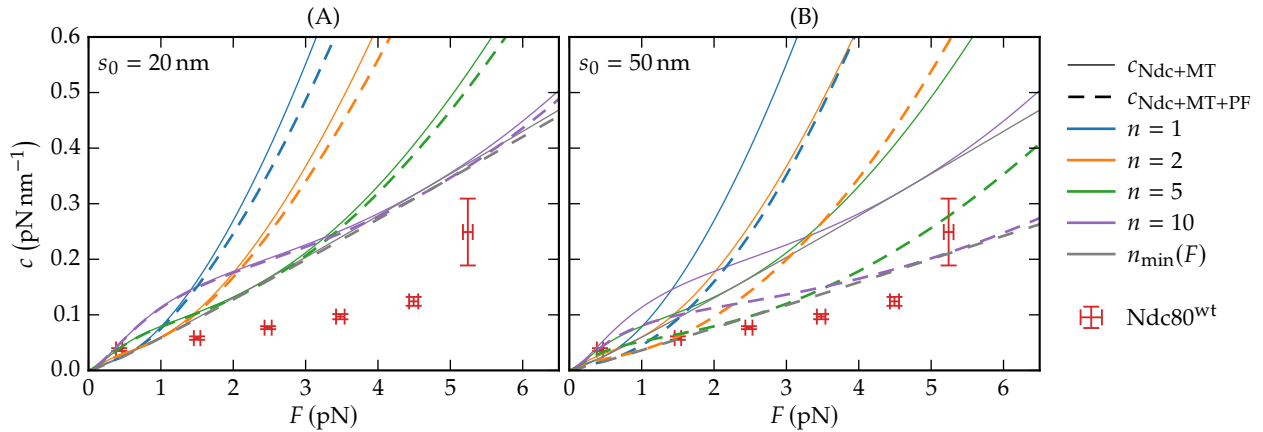


Figure 4.24: Protofilament stiffness. Stiffness of a MT in series with n parallel PFs and Ndc80 complexes (dashed lines) compared to a MT in series with just the Ndc80 complexes (bold lines). (A) When the attachment point on the curved PF has a distance of $s_0 = 20$ nm from the straight MT lattice, the stiffness is only slightly reduced. (B) For $s_0 = 50$ nm, the PF does have a significant contribution to the total stiffness. However, the combined stiffnesses of MT, Ndc80 complexes and PFs are still larger than the experimental outcomes for wild type Ndc80.

able to bind to straight PFs [131, 222]. We discuss below why this evidence might not apply to the conditions of the optical trap experiments of Volkov, Huis in 't Veld *et al.*

Even when long PFs are considered, the additional PF elasticity does not lower the calculated stiffness sufficiently to accurately describe the experimental outcomes if a *fixed* number n of parallel Ndc80 complexes is used over the whole range of applied forces. This motivates the last step of our analysis.

4.3.5 Catch bond behavior can minimize the cooperative stiffness

We now analyze how our model behaves when the number n of attached Ndc80 complexes depends on the applied force, $n = n(F)$. In principle, both a catch bond and a slip bond mechanism are conceivable for the Ndc80–MT bond. A catch (slip) bond is characterized by a binding affinity that increases (decreases) under tension [245]. In our model, a catch (slip) bond implies a monotonically increasing (decreasing) force-dependent number of attached Ndc80 complexes $n(F)$.

We find that a force-dependent $n(F)$ can lower the effective total stiffness of the entire Ndc80–MT link. The minimal cooperative stiffness that can be realized by allowing a dependence $n(F)$ is the envelope of the stiffness–force relations $c_n(F)$ for different n , see Figs. 4.20, 4.22 and 4.24. The envelope of the $c_n(F)$ relations is obtained by a force-dependent number $n_{\min}(F)$ of attached Ndc80 complexes that minimizes the stiffness $c_n(F)$ for each F . The resulting $n_{\min}(F)$ is shown in Fig. 4.25 and increases linearly,³² which also implies a catch bond behavior. For long PFs ($s_0 = 50$ nm), the envelope stiffness $c_{n_{\min}}(F)$ has actually the correct order of magnitude as compared to the experimental data shown in Fig. 4.24B. The number $n_{\min}(F)$ also remains below $n = 15$ in the examined force range, which is in agreement with estimates for the number

³² Though $n_{\min}(F)$ as depicted in Fig. 4.25 is determined numerically, its linear behavior can be derived directly: the number n that minimizes the cooperative stiffness $c_n(F) = n c(F/n)$ for a given force F is defined by

$$0 = \frac{\partial c_n(F)}{\partial n} = c\left(\frac{F}{n}\right) - \frac{F}{n} c'\left(\frac{F}{n}\right).$$

If $c(F=0) > 0$ and $c(F)$ is a convex function, which is the case for both $c_{\text{Ndc}}(F)$ and $c_{\text{PF}}(F)$, this equation can be solved by a constant $F_n^* = F/n_{\min} \neq 0$, i.e.,

$$n_{\min}(F) = \frac{F}{F_n^*} \propto F.$$

Moreover, since

$$\frac{\partial^2 c_n(F)}{\partial n^2} = \frac{F^2}{n^3} c''\left(\frac{F}{n}\right),$$

the convexity of $c(F)$ ensures that n_{\min} actually *minimizes* c_n .

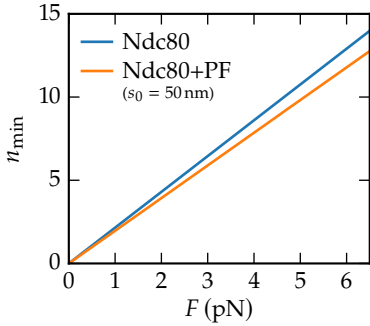


Figure 4.25: Stiffness minimizing Ndc80 numbers. Force-dependent numbers $n_{\min}(F)$ of attached Ndc80 complexes that minimize the cooperative stiffnesses $c_n(F)$ of bare Ndc80 complexes (blue) and Ndc80 complexes attached to PFs at $s_0 = 50$ nm (orange). The corresponding minimum stiffnesses $c_{n_{\min}}(F)$ are depicted in Figs. 4.20 (Ndc80) and 4.24B (Ndc80+PF).

³³ See Eqs. (4.14), (4.26) and (4.33).

of Ndc80 complexes in the proximity of the MT given the expected Ndc80 density on the bead [58, 120].

Apart from the absolute stiffness values, a model should reproduce the observed roughly linear strain stiffening behavior with an exponent m around unity (see Fig. 4.13). Our theory, on the other hand, predicts exponents of $3/2$, 2 and $5/2$ for the MT, the Ndc80 complexes and the PFs, respectively.³³ The relation $n(F)$ can change the latter two stiffening exponents. From Eq. (4.4), one can see that a linearly increasing $n(F)$ actually implies a linear stiffening as observed in the experiments since $F/n(F) = \text{const}$ and, therefore, $c_n(F) = n(F) c(\text{const}) \propto n(F)$. For a slip bond, on the other hand, where $\partial_F n(F) < 0$ and $n(F) \rightarrow 0$ for large forces by definition, the argument in Eq. (4.4), $F/n(F)$, increases rapidly. As a consequence, we can approximate c_{Ndc} and c_{PF} with the power laws from Eqs. (4.14) and (4.33), respectively, so that

$$c_n(F) \sim n(F) \left(\frac{F}{n(F)} \right)^m = \frac{F^m}{(n(F))^{m-1}} > \mathcal{O}(F^m), \quad (4.34)$$

We conclude that any kind of slip bond will increase the stiffening exponent for large forces. Stiffening exponents below the values $m = 2$ for Ndc80 stiffness or $m = 2.5$ for PF stiffness, as obtained in the experiments, are indicative of a catch bond mechanism. For the time-traces from single experiments in Fig. 4.14, 79 % of the stiffening exponents lie below 2.

4.4 Discussion

The novel analysis of time-traces of bead positions in optical trapping experiments allowed us to time-trace the stiffness during single experiments and to go beyond an analysis limited to the MT stall state [58]. This enabled us to increase the available number of stiffness measurements by 1 to 2 orders of magnitude and study strain stiffening of wild type Ndc80 in more detail. It also enabled us to study strain stiffening of Ndc80 variants with a truncated tail or with a mutated CH domain, both of which typically detach before the MT has been stalled, and to explore strain stiffening selectively in the shrinking, stalled and growing state of MTs.

We found that all variant Ndc80 complexes exhibit strain stiffening hinting at a central role of the Ndc80–Nuf2 coiled coil, rather than the MT binding sites in the CH-domain and the N-terminal tail. The measured stiffnesses of the entire Ndc80–MT link are lower than theoretical predictions from our Ndc80 model. Therefore, additional elastic elements in the Ndc80–MT link or a force-dependent number of attached Ndc80 complexes should be relevant. We

could exclude the PLL-PEG connection between Ndc80 complexes and the bead, which is too stiff to contribute. Effects from the MT and from protofilament flexibility are necessary for the model to conform to experimentally measured stiffnesses, and the observed linear stiffening may be explained by an increasing number of attached Ndc80 complexes under force (catch bond). Moreover, stiffness differences between variants allow us to draw some conclusions on the Ndc80–MT bond.

Effects from protofilaments

Time-tracing of the stiffness allowed us to study strain stiffening selectively in the shrinking, stalled and growing state of MTs. Both in single experiments with a MT rescue (Fig. 4.10C) and in the collective analysis in Fig. 4.16, we found no significant stiffness differences between MT states, leading to the conclusion that the stiffness of the bent PFs is either too large to contribute significantly to the total stiffness or that it does not depend on the MT's polymerization state.

Our PF model showed that the PF contribution to the overall stiffness depends strongly on the length of the PFs and the position along the PF where the Ndc80 complex is attached. An attachment point s_0 close to the straight part of the PF ($s_0 \leq 20$ nm) predicts a negligible contribution of the PF. Indeed, single Ndc80 complexes are only able to bind to straight but not to curved PFs [131, 222]. However, our stiffness measures derive from experiments where Ndc80 multimers were used that were able to tip-track—in contrast to the single Ndc80 complexes in Refs. [131, 222]. Moreover, these experiments were not performed with full wild type Ndc80 complexes but with Ndc80^{bonsai} lacking the flexible loop region [222] or with Ndc80^{broccoli} lacking Spc24 and Spc25 [131]. Together, these differences leave room for speculating that our experimental conditions allow for Ndc80 binding to curved PFs. For instance, a Ndc80 complex may bind initially to a straight PF, which becomes curved at the binding site during depolymerization while the Ndc80 complex stays attached.

Attachments of Ndc80 to long flaring PFs with attachment lengths around $s_0 = 50$ nm are predicted to reduce the stiffness of the Ndc80–MT link to values close to the measured stiffnesses (Fig. 4.24B). This favors the second possible explanation, namely that PFs contribute to the total stiffness but have identical elastic properties during MT shrinkage, stall and growth. This is also in agreement with the recent observation that the curvature of PFs is the same during polymerization and depolymerization [72].

Number of attached Ndc80 complexes and potential catch bond mechanism

The number n of simultaneously attached Ndc80 complexes could not be directly inferred from the experiments in Refs. [58, 59]. From the known Ndc80 densities on the bead we can estimate that 1 to 4 Ndc80 trimers, i.e., 3 to 12 Ndc80 complexes are in the vicinity of the MT end and can potentially bind [58].

From the equal stiffness–force relations before and after a rescue, we conclude that also the number of attached Ndc80 complexes is the same during polymerization and depolymerization. Dynamically, it is possible that the number of attached Ndc80 complexes changes in a force-dependent manner on a time scale that is small compared to typical time scale of MT dynamics. For force-free detachment and attachment of a single Ndc80^{wt} complex, time scales of $\tau_{\text{off}} = 1.6$ s and $\tau_{\text{on}} = 0.4$ s, respectively, were found [58]. With a phosphorylated tail, τ_{off} is supposed to be smaller [212]. Since the durations of MT depolymerization vary in a wide range from less than 1 s up to ~ 100 s, both a constant and a dynamic number of attached complexes are possible.

Our modeling results showed that the absolute stiffness values as well as the roughly linear strain stiffening relations in Fig. 4.13 are best reproduced by a force-dependent number $n(F)$ that increases linearly with force. Moreover, among the stiffening exponents for the time-traces from single experiments in Fig. 4.14, 79 % of the strain stiffening exponents lie below 2. Together, these results are indicative of a catch bond like behavior of Ndc80–MT binding.³⁴

Assuming that Ndc80 forms a catch bond to the MT, the question arises how this mechanism could work. The whole kinetochore, consisting of several additional proteins, has been proposed to act like a catch bond [246]. It is widely assumed that the Aurora B kinase, which was not present in the experiments of Volkov, Huis in 't Veld *et al.*, is important in the kinetochore's catch bond mechanism [123, 247, 248]. Kinetochores purified from *S. cerevisiae*, however, were shown to build catch bonds with MTs *in vitro* even without Aurora B activity [134].³⁵ There is evidence that Ndc80 stretching correlates with MT binding as the Ndc80 complex may exist in an auto-inhibited bent conformation with reduced MT binding capacity [250] and bends (“jackknives”) upon detachment [251]. This suggests that the binding affinity for MTs increases when the Ndc80 complex is stretched, which would further imply that Ndc80 has an intrinsic catch-bond-like mechanism. To what extent this effect is relevant for our experiments is unclear as according to our FJC model, the Ndc80 complex is already stretched by small forces. For instance, at $F = 1$ pN, we find a mean angle of $(44 \pm 23)^\circ$ between the arms \vec{a} and \vec{b} .³⁶

³⁴ As already noted above, the (apparently) linear stiffening may also result from the combination of the different stiffening behaviors of a single MT and a sufficiently large constant number of Ndc80 complexes and PFs, see Figs. 4.22 and 4.24 for $n = 10$ attached Ndc80 complexes.

³⁵ The catch bond behavior of the purified yeast kinetochores was abolished when Dam1 or Stu2 were absent, even in presence of Ndc80 [134, 249].

³⁶ The angle is 0° for a maximally stretched Ndc80 complex, see Side-note 21.

Speculating on other possible catch bond mechanisms, it is conceivable that by stretching the unstructured tail, additional binding sites become available, which are concealed in the entangled tail at low forces.³⁷ Force-enhanced adhesion by unfolding is a common catch bond mechanism [252]; examples are the von Willebrand factor [253, 254] and α -catenin bonding to F-actin in the cytoskeleton [255]. In conclusion, an intrinsic catch bond mechanism of Ndc80 complexes is compatible with current knowledge and worth considering as one of the ingredients that define the characteristics of Ndc80 strain stiffening. Such a mechanism could also contribute to the catch bond behavior of the entire kinetochore.

We finally note that the conclusion of a Ndc80–MT catch bond was drawn under the assumption that the force is equally shared among the attached Ndc80 complexes. Allowing for unequal force-sharing, i.e., for differently stretched linkers, the system will be dominated by a few very stiff Ndc80 complexes, which are the ones with the largest elongation. It is thinkable that the linker extensions approach a uniform distribution under force, for instance, because some extremely stretched Ndc80 complexes detach from the shrinking MT. Then, despite detachment of a few linkers, the number of linkers with a relevant stretch increases under force. Such a mechanism would result in an apparent catch bond behavior without the need for individual Ndc80–MT catch bonds.

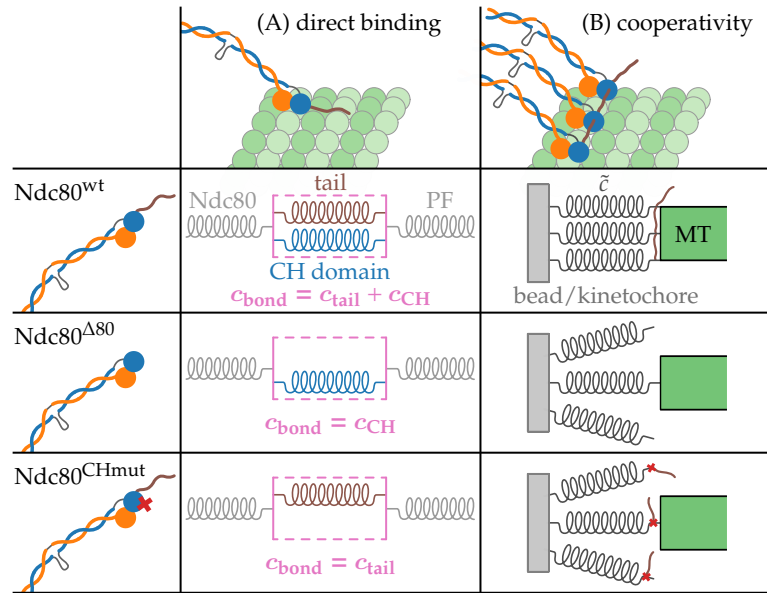
Structure of the Ndc80–MT bond and role of the N-terminal tail in MT binding

Stiffness differences between the wild type Ndc80^{wt} and the mutants Ndc80 ^{Δ 80} and Ndc80^{CHmut} should reflect roles in MT binding of the the N-terminal tail and the CH domain, respectively. In the following, we discuss these differences to draw some conclusions on the Ndc80–MT bond. As described in Sec. 4.1, the CH domain binds between two tubulin monomers via a structural element named the “toe”[222]. The N-terminal tail also supports MT binding, but its exact role is still under debate. The three models from Fig. 4.2 are currently discussed [221, 223]: direct binding to the MT lattice, cooperativity and clustering by interactions with neighboring Ndc80 complexes, and co-factor recruitment. Since no co-factors were present in the experiments that we have analyzed, we concentrate on the former two models.

Our comparative study of Ndc80^{wt}, Ndc80 ^{Δ 80} and Ndc80^{CHmut} allows us to dissect the role of the tail and the CH domain in Ndc80–MT binding. Both Ndc80 mutants displayed decreased stiffnesses compared to the wild type (Fig. 4.15B), an effect we ascribed either to a softened Ndc80–MT bond or to a reduced number of attached

³⁷ A mechanism that relies on the N-terminal tail and the CH domain could explain why, according to the power fits in Fig. 4.13, Ndc80 ^{Δ 80} and Ndc80^{CHmut} have stiffening exponents $m \approx 2$ as it is predicted by Eq. (4.13) for a constant number of attached Ndc80 complexes whereas Ndc80^{wt} and Ndc80^P exhibit a roughly linear strain stiffening ($m \approx 1$) indicating a catch bond behavior. If the linear stiffening rather follows from the serial arrangement of a MT with a sufficiently large number of Ndc80 complexes, the non-linear stiffening exponents of Ndc80 ^{Δ 80} and Ndc80^{CHmut} might be a consequence of their reduced binding affinity. However, as aforementioned, the current data records of Ndc80 ^{Δ 80} and Ndc80^{CHmut} are too poor to make reliable statements regarding their stiffening exponents.

Figure 4.26: Models of the Ndc80–MT bond for potential roles of the N-terminal tail. (A) When the tail binds directly to the PF, an elastic model of the Ndc80–MT bond comprises the tail and the CH domain as two parallel springs. If the tail is deleted (Ndc80^{Δ80}) or the CH binding domain is blocked (Ndc80^{CHmut}), either of those springs is missing, which lowers the bond stiffness c_{bond} and thereby the total stiffness \tilde{c} . (B) In the case of an interaction of the tail with CH domains of neighboring Ndc80 complexes, the number of parallelly attached linkers is reduced for the two mutants Ndc80^{Δ80} and Ndc80^{CHmut}.



Ndc80 complexes. In the elastic toy model in Fig. 4.26A, both the CH domain and the tail of Ndc80^{wt} bind to the MT, so that they can be represented by two parallel springs that add up to the total bond stiffness c_{bond} . Due to the parallel arrangement, lack of either of the two springs in Ndc80^{Δ80} or Ndc80^{CHmut} reduces the bond stiffness, predicting overall stiffnesses as depicted in Fig. 4.15B. If both the CH domain and the N-terminal tail bind directly to the MT lattice, the two Ndc80 mutants probably have a reduced MT binding affinity. Therefore, in the direct binding model, the reduction of the overall stiffness could be just as well a consequence of a reduced number of attached Ndc80 complexes as of a reduction of the individual bond stiffnesses.

When the N-terminal tail interacts with neighboring Ndc80 complexes instead of the tubulin, the induced cooperativity supports parallel attachments of multiple Ndc80^{wt} complexes, see Fig. 4.26B. Deletion of the tail or mutation of the CH domain may impair the cooperative behavior so that less linkers connect the bead (or the kinetochore) with the MT and the overall stiffness decreases. While there is evidence supporting a contribution of the tail to cooperative MT binding, there is at present no clear evidence indicating that the Ndc80 CH domain contributes to binding cooperativity.

Tail phosphorylation was shown to reduce the MT binding affinity of the Ndc80 complex [111, 209–212]. Moreover, the durations of the MT stalls were shorter when the Ndc80 tails are phosphorylated [59]. This suggests that phosphorylation impedes the function of the tail similarly as if the tail is truncated. However, in contrast to Ndc80^{Δ80}, the stiffness of Ndc80^P is not significantly reduced compared to Ndc80^{wt}, see Fig. 4.15B. It remains an open question how these observations are compatible with the binding models depicted in Fig. 4.26.

Comparison of model and experiment

Our model can explain the strain stiffening from the structure of the Ndc80 complex, an entropic stiffness of the MT and the bending elasticity of the long flaring PFs. If we allow for a force-dependent number of bound Ndc80 complexes, a linearly increasing number of bound complexes also reproduces the observed roughly linear strain stiffening relation. Ndc80, by itself or in series with PFs, gives absolute stiffness values that are still above the measured stiffnesses. Including a force-dependent number of bound Ndc80 complexes gives values which are close but still slightly higher than measured. As already mentioned, the missing part might be the Ndc80–MT bond, which is additionally in series with the Ndc80 complex and the PF as illustrated in Fig. 4.17. However, since the stiffness of the bond is hard to quantify due to the little knowledge of the exact binding mechanism, we did not go beyond the qualitative discussion above.

Regarding the Ndc80, we have also investigated possible effects from finite flexibility of the two Ndc80 arms by modeling both arms as semiflexible worm-like chains (WLCs). We performed Monte Carlo simulations in which each Ndc80 arm had the same persistence length L_p . Using persistence lengths in a realistic range of $L_p \gtrsim 100$ nm as they have been determined for other coiled coil proteins such as tropomyosin [256], our simulations lead to the conclusion that semiflexibility has only a minor effect on total stiffness.³⁸

Finally, we need to discuss the accuracy of our experimental method. While the trap stiffness was calibrated by fitting the power spectrum based on Brownian motion in a harmonic potential [231–233], this well-established PSD method can not be applied for measurements of the anharmonic Ndc80 stiffness. Therefore, we had to determine the Ndc80 stiffness from the variance of bead position, which is a simpler and universal but less accurate approach. In particular, the measured overall variance contains any systematic noise that is added to the actual variance of bead position, which is why the stiffness tends to be underestimated by $k_B T / \text{Var}(x)$ [228–230]. This systematic underestimation, which we can not quantify,³⁹ might explain why our model tends to predict higher stiffnesses than experimentally measured.

Conclusion

In conclusion, we accumulated extensive stiffness data of the Ndc80–MT link by optical trapping methods in combination with a novel time-tracing analysis. We were able to study wild type Ndc80 complexes and three variants. Our theoretical model for

³⁸ The WLC simulations and their results are presented in Appendix C.4.

³⁹ While there is much literature that lists various methods of stiffness determination and also highlights their advantages and disadvantages, see for instance Refs. [227–229, 257, 258], we found only few studies that compare the different methods quantitatively [230, 259, 260]. These studies report that the stiffnesses determined by the PSD method exceed $k_B T / \text{Var}(x)$ by a factor of 1.5–2. However, in all the references cited above, stiffness determination is only considered in the context of trap stiffness calibration, i.e., while the trapped object fluctuates around its equilibrium position in the harmonic potential of the optical tweezers. Therefore, it is questionable to what extent the observed factors 1.5–2 apply to experiments where the glass bead is displaced from the trap center and moves in an anharmonic potential.

the Ndc80–MT link consisting of a mechanical model of the Ndc80 complex, the MT and the flaring PFs at the MT tip is able to explain the strain stiffening and reproduces the correct order of magnitude of the stiffness. The theoretical model is based on the known structural features of the Ndc80 complex, the MT and the PFs at the MT tip. Thus, our results on the elastic properties further support these structural models from the mechanical point of view. Our model also reproduces the roughly linear strain stiffening behavior when taking a force-dependent binding affinity into account.

At present, the theoretical model predicts higher absolute stiffness values than observed in the experiments. One could argue that this discrepancy could be overcome if only the model were properly modified.⁴⁰ However, such modifications would be accompanied by probably speculative assumptions and would not be constructive as long as the absolute reliability of the experimental values is not clarified. We conclude that the qualitative discussion in terms of the stiffening exponents and by means of a model with a solid structural basis is the most reasonable approach at this stage, and that, after all, both experimental and modeling progress will be needed to achieve quantitative agreement of absolute stiffness values.

⁴⁰ For instance, we could ascribe the discrepancy to the bond stiffness and try to reverse engineer c_{bond} and to find a bond model that reproduces this stiffness.

In the last three chapters, we developed different quantitative models to examine dynamic instability of single MTs, cooperative MT and kinetochore dynamics in the mitotic spindle, and the strain stiffening of Ndc80 complexes observed in optical trap experiments. In the following we recapitulate and compare some methodological aspects of the models, which are summarized in Tab. 5.1. Afterwards, we provide a short summary of the major results and their biological implications before we finally give an outlook on how the models could be extended and linked in future work.

We always started by developing a model that is simple but still relies on a solid experimental or structural basis. Where such a basis was lacking, we needed to make assumptions like the simple elastic MT–kinetochore linkers or the stiff Ndc80 arms. Furthermore, we applied simplifications that went beyond the necessary assumptions and deliberately neglected or coarse-grained certain characteristics of the real system in order to keep the model comprehensible. For instance, each model ignored the complex spatial structure of the corresponding real system by mapping it to one dimension. Dynamic instability of both single MTs and the MTs in the mitotic spindle was implemented similarly as in the empirical Dogterom–Leibler model [29, 30], which treats the MT as a continuous one-dimensional object ignoring its microscopic structure and the GTP hydrolysis. In the model of the Ndc80 and the PF stiffness, we ignored the restrictions of the Ndc80 bending angle [192] or the thermal fluctuations of the PF.

The simplifications also reflected the aspects that the models were intended to examine. Coarse-graining the MT structure in Chapter 2 and manually incorporating multistep dynamics is reasonable as long as we are only interested in the effects of multistep catastrophes on the MT length distribution, but not in the multistep process itself and its probably microscopic origin. In Chapter 3, we concentrated on kinetochore oscillations during metaphase so that it was appropriate to assume the centrosome positions as fixed and to exclude astral MTs. The model in Chapter 4 should reflect the stiffness of an Ndc80 complex that is attached to a protofilament, and was not intended to reproduce how Ndc80 complexes track the depolymerizing MT tip under force. Therefore, we chose a simple static model of serial springs, whose stiffnesses were determined independently.

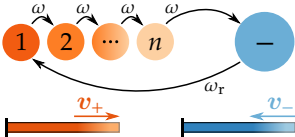
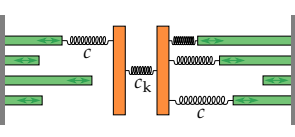
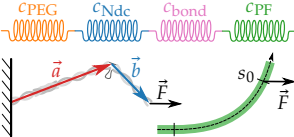
	Multistep MT (Chapter 2)	Mitotic spindle (Chapter 3)	Ndc80 stiffness (Chapter 4)
Sketch			
Experimental foundations	Dynamic instability [68] Multistep catastrophe [47–49]	Directional instability [50–56] Force-dep. MT dynamics [134] Parameter values (Tab. 3.2)	Optical trap experiments [58] Ndc80 structure [192] Elasticity of MT [243] and PF [72] PLL-PEG [238, 239]
General Simplifications and assumptions	Continuous 1d MT Constant v_{\pm} Same rate ω for each step Reflecting boundary at $x = 0$	1d model with continuous MTs One single chromosome No erroneous attachments Simple elastic linkers Fixed centrosomes	Static model, constant force Serial arrangement of springs Equal force sharing Ndc80 hinge fully flexible (FJC) Non-fluctuating, continuous PF
Additional assumptions / restrictions of mathematical model	Steady state of bounded regime Approximation for unbounded regime Exact for $t \rightarrow \infty$	One-sided model MTs permanently attached No confinement at centrosome Mean-field: $v_k = \text{const}$ Exact for $M \rightarrow \infty$	<i>no further assumptions</i>
Model extensions	<i>no extensions</i>	Poleward MT flux (Sec. 3.4.1) Position-dep. PEFs (Sec. 3.4.2) Non-pushing MTs (Sec. 3.4.3)	Catch bond (Sec. 4.3.5) Qualitative elastic model of Ndc80–MT bond (Fig. 4.26)
Examined parameter changes	Number of catastrophe steps n	Linker stiffness c MT number M MT flux v_f , PEFs k , ω_c^{kin}	Number of Ndc80 complexes n Attachment point on PF s_0
Decisive mechanisms and insights	Multistep catastrophe ($n > 1$) → smaller $\text{Var}(\tau_+)$ → lighter tailed, non-monotonic length distributions	$v_k(F)$ -relation as phase space for two-sided model: Bistability → oscillations Fixed point → no oscillations Boundaries for c , M , v_f , ω_c^{kin}	Ndc80, MT and PF structure explain strain stiffening Maybe catch bond

Table 5.1: Summary of the models used in this thesis. The table is not complete, but shows a selection of the most important features of each model.

¹ The FJC model of the Ndc80 complex could even be solved analytically, see Eqs. (4.9) to (4.13). Eq. (4.30), which defines the shape of a PF under force, had to be solved numerically, apart from the analytical approximation for large forces in Eq. (4.33).

² Eq. (2.9) is a system of $n + 1$ partial differential equations. Even in the case $n = 1$, i.e., with an ordinary single step catastrophe as in the Dogterom–Leibler model, a solution requires much effort, in particular if the reflecting boundary is taken into account [261].

³ After applying the reflecting boundary condition in the steady state, the system of $n + 1$ FPEs (2.9) turns into a system of n first order linear differential equations (2.13), which can be handled easily.

Once the models were designed in Chapters 2–4, we introduced mathematical descriptions as a basis for a thorough analysis. While the initial assumptions made for the model of the Ndc80, MT and PF stiffnesses already allowed for an exact mathematical solution,¹ the mathematical approaches presented in Chapters 2 and 3 have several restrictions and may require further simplifications. The system of FPEs (2.9) reflects the model of multistep MT dynamics without loss, but can not be solved offhand in general.² Therefore, we restricted our solutions to the steady state distributions in the bounded regime³ (Figs. 2.10 and 2.11) and to a Gaussian approximation in the unbounded regime (Fig. 2.13). In the mitotic spindle model, several further assumptions were necessary to set up the viable FPEs (3.10) and (3.11) in the first place: we considered only one side of the spindle with permanently attached MTs and without centrosomes, and started from a strong mean-field approximation neglecting fluctuations in the kinetochore velocity. Again, we could only obtain stationary solutions by incorporating the reflecting boundary condition.⁴ When we interpreted the force-velocity relations acquired from the stationary solutions as phase space diagrams for dynamic kinetochores in the full two-sided

model, we therefore always assumed that the MTs relax instantaneously to the new stationary distributions $p_{\pm}(x)$ in response to a change in the force on the kinetochore.⁵ The same assumption was made in Chapter 4 when we used equilibrium thermodynamics to determine stiffnesses of Ndc80 complexes tracing a dynamic MT and compared these values with an equilibrium model.

Despite their restrictions, the mathematical approaches proved very helpful for detecting the crucial parameters, whose influence was then analyzed further,⁶ and for revealing the decisive mechanisms of the models. For instance, the lighter tailed length distributions of multistep MTs could be traced back to a lower spread in the growth durations τ_{+} . By interpreting the force–velocity relations obtained from mean field solution of the one-sided spindle model as phase space for kinetochores in the two-sided model, we were able to link the occurrence or suppression of kinetochore oscillations to the absence or presence of fixed points, respectively. Moreover, the extensions we added to the models in later sections could be included in the mathematical approaches. These extensions were either based on known biological features neglected in the basic model, e.g., MT flux and PEFs in the mitotic spindle, or they were hypotheses that brought the model in line with experimental results like the force-enhanced Ndc80–MT binding.

Chapter 4 differs from the former two in the sense that it does not only contain purely theoretical work but also a reanalysis of experimentally obtained data. The availability of experimental data allowed for a direct comparison with the model results. Discrepancies between model and experiment can motivate new hypotheses like the speculation that Ndc80 forms a catch bond to the MT, and may reveal shortcomings of the model and/or the experimental evaluation. A further difference is that the elastic Ndc80–PF model was intended to reproduce the results of a specific *in vitro* experiment while the models in Chapters 2 and 3 should resemble MT dynamics and metaphase kinetochore dynamics, respectively, in a more general way. Therefore, we discussed these models in a mostly qualitative manner, and restricted the few quantitative comparisons with experimental results to single numerical values that can be found in literature, e.g., the frequency of kinetochore oscillations.⁷ An important numerical result of the spindle model was the lower bound of linker stiffness $c_{\text{osc}} \approx 16 \text{ pN } \mu\text{m}^{-1}$ for the occurrence of oscillations, since it gives insights into the elastic properties of the kinetochore. The Ndc80 experiments of Volkov, Huis in 't Veld *et al.* [58, 59] presented in Chapter 4 provided the first approach to measure this value. For wild type Ndc80, we obtained stiffnesses in a range of about⁸ $20 \text{ pN } \mu\text{m}^{-1}$ to $200 \text{ pN } \mu\text{m}^{-1}$, which is above c_{osc} and leaves room for further possibly elastic

⁴ The solution is formally expressed by Eq. (3.18), which has to be evaluated and normalized numerically.

⁵ More precisely, we assumed that the time scale of MT relaxation is much smaller than the time scale of kinetochore dynamics.

⁶ We only analyzed the few parameters listed in Tab. 5.1 and never varied more than two of them at the same time. The only exception is Sec. 3.4.4, where we adjusted eight parameters to reproduce numerical values measured in PtK1 cells.

⁷ Given the different sources for the input parameters in Tab. 3.2 and the strong simplifications of the spindle model, a theoretical result that predicts the correct order of magnitude can already be considered satisfactory. An example is the model prediction that directional instability is suppressed by flux velocities above $v_f \sim 3 \text{ nm s}^{-1}$ (see Fig. 3.20) while *in vivo* kinetochore oscillations still occur with flux velocities up to 10 nm s^{-1} .

⁸ See for instance Fig. 4.15. Note the different stiffness units used throughout Chapters 3 and 4, which are $\text{pN } \mu\text{m}^{-1}$ and pN nm^{-1} , respectively.

⁹ Examples are the Knl1 and the Mis12 protein complexes, which, together with the Ndc80 complex, build the so called *KMN network* [237].

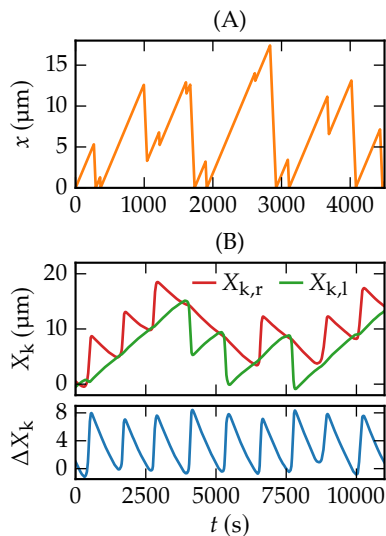


Figure 5.1: MT vs. kinetochore oscillations. While the length x of a *single* free MT exhibits stochastic switches between growth and shrinkage (A, MT in the bounded regime with a single step catastrophe), the *collective* dynamics of two opposite MT ensembles that are coupled via a chromosome results in regular oscillations of the two kinetochores with a distinct frequency (B, basic unconfined model with $M = 100$ and $c = 20 \text{ pN } \mu\text{m}^{-1}$).

proteins between the Ndc80 complexes and the inner kinetochore not present in the experiments.⁹

All of the models used in the last three chapters had in common that one or multiple MTs played a major role. Thereby, the three chapters illustrated exemplarily the importance of MTs during the whole cell cycle of a eukaryotic cell. In Chapter 2, we examined the characteristic dynamic instability of MT polymerization that follows from the hydrolysis of the GTP molecules that are bound to the tubulin dimers. Following experimental results [47–49], we extended the empirical Dogterom–Leibler model [29, 30] in a way that the catastrophe is described as a multistep process. The resulting length distributions had a lighter tail than with a single step catastrophe, and in the bounded regime, they had a maximum if rescues were allowed. Given that the number of required steps depends on the concentration of MAPs [49], the cell does not only have ways to adapt the mean MT lengths but also the shape of the distribution. For instance, during metaphase, concentration of MT lengths around the distribution maximum may help in positioning the chromosomes in the metaphase plate or in maintaining spindle length and position. During interphase on the other hand, where the MTs should reach the cell cortex, an exponential length distribution with a heavier tail might be advantageous.

While the polymerization dynamics of free MTs has a stochastic nature with unpredictable trajectories, we showed in Chapter 3 that the stochastic dynamics of individual MTs can be regularized if multiple MTs are coupled to each other and to an external force, see Fig. 5.1. Such a force-coupling can be found in the mitotic spindle, where two ensembles of MTs emerging from the opposite spindle poles are connected to a chromosome via kinetochores. In the one-sided spindle model with only one MT ensemble, the cooperative dynamics results in a kinetochore motion with a constant velocity that depends on an applied force and may be bistable in a certain force range. This bistability leads to kinetochore oscillations if two one-sided systems are elastically coupled in the full two sided model. Thereby, we were able to interpret the directional instability of chromosomes observed in various vertebrate cells [50–56] as an emergent phenomenon of the collective polymerization dynamics of multiple MTs. The stiffness of the MT–kinetochore linkers turned out to be a crucial parameter for the occurrence of both bistability and directional instability.

Our mathematical solution allowed us to easily include several extensions to the basic model. First, we showed that fast poleward flux suppresses kinetochore oscillations by inducing a fixed point in the phase space of kinetochore motion. Later, we analyzed how PEFs align the kinetochores at the spindle equator and assure for

regular oscillations. Moreover, we were able to explain further effects of PEFs on some oscillation characteristics like frequency and amplitude as they have been observed experimentally. As a third extension, we accounted for the experimental evidence that kinetochore MTs can only apply tensile forces. Then, we found that oscillations are only maintained if catastrophes are induced for MTs whose tip reaches the kinetochore. Finally, we applied our gained knowledge to reproduce kinetochore oscillations as observed in PtK1 cells quantitatively.

Though we did not discuss whether chromosome oscillations are just an artifact or really have a biological function,¹⁰ our model still provided new insights into mitosis by linking the occurrence of oscillations with several properties of the mitotic spindle. Thereby, we were able to rationalize several experimental findings and to deduce new hypotheses that bring these experiments in line with our model. For instance, we discussed the several effects that phosphorylation of Hec1 has on kinetochore oscillations. Moreover, we showed that the dichotomy between central and peripheral chromosomes in PtK1 cells can not be deduced to differences in PEFs as proposed earlier [105]. Instead, different linker stiffnesses or densities of catastrophe promoting proteins are more likely explanations.

The importance of the MT–kinetochore linker stiffness for the occurrence of directional instability raised interest in the elastic properties of the kinetochore. A first approach to measure the stiffness of the rod-like Ndc80 complexes, which mediate the linkage between the MT and the kinetochore, was provided by the optical trap experiments of Volkov, Huis in 't Veld *et al.* [58, 59]. Again, the MT and the GTP hydrolysis played an important role: the energy from the hydrolysis is stored mechanically in the MT lattice and its release allows the depolymerizing MT to pull the attached glass bead against the restoring force of the optical trap. In Chapter 4, we reanalyzed these experiments using a novel time-tracing method. Thereby, we generated a vastly higher amount of stiffness data, which allowed for a more thorough analysis of the strain-stiffening behavior. We were able to determine stiffening exponents and to compare the wild type with three further Ndc80 variants. Moreover, the stiffness measurements did not depend on the polymerization state of the attached MT.

Our elastic model revealed that the linear stiffening can be seen as a hint for a catch-bond-like Ndc80–MT attachment. The effective stiffness of PF bending depends strongly on the attachment point of the Ndc80 complex. Since experimental results, which were obtained under slightly different conditions, proposed that Ndc80 can only bind to straight PFs [131, 222], the independence of the stiffness from the MT state might be explained by a negligible

¹⁰ A possible function of chromosome oscillations is discussed in the outlook below.

contribution of PF. If, however, the conditions in the experiments of Volkov Huis in 't Veld *et al.* allowed for Ndc80 binding to curved PFs, the independence from MT state enforces recent results that the PF curvature does not depend on MT state either [72]. Moreover, in the context of the spindle model from Chapter 3, binding to curved PFs would mean that the effective linker stiffness does not only originate from the elastic properties of the kinetochore but also contains contributions from PF bending.

In the following final paragraphs, we briefly outline how the models could be extended in future work. A first step can always be to soften the simplifications. In the multistep MT model for instance, one could discard the assumptions of equal step rates.¹¹ This could be included in the current model without further modifications as the equations for the length distributions could still be set up and solved as shown in Chapter 2 if each step occurred with an individual rate ω_i . Also length dependent rates and velocities might be interesting, e.g., for MTs growing against an elastic barrier [180]. However, this could not be incorporated simply into our mathematical framework, which is, for the bounded state, based on numerically diagonalizing the *constant* coefficient matrix M in Eq. (2.13). Any model that has a finer-grained starting point than the continuous one-dimensional MT¹² requires a whole new approach. Moreover, such models would go beyond our original aim to examine the effects of a multistep catastrophe on the MT length distributions.

For the model of the mitotic spindle, one can think of various modifications and extensions, many of which have already been realized in the models reviewed in Sec. 3.2.1. For instance, the assumptions listed in Tab. 5.1 could be modified or discarded by replacing the simple elastic MT–kinetochore linkers with viscoelastic ones [105] or by including interpolar and/or astral MTs in order to take centrosome dynamics into account [162, 163]. The probably greatest but at the same time most complicated step towards a realistic model would be an extension to two or three dimensions with multiple chromosomes that interact sterically. Among many other things, a multidimensional model might answer whether the dichotomy between central and peripheral chromosomes observed in PtK1 cells [55] has geometric reasons. Finally, since we concentrated on metaphase throughout the chapter, a logical step would be to apply the model to the other mitotic phases.¹³ Of particular interest would be the prometaphase because recent experiments suggest a function of kinetochore oscillations for the correction of erroneous attachments [262, 263]: Aurora A kinase can stimulate detachment of erroneous MTs by phosphorylating the binding site on the kinetochore. Since Aurora A is most highly concentrated around the spindle poles, kinetochore oscillations with a

¹¹ A possible reasoning for unequal step rates is to interpret a step as an individual catastrophe of a single protofilament that occurs with a constant rate ω_{PF} , and to assume that the MT undergoes a catastrophe if n protofilaments have been destabilized [37]. If the protofilament catastrophes occur independently, the step rate will shrink with each step i as there is one protofilament less to potentially stop growing. Then, the step rate can be expressed as $\omega_i = (N - i)\omega_{PF}$, where N is the total number of PFs. In the same picture, one could assume that an individual catastrophe induces catastrophes of neighboring protofilaments resulting in a cascade with an increasing step rate.

¹² Some finer-grained models are illustrated in Fig. 1.1.

¹³ In Sec. 3.5, we shortly discussed the applicability to anaphase A.

sufficiently large amplitude are required to trigger this correction mechanism.¹⁴ In the same experiments, chromosome oscillations in cancer cells were observed to be attenuated. This might be a reason for *chromosomal instability*, a behavior that is typical for cancer cells and is characterized by significant numbers of uncorrected erroneous attachments leading to chromosome missegregation. To incorporate the Aurora A correction mechanism into our current model, one first had to allow for erroneous attachments and then could define a detachment rate that depends on the absolute kinetochore position analogously to the position-dependent PEFs in Sec. 3.4.2.

Lastly, we can also think of modifying the model of Ndc80–PF stiffness in several ways. Besides minor modifications like allowing for unequally extended linkers or considering thermal fluctuations of the PF, the probably most important step would be to include the dynamic MT tracing, which requires a continual detachment and reattachment of individual Ndc80 complexes. The attachment dynamics may result in an effective stiffness, which could explain the current discrepancy between model and experiment. Moreover, a dynamic model better reflects the dynamic nature of the experiment and would allow us to go beyond the static stiffness results by discussing dynamic quantities like detachment rates or stall durations.

Finally, since both MT dynamics, which is subject of Chapter 2, and the Ndc80 stiffness treated in Chapter 4 are crucial parts of the mitotic spindle model in Chapter 3, the question arises whether and how these independently developed and discussed models could be merged. While a mitotic spindle model with n -step MT dynamics could be easily implemented in stochastic simulations, an incorporation into our mathematical model is not possible: after eliminating one equation by use of the reflecting boundary condition, we would still have to solve a system of n stationary FPEs with coefficients that depend on the linker extensions to obtain the distribution of linker extensions $p(x)$. In contrast, MT–kinetochore linkers that stiffen under force can be included both in the computational and in the mathematical model by defining a superlinear force $F_{\text{mk}}(x)$ that replaces the linear relation $F_{\text{mk}}(x) = -cx$ used for the elastic linkers. In the FPEs (3.10) and (3.11), which result from the mean-field approach, an alternative $F_{\text{mk}}(x)$ changes the relative MT–kinetochore velocities $v_{\pm}(x)$. Though the change might complicate the following calculations, a solution as described for the current model should still be feasible.

¹⁴ A similar correction mechanism with Aurora B kinase, which is concentrated at the centromeres (see Fig. 3.4), was discussed in the model of Banigan *et al.* [57].

APPENDIX

Appendix to Chapter 2

A

A.1 Solution for an age-dependent catastrophe rate

Jemseena and Gopalakrishnan [32] found that in case of an age-dependent catastrophe rate $\omega_c(\tau)$ and a reflecting boundary at $x = 0$, the Laplace transformed overall probability density $\tilde{p}(s)$ of MT lengths is given by

$$\tilde{p}(s) = J_0 \frac{1 - \zeta(s)}{s - r(1 - \zeta(s))}, \quad (\text{A.1})$$

$$\zeta(s) = \int_0^\infty \omega_c(\tau) \exp(-v_+ \tau s - \Omega(\tau)) d\tau, \quad (\text{A.2})$$

$$\Omega(\tau) = \int_0^\tau \omega_c(\tau') d\tau'. \quad (\text{A.3})$$

Using Eq. (2.23), the normalization condition, which defines the constant J_0 , can be expressed as $\tilde{p}(0) = 1$.¹ Substituting the catastrophe rate $\omega_c(\tau) = -\partial_\tau \ln P_{\tau_+}(\tau)$ that hat follows from an arbitrary distribution of growth times,² we find $\Omega(\tau) = -\ln P_{\tau_+}(\tau)$ and

$$\begin{aligned} \zeta(s) &= \int_0^\infty \omega_c(\tau) P_{\tau_+}(\tau) e^{-v_+ \tau s} d\tau \\ &= \int_0^\infty p_{\tau_+}(\tau) e^{-v_+ \tau s} d\tau \\ &\approx 1 - v_+ \langle \tau_+ \rangle s = 1 - \langle x_+ \rangle s. \end{aligned} \quad (\text{A.4})$$

The last line is valid for small s . Next, we substitute $x = v_+ \tau$ to show that $\zeta(s)$ is the Laplace transform of the probability density of growth distances:

$$\begin{aligned} \zeta(s) &= \int_0^\infty \frac{1}{v_+} p_{\tau_+} \left(\frac{x}{v_+} \right) e^{-sx} dx \\ &= \int_0^\infty p_{x_+}(x) e^{-sx} dx = \tilde{p}_{x_+}(s). \end{aligned} \quad (\text{A.5})$$

For the purpose of normalization, we use the approximated form of $\zeta(s)$ from Eq. (A.4):

$$1 = \tilde{p}(0) = J_0 \frac{\langle x_+ \rangle s}{s - r \langle x_+ \rangle s} \Big|_{s=0} = J_0 \frac{\langle x_+ \rangle}{1 - r \langle x_+ \rangle}, \quad (\text{A.6})$$

$$J_0 = \frac{1}{\langle x_+ \rangle} - r. \quad (\text{A.7})$$

¹ The normalization condition can be written as

$$1 = \int_0^\infty p(x) dx = \langle x^0 \rangle = \tilde{p}(s),$$

where the last step follows from Eq. (2.23),

$$\langle x^m \rangle = (-1)^m \frac{\partial^m}{\partial s^m} \tilde{p}(s) \Big|_{s=0},$$

with $m = 0$.

² See Eq. (2.20).

Substituting Eqs. (A.5) and (A.7) into Eq. (A.1) finally results in $\tilde{p}(s)$ as given in Eq. (2.21).

A.2 Stationary solution for an infinite step catastrophe process

In the limit $n \rightarrow \infty$, the Laplace transformed probability density of growth distances is $\tilde{p}_{x_+}(s) = e^{-s/c_0}$. For the Laplace transform of the overall probability density of MT lengths in presence of rescue events follows:

$$\begin{aligned}\tilde{p}(s) &= (c_0 - r) \frac{1 - e^{-s/c_0}}{s - r(1 - e^{-s/c_0})} \\ &= (c_0 - r) \sum_{k=0}^{\infty} r^k \left(\frac{1 - e^{-s/c_0}}{s} \right)^{k+1} \\ &= (c_0 - r) \sum_{k=0}^{\infty} r^k \sum_{l=0}^{k+1} \binom{k+1}{l} (-1)^l \frac{e^{-ls/c_0}}{s^k + 1}\end{aligned}\quad (\text{A.8})$$

Inverse Laplace transformation yields:

$$\begin{aligned}p(x) &= (c_0 - r) \sum_{k=0}^{\infty} r^k \sum_{l=0}^{k+1} \frac{(k+1)(-1)^l}{l!(k+1-l)!} \left(x - \frac{l}{c_0}\right)^k \Theta\left(x - \frac{l}{c_0}\right) \\ &= (c_0 - r) \sum_{l=0}^{\infty} \frac{(-1)^l}{l!} \Theta\left(x - \frac{l}{c_0}\right) \sum_{k=l-1}^{\infty} \frac{(k+1)}{(k+1-l)!} \left(r\left(x - \frac{l}{c_0}\right)\right)^k \\ &= (c_0 - r) \sum_{l=0}^{\infty} \frac{(-1)^l}{l!} \Theta\left(x - \frac{l}{c_0}\right) \left(r\left(x - \frac{l}{c_0}\right)\right)^{l-1} \left(l + r\left(x - \frac{l}{c_0}\right)\right) \exp\left(r\left(x - \frac{l}{c_0}\right)\right) \\ &= (c_0 - r) e^{rx} \left[\Theta(x) - (1 + r(x - c_0^{-1})) e^{-r/c_0} \Theta(x - c_0^{-1}) \right. \\ &\quad \left. + \frac{1}{2} (r(x - 2c_0^{-1})) (2 + r(x - 2c_0^{-1})) e^{-2r/c_0} \Theta(x - 2c_0^{-1}) - \dots \right].\end{aligned}\quad (\text{A.9})$$

We see that the probability density increases exponentially until it has a step discontinuity at the (now deterministic) growth length $x = c_0^{-1}$. At each multiple of the growth length, the function is non-analytic since an additional term contributes thereafter. The first two non-analyticities can be seen in Fig. 2.11C. In absence of rescues ($r = 0$) the probability density correctly turns into the step function $c_0(\Theta(x) - \Theta(x - c_0^{-1}))$.

Appendix to Chapter 3

B

B.1 Behavior of linker length distributions near the boundary linker extensions

For $v_k > 0$ ($v_k < 0$), the linker length distributions $p_+(x, t)$ ($p_-(x, t)$) as given by Eq (3.18),

$$p_{\pm}(x) = \frac{\pm \mathcal{N}}{v_{\pm}(x)} \exp\left(-\int \left(\frac{\omega_c(x)}{v_+(x)} + \frac{\omega_r(x)}{v_-(x)}\right) dx\right), \quad (\text{B.1})$$

have singularities or peaks at $x = x_{\max}$ ($x = x_{\min}$) where $v_+(x_{\max}) = 0$ ($v_-(x_{\min}) = 0$), see Fig. 3.12. These singularities occur because the integral

$$I(x) \equiv -\int \left(\frac{\omega_c(x)}{v_+(x)} + \frac{\omega_r(x)}{v_-(x)}\right) dx, \quad (\text{B.2})$$

in the exponent and the prefactor $1/v_{\pm}(x)$ in the expression (B.1) diverge for $v_+(x_{\max}) = 0$ ($v_-(x_{\min}) = 0$).

To investigate the nature of these singularities or peaks in more detail, we expand around x_{\max} and x_{\min} to the leading order, starting with x_{\max} . Since $v_-(x_{\max}) \neq 0$, the second term of $I(x)$ in Eq. (B.2) simply yields a finite factor

$$\beta(x) \equiv \exp\left(-\int \frac{\omega_r(x)}{v_-(x)} dx\right). \quad (\text{B.3})$$

For the first term, we find for $x \lesssim x_{\max}$

$$\frac{\omega_c(x)}{v_+(x)} \approx \frac{\alpha_+ + 1}{x_{\max} - x}, \quad (\text{B.4})$$

$$\text{with } \alpha_+ + 1 = \frac{\omega_c^0 F_+}{c v_+^0} \left(\frac{v_k}{v_+^0}\right)^{-1+F_+/F_c} > 0, \quad (\text{B.5})$$

resulting in

$$I(x) \approx (\alpha_+ + 1) \ln(x_{\max} - x) + \ln \beta(x), \quad (\text{B.6})$$

$$\exp(I(x)) \approx \beta(x_{\max}) (x_{\max} - x)^{\alpha_+ + 1}. \quad (\text{B.7})$$

Because $\alpha_+ + 1 > 0$, we have for $x \lesssim x_{\max}$

$$p_-(x) \approx -\frac{\mathcal{N}}{v_-(x_{\max})} \exp(I(x)) \propto (x_{\max} - x)^{\alpha_+ + 1} \approx 0, \quad (\text{B.8})$$

and, therefore, $p(x) \approx p_+(x)$. Analyzing the prefactor

$$\frac{1}{v_+(x)} \approx \frac{\text{const}}{x_{\max} - x} > 0, \quad (\text{B.9})$$

we finally find a power law behavior

$$\begin{aligned} p(x) \approx p_+(x) &\approx \mathcal{N} \text{const} \beta(x_{\max})(x_{\max} - x)^{\alpha_+} \\ &\propto (x_{\max} - x)^{\alpha_+} \end{aligned} \quad (\text{B.10})$$

for x approaching x_{\max} .

In an analogous manner, we expand around $x = x_{\min}$ to the leading order and find a power law behavior

$$\begin{aligned} p(x) &\approx p_-(x) \propto (x - x_{\min})^{\alpha_-}, \\ \text{with } \alpha_- + 1 &= \frac{\omega_r^0 F_-}{c v_-^0} \left(\frac{v_k}{v_-^0} \right)^{-1+F_-/F_r} > 0. \end{aligned}$$

The resulting dependencies of the exponents on the linker stiffness c and the kinetochore velocities $|v_k|$,

$$\alpha_{\pm} + 1 \propto 1/c \quad \text{and} \quad \alpha_{\pm} + 1 \propto \left| \frac{v_k}{v_{\pm}^0} \right|^{-1-|F_{\pm}/F_{c,r}|},$$

are used and discussed in Sec. 3.3.1. Since $\alpha_{\pm} > -1$, the probability densities are always normalizable despite the singularities at x_{\max} and x_{\min} .

¹ for sufficiently large c or sufficiently large $|v_k|$

If $\alpha_{\pm} < 0$,¹ the resulting total distributions $p(x) = p_+(x) + p_-(x)$ are peaked around x_{\max} or x_{\min} . In the unstable regime around $v_k \approx 0$, however, the linker length distribution $p(x)$ becomes broad without pronounced peaks. This behavior is visualized in Fig 3.12. In this regime, the kurtosis

$$\frac{\langle (x - \langle x \rangle)^4 \rangle}{\langle (x - \langle x \rangle)^2 \rangle^2},$$

which is a measure of the sharpness of the peaks of the distribution $p(x)$ around x_{\min} and x_{\max} , becomes minimal indicating a broad distribution $p(x)$.

B.2 Mean-field theory assuming identical linker extensions

Here, we present an alternative but simpler mean-field approximation for the one-sided model.² We assume that all linkers have *identical* extensions ($x_i \approx x$ for all i), i.e., all MTs have identical

² This approach is discussed in more detail in my master thesis [95].

lengths and are in the same state (growing or shrinking). While we assume in the mean-field approach presented in Sec.3.3.1 that all MTs approximately *decouple* as soon as kinetochore velocity fluctuations are neglected ($v_k = \text{const}$), here we assume a *strong coupling* between MTs. Accordingly, the compound linker distribution does no longer factorize but can still be described by a single function $p_{\pm}(x, t)$, which is the probability to find *all* MTs in the growing (+) or shrinking (-) state with a MT–kinetochore linker extension x .

While this approximation appears much more restrictive regarding the MT length (and thus the linker extension) distribution, it allows us to include stochastic fluctuations of the kinetochore velocity, which we neglected in the mean-field approach in the main text. Here, the kinetochore velocity is a stochastic variable, depending on the stochastic (but identical) linker extension x :

$$v_k = \frac{1}{\gamma}(F_{\text{ext}} + cMx). \quad (\text{B.11})$$

The FPEs for the probability densities $p_{\pm}(x, t)$ are the same as for the $v_k = \text{const}$ approximation (Eqs (3.10) and (3.11)), but with a different relative velocity

$$\begin{aligned} v_{\pm}(x) &= v_{m\pm}(x) - v_k \\ &= v_{\pm}^0 \exp\left(-\frac{cx}{F_{\pm}}\right) - \frac{1}{\gamma}(F_{\text{ext}} + cMx). \end{aligned} \quad (\text{B.12})$$

The maximum and minimum MT–kinetochore distances $x_{\text{max},\text{min}}$ are reached if the relative velocity vanishes, $v_{\pm}(x_{\text{max},\text{min}}) = 0$, and Eq. (B.11) is fulfilled. Then, both the kinetochore and the MT tips move with the same velocity \tilde{v}_{\pm} given by Eq. (3.15):

$$\tilde{v}_{\pm} \equiv \frac{MF_{\pm}}{\gamma} W\left(\frac{\gamma v_{\pm}^0}{MF_{\pm}} \exp\left(\frac{F_{\text{ext}}}{MF_{\pm}}\right)\right). \quad (\text{B.13})$$

The corresponding MT–kinetochore distances are

$$\begin{aligned} x_{\text{max}/\text{min}} &= (F_{\pm}/c) \ln(v_{\pm}^0/v_k) \\ &= -\frac{F_{\pm}}{c} \left(\frac{F_{\text{ext}}}{MF_{\pm}} - W\left(\frac{\gamma v_{\pm}^0}{MF_{\pm}} e^{F_{\text{ext}}/MF_{\pm}}\right) \right), \end{aligned}$$

which agrees with Tab. 3.3, if Eq. (B.13) is used to eliminate v_k in favor of F_{ext} .

With the new relative velocities $v_{\pm}(x)$ from Eq.(B.12), we finally obtain a solution for the probability densities $p_{\pm}(x, t)$ analogous to Eq. (3.18).³ This solution can be used to calculate the mean linker

³ As with the $v_k = \text{const}$ approach, the probability densities $p_{\pm}(x)$ may diverge at the boundaries $x_{\text{max}/\text{min}}$. Therefore, we also need to expand them to a power function analogously to Sec. B.1 and extrapolate the numerical integration results to calculate the normalization constant [95].

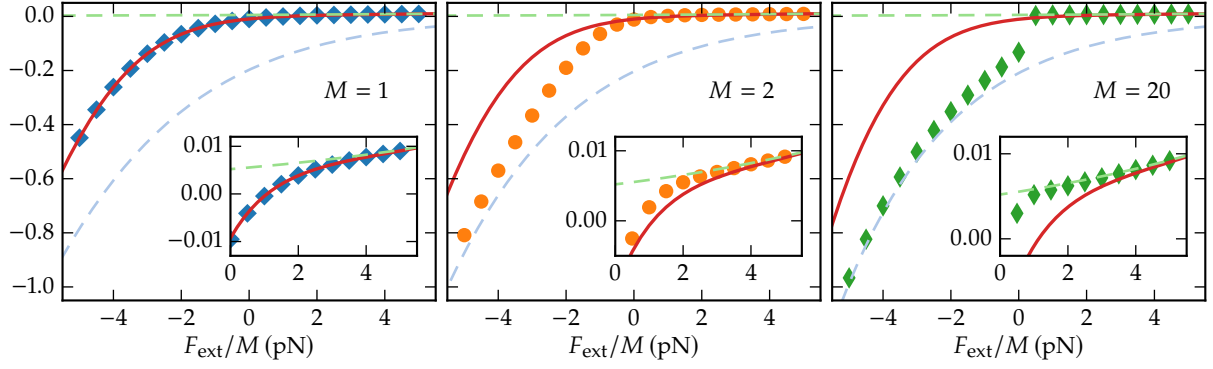
extensions $\langle x \rangle$ and the mean kinetochore velocity

$$\langle v_k \rangle = \frac{1}{\gamma} (F_{\text{ext}} + cM \langle x \rangle) \quad (\text{B.14})$$

as a function of the external force F_{ext} . This type of mean-field approach will never result in a bistable force–velocity relation as we always obtain a unique mean linker extension $\langle x \rangle$ and, according to Eq. (B.14), a unique mean kinetochore velocity as a function of the force F_{ext} . In order to map out bistability, it is technically advantageous to consider $\langle x \rangle$ and, thus, F_{ext} as a function of the kinetochore velocity v_k as in the mean-field approach in the main text. Then, a bistable force–velocity relation can emerge as a result of a non-monotonous (but unique) mean linker extension $\langle x \rangle$ as a function of v_k . Nevertheless, we find hints to a bistable behavior also in the mean-field theory with identical linker extensions: the probability density $p(x) = p_+(x) + p_-(x)$ becomes bimodal around $F_{\text{ext}} = 0$, which corresponds to bistable temporal switching of the whole ensemble between two linker extensions and, thus, two kinetochore velocities v_k .

In the present approach, we always assume identical linker extensions *and* identical MT states (all MTs growing or all MTs shrinking), while bistability in the $v_k = \text{const}$ mean-field approach in the main text is the result of a very broad and heterogeneous stationary linker extension distribution where parts of the MT population switch from shrinking to growing if the velocity is increased in the bistable region around $v_k \approx 0$. In this bistable region, not all MTs are in the same state anymore, and the assumption of identical linker extensions and states becomes invalid.

By definition, the mean-field theory with identical linker extensions is exact for a system with a single MT ($M = 1$), as can be seen in Fig. B.1. For an ensemble of MTs—even for the next smallest number $M = 2$ —the approach fails, however, to provide a good approximation of the mean kinetochore velocity. Then, even the simple assumption of exclusively shrinking or growing MTs, which results in $v_k = \tilde{v}_{\pm}$ from Eq. (B.13), gives a better approximation in the large force regimes. For $M = 20$, which is the relevant case for mammalian cells, the mean-field theory with identical linker extensions differs strongly from the simulation results. We conclude that the $v_k = \text{const}$ mean-field approach described in Sec. 3.3.1 is superior for analyzing bistability and oscillations in the spindle model.



B.3 Alternative polar ejection force distributions

In Sec. 3.4.2, we discuss in detail linearized PEFs, $F_{\text{PEF}}(X_k) = \pm k X_k$. Fig. B.2 shows that the results for a harmonic and a square root dependence,

$$F_{\text{PEF}}(X_k) = \pm k_2 X_k^2, \quad (\text{B.15})$$

$$F_{\text{PEF}}(X_k) = \pm k_{1/2} |X_k|^{1/2}, \quad (\text{B.16})$$

are qualitatively similar to the results for linearized PEFs in Fig. 3.21.

Figure B.1: Mean-field theory assuming identical linker extensions. The mean kinetochore velocities resulting from the approximation of identical linker extensions (red lines) are compared to simulation results (markers). For a one-sided system with a single MT ($M = 1$), the alternative mean-field approach is exact by definition and gives correct mean velocities. If $M > 1$, even the simple assumption of exclusively shrinking or growing MTs (\bar{v}_{\pm} from Eq (B.13)) gives a better approximation (green and blue dashed lines). In contrast to Fig. 3.11, where we aimed to detect the two bistable states separately in each simulation, here we average the simulations over a long period to measure the total mean velocity.

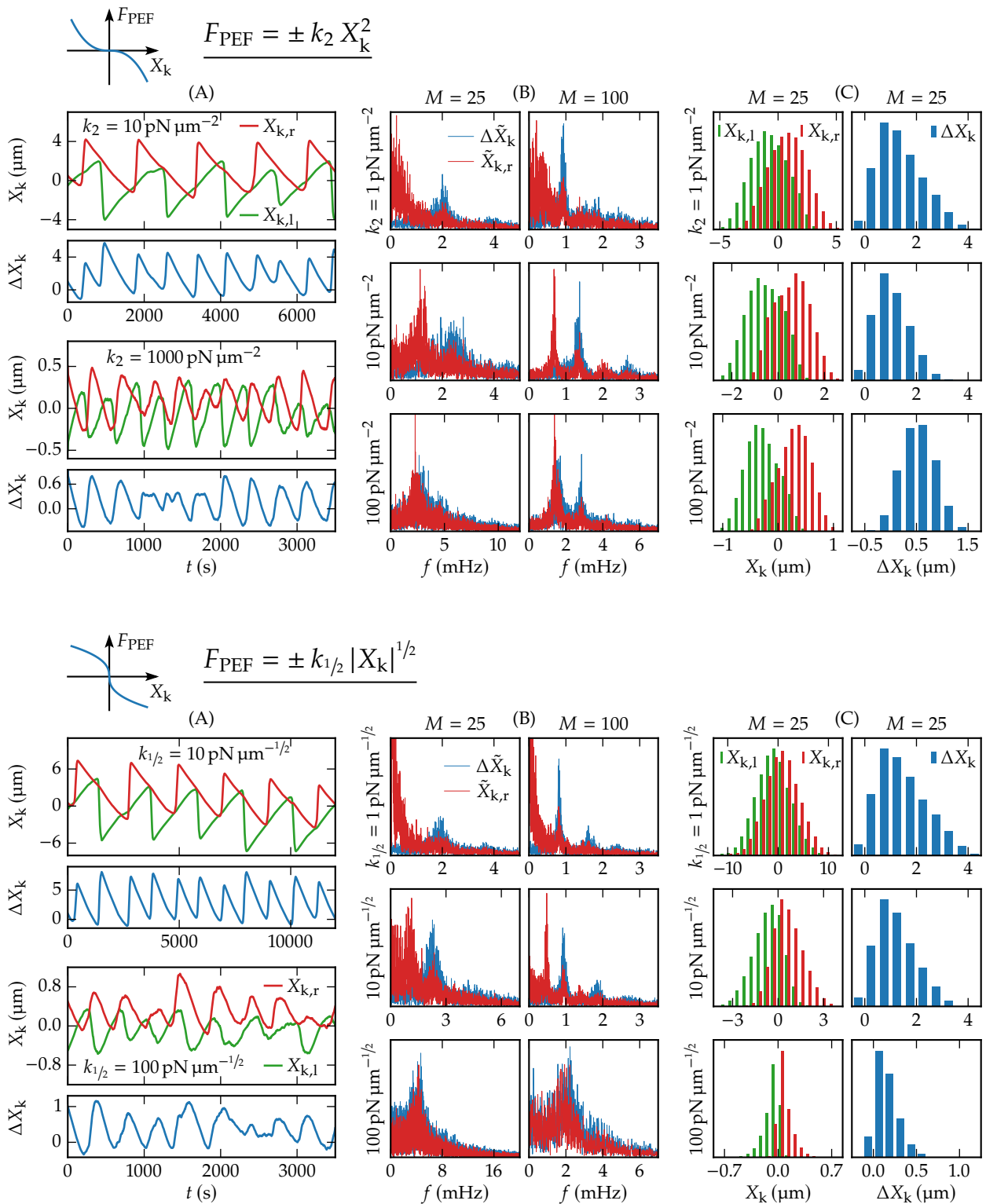


Figure B.2: Influence of alternative polar ejection forces that are a square (top) or a root function (bottom) of the kinetochore position. Qualitatively, the effects are the same as for linear PEFs which are discussed in Sec. 3.4.2. The values of k_2 and $k_{1/2}$ have been chosen so that the PEFs at a position of $X_k = 1 \mu\text{m}$ have the same strength as for the corresponding value of k in Fig. 3.22. Only, we plot the trajectories for $k_{1/2} = 100 \text{ pN } \mu\text{m}^{-1/2}$ instead of $1000 \text{ pN } \mu\text{m}^{-1/2}$ (bottom (A)) since in the latter case the time step in the stochastic simulation has to be uncomfortably small due to the steep ascent of the PEFs around $X_k = 0$.

Appendix to Chapter 4

C

C.1 Optical traps and stiffness calibration

Optical traps or *optical tweezers* are able to trap microscopic objects in a focused laser beam [227]. Trapping can be achieved when the object has a higher refraction index than the medium and the intensity of the beam decreases perpendicularly to its symmetry axis. Then, there is an equilibrium position \vec{r}_0 , in which the net force that acts on the object due to beam refraction and scattering is zero. When the object is displaced from the equilibrium in any direction of space, it is exposed to a restoring force, which can be described in good approximation by Hooke's law with trap stiffnesses c_i :

$$F_i = -c_i (r_i - r_{0,i}), \quad (\text{C.1})$$

where usually $c_x = c_y > c_z$ when z is the axial direction of the beam. In most experiments—as well as in the experiments of Volkov, Huis in 't Veld *et al.* [58, 59]—the object is displaced in radial direction, perpendicularly to the beam. Then, we can treat the motion of the object in one dimension, which we do by assigning x as the displacement, setting $x_0 = 0$, and referring to c_x as trap stiffness c_{trap} henceforth.

When an object is trapped in a medium of temperature T , it is exposed to thermal fluctuations and, following the Hookean approximation (C.1), it behaves as a Brownian particle in a harmonic potential.¹ This knowledge can be used to obtain the trap stiffness from a sample trajectory of displacements x . Among the various methods of trap stiffness calibration that have been described in literature [227–229, 257, 258], the easiest relies on the *equipartition theorem*, which predicts that²

$$c_{\text{trap}} = \frac{k_{\text{B}}T}{\text{Var}(x)}. \quad (\text{C.2})$$

While with the temperature, only one parameter, which is easy to control, has to be measured besides the sample of displacements, a disadvantage of the equipartition method is that the overall variance is increased by a potential drift as well as any additional noise that is added to the original signal, e.g., electronic noise of the measurement devices. Therefore, the trap stiffness tends to be underestimated by Eq. (C.2) [228–230].

¹ In stochastic analysis, Brownian motion in a harmonic potential is known as *Ornstein–Uhlenbeck process* [264, 265].

² Following the equipartition theorem, the mean potential energy is equal to $k_{\text{B}}T/2$:

$$\begin{aligned} \langle U(x) \rangle &= \left\langle \frac{1}{2} c_{\text{trap}} (x - x_0)^2 \right\rangle \\ &= \frac{1}{2} c_{\text{trap}} \text{Var}(x) = \frac{k_{\text{B}}T}{2}. \end{aligned}$$

³The motion of a Brownian particle with friction coefficient γ in a harmonic potential with stiffness c is described by a Langevin equation:

$$m\ddot{x}(t) = -\gamma\dot{x}(t) - cx(t) + \sqrt{2k_B T \gamma} \eta(t).$$

The last term represents the thermal forces, where $\eta(t)$ is a white noise with

$$\langle \eta(t) \rangle = 0, \quad \langle \eta(t)\eta(t') \rangle = \delta(t - t').$$

When the motion is overdamped, as it is usually the case for an optically trapped object, we can neglect the inertial term and get

$$\dot{x}(t) + 2\pi f_c x(t) = \sqrt{2D} \eta(t),$$

with corner frequency f_c and diffusion coefficient D as defined in Eq. (C.3). Fourier transform ($x(t) \rightarrow \tilde{x}(f)$) and solving for $\tilde{x}(f)$ yields

$$\tilde{x}(f) = \frac{\sqrt{2D} \tilde{\eta}(f)}{2\pi(f_c + if)}.$$

Finally, the PSD follows as

$$S_x(f) = \langle |\tilde{x}(f)|^2 \rangle = \frac{D/(2\pi^2)}{f_c^2 + f^2} \langle |\tilde{\eta}(f)|^2 \rangle,$$

with $\langle |\tilde{\eta}(f)|^2 \rangle = 1$. [231, 266]

⁴ According to Stoke's law, the friction coefficient of a sphere with radius R in a fluid with viscosity η is $\gamma = 6\pi\eta R$. To reach a higher accuracy, further hydrodynamic corrections of Stoke's law can be applied [231].

To overcome this inaccuracy, a more elaborate method analyzes the *power spectral density* (PSD) of the displacement [266, 267], which is defined as the mean absolute square of the Fourier transform, $S_x(f) \equiv \langle |\tilde{x}(f)|^2 \rangle$. In the case of a harmonic potential, it takes the form of a Lorentzian:³

$$S_x(f) = \frac{D/(2\pi^2)}{f_c^2 + f^2}, \quad D \equiv \frac{k_B T}{\gamma}, \quad f_c \equiv \frac{c_{\text{trap}}}{2\pi\gamma}. \quad (\text{C.3})$$

The trap stiffness can be determined from the *corner frequency* f_c , which results as a fit parameter of a Lorentzian fit to the PSD of the sample trajectory $x(t)$. Since the PSD contains the whole spectral information, unwanted disturbances, for instance, drift or low frequency noise, can be recognized and eliminated before fitting in order to overcome the aforementioned disadvantages of the equipartition method [233, 267]. The PSD method has been developed further during the last 25 years, and is nowadays well-established and considered to be the most reliable method of trap stiffness calibration [227, 231–233]. A disadvantage of the PSD as compared with the equipartition method is the need to know the friction coefficient γ . It can be either obtained from the diffusion coefficient D , which is a parameter of the Lorentzian fit in Eq. (C.3), or, if the trapped object is spherical, γ can be calculated by Stoke's law.⁴

C.2 Further examples of stiffness time-tracing

Fig. C.1 shows twelve more examples of stiffness time-tracing during individual experiments, three for each Ndc80 variant.

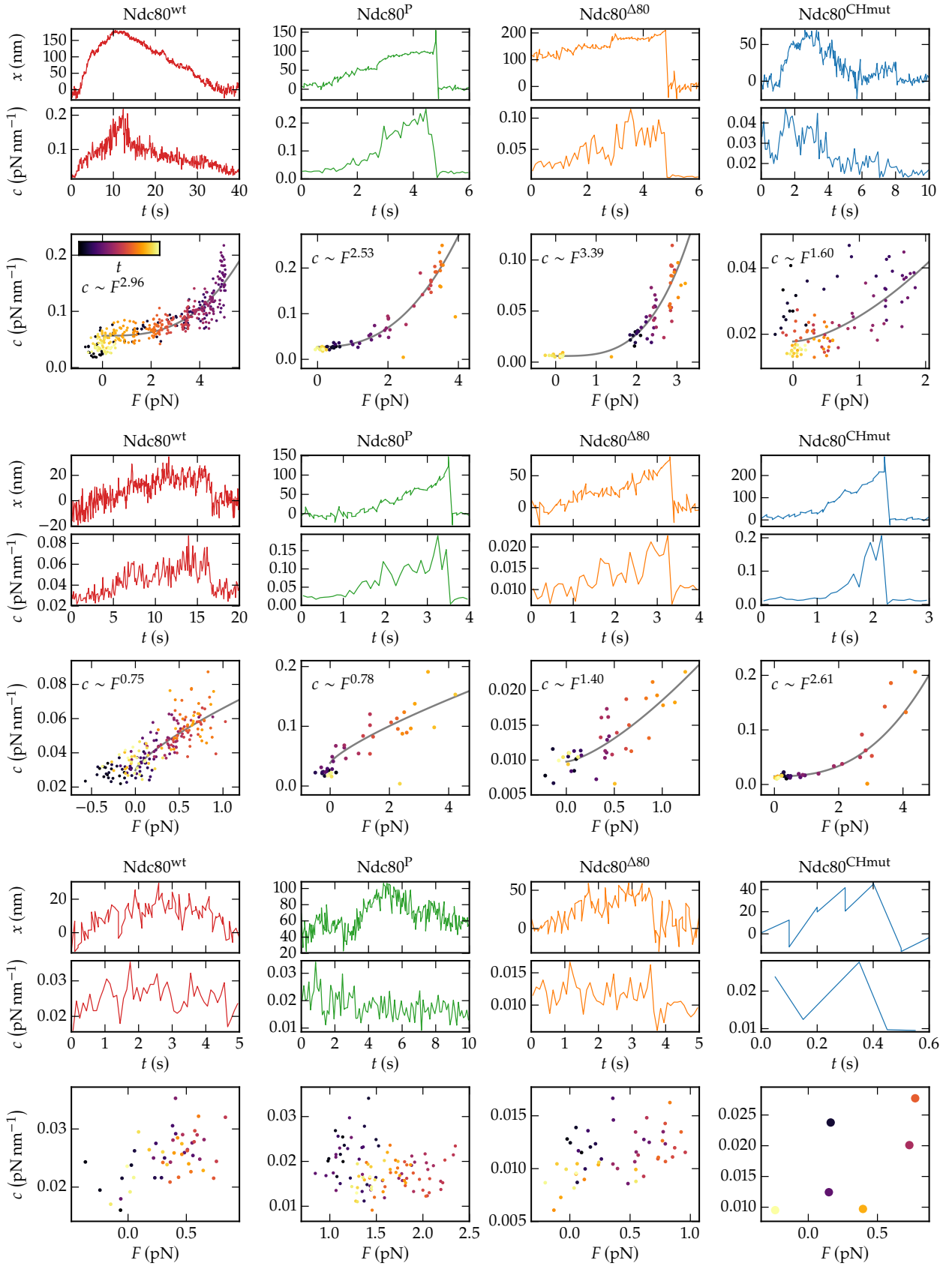


Figure C.1: Twelve more example experiments as explained in Fig. 4.10. The gray lines show power fits to the stiffness–force relations that exhibit strain stiffening, giving the stiffening exponents depicted in Fig. 4.14.

C.3 Robust regression by minimization of the Huber loss

Here, we describe the robust fitting procedure of power law functions $c(F) = aF^b + c_0$ to the force–stiffness data (F_i, c_i) . Since the stiffness values that result from the time-tracing analysis exhibit a high spread (see Fig. 4.13), we perform the power fits by use of a robust fitting method instead of a least squares fit, which is sensitive to outliers. While in a least squares fit, the sum of the squared residuals is minimized,

$$\min \frac{1}{2} \sum_i \epsilon_i^2, \quad \epsilon_i = \frac{c(F_i) - c_i}{\sigma_i}, \quad (\text{C.4})$$

the robust fitting method that we applied minimizes the sum of the Huber loss functions $\rho(\epsilon_i)$ [234]:

$$\min \sum_i \rho(\epsilon_i), \quad \rho(\epsilon) = \begin{cases} \frac{1}{2}\epsilon^2, & |\epsilon| < k \\ k|\epsilon| - \frac{1}{2}k^2, & |\epsilon| \geq k \end{cases}. \quad (\text{C.5})$$

Thereby, the residuals are weighted as in a least squares fit for $\epsilon < k$, and with an absolute estimator for $\epsilon \geq k$.⁵ The tuning parameter k is set to 1.345 to achieve a relative efficiency of 95 % in respect to the normal distribution [235, 268].

Finally, we need to estimate the errors σ_i of the stiffnesses that we determined from the sample variances of the bead positions x within each interval as described in Fig. 4.9. Since $c \propto 1/\text{Var}(x)$, the relative deviation of the stiffness is the same as for the variance, $\sigma_c/c = \sigma_{\text{Var}}/\text{Var}(x)$. From a sample of length n , the variance and its deviation can be estimated to [269]

$$\text{Var}(x) = \frac{1}{n-1} \sum_i (x_i - \langle x \rangle)^2, \quad \sigma_{\text{Var}} = \sqrt{\frac{2}{n-1}} \text{Var}(x). \quad (\text{C.6})$$

With $n = 1000$ in a 0.1 s interval at a sample frequency of 10 kHz and stiffnesses around $c = 0.1 \text{ pN nm}^{-1}$, the estimated error is

$$\sigma_c = \sqrt{\frac{2}{n-1}} c = 0.0045 \text{ pN nm}^{-1}. \quad (\text{C.7})$$

C.4 Worm-like chain model of the Ndc80 complex

To take into account an Ndc80 complex with possibly (semi)flexible arms, we model the Ndc80 complex as two worm-like chains (WLC) with persistence length L_p that are flexibly connected. To run Monte

⁵ The squared and the absolute estimator can be rationalized by how their minimization fits a constant \tilde{y} to a set of N sample points y_i : while the least squares method yields the arithmetic mean,

$$\min_{\tilde{y}} \frac{1}{2} \sum_{i=1}^N (\tilde{y} - y_i)^2 = \frac{1}{N} \sum_{i=1}^N y_i,$$

the absolute estimator results in the median,

$$\frac{\partial}{\partial \tilde{y}} \sum_{i=1}^N |\tilde{y} - y_i| = \sum_{i=1}^N \text{sgn}(\tilde{y} - y_i) \stackrel{!}{=} 0.$$

Carlo (MC) simulations, we describe each WLC by a more general bead–spring model called *semiflexible harmonic chain*⁶ (SHC) [241]: The Ndc80 arm \vec{a} (\vec{b}) is discretized into $N_a + 1$ ($N_b + 1$) beads, which are connected by N_a (N_b) springs each with rest length d_a (d_b) and stiffness k_a (k_b). The rest lengths are defined by $d_a = a/N_a$ and $d_b = b/N_b$ to be consistent with the observed Ndc80 arm lengths a and b . Given the extensions and directions of the springs as \vec{a}_i (\vec{b}_j) with $i = 1 \dots N_a$ ($j = 1 \dots N_b$), we find the total stretching energy

$$E_{\text{stretch}} = \frac{k_a}{2} \sum_{i=1}^{N_a} (|\vec{a}_i| - d_a)^2 + \frac{k_b}{2} \sum_{j=1}^{N_b} (|\vec{b}_j| - d_b)^2. \quad (\text{C.8})$$

The positions \vec{A}_m and \vec{B}_n of the beads are given by

$$\vec{A}_m = \vec{A}_0 + \sum_{i=1}^m \vec{a}_i, \quad \vec{B}_n = \vec{B}_0 + \sum_{j=1}^n \vec{b}_j, \quad (\text{C.9})$$

where $\vec{A}_0 = \vec{0}$ (the Ndc80 complex is fixed to the glass bead) and $\vec{B}_0 = \vec{A}_{N_a}$. The glass bead, which is modeled as a wall,⁷ is described by the boundary condition that each bead has to be located in the upper half space, i.e., for the z -components: $A_{m,z}, B_{n,z} > 0$ for each m, n .

Due to the bending rigidity $\kappa = k_B T L_p$, each bead \vec{A}_m, \vec{B}_n except $\vec{A}_0, \vec{A}_{N_a} = \vec{B}_0$ and \vec{B}_{N_b} is associated with a bending energy, which sums up to

$$E_{\text{bend}} = \frac{\kappa}{d_a} \sum_{m=1}^{N_a-1} (1 - \cos \alpha_m) + \frac{\kappa}{d_b} \sum_{n=1}^{N_b-1} (1 - \cos \beta_n), \quad (\text{C.10})$$

where α_m (β_n) is the angle between bonds m and $m + 1$ (n and $n + 1$), i.e., between the two bonds that are connected in bead m (n):

$$\cos \alpha_m = \frac{\vec{a}_m \cdot \vec{a}_{m+1}}{|\vec{a}_m| |\vec{a}_{m+1}|}, \quad \cos \beta_n = \frac{\vec{b}_n \cdot \vec{b}_{n+1}}{|\vec{b}_n| |\vec{b}_{n+1}|}. \quad (\text{C.11})$$

Finally, when a force F in z -direction is applied on the last bead, the total energy reads as:

$$E = E_{\text{stretch}} + E_{\text{bend}} - F B_{N_b, z}. \quad (\text{C.12})$$

The MC simulations are based on the Metropolis algorithm [270]. In each step, we randomly choose a bead ($i, j > 0$) and suggest to move it in a random direction for a constant distance s . If the move does not violate the boundary condition, it will be accepted with probability $\min(1, \exp(-\beta \Delta E))$, where $\Delta E = E_{\text{sugg}} - E_{\text{orig}}$ is the energy difference between the suggested and the original con-

⁶ In contrast to the WLC, the SHC is an extensible semiflexible chain. It contains the WLC in the limit of large bond stiffnesses k , where the SHC becomes nearly inextensible but still has a finite bending rigidity $\kappa = k_B T L_p$. A SHC is easier to implement in the Metropolis MC simulations described below since a single bead can be suggested to be moved in an arbitrary direction without influencing the positions of the other beads. In contrast, random changes of an angle in a genuinely inextensible WLC also alter the position of any subsequent bead.

⁷ See Fig. 4.19.

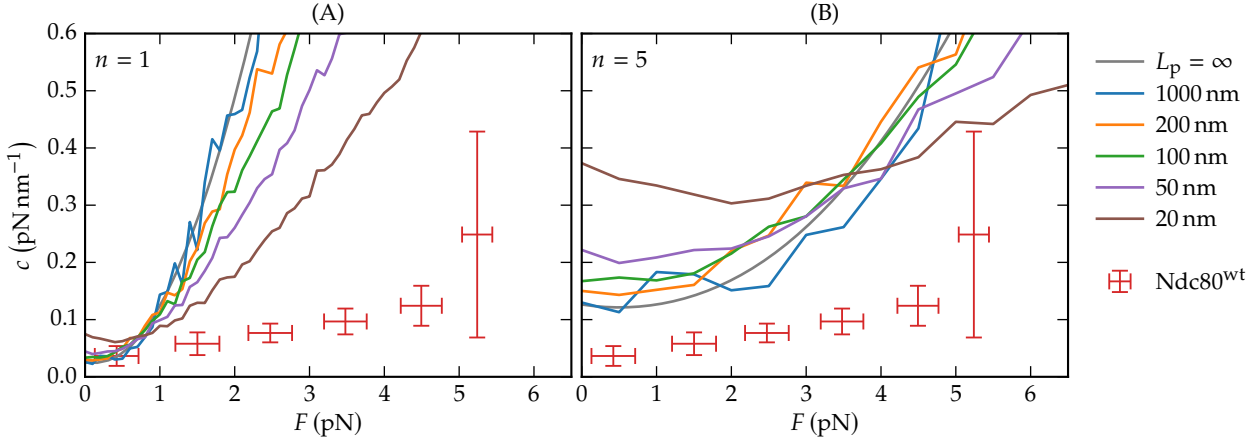


Figure C.2: Stiffness of semiflexible Ndc80 complexes. The plots show the stiffness–force relations of a single (A) and $n = 5$ parallel (B) Ndc80 complexes with persistence lengths L_p . As a check of the MC simulations, we added the large persistence length $L_p = 1000$ nm, which correctly resembles results of the FJC model ($L_p = \infty$) according to Eq. (4.13).

$$^8 \text{Var}(z) = \langle z^2 \rangle - \langle z \rangle^2$$

⁹ After generating force–stiffness data (F_i, c_i) of a single semiflexible Ndc80 complex, the respective relation $(F_{n,i}, c_{n,i})$ of n parallel Ndc80 complexes can be obtained without further simulations by the simple transformation

$$\begin{aligned} F_i &\rightarrow F_{n,i} \equiv n F_i, \\ c_i &\rightarrow c_{n,i} \equiv n c_i, \end{aligned}$$

since

$$\begin{aligned} c_n(F_{n,i}) &= n c\left(\frac{F_{n,i}}{n}\right) \\ &= n c(F_i) = n c_i = c_{n,i}. \end{aligned}$$

Therefore, Fig. C.2B shows the same data as Fig. C.2A but stretched by a factor $n = 5$.

figuration following Eq. (C.12). After a certain time of equilibration, we measure $z = B_{N_b, z}$ and z^2 after each sweep ($N_a + N_b$ moves), and calculate the mean extension and its variance⁸ at the end of a simulation. By repeating it for various external forces, we can record force–extension and force–stiffness relations.

In our simulations, we used $k_a = k_b = 1000$ pN nm⁻¹ to model the two Ndc80 arms as nearly inextensible. Moreover, we used the same discretization lengths $d_a = d_b = 1$ nm, i.e., $N_a = 40$ and $N_b = 16$. Fig. C.2 shows the stiffness–force relations of a single and $n = 5$ parallel⁹ semiflexible Ndc80 complexes with various persistence lengths L_p . The effect of semiflexibility on the stiffness is negligible for realistic persistence lengths above 100 nm [256].

Bibliography

- [1] B. Alberts *et al.* *Molecular Biology of the Cell*. 6th ed. New York: Garland Science, 2015 (cited on pages 1, 7, 25, 28, 87).
- [2] A. V. Hill. 'Why Biophysics?' *Science* 124.3234 (1956), 1233–1237. doi: [10.1126/science.124.3234.1233](https://doi.org/10.1126/science.124.3234.1233) (cited on page 1).
- [3] R. Gordon. *Encyclopedia of Biophysics*. Heidelberg: Springer-Verlag, 2013 (cited on page 1).
- [4] L. M. Adleman. 'Computing with DNA'. *Scientific American* 279.2 (1998), 54–61 (cited on page 1).
- [5] J. E. Cohen. 'Mathematics Is Biology's Next Microscope, Only Better; Biology Is Mathematics' Next Physics, Only Better'. *PLoS Biology* 2.12 (2004), e439. doi: [10.1371/journal.pbio.0020439](https://doi.org/10.1371/journal.pbio.0020439) (cited on page 1).
- [6] G. Binnig, C. F. Quate, and C. Gerber. 'Atomic Force Microscope'. *Physical Review Letters* 56.9 (1986). Ed. by R. Splinter, 930–933. doi: [10.1103/PhysRevLett.56.930](https://doi.org/10.1103/PhysRevLett.56.930) (cited on page 1).
- [7] A. Ashkin *et al.* 'Observation of a single-beam gradient force optical trap for dielectric particles'. *Optics Letters* 11.5 (1986), 288. doi: [10.1364/OL.11.000288](https://doi.org/10.1364/OL.11.000288) (cited on page 1).
- [8] F. Crick and A. Hughes. 'The physical properties of cytoplasm'. *Experimental Cell Research* 1.1 (1950), 37–80. doi: [10.1016/0014-4827\(50\)90048-6](https://doi.org/10.1016/0014-4827(50)90048-6) (cited on page 1).
- [9] K. C. Neuman and A. Nagy. 'Single-molecule force spectroscopy: optical tweezers, magnetic tweezers and atomic force microscopy'. *Nature Methods* 5.6 (2008), 491–505. doi: [10.1038/nmeth.1218](https://doi.org/10.1038/nmeth.1218) (cited on page 1).
- [10] S. B. Smith, L. Finzi, and C. Bustamante. 'Direct Mechanical Measurements of the Elasticity of Single DNA Molecules by Using Magnetic Beads'. *Science* 258.5085 (1992), 1122–1126. doi: [10.1126/science.1439819](https://doi.org/10.1126/science.1439819) (cited on page 1).
- [11] G. U. Lee, L. A. Chrisey, and R. J. Colton. 'Direct Measurement of the Forces Between Complementary Strands of DNA'. *Science* 266.5186 (1994), 771–773. doi: [10.1126/science.7973628](https://doi.org/10.1126/science.7973628) (cited on page 1).
- [12] T. R. Strick *et al.* 'The Elasticity of a Single Supercoiled DNA Molecule'. *Science* 271.5257 (1996), 1835–1837. doi: [10.1126/science.271.5257.1835](https://doi.org/10.1126/science.271.5257.1835) (cited on page 1).
- [13] M. Rief *et al.* 'Reversible Unfolding of Individual Titin Immunoglobulin Domains by AFM'. *Science* 276.5315 (1997), 1109–1112. doi: [10.1126/science.276.5315.1109](https://doi.org/10.1126/science.276.5315.1109) (cited on page 1).
- [14] M. S. Z. Kellermayer *et al.* 'Folding-Unfolding Transitions in Single Titin Molecules Characterized with Laser Tweezers'. *Science* 276.5315 (1997), 1112–1116. doi: [10.1126/science.276.5315.1112](https://doi.org/10.1126/science.276.5315.1112) (cited on page 1).
- [15] H. Dietz *et al.* 'Anisotropic deformation response of single protein molecules'. *Proceedings of the National Academy of Sciences* 103.34 (2006), 12724–12728. doi: [10.1073/pnas.0602995103](https://doi.org/10.1073/pnas.0602995103) (cited on page 1).
- [16] K. Svoboda *et al.* 'Direct observation of kinesin stepping by optical trapping interferometry'. *Nature* 365.6448 (1993), 721–727. doi: [10.1038/365721a0](https://doi.org/10.1038/365721a0) (cited on page 1).
- [17] K. Svoboda and S. M. Block. 'Force and velocity measured for single kinesin molecules'. *Cell* 77.5 (1994), 773–784. doi: [10.1016/0092-8674\(94\)90060-4](https://doi.org/10.1016/0092-8674(94)90060-4) (cited on page 1).

- [18] K. Visscher, M. J. Schnitzer, and S. M. Block. 'Single kinesin molecules studied with a molecular force clamp'. *Nature* 400.6740 (1999), 184–189. doi: [10.1038/22146](https://doi.org/10.1038/22146) (cited on page 1).
- [19] J. W. J. Kerssemakers *et al.* 'Optical trap setup for measuring microtubule pushing forces'. *Applied Physics Letters* 83.21 (2003), 4441–4443. doi: [10.1063/1.1629796](https://doi.org/10.1063/1.1629796) (cited on page 1).
- [20] L. Laan *et al.* 'Force-generation and dynamic instability of microtubule bundles'. *Proceedings of the National Academy of Sciences* 105.26 (2008), 8920–8925. doi: [10.1073/pnas.0710311105](https://doi.org/10.1073/pnas.0710311105) (cited on page 1).
- [21] E. L. Grishchuk *et al.* 'Force production by disassembling microtubules'. *Nature* 438.7066 (2005), 384–388. doi: [10.1038/nature04132](https://doi.org/10.1038/nature04132) (cited on pages 1, 32).
- [22] E. C. Yusko and C. L. Asbury. 'Force is a signal that cells cannot ignore'. *Molecular Biology of the Cell* 25.23 (2014), 3717–3725. doi: [10.1091/mbc.e13-12-0707](https://doi.org/10.1091/mbc.e13-12-0707) (cited on page 1).
- [23] A. Mogilner, R. Wollman, and W. F. Marshall. 'Quantitative Modeling in Cell Biology: What Is It Good for?' *Developmental Cell* 11.3 (2006), 279–287. doi: [10.1016/j.devcel.2006.08.004](https://doi.org/10.1016/j.devcel.2006.08.004) (cited on pages 2, 3).
- [24] R. Phillips *et al.* *Physical Biology of the Cell*. 2nd ed. New York: Garland Science, 2013 (cited on page 2).
- [25] R. H. Landau, M. J. Páez, and C. C. Bordeianu. *Computational Physics: Problem Solving with Python*. Weinheim: Wiley-VCH, 2015 (cited on page 2).
- [26] F. Dyson. 'A meeting with Enrico Fermi'. *Nature* 427.6972 (2004), 297–297. doi: [10.1038/427297a](https://doi.org/10.1038/427297a) (cited on page 2).
- [27] J. Mayer, K. Khairy, and J. Howard. 'Drawing an elephant with four complex parameters'. *American Journal of Physics* 78.6 (2010), 648–649. doi: [10.1119/1.3254017](https://doi.org/10.1119/1.3254017) (cited on page 2).
- [28] J. Harte. *Consider a spherical cow: A course in environmental problem solving*. Sausalito: University Science Books, 1988 (cited on page 2).
- [29] F. Verde *et al.* 'Control of microtubule dynamics and length by cyclin A- and cyclin B-dependent kinases in *Xenopus* egg extracts'. *The Journal of Cell Biology* 118.5 (1992), 1097–1108. doi: [10.1083/jcb.118.5.1097](https://doi.org/10.1083/jcb.118.5.1097) (cited on pages 3, 4, 8, 11, 13, 22, 24, 46, 117, 120).
- [30] M. Dogterom and S. Leibler. 'Physical aspects of the growth and regulation of microtubule structures'. *Physical Review Letters* 70.9 (1993), 1347–1350. doi: [10.1103/PhysRevLett.70.1347](https://doi.org/10.1103/PhysRevLett.70.1347) (cited on pages 3, 4, 8, 11, 13, 22, 46, 117, 120).
- [31] H. Flyvbjerg, T. E. Holy, and S. Leibler. 'Microtubule dynamics: Caps, catastrophes, and coupled hydrolysis'. *Physical Review E* 54.5 (1996), 5538–5560. doi: [10.1103/PhysRevE.54.5538](https://doi.org/10.1103/PhysRevE.54.5538) (cited on page 3).
- [32] V. Jemseena and M. Gopalakrishnan. 'Effects of aging in catastrophe on the steady state and dynamics of a microtubule population'. *Physical Review E* 91.5 (2015), 052704. doi: [10.1103/PhysRevE.91.052704](https://doi.org/10.1103/PhysRevE.91.052704) (cited on pages 3, 12, 13, 17, 127).
- [33] I. M. Jánosi, D. Chrétien, and H. Flyvbjerg. 'Structural Microtubule Cap: Stability, Catastrophe, Rescue, and Third State'. *Biophysical Journal* 83.3 (2002), 1317–1330. doi: [10.1016/S0006-3495\(02\)73902-7](https://doi.org/10.1016/S0006-3495(02)73902-7) (cited on page 3).
- [34] J. P. Keener and B. Shtylla. 'A Mathematical Model of Force Generation by Flexible Kinetochore-Microtubule Attachments'. *Biophysical Journal* 106.5 (2014), 998–1007. doi: [10.1016/j.bpj.2014.01.013](https://doi.org/10.1016/j.bpj.2014.01.013) (cited on pages 3, 37, 85).

- [35] L. Brun *et al.* 'A theory of microtubule catastrophes and their regulation'. *Proceedings of the National Academy of Sciences of the United States of America* 106.50 (2009), 21173–21178. doi: [10.1073/pnas.0910774106](https://doi.org/10.1073/pnas.0910774106) (cited on page 3).
- [36] R. Padinhateeri, A. B. Kolomeisky, and D. Lacoste. 'Random Hydrolysis Controls the Dynamic Instability of Microtubules'. *Biophysical Journal* 102.6 (2012), 1274–1283. doi: [10.1016/j.bpj.2011.12.059](https://doi.org/10.1016/j.bpj.2011.12.059) (cited on page 3).
- [37] H. Bowne-Anderson *et al.* 'Microtubule dynamic instability: A new model with coupled GTP hydrolysis and multistep catastrophe'. *BioEssays* 35.5 (2013), 452–461. doi: [10.1002/bies.201200131](https://doi.org/10.1002/bies.201200131) (cited on pages 3, 12, 122).
- [38] J. S. Aparna, R. Padinhateeri, and D. Das. 'Signatures of a macroscopic switching transition for a dynamic microtubule'. *Scientific Reports* 7.1 (2017), 45747. doi: [10.1038/srep45747](https://doi.org/10.1038/srep45747) (cited on page 3).
- [39] V. VanBuren, L. Cassimeris, and D. J. Odde. 'Mechanochemical Model of Microtubule Structure and Self-Assembly Kinetics'. *Biophysical Journal* 89.5 (2005), 2911–2926. doi: [10.1529/biophysj.105.060913](https://doi.org/10.1529/biophysj.105.060913) (cited on page 3).
- [40] V. Jemseena and M. Gopalakrishnan. 'Microtubule catastrophe from protofilament dynamics'. *Physical Review E* 88.3 (2013), 032717. doi: [10.1103/PhysRevE.88.032717](https://doi.org/10.1103/PhysRevE.88.032717) (cited on page 3).
- [41] C. E. Coombes *et al.* 'Evolving Tip Structures Can Explain Age-Dependent Microtubule Catastrophe'. *Current Biology* 23.14 (2013), 1342–1348. doi: [10.1016/j.cub.2013.05.059](https://doi.org/10.1016/j.cub.2013.05.059) (cited on pages 3, 12).
- [42] P. Zakharov *et al.* 'Molecular and Mechanical Causes of Microtubule Catastrophe and Aging'. *Biophysical Journal* 109.12 (2015), 2574–2591. doi: [10.1016/j.bpj.2015.10.048](https://doi.org/10.1016/j.bpj.2015.10.048) (cited on pages 3, 12).
- [43] M. Schmidt and J. Kierfeld. 'Chemomechanical Simulation of Microtubule Dynamics With Explicit Lateral Bond Dynamics'. *Frontiers in Physics* 9 (2021), 673875. doi: [10.3389/fphy.2021.673875](https://doi.org/10.3389/fphy.2021.673875) (cited on page 3).
- [44] M. Little and T. Seehaus. 'Comparative analysis of tubulin sequences'. *Comparative Biochemistry and Physiology Part B: Comparative Biochemistry* 90.4 (1988), 655–670. doi: [10.1016/0305-0491\(88\)90320-3](https://doi.org/10.1016/0305-0491(88)90320-3) (cited on page 3).
- [45] T. Splettstoesser. *Cartoon representation of the atomic structure of a GDP/GTP-bound Tubulin Dimer*. Original and adaption are licensed under CC BY-SA 4.0 [271]. URL: https://commons.wikimedia.org/wiki/File:Tubulin_dimer_1JFF.png (visited on 03/18/2021) (cited on pages 3, 9).
- [46] A. Mogilner *et al.* 'Modeling mitosis'. *Trends in Cell Biology* 16.2 (2006), 88–96. doi: [10.1016/j.tcb.2005.12.007](https://doi.org/10.1016/j.tcb.2005.12.007) (cited on pages 3, 35).
- [47] D. J. Odde, L. Cassimeris, and H. M. Buettner. 'Kinetics of microtubule catastrophe assessed by probabilistic analysis'. *Biophysical Journal* 69.3 (1995), 796–802. doi: [10.1016/S0006-3495\(95\)79953-2](https://doi.org/10.1016/S0006-3495(95)79953-2) (cited on pages 5, 8, 12, 14, 22, 118, 120).
- [48] T. Stepanova *et al.* 'History-Dependent Catastrophes Regulate Axonal Microtubule Behavior'. *Current Biology* 20.11 (2010), 1023–1028. doi: [10.1016/j.cub.2010.04.024](https://doi.org/10.1016/j.cub.2010.04.024) (cited on pages 5, 8, 12, 14, 118, 120).
- [49] M. K. Gardner *et al.* 'Depolymerizing Kinesins Kip3 and MCAK Shape Cellular Microtubule Architecture by Differential Control of Catastrophe'. *Cell* 147.5 (2011), 1092–1103. doi: [10.1016/j.cell.2011.10.037](https://doi.org/10.1016/j.cell.2011.10.037) (cited on pages 5, 8, 12, 14, 16, 22–24, 118, 120).

- [50] R. V. Skibbens, V. P. Skeen, and E. D. Salmon. 'Directional instability of kinetochore motility during chromosome congression and segregation in mitotic newt lung cells: a push-pull mechanism'. *The Journal of Cell Biology* 122.4 (1993), 859–875. doi: [10.1083/jcb.122.4.859](https://doi.org/10.1083/jcb.122.4.859) (cited on pages 5, 26, 31, 35, 61, 66, 76, 78, 118, 120).
- [51] J. C. Waters, R. V. Skibbens, and E. D. Salmon. 'Oscillating mitotic newt lung cell kinetochores are, on average, under tension and rarely push'. *Journal of Cell Science* 109.12 (1996), 2823–2831. doi: [10.1242/jcs.109.12.2823](https://doi.org/10.1242/jcs.109.12.2823) (cited on pages 5, 26, 31, 33, 36, 42, 60, 66, 76, 79, 118, 120).
- [52] T. J. Mitchison. 'Polewards microtubule flux in the mitotic spindle: evidence from photoactivation of fluorescence'. *The Journal of Cell Biology* 109.2 (1989), 637–652. doi: [10.1083/jcb.109.2.637](https://doi.org/10.1083/jcb.109.2.637) (cited on pages 5, 26, 31, 61, 76, 118, 120).
- [53] N. J. Ganem, K. Upton, and D. A. Compton. 'Efficient mitosis in human cells lacking poleward microtubule flux'. *Current Biology* 15.20 (2005), 1827–1832. doi: [10.1016/j.cub.2005.08.065](https://doi.org/10.1016/j.cub.2005.08.065) (cited on pages 5, 26, 31, 61, 76, 118, 120).
- [54] V. Magidson *et al.* 'The Spatial Arrangement of Chromosomes during Prometaphase Facilitates Spindle Assembly'. *Cell* 146.4 (2011), 555–567. doi: [10.1016/j.cell.2011.07.012](https://doi.org/10.1016/j.cell.2011.07.012) (cited on pages 5, 26, 31, 42, 66, 76, 118, 120).
- [55] X. Wan *et al.* 'The coupling between sister kinetochore directional instability and oscillations in centromere stretch in metaphase PtK1 cells'. *Molecular Biology of the Cell* 23.6 (2012), 1035–1046. doi: [10.1091/mbc.e11-09-0767](https://doi.org/10.1091/mbc.e11-09-0767) (cited on pages 5, 26, 31, 38, 53, 61, 66, 72–77, 82, 118, 120, 122).
- [56] S. Dumont, E. D. Salmon, and T. J. Mitchison. 'Deformations Within Moving Kinetochores Reveal Different Sites of Active and Passive Force Generation'. *Science* 337.6092 (2012), 355–358. doi: [10.1126/science.1221886](https://doi.org/10.1126/science.1221886) (cited on pages 5, 26, 31, 61, 66, 71, 76, 77, 80, 118, 120).
- [57] E. J. Banigan *et al.* 'Minimal model for collective kinetochore–microtubule dynamics'. *Proceedings of the National Academy of Sciences* 112.41 (2015), 12699–12704. doi: [10.1073/pnas.1513512112](https://doi.org/10.1073/pnas.1513512112) (cited on pages 5, 26, 35–42, 44, 51, 60, 61, 76, 77, 85, 123).
- [58] V. A. Volkov *et al.* 'Multivalency of NDC80 in the outer kinetochore is essential to track shortening microtubules and generate forces'. *eLife* 7 (2018), e36764. doi: [10.7554/eLife.36764](https://doi.org/10.7554/eLife.36764) (cited on pages 5, 32, 77, 78, 83, 85, 88, 89, 91, 92, 94, 95, 110, 112, 118, 119, 121, 135).
- [59] P. J. Huis in 't Veld *et al.* 'Molecular determinants of the Ska-Ndc80 interaction and their influence on microtubule tracking and force-coupling'. *eLife* 8 (2019), e49539. doi: [10.7554/eLife.49539](https://doi.org/10.7554/eLife.49539) (cited on pages 5, 32, 78, 86–89, 91, 93, 112, 114, 119, 121, 135).
- [60] F. Schwiertert, L. Heydenreich, and J. Kierfeld. 'Dynamics and length distributions of microtubules with a multistep catastrophe mechanism'. *bioRxiv* (2022). doi: [10.1101/2022.08.19.504495](https://doi.org/10.1101/2022.08.19.504495) (cited on page 7).
- [61] *Fluorescent Cells*. Example image from the ImageJ program package (public domain). URL: <https://en.wikipedia.org/wiki/File:FluorescentCells.jpg> (visited on 09/14/2021) (cited on page 7).
- [62] F. Gittes *et al.* 'Flexural rigidity of microtubules and actin filaments measured from thermal fluctuations in shape'. *The Journal of Cell Biology* 120.4 (1993), 923–934. doi: [10.1083/jcb.120.4.923](https://doi.org/10.1083/jcb.120.4.923) (cited on pages 7, 8).
- [63] L. G. Tilney *et al.* 'Microtubules: Evidence for 13 Protofilaments'. *Journal of Cell Biology* 59.2 (1973), 267–275. doi: [10.1083/jcb.59.2.267](https://doi.org/10.1083/jcb.59.2.267) (cited on page 8).

- [64] S. Chaaban and G. J. Brouhard. 'A microtubule bestiary: structural diversity in tubulin polymers'. *Molecular Biology of the Cell* 28.22 (2017), 2924–2931. doi: [10.1091/mbc.e16-05-0271](https://doi.org/10.1091/mbc.e16-05-0271) (cited on page 8).
- [65] M. Chalfie and J. N. Thomson. 'Structural and functional diversity in the neuronal microtubules of *Caenorhabditis elegans*.' *Journal of Cell Biology* 93.1 (1982), 15–23. doi: [10.1083/jcb.93.1.15](https://doi.org/10.1083/jcb.93.1.15) (cited on page 8).
- [66] R. Dallai, P. Lupetti, and C. Mencarelli. 'Unusual Axonemes of Hexapod Spermatozoa'. *International Review of Cytology* 254.06 (2006), 45–99. doi: [10.1016/S0074-7696\(06\)54002-1](https://doi.org/10.1016/S0074-7696(06)54002-1) (cited on page 8).
- [67] R. Dallai *et al.* 'Giant sperm cells with accessory macro-tubules in a neuropteran insect'. *Tissue and Cell* 37.5 (2005), 359–366. doi: [10.1016/j.tice.2005.05.002](https://doi.org/10.1016/j.tice.2005.05.002) (cited on page 8).
- [68] T. Mitchison and M. Kirschner. 'Dynamic instability of microtubule growth'. *Nature* 312.5991 (1984), 237–242. doi: [10.1038/312237a0](https://doi.org/10.1038/312237a0) (cited on pages 9, 10, 36, 40, 118).
- [69] A. Wegner. 'Head to tail polymerization of actin'. *Journal of Molecular Biology* 108.1 (1976), 139–150. doi: [10.1016/S0022-2836\(76\)80100-3](https://doi.org/10.1016/S0022-2836(76)80100-3) (cited on page 10).
- [70] R. L. Margolis and L. Wilson. 'Opposite end assembly and disassembly of microtubules at steady state in vitro'. *Cell* 13.1 (1978), 1–8. doi: [10.1016/0092-8674\(78\)90132-0](https://doi.org/10.1016/0092-8674(78)90132-0) (cited on pages 10, 61).
- [71] V. I. Rodionov. 'Microtubule Treadmilling in Vivo'. *Science* 275.5297 (1997), 215–218. doi: [10.1126/science.275.5297.215](https://doi.org/10.1126/science.275.5297.215) (cited on page 10).
- [72] J. R. McIntosh *et al.* 'Microtubules grow by the addition of bent guanosine triphosphate tubulin to the tips of curved protofilaments'. *Journal of Cell Biology* 217.8 (2018), 2691–2708. doi: [10.1083/jcb.201802138](https://doi.org/10.1083/jcb.201802138) (cited on pages 11, 108, 111, 118, 122).
- [73] A. Dimitrov *et al.* 'Detection of GTP-Tubulin Conformation in Vivo Reveals a Role for GTP Remnants in Microtubule Rescues'. *Science* 322.5906 (2008), 1353–1356. doi: [10.1126/science.1165401](https://doi.org/10.1126/science.1165401) (cited on page 11).
- [74] L. Cassimeris. 'Microtubule Assembly: Lattice GTP to the Rescue'. *Current Biology* 19.4 (2009), R174–R176. doi: [10.1016/j.cub.2008.12.035](https://doi.org/10.1016/j.cub.2008.12.035) (cited on page 11).
- [75] T. Horio and H. Hotani. 'Visualization of the dynamic instability of individual microtubules by dark-field microscopy'. *Nature* 321.6070 (1986), 605–607. doi: [10.1038/321605a0](https://doi.org/10.1038/321605a0) (cited on pages 11, 13).
- [76] L. Cassimeris, N. K. Pryer, and E. D. Salmon. 'Real-time observations of microtubule dynamic instability in living cells.' *Journal of Cell Biology* 107.6 (1988), 2223–2231. doi: [10.1083/jcb.107.6.2223](https://doi.org/10.1083/jcb.107.6.2223) (cited on pages 11, 13).
- [77] R. Mohan *et al.* 'End-binding proteins sensitize microtubules to the action of microtubule-targeting agents'. *Proceedings of the National Academy of Sciences* 110.22 (2013), 8900–8905. doi: [10.1073/pnas.1300395110](https://doi.org/10.1073/pnas.1300395110) (cited on page 12).
- [78] V. Čermák *et al.* 'Microtubule-targeting agents and their impact on cancer treatment'. *European Journal of Cell Biology* 99.4 (2020), 151075. doi: [10.1016/j.ejcb.2020.151075](https://doi.org/10.1016/j.ejcb.2020.151075) (cited on page 12).
- [79] L.-K. Heydenreich. 'Mikrotubuli-Dynamik mit altersabhängiger Katastrophenrate'. Bachelorarbeit. TU Dortmund, 2017 (cited on page 14).
- [80] F. W. J. Olver *et al.* *NIST Handbook of Mathematical Functions*. Cambridge: Cambridge University Press, 2010 (cited on pages 15, 17, 18, 47).

- [81] M. Kirschner and T. Mitchison. 'Beyond self-assembly: From microtubules to morphogenesis'. *Cell* 45.3 (1986), 329–342. doi: [10.1016/0092-8674\(86\)90318-1](https://doi.org/10.1016/0092-8674(86)90318-1) (cited on pages 23, 30, 35).
- [82] W. A. Voter, E. T. O'Brien, and H. P. Erickson. 'Dilution-induced disassembly of microtubules: Relation to dynamic instability and the GTP cap'. *Cell Motility and the Cytoskeleton* 18.1 (1991), 55–62. doi: [10.1002/cm.970180106](https://doi.org/10.1002/cm.970180106) (cited on page 23).
- [83] D. K. Fygenson, E. Braun, and A. Libchaber. 'Phase diagram of microtubules'. *Physical Review E* 50.2 (1994), 1579–1588. doi: [10.1103/PhysRevE.50.1579](https://doi.org/10.1103/PhysRevE.50.1579) (cited on page 23).
- [84] I. B. Alieva and I. A. Vorobjev. 'Interphase microtubules in cultured cells: Long or short?' *Membrane and Cell Biology* 14.1 (2000), 57–67 (cited on pages 23, 24).
- [85] M. Piehl and L. Cassimeris. 'Organization and Dynamics of Growing Microtubule Plus Ends during Early Mitosis'. *Molecular Biology of the Cell* 14.3 (2003), 916–925. doi: [10.1091/mbc.e02-09-0607](https://doi.org/10.1091/mbc.e02-09-0607) (cited on pages 23, 24).
- [86] Y. Jeune-Smith and H. Hess. 'Engineering the length distribution of microtubules polymerized in vitro'. *Soft Matter* 6.8 (2010), 1778. doi: [10.1039/b919488f](https://doi.org/10.1039/b919488f) (cited on page 23).
- [87] Y. Du, C. A. English, and R. Ohi. 'The Kinesin-8 Kif18A Dampens Microtubule Plus-End Dynamics'. *Current Biology* 20.4 (2010), 374–380. doi: [10.1016/j.cub.2009.12.049](https://doi.org/10.1016/j.cub.2009.12.049) (cited on page 23).
- [88] M. K. Gardner, M. Zanic, and J. Howard. 'Microtubule catastrophe and rescue'. *Current Opinion in Cell Biology* 25.1 (2013), 14–22. doi: [10.1016/j.ceb.2012.09.006](https://doi.org/10.1016/j.ceb.2012.09.006) (cited on page 23).
- [89] D. R. Drummond and R. A. Cross. 'Dynamics of interphase microtubules in *Schizosaccharomyces pombe*'. *Current Biology* 10.13 (2000), 766–775. doi: [10.1016/S0960-9822\(00\)00570-4](https://doi.org/10.1016/S0960-9822(00)00570-4) (cited on page 24).
- [90] Y. Zhai *et al.* 'Microtubule dynamics at the G2/M transition: Abrupt breakdown of cytoplasmic microtubules at nuclear envelope breakdown and implications for spindle morphogenesis'. *Journal of Cell Biology* 135.1 (1996), 201–214. doi: [10.1083/jcb.135.1.201](https://doi.org/10.1083/jcb.135.1.201) (cited on page 24).
- [91] P. D. Andrews *et al.* 'Aurora B Regulates MCAK at the Mitotic Centromere'. *Developmental Cell* 6.2 (2004), 253–268. doi: [10.1016/S1534-5807\(04\)00025-5](https://doi.org/10.1016/S1534-5807(04)00025-5) (cited on pages 24, 30).
- [92] D. O. Morgan. *The Cell Cycle: Principles of Control*. London: New Science Press, 2007 (cited on pages 24, 27–29, 34).
- [93] F. Schwietert and J. Kierfeld. 'Bistability and oscillations in cooperative microtubule and kinetochore dynamics in the mitotic spindle'. *New Journal of Physics* 22.5 (2020), 053008. doi: [10.1088/1367-2630/ab7ede](https://doi.org/10.1088/1367-2630/ab7ede) (cited on page 25).
- [94] Creative Commons. *Attribution 4.0 International (CC BY 4.0)*. URL: <https://creativecommons.org/licenses/by/4.0> (visited on 04/04/2022) (cited on pages 25, 85, 89).
- [95] F. Schwietert. 'Mikrotubuli- und Kinetochor-Dynamik in der Mitosespindel'. Masterarbeit. TU Dortmund, 2016 (cited on pages 25, 50, 130, 131).
- [96] P. Siekevitz. 'Powerhouse of the Cell'. *Scientific American* 197.1 (1957), 131–140. doi: [10.1038/scientificamerican0757-131](https://doi.org/10.1038/scientificamerican0757-131) (cited on page 25).
- [97] C. R. Woese, O. Kandler, and M. L. Wheelis. 'Towards a natural system of organisms: proposal for the domains Archaea, Bacteria, and Eucarya.' *Proceedings of the National Academy of Sciences* 87.12 (1990), 4576–4579. doi: [10.1073/pnas.87.12.4576](https://doi.org/10.1073/pnas.87.12.4576) (cited on page 25).
- [98] R. Virchow. *Die Cellularpathologie in ihrer Begründung auf physiologische und pathologische Gewebelehre*. Berlin: Verlag von August Hirschwald, 1858 (cited on page 25).

- [99] P. Maddox *et al.* 'Poleward Microtubule Flux Is a Major Component of Spindle Dynamics and Anaphase A in Mitotic Drosophila Embryos'. *Current Biology* 12.19 (2002), 1670–1674. doi: [10.1016/S0960-9822\(02\)01183-1](https://doi.org/10.1016/S0960-9822(02)01183-1) (cited on pages 26, 61).
- [100] A. Desai *et al.* 'Anaphase A Chromosome Movement and Poleward Spindle Microtubule Flux Occur At Similar Rates in Xenopus Extract Spindles'. *Journal of Cell Biology* 141.3 (1998), 703–713. doi: [10.1083/jcb.141.3.703](https://doi.org/10.1083/jcb.141.3.703) (cited on pages 26, 61).
- [101] A. P. Joglekar and A. J. Hunt. 'A Simple, Mechanistic Model for Directional Instability during Mitotic Chromosome Movements'. *Biophysical Journal* 83.1 (2002), 42–58. doi: [10.1016/S0006-3495\(02\)75148-5](https://doi.org/10.1016/S0006-3495(02)75148-5) (cited on pages 26, 35–39).
- [102] G. Civelekoglu-Scholey *et al.* 'Model of Chromosome Motility in Drosophila Embryos: Adaptation of a General Mechanism for Rapid Mitosis'. *Biophysical Journal* 90.11 (2006), 3966–3982. doi: [10.1529/biophysj.105.078691](https://doi.org/10.1529/biophysj.105.078691) (cited on pages 26, 35–39).
- [103] B. Shtylla and J. P. Keener. 'A mechanomolecular model for the movement of chromosomes during mitosis driven by a minimal kinetochore bicyclic cascade'. *Journal of Theoretical Biology* 263.4 (2010), 455–470. doi: [10.1016/j.jtbi.2009.12.023](https://doi.org/10.1016/j.jtbi.2009.12.023) (cited on pages 26, 35–39, 51, 56).
- [104] B. Shtylla and J. P. Keener. 'A Mathematical Model for Force Generation at the Kinetochore-Microtubule Interface'. *SIAM Journal on Applied Mathematics* 71.5 (2011), 1821–1848. doi: [10.1137/100802645](https://doi.org/10.1137/100802645) (cited on pages 26, 35–39).
- [105] G. Civelekoglu-Scholey *et al.* 'Dynamic bonds and polar ejection force distribution explain kinetochore oscillations in PtK1 cells'. *Journal of Cell Biology* 201.4 (2013), 577–593. doi: [10.1083/jcb.201301022](https://doi.org/10.1083/jcb.201301022) (cited on pages 26, 35–39, 62, 65, 66, 72, 74, 75, 79, 82, 85, 121, 122).
- [106] A. H. Klemm *et al.* 'Metaphase kinetochore movements are regulated by kinesin-8 motors and microtubule dynamic instability'. *Molecular Biology of the Cell* 29.11 (2018), 1332–1345. doi: [10.1091/mbc.E17-11-0667](https://doi.org/10.1091/mbc.E17-11-0667) (cited on pages 26, 35–39, 51, 56, 76, 79).
- [107] R. Wheeler and Wikimedia Commons users *Beao* and *Histidine*. *Schematic representation of the cell cycle*. Original and adaption are licensed under CC BY-SA 3.0 [272]. URL: https://commons.wikimedia.org/wiki/File:Cell_Cycle_2-2.svg (visited on 06/16/2021) (cited on page 27).
- [108] Wikipedia user *Afunguy*. *Image of the mitotic spindle in a human cell*. Original has been released into public domain. URL: <https://commons.wikimedia.org/wiki/File:Kinetochore.jpg> (visited on 06/16/2021) (cited on page 28).
- [109] B. F. McEwen *et al.* 'Kinetochore Fiber Maturation in PtK1 Cells and Its Implications for the Mechanisms of Chromosome Congression and Anaphase Onset'. *Journal of Cell Biology* 137.7 (1997), 1567–1580. doi: [10.1083/jcb.137.7.1567](https://doi.org/10.1083/jcb.137.7.1567) (cited on pages 28, 45, 53, 75, 76).
- [110] B. F. McEwen *et al.* 'CENP-E Is Essential for Reliable Bioriented Spindle Attachment, but Chromosome Alignment Can Be Achieved via Redundant Mechanisms in Mammalian Cells'. *Molecular Biology of the Cell* 12.9 (2001), 2776–2789. doi: [10.1091/mbc.12.9.2776](https://doi.org/10.1091/mbc.12.9.2776) (cited on pages 28, 76).
- [111] K. F. DeLuca, S. M. A. Lens, and J. G. DeLuca. 'Temporal changes in Hec1 phosphorylation control kinetochore–microtubule attachment stability during mitosis'. *Journal of Cell Science* 124.4 (2011), 622–634. doi: [10.1242/jcs.072629](https://doi.org/10.1242/jcs.072629) (cited on pages 30, 81, 87, 114).
- [112] S. L. McVey, J. K. Cosby, and N. J. Nannas. 'Aurora B Tension Sensing Mechanisms in the Kinetochore Ensure Accurate Chromosome Segregation'. *International Journal of Molecular Sciences* 22.16 (2021), 8818. doi: [10.3390/ijms22168818](https://doi.org/10.3390/ijms22168818) (cited on page 30).

- [113] K. Jaqaman *et al.* 'Kinetochore alignment within the metaphase plate is regulated by centromere stiffness and microtubule depolymerases'. *Journal of Cell Biology* 188.5 (2010), 665–679. doi: [10.1083/jcb.200909005](https://doi.org/10.1083/jcb.200909005) (cited on pages 31, 80).
- [114] I. M. Cheeseman. 'The Kinetochore'. *Cold Spring Harbor Perspectives in Biology* 6.7 (2014), a015826–a015826. doi: [10.1101/cshperspect.a015826](https://doi.org/10.1101/cshperspect.a015826) (cited on pages 32, 33, 72).
- [115] A. F. Long, J. Kuhn, and S. Dumont. 'The mammalian kinetochore–microtubule interface: robust mechanics and computation with many microtubules'. *Current Opinion in Cell Biology* 60 (2019), 60–67. doi: [10.1016/j.ceb.2019.04.004](https://doi.org/10.1016/j.ceb.2019.04.004) (cited on page 32).
- [116] I. M. Cheeseman and A. Desai. 'Molecular architecture of the kinetochore–microtubule interface'. *Nature Reviews Molecular Cell Biology* 9.1 (2008), 33–46. doi: [10.1038/nrm2310](https://doi.org/10.1038/nrm2310) (cited on page 32).
- [117] K. E. Gascoigne and I. M. Cheeseman. 'CDK-dependent phosphorylation and nuclear exclusion coordinately control kinetochore assembly state'. *Journal of Cell Biology* 201.1 (2013), 23–32. doi: [10.1083/jcb.201301006](https://doi.org/10.1083/jcb.201301006) (cited on page 32).
- [118] J. R. McIntosh *et al.* 'Fibrils Connect Microtubule Tips with Kinetochores: A Mechanism to Couple Tubulin Dynamics to Chromosome Motion'. *Cell* 135.2 (2008), 322–333. doi: [10.1016/j.cell.2008.08.038](https://doi.org/10.1016/j.cell.2008.08.038) (cited on pages 32, 37).
- [119] A. P. Joglekar and J. G. DeLuca. 'Chromosome Segregation: Ndc80 Can Carry the Load'. *Current Biology* 19.10 (2009), R404–R407. doi: [10.1016/j.cub.2009.04.014](https://doi.org/10.1016/j.cub.2009.04.014) (cited on pages 32, 37).
- [120] A. F. Powers *et al.* 'The Ndc80 Kinetochore Complex Forms Load-Bearing Attachments to Dynamic Microtubule Tips via Biased Diffusion'. *Cell* 136.5 (2009), 865–875. doi: [10.1016/j.cell.2008.12.045](https://doi.org/10.1016/j.cell.2008.12.045) (cited on pages 32, 37, 88, 89, 110).
- [121] I. M. Cheeseman *et al.* 'The Conserved KMN Network Constitutes the Core Microtubule-Binding Site of the Kinetochore'. *Cell* 127.5 (2006), 983–997. doi: [10.1016/j.cell.2006.09.039](https://doi.org/10.1016/j.cell.2006.09.039) (cited on page 32).
- [122] A. Suzuki, B. L. Badger, and E. D. Salmon. 'A quantitative description of Ndc80 complex linkage to human kinetochores'. *Nature Communications* 6.1 (2015), 8161. doi: [10.1038/ncomms9161](https://doi.org/10.1038/ncomms9161) (cited on page 32).
- [123] T. Y. Yoo *et al.* 'Measuring NDC80 binding reveals the molecular basis of tension-dependent kinetochore-microtubule attachments'. *eLife* 7 (2018), e36392. doi: [10.7554/eLife.36392](https://doi.org/10.7554/eLife.36392) (cited on pages 32, 112).
- [124] S. Westermann *et al.* 'Formation of a Dynamic Kinetochore- Microtubule Interface through Assembly of the Dam1 Ring Complex'. *Molecular Cell* 17.2 (2005), 277–290. doi: [10.1016/j.molcel.2004.12.019](https://doi.org/10.1016/j.molcel.2004.12.019) (cited on pages 32, 72).
- [125] J. L. Miranda *et al.* 'The yeast DASH complex forms closed rings on microtubules'. *Nature Structural & Molecular Biology* 12.2 (2005), 138–143. doi: [10.1038/nsmb896](https://doi.org/10.1038/nsmb896) (cited on pages 32, 72).
- [126] E. L. Grishchuk *et al.* 'The Dam1 ring binds microtubules strongly enough to be a processive as well as energy-efficient coupler for chromosome motion'. *Proceedings of the National Academy of Sciences* 105.40 (2008), 15423–15428. doi: [10.1073/pnas.0807859105](https://doi.org/10.1073/pnas.0807859105) (cited on page 32).
- [127] F. Lampert, P. Hornung, and S. Westermann. 'The Dam1 complex confers microtubule plus end-tracking activity to the Ndc80 kinetochore complex'. *Journal of Cell Biology* 189.4 (2010), 641–649. doi: [10.1083/jcb.200912021](https://doi.org/10.1083/jcb.200912021) (cited on pages 32, 72).

- [128] J. F. Tien *et al.* 'Cooperation of the Dam1 and Ndc80 kinetochore complexes enhances microtubule coupling and is regulated by aurora B'. *Journal of Cell Biology* 189.4 (2010), 713–723. doi: [10.1083/jcb.200910142](https://doi.org/10.1083/jcb.200910142) (cited on pages 32, 72, 88).
- [129] J. P. Welburn *et al.* 'The Human Kinetochore Ska1 Complex Facilitates Microtubule Depolymerization-Coupled Motility'. *Developmental Cell* 16.3 (2009), 374–385. doi: [10.1016/j.devcel.2009.01.011](https://doi.org/10.1016/j.devcel.2009.01.011) (cited on page 32).
- [130] A. A. Jeyaprakash *et al.* 'Structural and Functional Organization of the Ska Complex, a Key Component of the Kinetochore-Microtubule Interface'. *Molecular Cell* 46.3 (2012), 274–286. doi: [10.1016/j.molcel.2012.03.005](https://doi.org/10.1016/j.molcel.2012.03.005) (cited on page 32).
- [131] J. C. Schmidt *et al.* 'The Kinetochore-Bound Ska1 Complex Tracks Depolymerizing Microtubules and Binds to Curved Protofilaments'. *Developmental Cell* 23.5 (2012), 968–980. doi: [10.1016/j.devcel.2012.09.012](https://doi.org/10.1016/j.devcel.2012.09.012) (cited on pages 32, 87–89, 109, 111, 121).
- [132] P. Ł. Janczyk *et al.* 'Mechanism of Ska Recruitment by Ndc80 Complexes to Kinetochores'. *Developmental Cell* 41.4 (2017), 438–449.e4. doi: [10.1016/j.devcel.2017.04.020](https://doi.org/10.1016/j.devcel.2017.04.020) (cited on pages 32, 87).
- [133] S. L. Kline-Smith *et al.* 'Depletion of Centromeric MCAK Leads to Chromosome Congression and Segregation Defects Due to Improper Kinetochore Attachments'. *Molecular Biology of the Cell* 15.3 (2004), 1146–1159. doi: [10.1091/mbc.e03-08-0581](https://doi.org/10.1091/mbc.e03-08-0581) (cited on pages 33, 80).
- [134] B. Akiyoshi *et al.* 'Tension directly stabilizes reconstituted kinetochore-microtubule attachments'. *Nature* 468.7323 (2010), 576–579. doi: [10.1038/nature09594](https://doi.org/10.1038/nature09594) (cited on pages 33, 36–38, 40, 42, 72, 77, 88, 112, 118).
- [135] S. Inoué and E. D. Salmon. 'Force Generation by Microtubule Assembly/Disassembly in Mitosis and Related Movements'. *Molecular Biology of the Cell* 6.12 (1995), 1619–1640. doi: [10.1091/mbc.6.12.1619](https://doi.org/10.1091/mbc.6.12.1619) (cited on page 33).
- [136] I. M. Tolić-Nørrelykke *et al.* 'Positioning and Elongation of the Fission Yeast Spindle by Microtubule-Based Pushing'. *Current Biology* 14.13 (2004), 1181–1186. doi: [10.1016/j.cub.2004.06.029](https://doi.org/10.1016/j.cub.2004.06.029) (cited on page 33).
- [137] M. Vleugel, M. Kok, and M. Dogterom. 'Understanding force-generating microtubule systems through in vitro reconstitution'. *Cell Adhesion & Migration* 10.5 (2016), 475–494. doi: [10.1080/19336918.2016.1241923](https://doi.org/10.1080/19336918.2016.1241923) (cited on page 33).
- [138] I. A. Kent and T. P. Lele. 'Microtubule-based force generation'. *Wiley Interdisciplinary Reviews: Nanomedicine and Nanobiotechnology* 9.3 (2017), e1428. doi: [10.1002/wnan.1428](https://doi.org/10.1002/wnan.1428) (cited on page 33).
- [139] A. Khodjakov and C. L. Rieder. 'Kinetochores moving away from their associated pole do not exert a significant pushing force on the chromosome'. *The Journal of Cell Biology* 135.2 (1996), 315–327. doi: [10.1083/jcb.135.2.315](https://doi.org/10.1083/jcb.135.2.315) (cited on pages 33, 36, 42, 60, 66, 79).
- [140] A. A. Levesque and D. A. Compton. 'The chromokinesin Kid is necessary for chromosome arm orientation and oscillation, but not congression, on mitotic spindles'. *Journal of Cell Biology* 154.6 (2001), 1135–1146. doi: [10.1083/jcb.200106093](https://doi.org/10.1083/jcb.200106093) (cited on pages 34, 64, 78).
- [141] G. Goshima and J. M. Scholey. 'Control of Mitotic Spindle Length'. *Annual Review of Cell and Developmental Biology* 26.1 (2010), 21–57. doi: [10.1146/annurev-cellbio-100109-104006](https://doi.org/10.1146/annurev-cellbio-100109-104006) (cited on page 35).

- [142] G. Civelekoglu-Scholey and D. Cimini. 'Modelling chromosome dynamics in mitosis: a historical perspective on models of metaphase and anaphase in eukaryotic cells'. *Interface Focus* 4.3 (2014), 20130073. doi: [10.1098/rsfs.2013.0073](https://doi.org/10.1098/rsfs.2013.0073) (cited on page 35).
- [143] N. Pavin and I. M. Tolić. 'Self-Organization and Forces in the Mitotic Spindle'. *Annual Review of Biophysics* 45.1 (2016), 279–298. doi: [10.1146/annurev-biophys-062215-010934](https://doi.org/10.1146/annurev-biophys-062215-010934) (cited on page 35).
- [144] E. Nazockdast and S. Redemann. 'Mechanics of the spindle apparatus'. *Seminars in Cell & Developmental Biology* 107.July (2020), 91–102. doi: [10.1016/j.semcdb.2020.06.018](https://doi.org/10.1016/j.semcdb.2020.06.018) (cited on page 35).
- [145] E. Cytrynbaum, J. Scholey, and A. Mogilner. 'A Force Balance Model of Early Spindle Pole Separation in Drosophila Embryos'. *Biophysical Journal* 84.2 (2003), 757–769. doi: [10.1016/S0006-3495\(03\)74895-4](https://doi.org/10.1016/S0006-3495(03)74895-4) (cited on page 35).
- [146] S. C. Schaffner and J. V. Jose. 'Biophysical model of self-organized spindle formation patterns without centrosomes and kinetochores'. *Proceedings of the National Academy of Sciences* 103.30 (2006), 11166–11171. doi: [10.1073/pnas.0604721103](https://doi.org/10.1073/pnas.0604721103) (cited on page 35).
- [147] K. S. Burbank, T. J. Mitchison, and D. S. Fisher. 'Slide-and-Cluster Models for Spindle Assembly'. *Current Biology* 17.16 (2007), 1373–1383. doi: [10.1016/j.cub.2007.07.058](https://doi.org/10.1016/j.cub.2007.07.058) (cited on page 35).
- [148] C. Edelmaier *et al.* 'Mechanisms of chromosome biorientation and bipolar spindle assembly analyzed by computational modeling'. *eLife* 9 (2020), e48787. doi: [10.7554/eLife.48787](https://doi.org/10.7554/eLife.48787) (cited on page 35).
- [149] M. Dogterom and B. Yurke. 'Microtubule Dynamics and the Positioning of Microtubule Organizing Centers'. *Physical Review Letters* 81.2 (1998), 485–488. doi: [10.1103/PhysRevLett.81.485](https://doi.org/10.1103/PhysRevLett.81.485) (cited on page 35).
- [150] S. W. Grill *et al.* 'Polarity controls forces governing asymmetric spindle positioning in the *Caenorhabditis elegans* embryo'. *Nature* 409.6820 (2001), 630–633. doi: [10.1038/35054572](https://doi.org/10.1038/35054572) (cited on page 35).
- [151] L. Laan *et al.* 'Cortical Dynein Controls Microtubule Dynamics to Generate Pulling Forces that Position Microtubule Asters'. *Cell* 148.3 (2012), 502–514. doi: [10.1016/j.cell.2012.01.007](https://doi.org/10.1016/j.cell.2012.01.007) (cited on page 35).
- [152] N. Pavin *et al.* 'Positioning of microtubule organizing centers by cortical pushing and pulling forces'. *New Journal of Physics* 14.10 (2012), 105025. doi: [10.1088/1367-2630/14/10/105025](https://doi.org/10.1088/1367-2630/14/10/105025) (cited on page 35).
- [153] R. Ma *et al.* 'General theory for the mechanics of confined microtubule asters'. *New Journal of Physics* 16.1 (2014), 013018. doi: [10.1088/1367-2630/16/1/013018](https://doi.org/10.1088/1367-2630/16/1/013018) (cited on page 35).
- [154] G. Goshima *et al.* 'Length control of the metaphase spindle'. *Current Biology* 15.22 (2005), 1979–1988. doi: [10.1016/j.cub.2005.09.054](https://doi.org/10.1016/j.cub.2005.09.054) (cited on page 35).
- [155] N. P. Ferenz *et al.* 'Dynein Antagonizes Eg5 by Crosslinking and Sliding Antiparallel Microtubules'. *Current Biology* 19.21 (2009), 1833–1838. doi: [10.1016/j.cub.2009.09.025](https://doi.org/10.1016/j.cub.2009.09.025) (cited on page 35).
- [156] T. L. Hill. 'Theoretical problems related to the attachment of microtubules to kinetochores'. *Proceedings of the National Academy of Sciences* 82.13 (1985), 4404–4408. doi: [10.1073/pnas.82.13.4404](https://doi.org/10.1073/pnas.82.13.4404) (cited on pages 35, 37).

- [157] T. E. Holy and S. Leibler. 'Dynamic instability of microtubules as an efficient way to search in space.' *Proceedings of the National Academy of Sciences* 91.12 (1994), 5682–5685. doi: [10.1073/pnas.91.12.5682](https://doi.org/10.1073/pnas.91.12.5682) (cited on page 35).
- [158] R. Wollman *et al.* 'Efficient Chromosome Capture Requires a Bias in the 'Search-and-Capture' Process during Mitotic-Spindle Assembly'. *Current Biology* 15.9 (2005), 828–832. doi: [10.1016/j.cub.2005.03.019](https://doi.org/10.1016/j.cub.2005.03.019) (cited on page 35).
- [159] I. Kalinina *et al.* 'Pivoting of microtubules around the spindle pole accelerates kinetochore capture'. *Nature Cell Biology* 15.1 (2013), 82–87. doi: [10.1038/ncb2640](https://doi.org/10.1038/ncb2640) (cited on page 35).
- [160] Z. Bertalan *et al.* 'Role of the number of microtubules in chromosome segregation during cell division'. *PLOS ONE* 10.10 (2015). doi: [10.1371/journal.pone.0141305](https://doi.org/10.1371/journal.pone.0141305) (cited on page 35).
- [161] E. Vladimirov *et al.* 'Springs, clutches and motors: driving forward kinetochore mechanism by modelling'. *Chromosome Research* 19.3 (2011), 409–421. doi: [10.1007/s10577-011-9191-x](https://doi.org/10.1007/s10577-011-9191-x) (cited on page 35).
- [162] G. Gay *et al.* 'A stochastic model of kinetochore–microtubule attachment accurately describes fission yeast chromosome segregation'. *Journal of Cell Biology* 196.6 (2012), 757–774. doi: [10.1083/jcb.201107124](https://doi.org/10.1083/jcb.201107124) (cited on pages 35, 55, 85, 122).
- [163] H. Jiang. 'Cell Size Modulates Oscillation, Positioning and Length of Mitotic Spindles'. *Scientific Reports* 5 (2015), 10504. doi: [10.1038/srep10504](https://doi.org/10.1038/srep10504) (cited on pages 35, 40, 122).
- [164] B. L. Sprague *et al.* 'Mechanisms of Microtubule-Based Kinetochore Positioning in the Yeast Metaphase Spindle'. *Biophysical Journal* 84.6 (2003), 3529–3546. doi: [10.1016/S0006-3495\(03\)75087-5](https://doi.org/10.1016/S0006-3495(03)75087-5) (cited on pages 35, 76).
- [165] C. G. Pearson *et al.* 'Stable Kinetochore-Microtubule Attachment Constrains Centromere Positioning in Metaphase'. *Current Biology* 14.21 (2004), 1962–1967. doi: [10.1016/j.cub.2004.09.086](https://doi.org/10.1016/j.cub.2004.09.086) (cited on page 35).
- [166] M. K. Gardner *et al.* 'Tension-dependent Regulation of Microtubule Dynamics at Kinetochores Can Explain Metaphase Congression in Yeast'. *Molecular Biology of the Cell* 16.8 (2005), 3764–3775. doi: [10.1091/mbc.e05-04-0275](https://doi.org/10.1091/mbc.e05-04-0275) (cited on page 35).
- [167] J. Liu *et al.* 'A mechanobiochemical mechanism for monooriented chromosome oscillation in mitosis'. *Proceedings of the National Academy of Sciences* 104.41 (2007), 16104–16109. doi: [10.1073/pnas.0707689104](https://doi.org/10.1073/pnas.0707689104) (cited on page 35).
- [168] O. Campàs and P. Sens. 'Chromosome Oscillations in Mitosis'. *Physical Review Letters* 97.12 (2006), 128102. doi: [10.1103/PhysRevLett.97.128102](https://doi.org/10.1103/PhysRevLett.97.128102) (cited on page 35).
- [169] A. S. Bajer. 'Functional autonomy of monopolar spindle and evidence for oscillatory movement in mitosis'. *Journal of Cell Biology* 93.1 (1982), 33–48. doi: [10.1083/jcb.93.1.33](https://doi.org/10.1083/jcb.93.1.33) (cited on page 35).
- [170] C. L. Rieder *et al.* 'Oscillatory movements of monooriented chromosomes and their position relative to the spindle pole result from the ejection properties of the aster and half-spindle'. *The Journal of Cell Biology* 103.2 (1986), 581–591. doi: [10.1083/jcb.103.2.581](https://doi.org/10.1083/jcb.103.2.581) (cited on page 35).
- [171] B. H. Kwok and T. M. Kapoor. 'Microtubule flux: drivers wanted'. *Current Opinion in Cell Biology* 19.1 (2007), 36–42. doi: [10.1016/j.ceb.2006.12.003](https://doi.org/10.1016/j.ceb.2006.12.003) (cited on pages 36, 42, 60).
- [172] M. Mazumdar and T. Misteli. 'Chromokinesins: multitasking players in mitosis'. *Trends in Cell Biology* 15.7 (2005), 349–355. doi: [10.1016/j.tcb.2005.05.006](https://doi.org/10.1016/j.tcb.2005.05.006) (cited on pages 36, 42, 62).

- [173] D. Ghanti, S. Patra, and D. Chowdhury. 'Molecular force spectroscopy of kinetochore-microtubule attachment in silico : Mechanical signatures of an unusual catch bond and collective effects'. *Physical Review E* 97.5 (2018), 052414. DOI: [10.1103/PhysRevE.97.052414](https://doi.org/10.1103/PhysRevE.97.052414) (cited on pages 37, 51).
- [174] C. B. O'Connell, A. Khodjakov, and B. F. McEwen. 'Kinetochore flexibility: creating a dynamic chromosome-spindle interface'. *Current Opinion in Cell Biology* 24.1 (2012), 40–47. DOI: [10.1016/j.ceb.2011.12.008](https://doi.org/10.1016/j.ceb.2011.12.008) (cited on page 37).
- [175] Y. Dong *et al.* 'The outer plate in vertebrate kinetochores is a flexible network with multiple microtubule interactions'. *Nature Cell Biology* 9.5 (2007), 516–522. DOI: [10.1038/ncb1576](https://doi.org/10.1038/ncb1576) (cited on page 37).
- [176] J. R. McIntosh *et al.* 'Conserved and divergent features of kinetochores and spindle microtubule ends from five species'. *Journal of Cell Biology* 200.4 (2013), 459–474. DOI: [10.1083/jcb.201209154](https://doi.org/10.1083/jcb.201209154) (cited on page 37).
- [177] K. J. VandenBeldt *et al.* 'Kinetochores Use a Novel Mechanism for Coordinating the Dynamics of Individual Microtubules'. *Current Biology* 16.12 (2006), 1217–1223. DOI: [10.1016/j.cub.2006.04.046](https://doi.org/10.1016/j.cub.2006.04.046) (cited on pages 38, 67).
- [178] J. W. Armond *et al.* 'Probing microtubule polymerisation state at single kinetochores during metaphase chromosome motion'. *Journal of Cell Science* 128.10 (2015), 1991–2001. DOI: [10.1242/jcs.168682](https://doi.org/10.1242/jcs.168682) (cited on page 38).
- [179] B. Zelinski and J. Kierfeld. 'Cooperative dynamics of microtubule ensembles: Polymerization forces and rescue-induced oscillations'. *Physical Review E* 87.1 (2013), 012703. DOI: [10.1103/PhysRevE.87.012703](https://doi.org/10.1103/PhysRevE.87.012703) (cited on page 45).
- [180] B. Zelinski, N. Müller, and J. Kierfeld. 'Dynamics and length distribution of microtubules under force and confinement'. *Physical Review E* 86.4 (2012), 041918. DOI: [10.1103/PhysRevE.86.041918](https://doi.org/10.1103/PhysRevE.86.041918) (cited on pages 46, 48, 68, 122).
- [181] M. Zeitz and J. Kierfeld. 'Feedback Mechanism for Microtubule Length Regulation by Stathmin Gradients'. *Biophysical Journal* 107.12 (2014), 2860–2871. DOI: [10.1016/j.bpj.2014.10.056](https://doi.org/10.1016/j.bpj.2014.10.056) (cited on page 46).
- [182] G. C. Rogers, S. L. Rogers, and D. J. Sharp. 'Spindle microtubules in flux'. *Journal of Cell Science* 118.6 (2005), 1105–1116. DOI: [10.1242/jcs.02284](https://doi.org/10.1242/jcs.02284) (cited on page 61).
- [183] Y. Zhai, P. J. Kronebusch, and G. G. Borisy. 'Kinetochore microtubule dynamics and the metaphase-anaphase transition.' *The Journal of Cell Biology* 131.3 (1995), 721–734. DOI: [10.1083/jcb.131.3.721](https://doi.org/10.1083/jcb.131.3.721) (cited on page 61).
- [184] T. J. Mitchison and E. D. Salmon. 'Poleward kinetochore fiber movement occurs during both metaphase and anaphase-A in newt lung cell mitosis'. *Journal of Cell Biology* 119.3 (1992), 569–581. DOI: [10.1083/jcb.119.3.569](https://doi.org/10.1083/jcb.119.3.569) (cited on page 61).
- [185] I. Brust-Mascher and J. M. Scholey. 'Microtubule Flux and Sliding in Mitotic Spindles of *Drosophila* Embryos'. *Molecular Biology of the Cell* 13.11 (2002), 3967–3975. DOI: [10.1091/mbc.02-05-0069](https://doi.org/10.1091/mbc.02-05-0069) (cited on page 61).
- [186] D. T. Miyamoto *et al.* 'The kinesin Eg5 drives poleward microtubule flux in *Xenopus laevis* egg extract spindles'. *Journal of Cell Biology* 167.5 (2004), 813–818. DOI: [10.1083/jcb.200407126](https://doi.org/10.1083/jcb.200407126) (cited on page 61).

- [187] K. Ke, J. Cheng, and A. J. Hunt. 'The Distribution of Polar Ejection Forces Determines the Amplitude of Chromosome Directional Instability'. *Current Biology* 19.10 (2009), 807–815. doi: [10.1016/j.cub.2009.04.036](https://doi.org/10.1016/j.cub.2009.04.036) (cited on pages 63, 79).
- [188] L. Wordeman and T. J. Mitchison. 'Identification and partial characterization of mitotic centromere-associated kinesin, a kinesin-related protein that associates with centromeres during mitosis.' *Journal of Cell Biology* 128.1 (1995), 95–104. doi: [10.1083/jcb.128.1.95](https://doi.org/10.1083/jcb.128.1.95) (cited on page 67).
- [189] C. N. Newton *et al.* 'MCAK, a Kin I kinesin, increases the catastrophe frequency of steady-state HeLa cell microtubules in an ATP-dependent manner in vitro'. *FEBS Letters* 572.1-3 (2004), 80–84. doi: [10.1016/j.febslet.2004.06.093](https://doi.org/10.1016/j.febslet.2004.06.093) (cited on pages 67, 71, 73, 79).
- [190] B. M. Mulder. 'Microtubules interacting with a boundary: Mean length and mean first-passage times'. *Physical Review E* 86.1 (2012), 011902. doi: [10.1103/PhysRevE.86.011902](https://doi.org/10.1103/PhysRevE.86.011902) (cited on page 68).
- [191] R. R. Wei, P. K. Sorger, and S. C. Harrison. 'Molecular organization of the Ndc80 complex, an essential kinetochore component'. *Proceedings of the National Academy of Sciences* 102.15 (2005), 5363–5367. doi: [10.1073/pnas.0501168102](https://doi.org/10.1073/pnas.0501168102) (cited on pages 71, 80, 86, 98, 100).
- [192] H.-W. Wang *et al.* 'Architecture and Flexibility of the Yeast Ndc80 Kinetochore Complex'. *Journal of Molecular Biology* 383.4 (2008), 894–903. doi: [10.1016/j.jmb.2008.08.077](https://doi.org/10.1016/j.jmb.2008.08.077) (cited on pages 71, 80, 86, 87, 100, 101, 117, 118).
- [193] T. J. Maresca and E. D. Salmon. 'Intrakinetochore stretch is associated with changes in kinetochore phosphorylation and spindle assembly checkpoint activity'. *Journal of Cell Biology* 184.3 (2009), 373–381. doi: [10.1083/jcb.200808130](https://doi.org/10.1083/jcb.200808130) (cited on pages 71, 80).
- [194] K. H. Walen and S. W. Brown. 'Chromosomes in a Marsupial (*Potorous tridactylis*) Tissue Culture'. *Nature* 194.4826 (1962), 406–406. doi: [10.1038/194406a0](https://doi.org/10.1038/194406a0) (cited on page 72).
- [195] Cellosaurus – a knowledge resource on cell lines [273]. *Pt K1 (CVCL_0489)*. URL: https://web.expasy.org/cellosaurus/CVCL_0489 (visited on 05/25/2021) (cited on page 72).
- [196] D. Cimini, L. A. Cameron, and E. D. Salmon. 'Anaphase Spindle Mechanics Prevent Mis-Segregation of Merotelically Oriented Chromosomes'. *Current Biology* 14.23 (2004), 2149–2155. doi: [10.1016/j.cub.2004.11.029](https://doi.org/10.1016/j.cub.2004.11.029) (cited on pages 72, 82).
- [197] L. A. Cameron *et al.* 'Kinesin 5-independent poleward flux of kinetochore microtubules in PtK1 cells'. *Journal of Cell Biology* 173.2 (2006), 173–179. doi: [10.1083/jcb.200601075](https://doi.org/10.1083/jcb.200601075) (cited on pages 72, 82).
- [198] M. Winey *et al.* 'Three-dimensional ultrastructural analysis of the *Saccharomyces cerevisiae* mitotic spindle.' *Journal of Cell Biology* 129.6 (1995), 1601–1615. doi: [10.1083/jcb.129.6.1601](https://doi.org/10.1083/jcb.129.6.1601) (cited on pages 72, 76).
- [199] A. F. Straight. 'Mitosis in Living Budding Yeast: Anaphase A But No Metaphase Plate'. *Science* 277.5325 (1997), 574–578. doi: [10.1126/science.277.5325.574](https://doi.org/10.1126/science.277.5325.574) (cited on pages 76, 78).
- [200] C. G. Pearson *et al.* 'Budding Yeast Chromosome Structure and Dynamics during Mitosis'. *Journal of Cell Biology* 152.6 (2001), 1255–1266. doi: [10.1083/jcb.152.6.1255](https://doi.org/10.1083/jcb.152.6.1255) (cited on page 76).
- [201] K. Nabeshima *et al.* 'Dynamics of Centromeres during Metaphase–Anaphase Transition in Fission Yeast: Dis1 Is Implicated in Force Balance in Metaphase Bipolar Spindle'. *Molecular Biology of the Cell* 9.11 (1998), 3211–3225. doi: [10.1091/mbc.9.11.3211](https://doi.org/10.1091/mbc.9.11.3211) (cited on page 76).

- [202] R. Ding, K. L. McDonald, and J. R. McIntosh. 'Three-dimensional reconstruction and analysis of mitotic spindles from the yeast, *Schizosaccharomyces pombe*.' *Journal of Cell Biology* 120.1 (1993), 141–151. doi: [10.1083/jcb.120.1.141](https://doi.org/10.1083/jcb.120.1.141) (cited on page 76).
- [203] H. Mary *et al.* 'Fission yeast Kinesin-8 controls chromosome congression independently of oscillations'. *Journal of Cell Science* 128.20 (2015), 3720–3730. doi: [10.1242/jcs.160465](https://doi.org/10.1242/jcs.160465) (cited on page 79).
- [204] Z. R. Gergely *et al.* 'Kinesin-8 effects on mitotic microtubule dynamics contribute to spindle function in fission yeast'. *Molecular Biology of the Cell* 27.22 (2016), 3490–3514. doi: [10.1091/mbc.e15-07-0505](https://doi.org/10.1091/mbc.e15-07-0505) (cited on page 79).
- [205] M. I. Mayr *et al.* 'The Human Kinesin Kif18A Is a Motile Microtubule Depolymerase Essential for Chromosome Congression'. *Current Biology* 17.6 (2007), 488–498. doi: [10.1016/j.cub.2007.02.036](https://doi.org/10.1016/j.cub.2007.02.036) (cited on page 79).
- [206] V. Wood *et al.* 'The genome sequence of *Schizosaccharomyces pombe*'. *Nature* 415.6874 (2002), 871–880. doi: [10.1038/nature724](https://doi.org/10.1038/nature724) (cited on page 79).
- [207] V. Varga *et al.* 'Yeast kinesin-8 depolymerizes microtubules in a length-dependent manner'. *Nature Cell Biology* 8.9 (2006), 957–962. doi: [10.1038/ncb1462](https://doi.org/10.1038/ncb1462) (cited on page 79).
- [208] V. Varga *et al.* 'Kinesin-8 Motors Act Cooperatively to Mediate Length-Dependent Microtubule Depolymerization'. *Cell* 138.6 (2009), 1174–1183. doi: [10.1016/j.cell.2009.07.032](https://doi.org/10.1016/j.cell.2009.07.032) (cited on page 79).
- [209] J. G. DeLuca *et al.* 'Kinetochores Microtubule Dynamics and Attachment Stability Are Regulated by Hec1'. *Cell* 127.5 (2006), 969–982. doi: [10.1016/j.cell.2006.09.047](https://doi.org/10.1016/j.cell.2006.09.047) (cited on pages 81, 87, 114).
- [210] A. V. Zaytsev *et al.* 'Accurate phosphoregulation of kinetochore–microtubule affinity requires unconstrained molecular interactions'. *Journal of Cell Biology* 206.1 (2014), 45–59. doi: [10.1083/jcb.201312107](https://doi.org/10.1083/jcb.201312107) (cited on pages 81, 87, 114).
- [211] K. F. DeLuca *et al.* 'Aurora A kinase phosphorylates Hec1 to regulate metaphase kinetochore–microtubule dynamics'. *Journal of Cell Biology* 217.1 (2018), 163–177. doi: [10.1083/jcb.201707160](https://doi.org/10.1083/jcb.201707160) (cited on pages 81, 87, 114).
- [212] N. T. Umbreit *et al.* 'The Ndc80 kinetochore complex directly modulates microtubule dynamics'. *Proceedings of the National Academy of Sciences* 109.40 (2012), 16113–16118. doi: [10.1073/pnas.1209615109](https://doi.org/10.1073/pnas.1209615109) (cited on pages 81, 87, 88, 112, 114).
- [213] F. Schwietert *et al.* 'Strain stiffening of Ndc80 complexes attached to microtubule plus ends'. *Biophysical Journal* (2022), in press. doi: [10.1016/j.bpj.2022.09.039](https://doi.org/10.1016/j.bpj.2022.09.039) (cited on page 85).
- [214] L. Zheng, Y. Chen, and W.-H. Lee. 'Hec1p, an Evolutionarily Conserved Coiled-Coil Protein, Modulates Chromosome Segregation through Interaction with SMC Proteins'. *Molecular and Cellular Biology* 19.8 (1999), 5417–5428. doi: [10.1128/MCB.19.8.5417](https://doi.org/10.1128/MCB.19.8.5417) (cited on page 86).
- [215] Wikimedia Commons user *YassineMrabet*. *The typical structure of the amino acid*. Original has been released into public domain. URL: <https://commons.wikimedia.org/wiki/File:AminoAcidball.svg> (visited on 11/02/2021) (cited on page 87).
- [216] C. Ciferri *et al.* 'Architecture of the Human Ndc80-Hec1 Complex, a Critical Constituent of the Outer Kinetochore'. *Journal of Biological Chemistry* 280.32 (2005), 29088–29095. doi: [10.1074/jbc.M504070200](https://doi.org/10.1074/jbc.M504070200) (cited on page 86).

- [217] A. Maiolica *et al.* 'Structural Analysis of Multiprotein Complexes by Cross-linking, Mass Spectrometry, and Database Searching'. *Molecular & Cellular Proteomics* 6.12 (2007), 2200–2211. doi: [10.1074/mcp.M700274-MCP200](https://doi.org/10.1074/mcp.M700274-MCP200) (cited on page 86).
- [218] M. Gimona *et al.* 'Functional plasticity of CH domains'. *FEBS Letters* 513.1 (2002), 98–106. doi: [10.1016/S0014-5793\(01\)03240-9](https://doi.org/10.1016/S0014-5793(01)03240-9) (cited on page 87).
- [219] K. C. Slep and R. D. Vale. 'Structural Basis of Microtubule Plus End Tracking by XMAP215, CLIP-170, and EB1'. *Molecular Cell* 27.6 (2007), 976–991. doi: [10.1016/j.molcel.2007.07.023](https://doi.org/10.1016/j.molcel.2007.07.023) (cited on page 87).
- [220] R. R. Wei, J. Al-Bassam, and S. C. Harrison. 'The Ndc80/HEC1 complex is a contact point for kinetochore-microtubule attachment'. *Nature Structural & Molecular Biology* 14.1 (2007), 54–59. doi: [10.1038/nsmb1186](https://doi.org/10.1038/nsmb1186) (cited on pages 87, 98).
- [221] C. Ciferri *et al.* 'Implications for Kinetochore-Microtubule Attachment from the Structure of an Engineered Ndc80 Complex'. *Cell* 133.3 (2008), 427–439. doi: [10.1016/j.cell.2008.03.020](https://doi.org/10.1016/j.cell.2008.03.020) (cited on pages 87, 88, 98, 113).
- [222] G. M. Alushin *et al.* 'The Ndc80 kinetochore complex forms oligomeric arrays along microtubules'. *Nature* 467.7317 (2010), 805–810. doi: [10.1038/nature09423](https://doi.org/10.1038/nature09423) (cited on pages 87, 98, 109, 111, 113, 121).
- [223] R. T. Wimbish and J. G. DeLuca. 'Hec1/Ndc80 Tail Domain Function at the Kinetochore-Microtubule Interface'. *Frontiers in Cell and Developmental Biology* 8.February (2020), 1–16. doi: [10.3389/fcell.2020.00043](https://doi.org/10.3389/fcell.2020.00043) (cited on pages 87, 88, 113).
- [224] S. A. Miller, M. L. Johnson, and P. T. Stukenberg. 'Kinetochore Attachments Require an Interaction between Unstructured Tails on Microtubules and Ndc80^{Hec1}'. *Current Biology* 18.22 (2008), 1785–1791. doi: [10.1016/j.cub.2008.11.007](https://doi.org/10.1016/j.cub.2008.11.007) (cited on page 87).
- [225] G. M. Alushin *et al.* 'Multimodal microtubule binding by the Ndc80 kinetochore complex'. *Nature Structural & Molecular Biology* 19.11 (2012), 1161–1167. doi: [10.1038/nsmb.2411](https://doi.org/10.1038/nsmb.2411) (cited on page 87).
- [226] SuSoS AG, Switzerland. *SuSoS PLL-g-PEG Polymers*. URL: <https://susos.com/beschichtungstechnologien/pll-g-peg-polymere> (visited on 01/27/2022) (cited on page 89).
- [227] P. H. Jones, O. M. Maragò, and G. Volpe. *Optical Tweezers: Principles and Applications*. Cambridge: Cambridge University Press, 2015 (cited on pages 90, 115, 135, 136).
- [228] K. Visscher and S. M. Block. 'Versatile optical traps with feedback control'. *Methods in Enzymology* 298 (1998), 460–489. doi: [10.1016/S0076-6879\(98\)98040-5](https://doi.org/10.1016/S0076-6879(98)98040-5) (cited on pages 90, 115, 135).
- [229] K. C. Neuman and S. M. Block. 'Optical trapping'. *Review of Scientific Instruments* 75.9 (2004), 2787–2809. doi: [10.1063/1.1785844](https://doi.org/10.1063/1.1785844) (cited on pages 90, 115, 135).
- [230] M. Sarshar, W. T. Wong, and B. Anvari. 'Comparative study of methods to calibrate the stiffness of a single-beam gradient-force optical tweezers over various laser trapping powers'. *Journal of Biomedical Optics* 19.11 (2014), 115001. doi: [10.1117/1.JBO.19.11.115001](https://doi.org/10.1117/1.JBO.19.11.115001) (cited on pages 90, 115, 135).
- [231] K. Berg-Sørensen and H. Flyvbjerg. 'Power spectrum analysis for optical tweezers'. *Review of Scientific Instruments* 75.3 (2004), 594–612. doi: [10.1063/1.1645654](https://doi.org/10.1063/1.1645654) (cited on pages 90, 102, 115, 136).

- [232] I. M. Tolić-Nørrelykke, K. Berg-Sørensen, and H. Flyvbjerg. 'MatLab program for precision calibration of optical tweezers'. *Computer Physics Communications* 159.3 (2004), 225–240. doi: [10.1016/j.cpc.2004.02.012](https://doi.org/10.1016/j.cpc.2004.02.012) (cited on pages 90, 102, 115, 136).
- [233] M. P. Nicholas, L. Rao, and A. Gennerich. 'An Improved Optical Tweezers Assay for Measuring the Force Generation of Single Kinesin Molecules'. *Methods in Molecular Biology* 1136 (2014), 171–246. doi: [10.1007/978-1-4939-0329-0_10](https://doi.org/10.1007/978-1-4939-0329-0_10) (cited on pages 90, 102, 115, 136).
- [234] P. J. Huber. 'Robust Estimation of a Location Parameter'. *The Annals of Mathematical Statistics* 35.1 (1964), 73–101. doi: [10.1214/aoms/1177703732](https://doi.org/10.1214/aoms/1177703732) (cited on pages 94, 138).
- [235] D. de Menezes *et al.* 'A review on robust M-estimators for regression analysis'. *Computers & Chemical Engineering* 147 (2021), 107254. doi: [10.1016/j.compchemeng.2021.107254](https://doi.org/10.1016/j.compchemeng.2021.107254) (cited on pages 94, 138).
- [236] J. G. DeLuca and A. Musacchio. 'Structural organization of the kinetochore–microtubule interface'. *Current Opinion in Cell Biology* 24.1 (2012), 48–56. doi: [10.1016/j.ceb.2011.11.003](https://doi.org/10.1016/j.ceb.2011.11.003) (cited on page 99).
- [237] A. Musacchio and A. Desai. 'A Molecular View of Kinetochore Assembly and Function'. *Biology* 6.1 (2017), 5. doi: [10.3390/biology6010005](https://doi.org/10.3390/biology6010005) (cited on pages 99, 120).
- [238] S. Pasche *et al.* 'Relationship between Interfacial Forces Measured by Colloid-Probe Atomic Force Microscopy and Protein Resistance of Poly(ethylene glycol)-Grafted Poly(L-lysine) Adlayers on Niobia Surfaces'. *Langmuir* 21.14 (2005), 6508–6520. doi: [10.1021/la050386x](https://doi.org/10.1021/la050386x) (cited on pages 99, 118).
- [239] F. Oesterhelt, M. Rief, and H. E. Gaub. 'Single molecule force spectroscopy by AFM indicates helical structure of poly(ethylene-glycol) in water'. *New Journal of Physics* 1 (1999), 6–6. doi: [10.1088/1367-2630/1/1/006](https://doi.org/10.1088/1367-2630/1/1/006) (cited on pages 99, 100, 118).
- [240] P. J. Flory. *Statistical mechanics of chain molecules*. New York: Interscience Publishers, 1969 (cited on pages 99, 102).
- [241] J. Kierfeld *et al.* 'Stretching of semiflexible polymers with elastic bonds'. *The European Physical Journal E* 14.1 (2004), 17–34. doi: [10.1140/epje/i2003-10089-3](https://doi.org/10.1140/epje/i2003-10089-3) (cited on pages 102, 139).
- [242] J. A. Tuszyński *et al.* 'Anisotropic elastic properties of microtubules'. *The European Physical Journal E* 17.1 (2005), 29–35. doi: [10.1140/epje/i2004-10102-5](https://doi.org/10.1140/epje/i2004-10102-5) (cited on page 103).
- [243] F. Pampaloni *et al.* 'Thermal fluctuations of grafted microtubules provide evidence of a length-dependent persistence length'. *Proceedings of the National Academy of Sciences* 103.27 (2006), 10248–10253. doi: [10.1073/pnas.0603931103](https://doi.org/10.1073/pnas.0603931103) (cited on pages 105, 118).
- [244] J. F. Marko and E. D. Siggia. 'Stretching DNA'. *Macromolecules* 28.26 (1995), 8759–8770. doi: [10.1021/ma00130a008](https://doi.org/10.1021/ma00130a008) (cited on page 106).
- [245] W. E. Thomas, V. Vogel, and E. Sokurenko. 'Biophysics of Catch Bonds'. *Annual Review of Biophysics* 37.1 (2008), 399–416. doi: [10.1146/annurev.biophys.37.032807.125804](https://doi.org/10.1146/annurev.biophys.37.032807.125804) (cited on page 109).
- [246] K. K. Sarangapani and C. L. Asbury. 'Catch and release: how do kinetochores hook the right microtubules during mitosis?' *Trends in Genetics* 30.4 (2014), 150–159. doi: [10.1016/j.tig.2014.02.004](https://doi.org/10.1016/j.tig.2014.02.004) (cited on page 112).
- [247] D. Liu *et al.* 'Sensing Chromosome Bi-Oriented by Spatial Separation of Aurora B Kinase from Kinetochore Substrates'. *Science* 323.5919 (2009), 1350–1353. doi: [10.1126/science.1167000](https://doi.org/10.1126/science.1167000) (cited on page 112).

- [248] G. V. Caldas, K. F. DeLuca, and J. G. DeLuca. 'KNL1 facilitates phosphorylation of outer kinetochore proteins by promoting Aurora B kinase activity'. *Journal of Cell Biology* 203.6 (2013), 957–969. DOI: [10.1083/jcb.201306054](https://doi.org/10.1083/jcb.201306054) (cited on page 112).
- [249] M. P. Miller, C. L. Asbury, and S. Biggins. 'A TOG Protein Confers Tension Sensitivity to Kinetochore-Microtubule Attachments'. *Cell* 165.6 (2016), 1428–1439. DOI: [10.1016/j.cell.2016.04.030](https://doi.org/10.1016/j.cell.2016.04.030) (cited on page 112).
- [250] E. A. Scarborough, T. N. Davis, and C. L. Asbury. 'Tight bending of the Ndc80 complex provides intrinsic regulation of its binding to microtubules'. *eLife* 8 (2019), e44489. DOI: [10.7554/eLife.44489](https://doi.org/10.7554/eLife.44489) (cited on page 112).
- [251] E. Roscioli *et al.* 'Ensemble-Level Organization of Human Kinetochores and Evidence for Distinct Tension and Attachment Sensors'. *Cell Reports* 31.4 (2020), 107535. DOI: [10.1016/j.celrep.2020.107535](https://doi.org/10.1016/j.celrep.2020.107535) (cited on page 112).
- [252] E. V. Sokurenko, V. Vogel, and W. E. Thomas. 'Catch-Bond Mechanism of Force-Enhanced Adhesion: Counterintuitive, Elusive, but ... Widespread?' *Cell Host & Microbe* 4.4 (2008), 314–323. DOI: [10.1016/j.chom.2008.09.005](https://doi.org/10.1016/j.chom.2008.09.005) (cited on page 113).
- [253] S. W. Schneider *et al.* 'Shear-induced unfolding triggers adhesion of von Willebrand factor fibers'. *Proceedings of the National Academy of Sciences* 104.19 (2007), 7899–7903. DOI: [10.1073/pnas.0608422104](https://doi.org/10.1073/pnas.0608422104) (cited on page 113).
- [254] G. Interlandi and W. Thomas. 'The catch bond mechanism between von Willebrand factor and platelet surface receptors investigated by molecular dynamics simulations'. *Proteins: Structure, Function and Bioinformatics* 78.11 (2010), 2506–22. DOI: [10.1002/prot.22759](https://doi.org/10.1002/prot.22759) (cited on page 113).
- [255] C. Arbore *et al.* ' α -catenin switches between a slip and an asymmetric catch bond with F-actin to cooperatively regulate cell junction fluidity'. *bioRxiv* (2021). DOI: [10.1101/2020.04.15.035527](https://doi.org/10.1101/2020.04.15.035527) (cited on page 113).
- [256] S. Hvidt *et al.* 'Flexibility of light meromyosin and other coiled-coil α -helical proteins'. *Macromolecules* 16.5 (1983), 740–745. DOI: [10.1021/ma00239a007](https://doi.org/10.1021/ma00239a007) (cited on pages 115, 140).
- [257] A. Ranaweera and B. Bamieh. 'Modelling, identification, and control of a spherical particle trapped in an optical tweezer'. *International Journal of Robust and Nonlinear Control* 15.16 (2005), 747–768. DOI: [10.1002/rnc.1022](https://doi.org/10.1002/rnc.1022) (cited on pages 115, 135).
- [258] M. D. Koch and J. W. Shaevitz. 'Introduction to Optical Tweezers'. In: *Optical Tweezers: Methods and Protocols*. Ed. by A. Gennerich. New York: Springer New York, 2017, 3–24. DOI: [10.1007/978-1-4939-6421-5_1](https://doi.org/10.1007/978-1-4939-6421-5_1) (cited on pages 115, 135).
- [259] M. M. Shindel, J. W. Swan, and E. M. Furst. 'Calibration of an optical tweezer microrheometer by sequential impulse response'. *Rheologica Acta* 52.5 (2013), 455–465. DOI: [10.1007/s00397-013-0698-2](https://doi.org/10.1007/s00397-013-0698-2) (cited on page 115).
- [260] Y. Jun *et al.* 'Calibration of Optical Tweezers for In Vivo Force Measurements: How do Different Approaches Compare?' *Biophysical Journal* 107.6 (2014), 1474–1484. DOI: [10.1016/j.bpj.2014.07.033](https://doi.org/10.1016/j.bpj.2014.07.033) (cited on page 115).
- [261] D. J. Bicut. 'Green's functions and first passage time distributions for dynamic instability of microtubules'. *Physical Review E* 56.6 (1997), 6656–6667. DOI: [10.1103/PhysRevE.56.6656](https://doi.org/10.1103/PhysRevE.56.6656) (cited on page 118).
- [262] K. Iemura *et al.* 'Chromosome oscillation promotes Aurora A-dependent Hec1 phosphorylation and mitotic fidelity'. *Journal of Cell Biology* 220.7 (2021). DOI: [10.1083/jcb.202006116](https://doi.org/10.1083/jcb.202006116) (cited on page 122).

- [263] K. Iemura *et al.* 'Attenuated Chromosome Oscillation as a Cause of Chromosomal Instability in Cancer Cells'. *Cancers* 13.18 (2021), 4531. doi: [10.3390/cancers13184531](https://doi.org/10.3390/cancers13184531) (cited on page 122).
- [264] G. E. Uhlenbeck and L. S. Ornstein. 'On the Theory of the Brownian Motion'. *Physical Review* 36.5 (1930), 823–841. doi: [10.1103/PhysRev.36.823](https://doi.org/10.1103/PhysRev.36.823) (cited on page 135).
- [265] C. W. Gardiner. *Handbook of Stochastic Methods for Physics, Chemistry and the Natural Sciences*. 2nd ed. Berlin: Springer-Verlag, 1985 (cited on page 135).
- [266] K. Svoboda and S. M. Block. 'Biological Applications of Optical Forces'. *Annual Review of Biophysics and Biomolecular Structure* 23.1 (1994), 247–285. doi: [10.1146/annurev.bb.23.060194.001335](https://doi.org/10.1146/annurev.bb.23.060194.001335) (cited on page 136).
- [267] F. Gittes and C. F. Schmidt. 'Signals and Noise in Micromechanical Measurements'. *Methods in Cell Biology* 55 (1997), 129–156. doi: [10.1016/S0091-679X\(08\)60406-9](https://doi.org/10.1016/S0091-679X(08)60406-9) (cited on page 136).
- [268] P. W. Holland and R. E. Welsch. 'Robust regression using iteratively reweighted least-squares'. *Communications in Statistics - Theory and Methods* 6.9 (1977), 813–827. doi: [10.1080/03610927708827533](https://doi.org/10.1080/03610927708827533) (cited on page 138).
- [269] G. Casella and R. L. Berger. *Statistical inference*. 2nd ed. Pacific Grove: Duxbury, 2002 (cited on page 138).
- [270] N. Metropolis *et al.* 'Equation of State Calculations by Fast Computing Machines'. *The Journal of Chemical Physics* 21.6 (1953), 1087–1092. doi: [10.1063/1.1699114](https://doi.org/10.1063/1.1699114) (cited on page 139).
- [271] Creative Commons. *Attribution-ShareAlike 4.0 International (CC BY-SA 4.0)*. URL: <https://creativecommons.org/licenses/by-sa/4.0> (visited on 04/04/2022) (cited on page 143).
- [272] Creative Commons. *Attribution-ShareAlike 3.0 Unported (CC BY-SA 3.0)*. URL: <https://creativecommons.org/licenses/by-sa/3.0> (visited on 04/04/2022) (cited on page 147).
- [273] A. Bairoch. 'The Cellosaurus, a Cell-Line Knowledge Resource'. *Journal of Biomolecular Techniques* 29.2 (2018), 25–38. doi: [10.7171/jbt.18-2902-002](https://doi.org/10.7171/jbt.18-2902-002) (cited on page 153).

Notation

List of abbreviations

ADP	adenosine diphosphate
AFM	atomic force microscope
AP	away from the pole, antipolewards
ATP	adenosine triphosphate
CH	calponin homology
DNA	deoxyribonucleic acid
FJC	freely jointed chain
FPE	Fokker–Planck equation
GDP	guanosine diphosphate
GTP	guanosine triphosphate
k-fiber	kinetochore fiber
MAP	microtubule-associated protein
MC	Monte Carlo (simulation)
MCAK	mitotic centromere-associated kinesin
MT	microtubule
MTOC	microtubule organizing center
Ndc80 ^{CHmut}	Ndc80 mutant with mutated CH domains
Ndc80 ^P	Ndc80 with a phosphorylated N-terminal tail
Ndc80 ^{wt}	wild type Ndc80
Ndc80 ^{Δ80}	Ndc80 mutant without N-terminal tail
P	polewards
PEF	polar ejection force
PEG	polyethylene glycol
PF	protofilament
PLL	poly-L-lysine
PSD	power spectral density
S	streptavidin
T	traptavidin

List of symbols used in Chapter 2

$A(k)$	coefficient matrix of Fourier transformed FPEs
c	ω/v_+
C_c	critical concentration
$D_{(n)}$	Diffusion constant in the unbounded regime (with an n -step catastrophe)
$f(\lambda, k)$	characteristic polynomial of $A(k)$
j	probability current density
k_{off}	depolymerization rate
k_{on}	polymerization rate
k_{\pm}	effective elongation rates
M	coefficient matrix of stationary FPEs
n	number of catastrophe steps
$p(x, t)$	time-dependent overall probability density of MT lengths
$p(x)$	steady state overall probability density of MT lengths
$\tilde{p}(s)$	Laplace transform of $p(x)$
$P(n, x)$	regularized lower incomplete gamma function
$p_i(x, t)$	time-dependent probability density of MT lengths in i -th growing state
$p_i(x)$	steady state probability density of MT lengths in i -th growing state
$p_{x_+}(x_+)$	probability density of length gains
$p_{\tau_+}(\tau_+)$	probability density of growth durations
$P_{\tau_+}(\tau)$	survival probability of a growing MT
$p_{\pm}(x, t)$	time-dependent probability density of MT lengths in growing/shrinking state
$p_{\pm}(x)$	steady state probability density of MT lengths in growing/shrinking state
$Q(n, x)$	regularized upper incomplete gamma function
$q_i(k, t)$	Fourier transform of $p_i(x, t)$
r	ω_r/v_-
t	time
$V_{(n)}$	mean velocity of the MT tip (with an n -step catastrophe)
$\vec{v}_j(k)$	eigenvectors of $A(k)$
v_{\pm}	growth/shrinking velocity
x	MT length
x_{\pm}	length gain/loss
$\Gamma(n)$	gamma function
$\Gamma(n, x)$	upper incomplete gamma function
Δt	simulation time step
Δx	monomer length
$\lambda_j(k)$	eigenvalues of $A(k)$
τ	MT age, time since last rescue
τ_{\pm}	growth/shrinking duration
ω	catastrophe step rate
ω_c	catastrophe rate
ω_r	rescue rate

List of symbols used in Chapter 3

c	stiffness of MT–kinetochore linker
c_{bist}	lower bound of linker stiffness for bistable force–velocity relation
c_{k}	stiffness of cohesin bond
c_{osc}	lower bound of linker stiffness for occurrence of kinetochore oscillations
d_0	rest length of cohesin bond
F_c	characteristic force of catastrophe
$F_{\text{d}\pm}$	characteristic force of detachment of a growing/shrinking MT
F_{ext}	external force on kinetochore in one-sided model
$F_{\text{k}(l/r)}$	AP force acting on (left/right) kinetochore by cohesin bond and PEFs ($F_{\text{kk}} + F_{\text{PEF}}$)
F_{kk}	inter-kinetochore force from cohesin bond
F_{km}	force acting on a kinetochore by the attached MTs
$F_{\text{min/max}}$	lower/upper critical force of bistable force–velocity relation
F_{mk}	force acting on a MT tip by the MT–kinetochore linker
$F_{\text{PEF}(l/r)}$	PEFs acting on (left/right) kinetochore in AP-direction
F_r	characteristic force of rescue
F_{\pm}	characteristic force of growth/shrinking velocity
j	probability current density
k	strength (“spring constant”) of PEFs
$k_{\text{B}}T$	thermal energy
M	number of MTs per spindle pole
$M_{\text{att}(l/r)}$	number of MTs attached to (left/right) kinetochore
n	catastrophe enhancement factor at the kinetochore ($\omega_c^{\text{kin}} = n\omega_c^0$)
\mathcal{N}	normalization constant
$p(x, t)$	time-dependent overall probability density of linker extensions
$p(x)$	steady state overall probability density of linker extensions
$p_{\pm}(x, t)$	time-dependent probability density of linker extensions in growing/shrinking state
$p_{\pm}(x)$	steady state probability density of linker extensions in growing/shrinking state
Q	probability to find a MT confined at the kinetochore
t	time
x_c	fixed position of the centrosomes
$x_{(i)}$	distance of (i -th) MT tip to kinetochore, (i -th) linker extension
$X_{\text{k}(l/r)}$	position of (left/right) kinetochore
$\tilde{X}_{\text{k}(l/r)}$	position of (left/right) kinetochore in Fourier space
$x_{\text{m}(i)}$	position of (i -th) MT tip
$x_{\text{min/max}}$	minimum/maximum linker extension
$x_{\text{min/max}}^{\text{conf}}$	minimum/maximum linker extension with confinement at the kinetochore
v_{f}	velocity of poleward MT flux
$v_{\text{k}(l/r)}$	AP velocity of (left/right) kinetochore
v_{k}^{\pm}	AP kinetochore velocity in upper/lower branch of bistable force–velocity relation
$v_{\text{m}\pm}$	growth/shrinking velocity
v_{\pm}	relative velocity of a growing/shrinking MT and kinetochore
\tilde{v}_{\pm}	steady state MT and kinetochore velocity if MTs exclusively grow/shrink
v_{\pm}^0	force-free growth/shrinking velocity
$W()$	Lambert W function
α_{\pm}	leading order exponents of stationary linker length distributions near $x_{\text{max/min}}$

γ	friction coefficient of kinetochore
Δt	simulation time step
ΔX_k	inter kinetochore distance
$\Delta \tilde{X}_k$	inter kinetochore distance in Fourier space
ω_a	attachment rate
ω_a^0	force-free attachment rate
ω_c	catastrophe rate
ω_c^0	force-free catastrophe rate
ω_c^{kin}	(enhanced) catastrophe rate at kinetochore
$\omega_{d\pm}$	detachment rate of a growing/shrinking MT
$\omega_{d\pm}^0$	force-free detachment rate of a growing/shrinking MT
ω_r	rescue rate
ω_r^0	force-free rescue rate

List of symbols used in Chapter 4

a	length of long Ndc80 arm
A	coefficient in power fits
\vec{a}	vector describing long Ndc80 arm in FJC model
b	length of short Ndc80 arm
\vec{b}	vector describing short Ndc80 arm in FJC model
c	total stiffness as measured in experiments
\tilde{c}	stiffness of a single MT-bead linker (series of c_{PEG} , c_{Ndc} , c_{bond} and c_{PF})
c_0	stiffness offset in power fits
c_{bond}	stiffness of the Ndc80–MT bond
c_{mech}	mechanical MT stiffness
c_{MT}	(entropic) MT stiffness
\tilde{c}_n	stiffness of n parallel MT-bead linkers with stiffness \tilde{c}
c_{Ndc}	stiffness of Ndc80 complex
c_{PEG}	stiffness of PEG
c_{PF}	effective stiffness of PF bending
c_{trap}	trap stiffness
E_{FJC}	energy in FJC model of Ndc80 complex
E_{MT}	energy of MT in the mechanical model
E_{PF}	energy of PF stretching
F	force from optical trap or force stretching PEG, Ndc80, MT or PF in models
F_h	Lagrange multiplier in mechanical MT model (force to hold MT tip at height h)
$f_k(t)$	linear fit of bead position $x_k(t)$ during interval k
F_k	mean force during interval k
h	height of MT tip in mechanical MT model
$k_{\text{B}}T$	thermal energy
K_{S}	PEG segment elasticity
L	elongation of PEG or length of free MT end or length of curved PF
L_0	characteristic MT length of length dependent MT persistence length, see Eq. (4.24)
L_{C}	contour length

L_{hel}	segment length of helical PEG conformation
L_K	Kuhn length
L_p	persistence length (of the MT or the PF)
L_p^∞	persistence length of a long MT ($L \gg L_0$), see Eq. (4.24)
L_{pl}	segment length of planar PEG conformation
m	stiffening exponent, exponent in power fits
n	number of Ndc80 complexes attached to the MT
n_{min}	stiffness minimizing number of attached Ndc80 complexes
N_S	number of C–C–O segments in PEG
s	position along curved MT or curved PF
s_0	position of force application along PF
t	time
x	bead displacement from the trap center
z	extension of MT in force direction
$z_{(a/b)}$	extension in force direction (of long/short arm) of Ndc80 complex in FJC model
z_0	effective elongation of PF in force direction
Z	canonical partition function
α	bending stiffness of MT or PF
β	$1/k_B T$
$\theta(s)$	local bending angle of MT or PF
$\theta_{a/b}$	polar angle of long/short Ndc80 arm (\vec{a}/\vec{b})
ϕ	preferred curvature of PF
$\varphi_{a/b}$	azimuthal angle of long/short Ndc80 arm (\vec{a}/\vec{b})

Acknowledgments

An dieser Stelle möchte ich die Gelegenheit nutzen, den vielen Menschen zu danken, die in unterschiedlicher Weise zur Entstehung meiner Doktorarbeit beigetragen haben.

Darunter ist zuerst Jan Kierfeld zu nennen, dem ich für die Betreuung meiner Arbeit, für die vielen konstruktiven Diskussionen und kritischen Anmerkungen sowie für seine stets offene Tür danke.

Herre Jelger Risselada danke ich für die Übernahme des Zweitgutachtens.

Ein weiterer Dank gilt unseren Kollaborateuren Vladimir Volkov, Pim Huis in 't Veld, Andrea Musacchio und Marileen Dogterom für die Bereitstellung ihrer experimentellen Daten und die zahlreichen Diskussionen, die maßgeblich zur Entstehung des 4. Kapitels beigetragen haben. Nach drei Jahren ausschließlich theoretischer Arbeit waren sowohl die direkte Verfügbarkeit experimenteller Daten als auch die fächerübergreifende Zusammenarbeit zwischen Physikern und Biologen eine lehrreiche Erfahrung.

Fürs Korrekturlesen und viele hilfreiche Anmerkungen bedanke ich mich bei Tobias Kampmann, Lukas Weise und Lina Heydenreich. Lina gebührt ein weiterer Dank, da ihre Bachelorarbeit den Anstoß zu Kapitel 2 gab.

Meinen Kolleginnen und Kollegen, mit denen ich die Jahre am Lehrstuhl verbracht habe, danke ich für die angenehme Arbeitsatmosphäre und die vielen Gespräche abseits der Physik, die für die nötige Zerstreuung gesorgt haben.

Der letzte und größte Dank gilt meiner Familie und besonders meinen Eltern für die Liebe und die Unterstützung, mit der sie mich auf meinem bisherigen Lebensweg begleitet haben.